University of Nottingham
UK | CHINA | MALAYSIA

Condition Monitoring of Tool Performance Using Machine Learning-Based On-Machine Vision System During Face Milling of Inconel 718

Thesis Submitted To The University of Nottingham for The Degree of

Doctor of Philosophy in Mechanical Engineering

Author:
Tiyamike Banda
(MSc., BSc)

Main Supervisor
Prof. Chin Seong Lim

Co-Supervisor:
Prof. Ali Akhavan Farid

February 4, 2024

Abstract

0.1 General Abstract

The superior properties of Inconel 718 necessitate its use in manufacturing more than 50% of aircraft engine structural components, including high-pressure compressor blades, casings, and discs. However, literature attributed the synergistic impact of these properties and process parameters as the primary cause of wear complexity, notably affecting the performance of PVD-coated carbide inserts during CNC milling of Inconel 718. Features stemming from the wear complexity include uncontrolled wear mechanisms, failure modes, and a rapid flank wear rate, serving as significant indicators of sub-optimal cutting conditions. In trying to diagnose tool wear, previous Tool Condition Monitoring (TCM) techniques could not decipher, explore, and synthesise the diverse features essential for the predictive control of tool performance in challenging CNC machining conditions. Therefore, the successful implementation of advanced feature engineering and Machine Learning (ML) models in Machine Vision-based TCM (MV-TCM) offers a proactive approach in predicting and controlling the performance of PVD-coated carbide tools in challenging CNC machining domains.

The hypothesis of this study encompassed three aspects. The first aspect focused on the study of tool wear complexity by characterizing the dominant wear mechanisms, failure modes, and flank wear depth (VB) during face milling of Inconel 718. These features were correlated with the process parameters to establish a coherent tool wear dataset for training the feature engineering and ML models. The second aspect involved the development of feature engineering and ML models, including the multi-sectional singular value decomposition (SVD), a YOLOv3 Tool Wear Detection Model (YOLOv3-TWDM), a multi-layer perceptron neural network (MLPNN), and an inductive-reasoning algorithm. The final aspect pertained to the development of a volatile MV-TCM system's design, which was integrated with feature engineering and ML techniques to create an enhanced ML-based MV-TCM system. The system was vigorously validated by conducting an online experiment, where the predicted were compared with the actual wear measurements. Furthermore, the inductive reasoning algorithm was devised to regulate process parameters for in-process control of flank wear evolution.

The findings demonstrate that the Diverse Feature Synthesis Vector devised in this research was superior in representing the complex flank wear morphology as compared to some data reported by relevant literature, where geometric and fractal features were used to predict VB progression online. In addition, the ML-based MV-TCM system successfully utilized the DFSV to predict and control VB rate during face milling of Inconel 718. The system achieved higher predictive efficiency than image processing-based MV-TCM systems applied in the previous studies, with an offline validation RMSE of 45.5μm, R2 of 96.52%, and MAPE of 2.36%, as well as an online validation RMSE of 29.09μm, R2 of 97%, and MAPE of 3.52%. Additionally, the system employed a multi-stage optimization strategy that regulated process parameters at different VB levels to minimize the magnitudes of flank wear and chipping. This strategy extended tool life by 63.63% (relative to the conventional method) and 56.52% (relative to the GKRR soft-computing technique). Therefore, this research demonstrates the significance of applying ML-based MV-TCM system for predictive control of tool wear evolution during CNC milling of Inconel 718.

0.2 Graphical Abstract

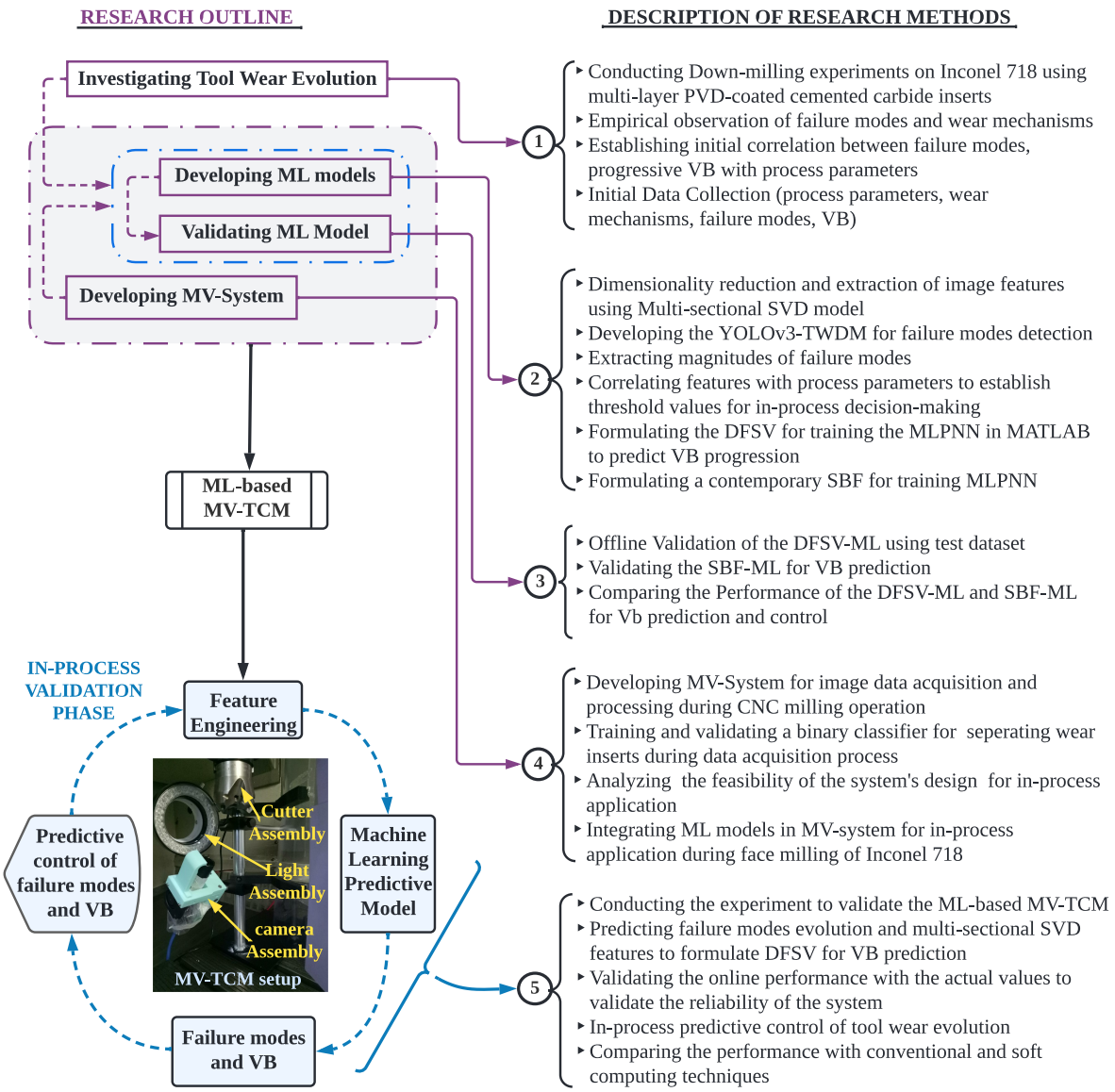

Figure 1: *Graphical outline of research concepts*

Acknowledgement

I would like to extend my sincere gratitude to a number of individuals who provided me with technical, emotional and psychological support throughout the entire Doctoral study at the University of Nottingham Malaysia.

In the first place, I would like to express my heartfelt gratitude to Prof. Chin Seong Lim for his steadfast mentorship in guiding me through the labyrinthine bureaucracy of Ph.D studies and the academic realm at large. His indomitable support constituted a pivotal foundation for the crucial research benchmarks of my thesis. I owe him a profound debt of gratitude, especially for his sagacious demeanor, forbearance, and unwavering empathy during my scholarly pursuits. I am thus supremely fortunate to have been under his guidance and supervision.

Additionally, I would like to extend my appreciations to Prof. Ali Akhavan Farid, who imparted invaluable perspectives on my work. His industriousness served as an exemplar of my advancement as an early carrier researcher in the field of design and manufacture. Furthermore, I am thankful to Prof. Khameel Bayo Mustapha for his astute review, critiques and suggestions, acting as an internal examiner throughout the entire course of my Ph.D program.

I would like to extend my heartfelt appreciation to Professor Chuan Li of the School of Mechanical Engineering at Dongguan University of Technology in Dongguan, China, and Yu-Chen Liu from the Department of Materials Science and Engineering at National Cheng Kung University in Tainan, Taiwan. Their exceptional collaboration has significantly enriched my understanding of the application of machine learning models for tool condition monitoring and tool performance optimization.

To my mother, Natalia Banda, and my mentors, Dr. N.T. Ben, Prof. B.O. Mkandawire and Dr. S. Kaunda, your benedictory words of inspiration and support shall be indelibly etched in my memory. I am also deeply indebted to my wife, Shakira Waya Manyamba, my son, Kyle Banda, and my sister, Hilda Banda, who provided me with encouragement and motivation to realize my full potential during this solitary journey of obtaining my doctorate.

List of Publications

Published Articles

1. Banda, T., Farid, A.A., Li, C. et al. Application of machine vision for tool condition monitoring and tool performance optimization–a review. Int J Adv Manuf Technol 121, 7057–7086 (2022). $https://doi.org/10.1007/s00170-022-09696-x$ [Chapters 1 and 2.]

2. Banda, T., Ho, K.Y., Akhavan Farid, A. et al. Characterization of Tool Wear Mechanisms and Failure Modes of TiAlN-NbN Coated Carbide Inserts in Face Milling of Inconel 718. J. of Materi Eng and Perform 31, 2309–2320 (2022). $https://doi.org/10.1007/s11665-021-06301-2$ [Chapters 3 and 4]

3. Banda, T., Jauw, V., Li, C. et al. Flank wear prediction using spatial binary properties and artificial neural network in face milling of Inconel 718. Int J Adv Manuf Technol 120, 4387–4401 (2022). $https://doi.org/10.1007/s00170-022-09039-w$ [Chapters 3 and 5]

4. Banda, T., Liu, Yc., Farid, A.A. et al. A machine learning model for flank wear prediction in face milling of Inconel 718. Int J Adv Manuf Technol (2023). *https://doi.org/10.1007/s00170-023-11152-3* [Chapters 3 and 6]

5. Banda, T., Jauw, V.L., Farid, A.A. et al. In-process detection of failure modes using YOLOv3-based on-machine vision system in face milling Inconel 718. Int J Adv Manuf Technol 128, 3885–3899 (2023). *https://doi.org/10.1007/s00170-023-12168-5* [Chapters 3, 5 and 6]

Published Book Chapters

1. Banda, T., Song, M.S., Farid, A., Lim, C.S. (2022). Investigation of Tool Wear Mechanisms in Face Milling of Inconel 718 with Different Cutting Fluids. In: , et al. Enabling Industry 4.0 through Advances in Manufacturing and Materials. Lecture Notes in Mechanical Engineering. Springer, Singapore. $https://doi.org/10.1007/978-981-19-2890-1-4$ [Chapters 2 and 3]

2. Banda, T., Wong, KC., Farid, A.A., Lim, C.S. (2021). Comparative Study of Temperature Prediction in the Machining Process of Ti-6Al-4V, Inconel 718 and AISI4340 Using Numerical Analysis. In: Osman Zahid, M.N., Abdul Sani, A.S., Mohamad Yasin, M.R., Ismail,

Z., Che Lah, N.A., Mohd Turan, F. (eds) Recent Trends in Manufacturing and Materials Towards Industry 4.0. Lecture Notes in Mechanical Engineering. Springer, Singapore. $https://doi.org/10.1007/978-981-15-9505-9-52$ [Chapters 2 and 3]

3. Banda, T., Jie, B.Y.W., Farid, A.A., Lim, C.S. (2022). Machine Vision and Convolutional Neural Networks for Tool Wear Identification and Classification. In: Ab. Nasir, A.F., Ibrahim, A.N., Ishak, I., Mat Yahya, N., Zakaria, M.A., P. P. Abdul Majeed, A. (eds) Recent Trends in Mechatronics Towards Industry 4.0. Lecture Notes in Electrical Engineering, vol 730. Springer, Singapore. $https://doi.org/10.1007/978-981-33-4597-3-66$ [Chapters 3 and 5]

In the Pipeline

1. Tiyamike Banda, Than Yeong Zhen, Ali Akhavan Farid, and Chin Seong Lim. Study of Chip Morphology through the Measurement of Fractal Dimension in Face-Milling Inconel 718– [Chapters 3 and 4]

2. Tiyamike Banda, Veronica Lestari Jauw, Ali Akhavan Farid, and Chin Seong Lim. Predictive Control of Flank Wear and Chipping Magnitudes Using a YOLOv3-based Machine Vision System in Face-Milling Inconel 718– [Chapters 3, 5, and 6]

3. Tiyamike Banda, Ali Akhavan Farid, and Chin Seong Lim. Multi-sectional Singular Value Decomposition for Flank Wear Prediction in Face Milling of Inconel 718– [Chapters 3, 5, and 6]

Abbreviation	Description
ADOC	***A***xial ***D***epth of ***C***ut [a_p]
CCD camera	***C***harged-***C***oupled ***D***evice
CMOS camera	***C***omplementary ***M***etal-***O***xide-***S***emiconductor camera
CNC	***C***omputer ***N***umerical ***C***ontrol
CNN	***C***onvolution ***N***eural ***N***etwork
DCGAN	***D***eep ***C***onvolution ***G***enerative ***A***dversary ***N***etwork
DCNN	***D***eep ***C***oncolution ***N***eural ***N***etwork
DFSV	***D***iverse ***F***eature ***S***ynthesis ***V***ector
DL	***D***eep ***L***earning
MLPNN	***M***ulti-***L***ayer ***P***erceptron ***N***eural ***N***etwork
DNN	***D***eep ***N***eural ***N***etwork
DRL	***D***eep ***R***einforcement ***L***earning
GCN	***G***raphical ***C***onvolution ***N***etwork
GGRNN	***G***ated ***G***raph ***R***eccurent ***N***eural ***N***etwork
GKRR	***G***aussian ***K***ernel ***R***idge ***R***egression
HOSVD	***H***igher ***O***rder ***S***ingular ***V***alue ***D***ecomposition
ML-MV-TCM	***M***achine ***L***earning ***M***achine ***V***ision-based ***T***ool ***C***ondition ***M***onitoring
ML	***M***achine ***L***earning
MRR	***M***aterial ***R***emoval ***R***ate
PCA	***P***rinciple ***C***omponent ***A***nalysis
R-CNN	***R***egional-***C***onvolution ***N***eural ***N***etwork
RDOC	***R***adial ***D***epth of ***C***ut [a_e]
RUL	***R***emaining ***U***seful ***L***ife
SVD	***S***ingular ***V***alue ***D***ecomposition
TCM	***T***ool ***C***ondition ***M***onitoring
TPO	***T***ool ***P***erformance ***O***ptimisation
YOLOv3	***Y***ou ***O***nly ***L***ook ***O***nce version 3

Contents

List of Tables

List of Figures

Chapter 1

Introduction

1.1 Research Background

Inconel 718 is a nickel-based superalloy with exceptional properties, such as creep, oxidation, hot corrosion resistance, and high hot hardness [1, 2]. Its ability to withstand extreme temperatures above 700°C [3, 4] has led to its extensive use in producing more than 50% of the modern aircraft engine structural components, including high-pressure compressor blades, casings, and discs [5, 6]. However, out-of-tolerance dimensions and poor surface finish of these components can result in stress concentration, fatigue crack initiation, and decreased engine efficiency. To mitigate this problem, precision machining, particularly CNC face-milling, is employed to control machining errors and improve the integrity of functional surfaces [7]. Despite this, Inconel 718 still has high affinity to form a built-up edge on the tools, react with tool elements, and undergo precipitation hardening at high cutting temperatures. It was reported that the precipitation hardening of its γ' and γ" phases intensifies between 650-850°C [8], thus exacerbating tool wear mechanisms, such as abrasion, diffusion, oxidation, and adhesion during machining [9].

These wear mechanisms cause rapid tool degradation, which covers a spectrum of damage scales from micro-chipping to catastrophic failure, resulting in several failure modes, such as flank wear, chipping, flaking, built-up edge (BUE), coating delamination, thermal cracks, and notching [10]. Flank wear predominantly determines tool life and is primarily caused by the abrasion wear mechanism [11]. According to the ISO-8688-1 face milling standard [12], the

acceptable average flank wear depth (VB) for CNC face-milling operations ranges between 0.2 and 0.5 mm. The evolution of VB typically occurs in three phases: break-in, steady wear, and failure stages (which can also be divided into critical and failure regions) [9]. However, in cases where tools experience uncontrolled failure modes, such as progressive chipping, in the early and steady wear phases, there is rapid VB rate that limits the extension of tool life during machining.

To improve tool life, modern tools are tailored to withstand the synergistic impact of wear mechanisms and failure modes by applying coatings with superior tribological properties, such as high heat dissipation capacity, hardness, toughness, and abrasion resistance [13]. While single-layer coatings have shown improved performance as compared to uncoated tools during machining of Ni-based superalloys [14], they have reported fretting fatigue life, which exacerbates mechanical wear [15]. Conversely, multi-layer coated tools have exhibited high hardness, elastic modulus, and ductility, which enhance tool life extension during machining of superalloys [16]. As a result, multi-layer coated tools with fine-crystalline TiAlN layer are well known for their high performance [1, 17] despite the uncontrolled failure modes still evolving under the sub-optimal processing conditions. Therefore, the selection of optimal cutting parameters is crucial in limiting the in-process evolution of these failure modes to enhance tool life [5].

Previous studies reported that the cutting speed, feed rate, and axial depth of cut (ADOC) are crucial parameters that affect tool wear progression for most PVD-coated carbide inserts during face milling of Inconel 718 [18, 19]. As a result, the correlation between these parameters and VB progression was leveraged to develop tool life predictive models. However, there was no substantial correlation that demonstrates the synergistic impact of these parameters on the wear mechanisms and failure modes experienced by the multi-layer PVD-coated carbide inserts during face milling of Inconel 718 [20]. Furthermore, the commonly used numerical, analytical, or physics-based models, which were used to predict tool life or VB, had rigid coefficients, derived from numerical features, which did not adapt to changing process conditions. Moreover, these models were not informed by the in-process evolution of wear mechanisms and failure modes, thus their reasoning capability was limited by rigid numerical features, which are not diverse enough to extrapolate and control tool performance under

complex wear morphology [21]. Therefore, Tool Condition Monitoring (TCM) is now imperative in providing real-time predictive control of failure modes, wear mechanisms and VB rate through the utilization of the Machine Learning (ML) models, which are typically trained from historical data through supervised or unsupervised learning to predict and control tool wear evolution online [22, 23].

1.1.1 Overview of Tool Condition Monitoring

In line with Industry 4.0, the manufacturing sector is undergoing a digital transformation to fulfil the requirement for products of impeccable quality [24]. In this context, Tool Condition Monitoring (TCM) is employed to predict critical indicators of the cutting mechanism, such as cutting force and tool wear evolution [25]. By predicting these indicators, machinists can make informed decisions on when to change tools, optimize cutting parameters, and improve overall cutting efficiency [26]. Therefore, TCM has been leveraged to predict tool wear progression to determine the failure criteria and remaining useful life of the tools before replacement [22]. However, predicting tool wear without considering the synergistic impact of process parameters on wear mechanisms and failure modes does not guarantee tool life extension during machining [27]. Therefore, a correlation between the process parameters, wear mechanisms and failure modes should be elucidated to enhance the in-process control of tool performance.

Meanwhile, the utilization of indirect TCM tried to resolve this issue by correlating process parameters with indirect indicators of tool wear, such as force, torque, vibration, Acoustic Emission (AE), power, motor current, and sound signals [28, 29]. The implementation of sensors in disparate locations of the CNC milling setup enhances the acquisition of diverse arrays of tool wear signals. These signals are processed using statistical analysis, Fourier and wavelet transforms, time series and amplitude analysis, to extract pertinent features that exhibit high correlation with flank wear progression during machining [30]. It was noted that force features from the dynamometers were more reliable, despite the technique being a costlier as compared to a low-cost vibration or acoustic emission sensor. On the other hand, a successful implementation of a multi-feature fusion can achieve high predictive efficiency [28], despite its complex data processing during features extraction [31].

After extraction, the features were used to train various machine learning (ML) models,

such as artificial neural networks, fuzzy logic, support vector machines, and deep learning, for online prediction of tool wear progression. Among these, deep learning convolves high-level features to reduce the complexity of feature selection while predicting tool wear progression [32], despite its overfitting issues, which typically arise under limited dataset [33]. While a sensor-based TCM offers adaptive monitoring of tool wear progression, it cannot predict the in-process evolution of dominant tool failure modes to reveal the sub-optimal processing conditions. Thus, its application is limited to quantifying tool breakage, tool life, and VB levels. Moreover, it cannot predict the underlying causative mechanisms of rapid VB rate to enhance the predictive control of tool performance. Therefore, a direct method of machine vision was found to be more effective in TCM as compared to the sensor-based approach.

In the context of direct TCM, digital microscopes are used to diagnose the wear mechanisms and measure the magnitudes of failure modes to determine the failure criteria and actual time for tool replacement [34, 35]. By characterizing the wear mechanisms and failure modes, it enhances the diversity of features for in-process tool performance control and optimization. However, it is plagued with high processing time, manual handling of tools, and human observation. This ignited a need for a more improved system for in-process predictive control of tool wear evolution. In the meantime, recent advances in imaging technology, computer vision, and artificial intelligence have improved the classification of tool wear and prediction of VB during Machine Vision-based TCM (MV-TCM) [36], as depicted in Figure 1.1.

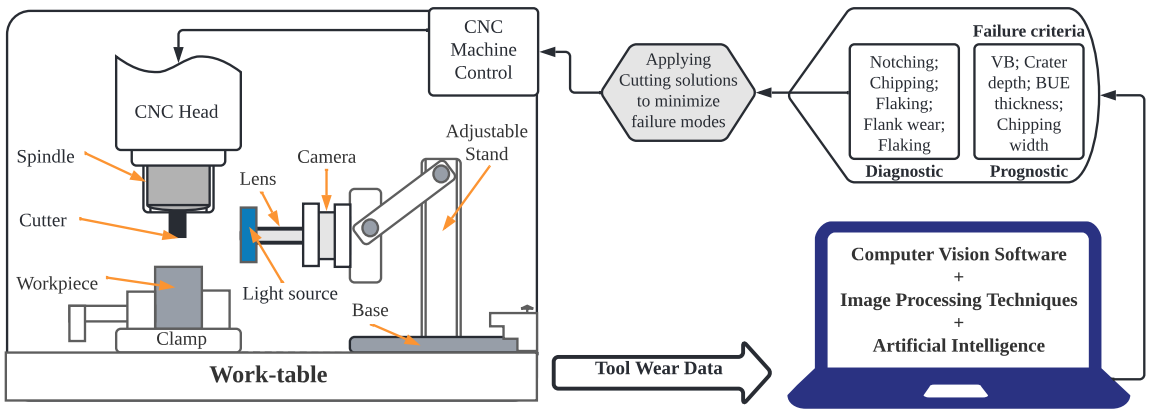

Figure 1.1: *Mounting MV-TCM system's design in a CNC milling machine*

1.1.2 Overview of MV-TCM

The efficacy of MV-TCM in capturing, classifying, and analysing tool wear was established, including the prediction of progressive VB with an accuracy exceeding 95% [37]. MV-TCM is also capable of quantifying the area, volume, and thickness of BUE on the tool's cutting edge [38]. Despite the established nature of MV-TCM, constructing a substantial dataset that incorporates the diverse failure modes to train feature engineering and ML models still remains a challenge. It is also worth noting that the tool wear images used to create the dataset should have a variety of failure modes scenarios associated with different wear mechanisms. However, lack of such incoherent dataset compromises the robustness of custom ML models as they are not informed by other significant wear descriptors, such as diverse failure modes, in creating diverse feature synthesis vector (DFSV) for predicting tool wear evolution during machining. In addition, the application of in-process MV-TCM is further hindered by the smeared noise resulting from coolant droplets, swarf, and inconsistent lighting conditions, which affect the resolution of tool wear images during data acquisition [25]. These issues were previously addressed by applying image processing techniques, such as wavelet transform, structural similarity index, threshold segmentation, textural analysis, and edge detection, to extract geometric and textural features that correlated with flank wear progression during machining [39, 40]. However, these features were found unreliable due to the multi-modal nature of tool wear images, especially when machining superalloys, which generate complex wear morphology, non-uniform textural structure, and incoherent data.

To enhance the pattern recognition, dimensionality reduction, extraction, and selection of diverse features on the complex flank wear morphology, researchers can apply advanced feature engineering techniques, including Principal Component Analysis (PCA) [41], Singular Value Decomposition (SVD) [42], Tensor Decomposition (TD) [43] and Deep Learning (DL) [44], which demonstrated impeccable strides in various computer vision applications. Specifically, SVD and TD techniques can harness the potency of singular values to distinguish the dominant features and noise components of time-series imagery signals [45]. This can be leveraged to extract the magnitude of energy layers localized by the dominant feature embeddings of the complex wear morphology, thus predicting the propagation of the wear region during machining. Except for DL, these methods cannot provide a means of extracting high-level

features for real-time detection of the wear mechanisms and uncontrolled failure states. As a result, DL is the leading-edge technology in extracting latent features from time-series tool wear images for identifying and classifying failure modes on the tool's cutting edge.

A more related study employed pre-trained CNN auto-encoders to extract high-level features from custom tool wear data to classify regional-based wear states, including flank wear, tool breakage, adhesion, and rake face wear, for CVD and PVD-coated carbide tools at an accuracy above 96% during down-milling of Inconel 718 [46]. In addition, the auto-edge detection was used to extract the wear region and predict the VB rate using a Sobel operator through the automatic wear value detection of the tools. Despite its high predictive efficiency, the model was not used to detect magnitudes of multiple failure modes (nominal features) to describe the extent of wear severity and the complexity of wear morphology that accelerate the tool's degradation during machining. Therefore, there is a need to enhance the MV-TCM system to detect multiple failure modes as nominal features that characterise the causative mechanisms of rapid VB rate during machining. This can enhance tool wear prediction during TCM by ensuring that the robustness of the predictive models are contingent upon the features diversity. Meanwhile, a Regional-based CNN (R-CNN) can effectively partition the tool wear image into distinct segments to extract pixel-based information as latent features that can facilitate the detection of multiple objects on the same image [47]. This resolves the localization of multiple failure modes on the tool's cutting edge despite its implementation being criticized for the computationally-intensive nature and slow detection rate, which was later addressed by introducing a new variant called You Only Look Once (YOLO).

The YOLO architecture evolved over the years, with YOLOv3 being the final official and advanced network that effectively eliminated the prevailing limitations of accuracy and speed during real-time object detection [48]. Its network can easily be integrated with highly compressed CNN architectures [49], such as SqueezeNet to improve accuracy and detection speed during failure modes detection. To enhance its practicality during MV-TCM, an inductive-reasoning technique was devised to generate the informed decisions that can suggest proper solutions to minimize the rate of failure modes evolution in the early cutting stages. Therefore, the utilization of the feature engineering and ML models can enable the MV-TCM system to extract a more comprehensive DFSV for online detection, prediction, and control of flank wear

evolution, thereby enhancing tool life extension during face milling of Inconel 718.

1.2 Problem Statement and Research Questions

The successful implementation of the MV-TCM system's design experiences significant challenges during heavily interrupted CNC milling of Inconel 718 under high-pressure flood cooling condition. These include poor resolution of imagery signals, scarcity of compressive data with diverse failure modes, and smeared image noise due to coolant adhesion, swarf and inconsistent lighting conditions. Previous studies have demonstrated that the application of image processing techniques can enhance the MV-TCM system to extract geometric, textural, wavelet, and fractal features that can be used to predict VB progression online [39, 46, 50]. However, these low-level features cannot delineate the complexity of wear morphology, such as distinguishing multiple failure modes on the tool's cutting edge, as critical indicators of rapid wear rate of PVD-coated carbide inserts, as well as sub-optimal cutting conditions during CNC milling of Inconel 718. Therefore, there is a need to apply advanced feature engineering and deep learning techniques (i.e., SVD and YOLOv3) to detect and extract the DFSV (including different types of failure modes) for training ML models to predict and control the flank wear rate at an early cutting stage, thus enhancing the performance of PVD-coated carbide inserts and tool life extension during face milling of Inconel 718. The problem statement is supported by the following questions to achieve the aim and objectives of this research:

- *Considering that the distinct CNC milling operations are associated with specific dominant wear mechanisms, how accurately can the wear mechanisms, failure modes, or high-level features be extracted and empirically correlated with the process parameters to enhance the feature diversity for training machine learning models for tool wear prediction?*

- *Considering the scarcity of big data sources with diverse wear mechanisms and failure modes, and the imbalanced nature of custom tool wear data resulting from specific machining operations, materials, and tools, how will the feature engineering and machine learning models be effectively trained to ensure the proficient detection of the Diverse Feature Synthesis Vector (DFSV) to address under-fitting issues during tool wear prediction and control?*

- *In the context of varying process conditions during in-process application of the ML-based MV-TCM system's design, how will the ML ensure high predictive efficiency of in-process failure modes and flank wear evolution, especially when new parameters outside the training range are applied during CNC milling of Inconel 718?*

1.3 Aim and Objectives

The aim of this study is to leverage the ML-based MV-TCM system in predicting and controlling the in-process performance of the PVD-coated carbide inserts during CNC milling of Inconel 718. To achieve this objective, a climb CNC milling operation was conducted to establish the empirical correlation between the process parameters and various tool wear features, such as wear mechanisms, failure modes, and progressive VB of the multi-layer PVD-coated carbide inserts. The experiment yielded a comprehensive tool wear dataset, which was subsequently leveraged to develop feature engineering and ML models. These models were then integrated into the MV-TCM system's design to enhance the in-process detection of diverse features, prediction and control of tool wear evolution during machining. The following objectives summarize the overall aim of this research:

Objective 1

To investigate the empirical correlation between the process parameters and diverse tool wear features (which includes the wear mechanisms, failure modes, and progressive VB) of PVD-coated carbide inserts during CNC milling of Inconel 718.

Objective 2

To develop the feature engineering (multi-sectional SVD and YOLOv3) and ML (Multi-layer perceptron neural network and induction-reasoning) models using diverse features extracted from the experimental data and data reported by relevant machining standards to predict tool wear evolution during face milling of Inconel 718.

Objective 3

To develop the MV-TCM system's design that utilizes the efficient predictive capability of the ML models to predict and control in-process tool wear evolution during face milling of Inconel 718.

1.4 Research Scope

In this study, the correlation of the synergistic process parameters, wear mechanisms, failure modes, and flank wear depth (VB) of multi-layer PVD-TiAlN/NbN coated carbide inserts was investigated during a climb-milling operation of Inconel 718. The research was conducted in a laboratory setting using a cyber-physical MV-TCM setup, which was able to acquire time-series tool wear data during CNC milling operations. By utilizing the empirical observations made during the physical experiment, a custom tool wear dataset with diverse features was established through the application of conventional methods and the ISO-8688-1 standard. This dataset was used to develop and train the feature engineering techniques, including the multi-sectional Singular Value Decomposition (multi-sectional SVD) and the YOLOv3-Tool Wear Detection Model (YOLOv3-TWDM) for the purpose of detecting and extracting a diverse feature synthesis vector (DFSV) for in-process VB prediction and control. The feature vector was then used to train a multi-layer perceptron neural network, which was successfully implemented to predict the VB rate at the early cutting stages, enhancing the MV-TCM system's ability to predict and control the rate of flank wear evolution during face milling of Inconel 718.

1.5 Research Significance and Expected Deliverables

The main significance and novelty of this study is the performance improvement of the PVD-coated carbide inserts through the utilization of ML models that detected and controlled the evolution of failure modes and wear mechanisms at the early cutting stage to improve the cutting mechanism during face milling of Inconel 718. By utilizing the Diverse Feature Synthesis Vector (DFSV) extracted from time-series flank wear data, the ML-based MV-TCM system extracted significant information of flank wear features, which was utilized to regulate the pro-

cess parameters at various flank wear stages, thus controlling the VB rate at the early cutting stage to improve the economic life of the tools during machining. In addition, the automation of the MV-TCM system's design via the utilization of ML techniques improved processing time during online tool wear detection and control.

Based on the above significance, the first deliverable of this research, which corresponds to the first objective, is the tool wear dataset generated through the empirical correlation between process parameters, wear mechanisms, failure modes, and flank wear depth (VB). The second deliverable, which corresponds to the second objective, is the innovative feature engineering and ML techniques that detect and extract diverse features to predict tool wear evolution during machining. The third deliverable, which corresponds to the last objective, is the design of the on-machine vision system that utilizes the ML models to predict and optimize tool wear evolution during face milling of Inconel 718.

1.6 Thesis Structure

The remainder of this Thesis is structured as follows: ***Chapter 2*** provides a review of the machinability of Inconel 718 (Section 2.1), tool performance optimization (Section 2.2), and tool condition monitoring (Section 2.3). ***Chapter 3*** describes the detailed methodology used in this research. ***Chapter 4*** discusses the key findings of the experiment, with emphasis on generating the dataset for training the ML models. ***Chapter 5*** discusses the training and offline validation of the ML models. ***Chapter 6*** focuses on the application and validation of the ML-MV-TCM against conventional and soft-computing techniques. ***Chapter 7*** highlights the summary of the research findings, contributions, limitations, and potential areas for future exploration.

Chapter 2

Literature Review

The review of knowledge encompasses the four principle aspects: (1) Machinability of Inconel 718 (Section 2.1); (2) Overview of Tool Performance Optimization (TPO) (Section 2.2); and (3) Tool Condition Monitoring (TCM) (Section 2.3). From the synergistic qualitative and quantitative understanding of these aspects, the overall knowledge gaps were established (Section 2.4).

2.1 Machinability of Inconel 718

Inconel 718 is a nickel-based superalloy that possesses exceptional properties, such as thermal stability [51], excellent weldability, and corrosion resistance up to 650°C [8]. This has made it a ”workhorse” for high-temperature applications, including the manufacturing of aircraft engine’s structural components, such as high-pressure compressor blades, casings and discs [52]. Despite its popularity, Inconel 718 is a hard-to-cut metal due to its complex mechanical, thermal, and microstructural properties that can affect the tool’s cutting efficiency [53]. Unlike other metallic alloys, Inconel 718 displays a high susceptibility to strain rate, resulting in the retention of its mechanical strength through precipitation hardening at high cutting temperatures during machining [54]. The presence of hard carbides in its microstructure further exacerbates the issue, as they intensify the surface hardness of the workpiece material, leading to high abrasive forces and uncontrolled tool’s failure states during machining. Therefore, cutting Inconel 718 requires tools with high shearing strength to deform the hard surface layer

of the workpiece material [2].

Additionally, it was reported that Inconel 718 has poor thermal conductivity [55], which poses a terminal challenge in dissipating heat during machining. Consequently, heat accumulates in the tool-workpiece contact zone, resulting in thermal degradation of the tool's cutting edge. The high temperature increases the molecular kinetic energy, accelerating the diffusion of tool's constituents into the chips or workpiece material. Furthermore, elevated temperatures cause the melting of the coating-substrate binder, particularly for coated carbide tools, which eventually exposes the tool's substrate to chemical wear by oxidation. The synergistic effect of these wear mechanisms leads to thermal cracks, flaking, progressive chipping, galling, pitting corrosion, and coating delamination during machining [56]. Moreover, Inconel 718's tendency to weld onto the tool material at high temperatures contributes to the formation of built-up edge (BUE) and built-up layer (BUL) on the tool's cutting edge [57]. Therefore, a comprehensive understanding of Inconel 718's machinability necessitates the study of the wear mechanisms and failure modes as key indicators of inefficient cutting mechanism, undesirable tool performance, and sub-optimal processing conditions during machining of Inconel 718.

2.1.1 Wear Mechanisms and Failure Modes

The tool wear mechanisms during machining of Inconel 718 include adhesion, abrasion, diffusion, and oxidation [3, 4, 10]. The adhesion wear is characterized by the formation of a cold weld as a result of high plastic deformation under extreme thermomechanical conditions, leading to the accumulation of adhesive particles that form a built-up edge (BUE) or built up-layer (BUL) on the tool's cutting edge [58, 59]. The persistent removal of such particles results in small cavities of attrition wear [60]. Thus, attrition is characterized by the progressive removal of adhesive particles along with the chip flow during machining [61]. This phenomenon is primarily caused by high friction and the rubbing action of hard Inconel carbides. The severe friction or rubbing on the rake or flank face of the tool results in severe abrasion, which can eventually cause mechanical tool failure [62–64].

Furthermore, the elevated cutting temperature elicits thermally-induced wear mechanisms, such as diffusion and oxidation [65]. Diffusion wear is contingent upon the solubility of atomic particles and is accentuated by the longer tool-workpiece contact time in the primary

and secondary shear zones. It also results from the heat generated by the high deformation and strain rates in these zones [10]. Its prolonged impact leads to high friction force, resulting in cavities on the surface of the coating layers [66]. Additionally, the high temperature exacerbates the chemical wear by oxidation, which gradually degrades the coating layers by dissolving the binder between the substrate and coating layers. This occurs when the components of the tool coating react with atmospheric oxygen, forming oxides which are more brittle and can easily be ploughed by the hard carbides. Such a phenomenon reduces the tool's strength to shear hard surface layers of Inconel 718 [67]. As a result, tools subjected to these wear mechanisms are susceptible to thermal cracks, progressive chipping, and coating delamination.

It is evident from the analysis above that the synergistic impact of wear mechanisms contributes to rapid tool failure, which covers a spectrum of damage scales from micro-chipping to catastrophic failure, including flank wear, notching, pitting corrosion, coating delamination, thermal cracks, flaking, and progressive chipping [10]. Flank wear is attributed to the abrasion wear mechanisms on the flank face of the tool's cutting edge [68]. Its severity can be exacerbated by other wear mechanisms such as cyclic adhesion, oxidation, and attrition. Flank wear can either be uniform or non-uniform, with uniform flank wear being the most prevalent failure mode that determines tool life, as per the ISO-8688-1 standard. The non-uniform flank wear, on the other hand, arises from the uncontrolled failure modes on the tool's cutting edge. Notching is the first uncontrolled failure mode, which is attributed to the high impact force of the tools upon entering the hard surface layer of the workpiece material. Another uncontrolled failure mode is Chipping, which is a saw-like structure along the tool's cutting edge. In its initial stage, chipping manifests as pitting corrosion, and is attributed to diffusion, cyclic adhesion, and chemical wear [69].

With more subsequent passes, pitting corrosion intensifies to coating delamination as the coating layers get ploughed due to asperities deformation, which is also attributed to the cyclic adhesion and abrasion. This was reported to exacerbate the subsurface cracks [70], which then propagate to the outer layer to form thermal cracks. The result of this wear prodigy leads to progressive chipping especially when thermal cracks intersect any perpendicular mechanical cracks [64]. When such a wear phenomenon prevails below the cutting-edge line, it causes

flaking, especially at high cutting temperatures where the bonding strength of the coating binder is weakened [69, 71]. Finally, galling is induced by adhesion and particle diffusion when the surfaces are in contact or slide against each other [72]. Despite the metallurgical properties of Inconel 718, the prevalence of these uncontrolled failure modes is influenced by the synergistic impact of process conditions. Thus, selecting optimal milling operations, cutting fluids, process parameters, tool coatings and geometry, can enhance the tool performance during face milling of Inconel 718.

2.1.2 Face Milling Operation

Face milling is a machining process utilized for either roughing or surface finishing of the workpiece material, as reported in [7]. It can be classified as up- or down-milling, dependent on the orientation of the workpiece in relation to the direction of the cutter's rotation. In down milling, the workpiece is fed in the same direction as the rotating cutter, thereby reducing the thickness of the chips and the shearing strength at the workpiece's exit point. This in turn leads to a reduction in mechanical wear, such as severe abrasion, localized chipping, and notching, thereby limiting the progression of flank wear rate, as shown in Figure 2.1 [73]. Conversely, in up-milling, the workpiece is fed in the opposite direction to the cutter's rotation, resulting in a high shear strength, thereby rapidly increasing the flank wear and uncontrolled tool's failure rate during machining. This often leads to mechanical failure modes, such as progressive chipping and notching, indicating sub-optimal tool performance. Considering that this research fosters the creation of sufficient data and features for training ML models, the utilization of ***down-milling*** provided longer time and more data as compared to up-milling operation.

2.1.3 Micro-mechanics of Tool Coatings

In machining of Inconel 718, the tools must exhibit exceptional characteristics, such as robust shear strength, hardness, toughness, chemical stability, wear resistance, and thermal stability, to mitigate the synergistic impact of the metallurgical properties of the workpiece [74, 75]. Unfortunately, most uncoated tools cannot fulfil such demands, which is why carbide tools are

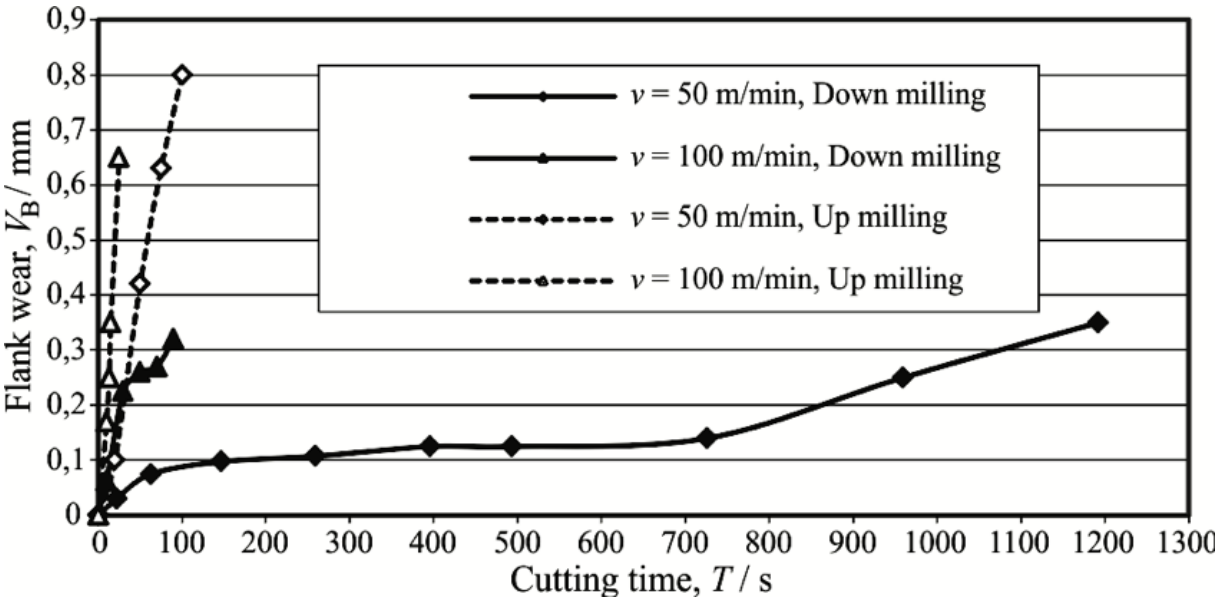

Figure 2.1: *Effect of face milling techniques on flank wear of TiAlN/TiN at V = 50 and 100 m/min* [73]

enhanced with coatings to withstand thermally and mechanically induced wear mechanisms [76]. The performance of these tools is thus contingent upon the superior tribological properties of the coatings, which are formed through Chemical or Physical Vapour Deposition (CVD or PVD). The PVD process produces hard nitride coatings that are somehow stable chemically, mechanically, and thermally [77, 78]. The most commonly used PVD nitride compounds are TiAlN and CrAlN [79–84].

The relative proportion of Ti, Cr, and Al in TiAlN and CrAlN has a profound impact on tool's efficacy during machining. The conventional $Ti : Al$ ratio of $50 : 50$ leads to a B1 crystal structure with finer grains, thereby enhancing its hardness. Conversely, the $Cr : Al$ ratio of $30 : 70$ results in a columnar crystal structure that decreases its hardness, thus making TiAlN more resistant to abrasion wear as compared to CrAlN coating layer. Previous research demonstrated that chipping and coating delamination during machining are consequences of the poor hardness and load-bearing support (denoted as $H3/E2$) of the TiAlN coating layers [85]. The implementation of ion implantation, specifically with C, Zr, Ti, N, Nb, and W ions in TiN and CrN coatings, augmented the load-bearing support and hardness of these materials, thereby improving their resistance to mechanically induced wear mechanisms[67, 86–89]. Despite these advances, the impact of ion implantation on TiAlN coatings, especially on tool wear mechanisms and failure modes during CNC milling of Inconel 718, is not clarified up to

date.

The presence of Al in the PVD-coated carbide tools contributes to high resistance in mechanical wear, as well as chemical wear through oxidation [90, 91]. Under high-cutting temperatures, Al diffuses externally while O diffuses internally within the TiAlN film. Upon collision, the two elements react to generate an amorphous layer of Al_2O_3. This new layer serves to reduce the rate of oxygen diffusion, thereby curbing further oxidation of Ti element. It was reported that the fluctuation of Gibbs free energy for oxidized Ti (TiO_2) and Al (Al_2O_3) impacted the oxidation rate at high-cutting temperatures [92]. The higher stability of Al_2O_3 as compared to TiO_2 (DG1 = 954 kJ/mol and DG1 = 756 kJ/mol at 500°C, respectively) contributed to its efficacy in reducing oxidation wear during machining. Additionally, complete oxidation of the TiAlN film occurs at 800°C, leading to a decrease in its micro-hardness to approximately 2200 kg/mm^2 when heated above 700°C in air [93].

Furthermore, the micro-hardness of TiAlN was augmented by incorporating boron ions, which engenders the formation of TiB and BN crystal structures [94]. Similarly, Nb atoms, when deposited as interstitial particles, hinder the movement of dislocations, resulting in surface hardening of the TiAlN coating layer [95, 96]. Furthermore, the superposition of two planes with shared periodicity generates moiré fringes, disrupting the crystal lattice structure and forming an NbN phase, thereby improving strain hardening effect via lattice mismatch [97]. This leads to the formation of a chemically inert, amorphous crystalline structure with a high degree of lattice distortion in the NbN layer. Therefore, the exceptional micro-hardness and resistance to wear in PVD-TiAlN/NbN coated tools can be attributed to the superior properties of the NbN layer. Nonetheless, the PVD-deposited NbN layer on a fine-crystalline TiAlN substrate is porous [61] (Figure 2.2a), rendering it susceptible to abrasion and pitting corrosion at elevated temperatures.

2.1.4 Tool Geometry

Apart from the micro-mechanical properties of coating layers, the tool geometry, or the specific configuration of angles, is a crucial factor that influences the progression of flank wear during the down-milling of Inconel 718. One such angle, referred to as the leading angle (KAPR), determines the distribution of axial and radial forces experienced during the machin-

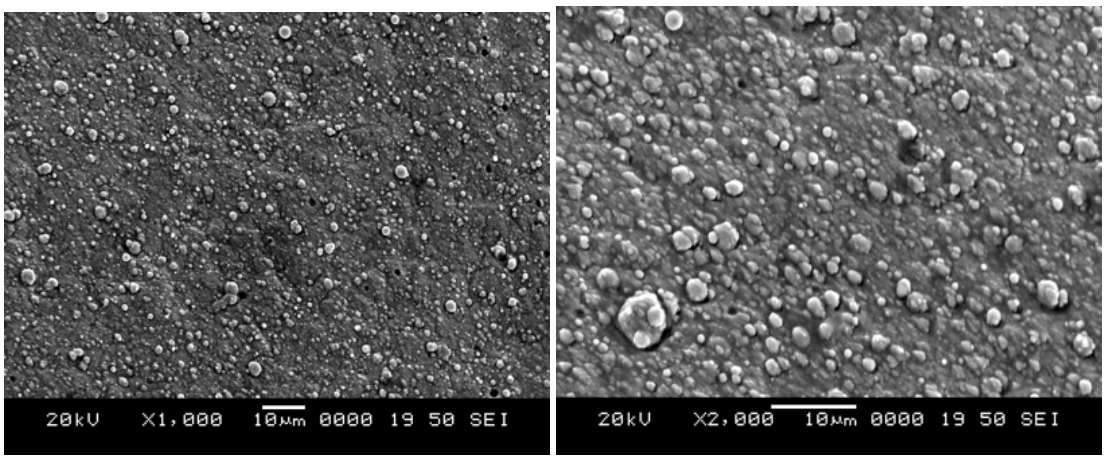

(a) (b)

Figure 2.2: *Microstructure of coatings at (a) 1000X magnification; (b) 2000X magnification* [61]

ing operation [98]. A large KAPR, for instance, boosts the axial force, which acts against the full rigidity of the rotating spindle, leading to increased demands on the spindle's design to accommodate the greater axial forces encountered during down-milling. Conversely, a small KAPR increases the radial force, causing deleterious outcomes such as cutter deflection, chatter, spindle tilting, and mechanical failure modes, such as edge chipping. Furthermore, a diminished KAPR also results in thinned chips and an increased tool-workpiece contact area, as shown in Figure 2.3 [98], leading to a more widespread distribution of thermal stress and thus promoting efficient heat dissipation. This, in turn, mitigates thermally-induced wear mechanisms, including oxidation, diffusion, and adhesion.

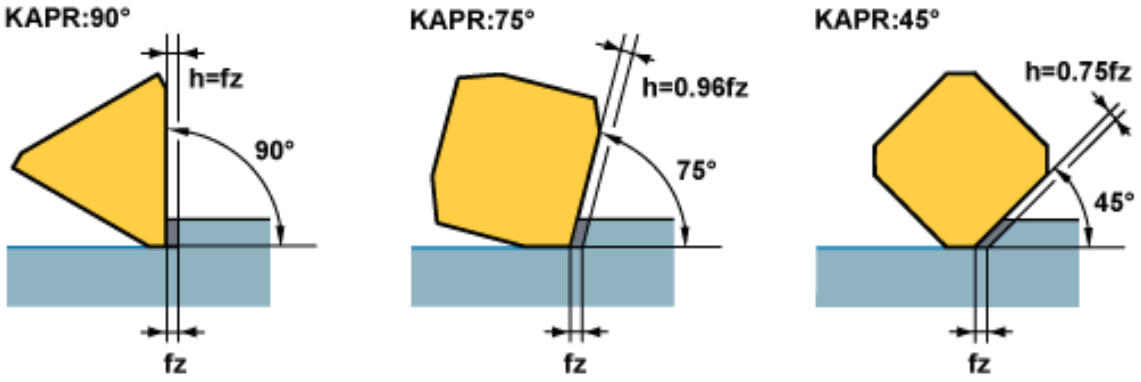

Figure 2.3: *Effect of lead angle on chip formation during face milling* [98]

The rake, relief and helix angles also influence flank wear evolution during high-speed milling of Inconel 718, as per the findings reported in [99]. The results revealed that the rake

angle influences the shearing force experienced by the tool. A significantly large rake angle sharpens the cutting edge, thereby enhancing the rate of tool's penetration into the workpiece material. However, the high friction and impact forces that arise from the precipitation-hardened layer of Inconel 718 during tool entry into the workpiece result in elevated mechanical failures at the sharp edge. On the other hand, a small rake angle results in a blunt cutting edge, leading to increased shear force and mechanical tool failure. This, in turn, exacerbates flank wear evolution through the abrasion wear mechanism. A considerably large relief angle reduces the tool-workpiece contact area, leading to reduced friction and abrasive forces, thus mitigating the progression of flank wear. The helix angle affects the stress distribution and chip disposal, thus influencing friction and heat dissipation rates during machining. Research showed that high helix angles exceeding 30°results in elevated axial force and inadequate chip disposal, leading to increased heat accumulation in the tool-workpiece contact zone [99]. This accelerates flank wear evolution through cyclic adhesion and diffusion wear mechanisms during face milling of Inconel 718.

2.1.5 Process Parameters

Besides the tool's geometry, the progression of flank wear is also correlated with the machining parameters. The alteration of cutting speed, feed rate, radial and axial depth of cut was shown to escalate the wear mechanisms of PVD-coated carbide inserts during face milling of Inconel 718 [18, 19]. Hence, the selection of cutting parameters that optimize the flank wear progression is a challenging task due to the synergistic impact of these parameters on the complex and diverse wear mechanisms and failure modes during face milling of Inconel 718 [100, 101]. An increase in axial depth of cut expands the tool-workpiece contact area, thereby escalating the shearing force, friction, and abrasive wear mechanisms, leading to a swift progression of flank wear evolution on the tool's cutting edge. On the other hand, a substantial increase in radial depth of cut raises radial forces, tool deflection, vibration, and chatter, which engenders mechanical wear mechanisms such as severe abrasion, which can cause chipping, notching, and even catastrophic failure.

The feed rate influences both thermally and mechanically induced wear mechanisms, resulting in a synergistic impact of failure modes that contribute to rapid evolution of flank

wear rate during the down-milling operation. An increase in the feed rate increases the size of the chip load, which exacerbates shear force and adhesion wear on the tool's cutting edge, thus enhancing mechanically-induced failure modes, such as BUE and BUL formation. On the other hand, a rapid increase in the cutting speed raises the cutting temperature, which exacerbates the thermally-induced wear mechanisms and failure modes of PVD-coated carbide inserts, leading to a rapid progression of flank wear, as depicted in Figures 2.4a and 2.4b [102]. It was observed that the negative TiAlN inserts provided a more improved flank wear resistance and longer cutting length as compared to positive TiAlN inserts. The utilization of positive TiAlN inserts is characterized by a non-zero relief angle. This pertains to the fact that the insert is only equipped with cutting edges on one side. At temperatures above 700°C, Inconel 718 undergoes intense precipitation hardening, causing severe abrasion as the tool encounters the hardened Inconel 718 layer at high friction rate. This prompts both thermally and mechanically-induced failure modes, including progressive chipping, notching, built-up edge, coating delamination, asperity deformation, and potentially catastrophic failure. Additionally, this also results in flaking on the rake face, exposing the tool's substrate to chemical wear by oxidation [103].

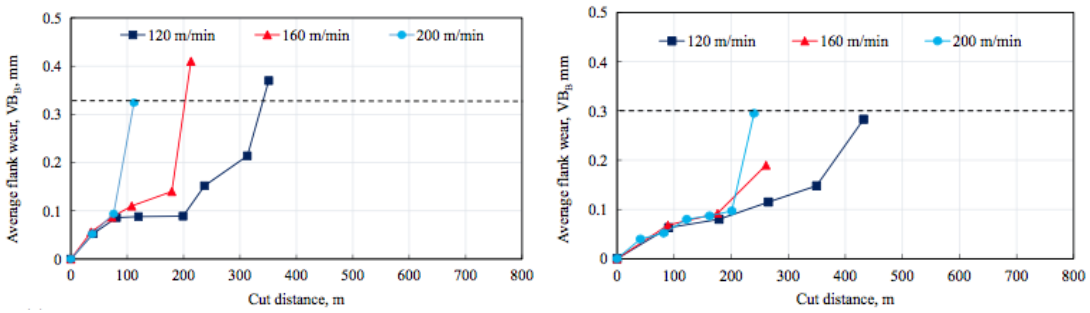

Figure 2.4: *Effect of cutting speed on flank wear: (a) positive TiAlN inserts and (b) negative TiAlN inserts* [102]

2.1.6 Cooling Techniques and Cutting Fluids

Cutting fluids play a crucial role in mitigating heat and friction generated during the machining process. By cooling and lubricating the tool-workpiece contact zone, the thermomechanical wear mechanisms are reduced, resulting in improved tool performance. Various cutting fluids were utilized for milling Inconel 718, such as recycled oil, oleic oil, ethanol-based oil and canola oil [104, 105]. A recent trend shows the application of nanofluids, particularly those

incorporating the solid lubricant Molybdenum disulphide (MoS_2)[106]. The use of nanofluids enhanced the surface finish and tool wear evolution as compared to mineral oil-based cutting fluids. This results in reduced circularity errors, burr heights, and thrust force, thereby offering proven benefits over mineral oil-based cutting fluids for machining Inconel 718[107].

Numerous cutting fluids and cooling techniques were utilized to optimize the evolution of flank wear during machining of Inconel 718. For instance, Vinothkumar et al. [108] demonstrated that the utilization of an atomized spray cooling solution comprising of vegetable oil, graphite, and molybdenum disulphide significantly increased the longevity of ceramic tools by 40-60% compared to dry cutting, where the dominant wear mechanisms were attrition, built-up edge, abrasion, notching, and chipping. Similarly, Zhang et al. [109] found that PVD-TiAlN coated cemented carbide tools experienced severe chipping when utilizing MQL with cryogenic compressed air and micro-droplets of vegetable oil, resulting in a 1.57-fold improvement in tool life as compared to dry cutting. Moreover, Armando et al. [110] revealed that incorporating the MoS_2 solid lubricant in the LB 2000 oil-based coolant resulted in a 12% improvement in tool performance compared to dry cutting and a 46% improvement compared to the utilization of pure LB 2000-based cutting fluid, where notching, abrasion, diffusion, and chipping were the predominant wear mechanisms.

Additionally, Bertolini et al. [111] found that the utilization of graphene nano-platelets in MQL improved the cutting force by 59% compared to oil-based fluids, with PVD-TiAlN coated inserts exhibiting exceptional performance. The addition of Multi-Walled Carbon Nanotubes (MWCNTs) to MQL was further observed to reduce the cutting force by 10% and temperature by 67% [112], thereby minimizing thermally induced wear mechanisms as compared to dry cutting. This demonstrates the ongoing evolution of cutting fluids research, transitioning from mineral oil-based and synthetic coolants to nanofluids and vegetable oil-based fluids, with the goal of minimizing thermal and mechanical wear mechanisms and failure modes to optimize tool performance during the machining of Inconel 718.

The application of cutting fluids in the machining of Inconel 718 is executed via a variety of techniques. As documented by Bartolomeis et al. in [113], the comparative analysis of flood cooling, Electrical Lubrication (EL), and Minimum Quantity Lubrication (MQL) was performed during an end milling operation utilizing PVD-TiSiN coated tools. Adhesion and

abrasion wear mechanisms, leading to flank wear progression, were prevalent at lower cutting speeds, while severe abrasion that resulted in progressive chipping was more pronounced at the highest cutting speed. On the other hand, de Paula Oliveira et al. [114] observed that while tools subjected to flood cooling experienced mechanically induced wear mechanisms owing to inadequate lubrication, tools in MQL encountered both thermal and mechanical wear mechanisms during end milling using PVD-TiAlN coated tungsten carbide tools. Despite this, flood cooling exhibited better tool performance, reducing flank wear evolution by 18.3% and 4.3% during the early and rapid failure regions, respectively, when compared to MQL. Finally, Makhesana et al. [115] found that the application of molybdenum disulfide and graphite in MQL (MQSL) improved the performance of PVD-TiAlN/TiN coated tools compared to both dry and conventional cooling conditions, owing to enhanced lubrication and reduced friction force, thus mitigating severe abrasion and rapid flank wear progression.

In furtherance, Pereira et al. [116] determined that the peak tool performance was obtained through utilization of flood cooling, followed by internal and external Cryogenic Minimum Quantity Lubrication (CryoMQL). However, Halim et al. [34] established that cryogenic carbon dioxide cooling mitigated thermally-induced wear mechanisms and flank wear progression, resulting in a 63.2% enhancement of tool life as compared to dry cutting. Moreover, the use of cryogenic carbon dioxide cooling was found to elevate the performance of PVD-TiAlN/AlCrN coated tools relative to dry cutting, conventional MQL and cryogenic liquid nitrogen cooling techniques. Though, it exacerbates the precipitation hardening of the Inconel 718 surface [117], thereby inciting mechanically-induced wear mechanisms, such as intense abrasion, causing notching on the flank wear region and flaking on the rake face [103].

In essence, the utilization of bio-oils as cutting fluids exhibits a positive trend in terms of lubrication performance at low cutting temperatures, which serves to reduce mechanical wear at lower cutting speeds and feed rates [118]. Nonetheless, the presence of triglycerides, a form of free fatty acids, in bio-oils can result in oxidation and hydrolysis instabilities at low temperatures [118]. These instabilities can be mitigated by incorporating anti-oxidants, particularly those derived from lemon extracts which are high in vitamin C [119]. Nevertheless, this can negatively impact the filtration process during the CNC milling process. Additionally, it has been noted that the use of bio-oil cutting fluids can negatively impact cooling efficiency

at high cutting speeds, thus promoting thermally induced wear mechanisms. In contrast, the utilization of mineral oil-based cutting fluids, which utilizes water as the primary cooling element, can effectively mitigate thermally induced wear mechanisms. While mineral oil-based cutting fluids contain sulfur and chlorine, which can generate toxic fumes at high temperatures [119, 120], they still serve to improve cooling efficiency, thus reducing the risk of unforeseen failure modes.

2.1.7 Chip Morphology

The chip morphology of Inconel 718 exhibits similar characteristics to ductile work material, forming serration at high cutting temperatures [121]. This phenomenon is due to the derivatives in the shear plane angle. As the tool enters the workpiece at a high cutting force, compressive and bending stresses decrease the shear angle to a minimum threshold, where chips experience severe plastic deformation. During this phase, the maximum temperature is observed in the deformation zone, where chips experience a high thermal softening effect. The plastic deformation decreases as the shear angle increases, up to a maximum combined stress. The cycle is then repeated, thereby forming a continuous serration. Since the serration is a function of high cutting temperature, it is ideal during dry cutting of Inconel 718. However, this is not the case with Inconel 718 chips formed under flood cooling conditions due to temperature fluctuation.

In the meantime, the adiabatic shear and periodic crack theories explain the formation of serrated chips when machining Inconel 718 [121]. The former is caused by the recurring thermoplastic shear instability in the deformation zone, where the material softening effect outweighs the combined effect of the strain hardening rate [122]. In addition, due to the low thermal conductivity and low heat dissipation capacity of Inconel 718, heat saturates in the narrow shear-localized bands. The latter defines the formation of periodic cracks due to sufficient penetration force, where slip-line deformation is formed due to compressive and bending stresses, initiating cracks on the free surface. The serrated chip formation started from crack initiation on the sliding surface, whose propagation is halted by the severely deformed surface near the tool-chip contact zone. Research has shown that ship morphology correlates with process parameters during machining of Inconel 718.

It was observed that the shear band thickness positively correlates with the cutting speed [123]. This was attributed to the intense strain localization caused by the thermal softening effect when machining at a high cutting speed. It was further observed that a large pitch distance and variance were attributed to a high tool wear rate during high-speed machining, resulting in chip forming instability. In addition, the chip compression ratio increases with the cutting speed due to the high tool wear rate, resulting in the formation of thicker deformed chips as the shear angle decreases [123]. A similar phenomenon was noticed in the side milling of Inconel 718 by Li et al. [124], where rapid tool wear progression increased the deformed chip thickness due to high cutting speed, causing highly serrated chips during the milling operation. A more clear picture of the evolution of chip morphology with cutting speed for AISI 1045 is presented in Figure 2.5 [125].

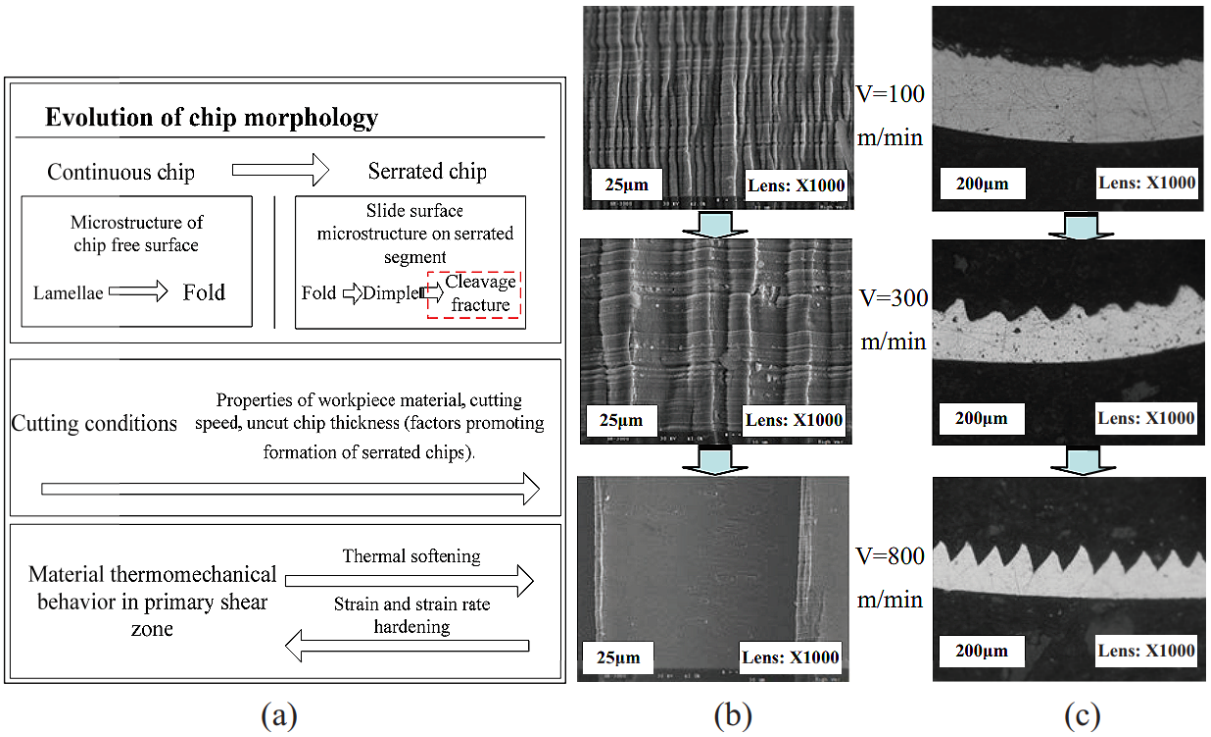

Figure 2.5: *(a) Evolution of chips in the primary shear zone; (b) free surface; and (c) chip cross sections* [125]

Furthermore, Liao et al. [3] discovered that the low cutting temperature at low speed lies below the softening point of the γ phase with a high strain hardening effect of Inconel 718, which resulted in high cutting force and chip embrittlement during slot and side milling operations. In addition, low and high cutting speeds produced disintegrated chips compared to medium cutting speeds. It was further observed that the welding effect of chips, which led

to BUE and BUL at a high cutting speed, was attributed to the low thermal conductivity and insufficient heat dissipation capacity of Inconel 718.

The serrated teeth become more evident and regular as the feed rate increases. Fei et al. [126] discovered that micro-saw-tooth formation is due to strain hardening and low ductility. As a result, the chip-free surface shows a more serrated tooth with an increased chip thickness due to the high feed rate. However, Thakur et al. [127] depicted that the cutting speed has a more significant effect on cutting force, chip morphology, and tool wear than feed rate during side and slot milling operations. Liao also confirms that the cutting speed significantly contributed to high plastic deformation of chip microstructure as compared to other process parameters under the orthogonal cutting operation of Inconel 718 [3]. Therefore, the serration of chips predicts the proper chip disposal, which enhances the heat dissipation capacity to minimize the thermally induced wear mechanisms during face milling of Inconel 718.

2.1.8 Literature summary for CNC milling of Inconel 718

During the CNC milling of Inconel 718, it is customary to maintain the characteristics of the tool and the cutting fluid, thus rendering the tool performance contingent upon the process parameters. Numerous studies have delved into the synergistic impact of process parameters on the Inconel 718 metallurgical properties. Nonetheless, no clear correlation has been established between the process parameters, wear mechanisms, failure modes, and progressive VB. As a result, there is still a dearth of empirical correlations that needs to be established to determine salient features for extrapolating tool wear during CNC milling of Inconel 718. Furthermore, the behaviour of chip morphology still needs to be comprehended to establish the properties that predict optimal process parameters.

2.2 Overview of Tool Performance Optimisation (TPO)

In order to overcome the difficulties encountered in face-milling Inconel 718, TPO techniques are utilized to determine optimal cutting conditions, such as cutting parameters, tool geometry, cutting fluids, and cooling methods, that minimize the rate of flank wear evolution during machining. For instance, Halim et al. [34] employed the cryogenic CO2 cooling technique to

optimize wear mechanisms and failure modes during high-speed milling of hardened Inconel 718, as abrasion, chipping, and built-up edge (BUE) were observed through SEM analysis. Another study revealed that the adhesion of BUE to the depth-of-cut line (DOC line) increased with the cutting temperature, owing to increase in the cutting speed and feed rate [3]. In addition, cutting speed and depth of cut had a profound impact on flank wear evolution during rough turning of Inconel 625, with abrasion and notching being the dominant failure modes identified in the process [19]. In such cases, cutting parameters are considered as in-process variables, which exacerbate failure modes and the rate of flank wear evolution during machining. Hence, TPO techniques were specifically developed to identify the significant levels of process parameters that can enhance tool performance during machining. These techniques are summarized in Figure 2.6.

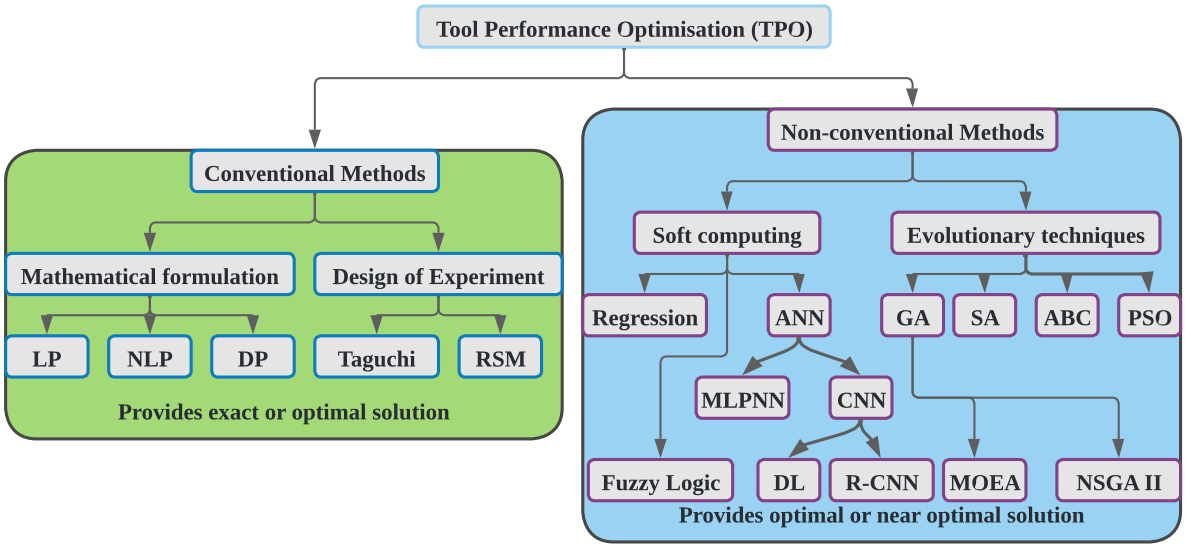

Figure 2.6: *Summary of techniques applied in tool performance optimisation*

2.2.1 Conventional Methods

Taguchi Method

The conventional methods include the Taguchi Method, Response Surface Methodology, and Mathematical Search Techniques. The Taguchi Method examines the impact of various machining parameters on both the mean and variance of performance characteristics, with the aim of optimally enhancing the overall machining process. It employs orthogonal arrays to arrange deviations in machining parameters and their corresponding levels, and test the ef-

fects of factor interactions on tool performance [128–130]. The method reduces the number of required tests and thus minimizes the cost of materials associated with a full factorial experimental design. The steps involved in Taguchi Method are outlined in [131].

The utilization of the Taguchi method offers a distinct advantage by enabling the assessment of numerous input variables without being hampered by large Design of Experiments (DOE). Nonetheless, it has been criticized for its insufficiency in producing results that clearly demonstrate the impact of individual parameters on performance indicators during multi-objective optimization [131]. Additionally, its reliance on orthogonal arrays means that it does not thoroughly evaluate the effect of every parameter combination, thereby neglecting the contribution of other detrimental interactions in predicting reliable TPO solutions.

Response Surface Methodology (RSM)

Response Surface Methodology (RSM) leverages techniques such as Central Composite Design (CCD) and Central Composite Rotatable Design (CCRD) to optimize tool performance by statistically varying cutting parameters during a machining process [132]. CCD implements factorial and axial points, along with center points, to examine the effects of interaction terms. The axial points are used to estimate quadratic terms and their interactions, with the rotatable design being referred to as CCRD, which provides equidistant points from the design center with desirable predicted variance for enhanced performance quality [133]. The significant interaction terms are then used to derive a second-order polynomial function through regression analysis, which constitutes a mathematical model to predict tool wear progression.

Such a technique was applied to optimize different machining operations. For instance, an RSM was used to formulate a second-order mathematical model that correlated cutting force and surface roughness with cutting speed and feed rate as significant parameters during high-speed drilling of Al-Si [134]. In addition, ANOVA analysis was performed to verify the impact of feed rate on tool wear progression during machining [135]. Similarly, Davoodi et al. [136] utilized RSM through CCRD to analyze the effect of cutting speed and feed rate on tool wear progression during the turning of N155 Iron-Nickel-based superalloy. The benefit of RSM lies in its ability to reduce material cost by utilizing significant interaction terms to formulate an objective function, however, it is limited to highly correlated and structured data

for linear regression analysis and a second-order regression model may not fit all machining data.

Mathematical Search Techniques (MST)

The Mathematical Search Techniques (MSTs) encompass linear, non-linear, and dynamic algorithms used for optimizing an objective function subject to specified constraints, where the objective and constraint functions are differentiable. Linear Programming (LP) specifically deals with linear objective and constraint functions, and has been successfully applied to linear problems of tool performance optimization, such as the selection of the optimal depth of cut in a multi-pass turning operation to minimize machining cost [137]. Non-Linear Programming (NLP) is capable of formulating multi-variable and multi-objective functions, however it may not provide an optimal solution for highly complex non-linear or discrete problems, such as 4-stage machining operations [138]. In such cases, Dynamic Programming (DP) techniques have proven to be more efficient in solving the limitations posed by LP and NLP. Nevertheless, MSTs have not been widely employed in the prediction of tool wear progression during the machining process due to the high cost associated with considering numerous inter-dependent variables and their relationships, as well as the limitation of MSTs to differentiable problems, which may not be applicable to some real-life machining scenarios [131].

2.2.2 Evolution Techniques (ET)

Genetic Algorithm (GA)

The Evolutionary Technique (ET) encompasses the use of Genetic Algorithm (GA), Particle Swarm Optimization (PSO), and Artificial Bee Colony (ABC). GA is the most frequently utilized ET method and facilitates the production of a population of optimal parameters through the application of reproduction, crossover, and mutation [139]. It creates new generations of parameters from the initial population or solutions that are obtained through various combinations of process parameters. Prasad et al. [140] applied GA to identify the optimum speed, feed rate, and depth of cut during turning, and observed that near-optimal tool wear was achieved at the 33rd generation of iteration. In another research, Gao et al. [141] utilized GA

to optimize tool wear progression and cutting force by adjusting speed, feed rate, and axial depth of cut, and concluded that GA was effective in avoiding local optimal solutions for both single and multi-pass cutting operations. In a comparative study conducted by Sen et al. [142], the performance of various artificial intelligence meta-modeling tools in predicting flank wear of TiAlN coated carbide inserts was assessed. The results indicated that Gene Expression Programming (GEP), a variant of GA, outperformed Artificial Neural Network (ANN). However, like any other GA technique, GEP necessitates the prior specification of a suitable approximation function for linear and non-linear objective functions [143]. The general process of GA is summarised in Figure 2.7.

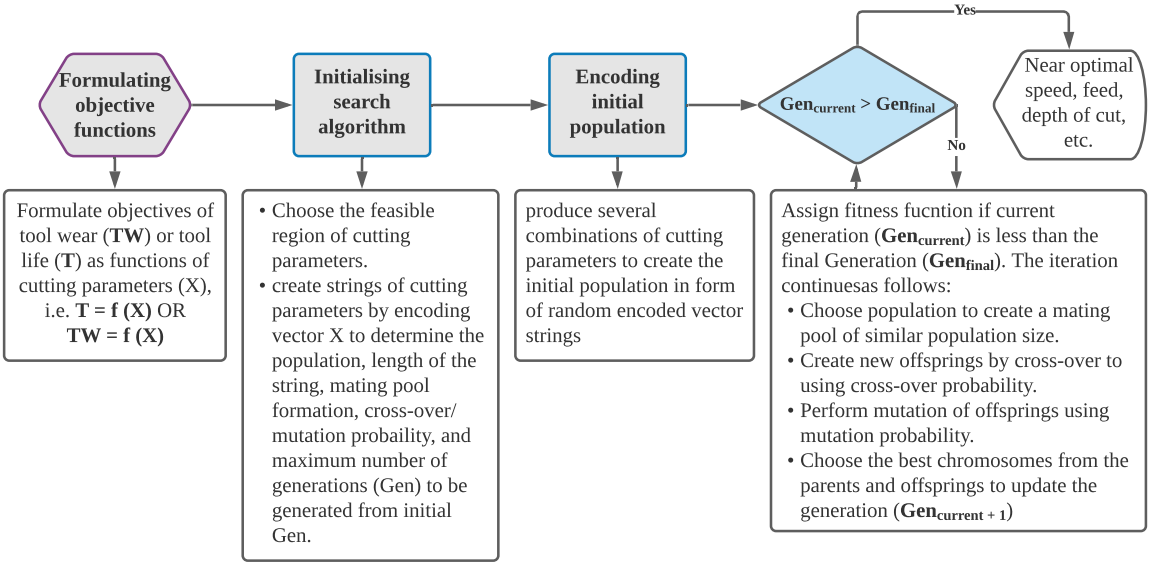

Figure 2.7: *The general methodology of GA in TPO* [143]

Furthermore, Multi-Objective Evolutionary Algorithms (MOEAs) hold a crucial position in discovering multiple Pareto solutions through a single run in order to minimize computational time. Bouzakis et al. [81] applied MOEA to determine the optimal cutting parameters for various objective functions in the milling process, and it was observed that the technique could also be utilized to optimize the performance metrics of multi-objective turning operations [144]. The Non-dominant Sorting Genetic Algorithm (NSGA) was introduced to attain true Pareto-optimal solutions [145], thereby alleviating the general weakness of MOEAs in generating diverse solutions in a single run. However, NSGA was prone to high computational time and low accuracy in identifying optimal solutions, leading to the development of

NSGA II which provided more accurate process parameters as compared to NSGA and other contemporary MOEAs such as Pareto-Archived Evolution Strategy (PAES) [146] and Strategy Pareto Evolution Algorithm (SPEA) [147]. Yusoff et al. [148] compared NSGA II, Single Objective GA (SoGA), and MOEA in optimizing MRR and surface roughness through pulse time, pulse current, flushing pressure, and electrode rotation of die sink EDM, and found that SoGA converged faster compared to MOEA and NSGA II during optimization, although NSGA II provided more accurate solutions than SoGA and MOEA. However, the full potential of NSGA II in optimizing tool performance in the machining operation has yet to be fully exploited. The general methodology of NSGA II is presented in Figure 2.8 [149].

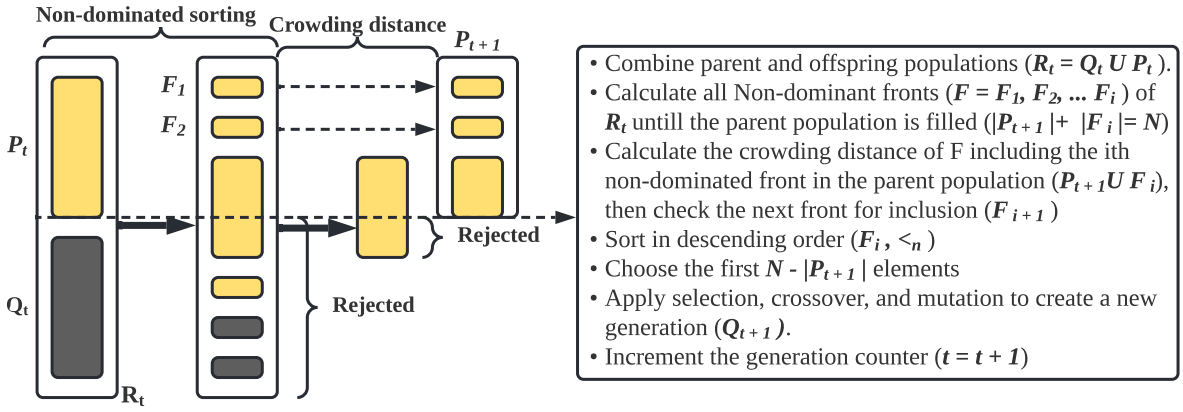

Figure 2.8: *The principal operation of NSGA II in machining process optimisation* [149]

In order to enhance the effective of GA, hybrid systems are employed to leverage the merits of various TPO methods and attain a superior optimization capability. For instance, the integration of ANN (Artificial Neural Network) with NSGA II was utilized to optimize tool wear, surface roughness, and MRR during the die sink EDM machining operation [150]. Additionally, the hybrid system of RSM-NSGA II demonstrated a superior tool optimization performance in comparison to the ANN-PSO approach during the turning operation of AISI 52100 steel with CBN (Cubic Boron Nitride) tools [151]. However, one of the primary obstacles encountered by both MOEAs and NSGA II is the computational complexity [152], particularly when evaluating the fitness function. To address this challenge, the fitness approximation technique is utilized in TPO [153]. This entails the usage of the parent fitness function to estimate the values of the offspring, or selecting the representative through clustering the solutions. Nonetheless, fitting the approximate function does not assure the attainment of an

optimal solution during TPO, as it restricts the relevance of other solutions that could contribute to determining an optimal tool performance.

Particle Swarm Optimisation (PSO)

To improve the accuracy in TPO, PSO utilizes a swarm of particles equipped with stochastic velocities to represent optimal cutting parameters that align with the objective function. The PSO algorithm converges to a global optimum by iteratively adjusting the position of these particles in the solution space. The efficacy of PSO in predicting tool performance is documented in [154] and [155]. PSO has been effectively utilized to optimize tool life, dimensional accuracy, and MRR in electrochemical machining [156], as well as minimizing surface roughness, cutting power, and force in milling operations [157]. To address its limitations in optimizing highly non-linear problems, it was integrated with a Wavelet Neural Network (WNN) to improve its convergence and prediction accuracy, which was found to be more efficient as compared to conventional WNN or hybrid GA-WNN models [158]. Despite its advantages of high speed, simple mathematical operations, and low memory requirements, PSO remains limited in solving highly complex non-linear and discrete objective functions in machining operations.

Artificial Bee Colony (ABC)

The Artificial Bee Colony (ABC) algorithm emulates the behavior of a bee colony to optimize the tool performance by maximizing the objective function, represented as the quantity of nectar collected by the bees and unloaded at the hive [159]. The employed bees carry out a greedy selection to locate, memorize and evaluate the quality of food sources, which are then communicated through a waggle dance. The onlookers select the most advantageous sources based on probabilistic selection and modify them accordingly. Inferior food sources are abandoned and their corresponding employed bees become scouts. The Deb rule, introduced by Karaboga et al. [159], facilitates the evaluation of the feasibility and cost of infeasibility by enabling the selection of the lowest cost and most feasible process parameters during tool performance evaluation. Samanta et al. [160] employed the ABC technique to determine the best process parameters for EDM and Electro-Chemical Micro-Machining (ECMM) operations.

The results indicated that the ABS algorithm was particularly suitable for finding the optimal voltage, electrolyte concentration, and inter-electrode gap, which optimized the Radial Overcut (ROC) and Heat Affected Zone (HAZ). However, like GA techniques, ABC is also hindered by slow convergence, which arises from the selection of the initial population of the machining parameters.

2.2.3 Soft Computing Techniques

The problem of computational complexity encountered by both conventional and evolutionary techniques can be abated by the implementation of Machine Learning in TPO [131]. These methods encompass, though not restricted to, regression, Artificial Neural Networks (ANNs), and fuzzy logic models. Regression analysis constitutes modeling of mathematical equations (linear, non-linear, logistic, multi-variant, etc.), that predicts tool performance through the utilization of input variables such as sensor signals, cutting parameters, and image features. It was reported to be quicker and more accurate than ANN in predicting tool wear progression under limited dataset [161]. Due to their simplicity, efficiency, and integrability, regression models play an essential role in modelling the objective functions when using other TPO techniques [136]. Thangavel et al. [162] developed a regression model using RSM to predict flank wear progression using cutting speed, feed, and depth of cut, and the model showed a high performance with a standard estimated error of 0.012 mm. Contrary to findings found in [161], Gupta et al. [163] discovered that ANN was better than regression and SVM in predicting tool wear progression.

In general, previous research applied the regression model by assuming tool wear data can fit a quadratic polynomial function, as presented by [162–164], among others. However, such modelling works better when the absolute curvature of the response function is already known or established by experts based on the underlying tool wear behaviour of a particular machining operation [163]. Such a complexity gets worse when machining superalloys, such as Inconel 718, where the key descriptors are not easily defined under highly complex wear mechanisms and failure modes.

Conversely, ANNs employ artificial neurons to learn and extrapolate the trends of wear behaviour without the need for mathematical models, making it more adaptable and efficient

for linear, non-linear, and discrete machining operations [165]. Unlike regression models, ANN eliminates the need for formulating complicated objective functions for intricate tool wear behavior by employing backpropagation to optimize the neurons' weights during learning, thereby effectively adjusting feature attributes to be aligned with tool wear evolution during machining [166]. This characteristic was utilized to optimize creep feed during the grinding of superalloys [167], and predict the MRR and surface roughness of abrasive flow machining [168]. Furthermore, it was established that ANNs have flexible architectures that could easily integrate with traditional methods to optimize tool performance [169]. For instance, Taguchi-ANN and Taguchi-regression hybrid models were applied to select the optimal speed, feed, and axial depth of cut during machining of composites [170]. The hybrid systems were observed to predict tool performance more rapidly and with greater accuracy than regression models. Nonetheless, the risk of over or under-fitting issues in ANNs persists if the dataset is inadequate, unless the training process is terminated prior to reaching an optimal point, making it unlikely to achieve optimal solutions for various machining operations [171].

To overcome overfitting issues with small dataset, fuzzy logic models are applied by utilizing the relationship between input features and outputs. This is achieved through a process referred to as fuzzification, which involves the generation of analytical computations or rules to relate inputs and outputs [172]. It was used to optimize tool life and cutting efficiency in surface milling operations through the development of a logical rule-based operator [173]. However, it can be challenging to formulate logical rules with more input features, especially in the case of multi-variable and multi-objective machining problems. To mitigate this issue, Fuzzy Logic can be integrated with Artificial Neural Network (ANN) architectures, forming hybrid systems that can leverage the strengths of both methods to minimize computational complexity and improve prediction accuracy [172]. One such example is the Artificial Neural Fuzzy Inference System (ANFIS), which was modelled using features extracted from sound and force signals to predict flank wear progression during a milling operation and demonstrated its ability to quickly and accurately predict tool wear [174]. However, the computation complexity in modelling logical rule operators still persists even in hybrid systems.

Therefore, to combat the high computation complexity for multi-feature modelling in fuzzy logic, the Support Vector Machines (SVM) algorithm leverages linear functions to cate-

gorize both structured and unstructured data into a hyper-space [175]. It optimizes the separation of tool wear features using hyper-planes within a hyper-space [176]. SVM has been utilized in conjunction with other machine learning models to improve the accuracy of tool wear prediction, such as an integrated model of SVM, ANN, and Gaussian regression model to enhance the tool wear monitoring process [177]. Moreover, it was integrated with deep convolution neural networks to classify tool wear during the machining process [175]. It has been observed that SVM is effective for unsupervised learning of structured and unstructured tool wear data, although the challenge lies in selecting an appropriate kernel function and adjusting hyper-parameters to enhance the robustness of the trained network [178]. However, the "black-box" prediction process created by the lack of efficient hyper-parameters tuning of SVM can affect the prediction accuracy during machining [176].

2.2.4 Summary of In-Process TPO

One of the challenges is to integrate the TPO techniques into machine settings for the predictive control of tool wear evolution. Because of this, an in-process Tool Performance Optimization (TPO) is commonly used offline to optimize tool wear progression. To that end, ANN-based and regression-based models were found suitable for predicting in-process evolution of tool wear progression during machining [174]. A summary of TPO techniques and their respective advantages and disadvantages in predicting tool wear evolution online are presented in Table 2.1.

Table 2.1: Summary of applying TPO techniques for in-process predictive control of tool wear evolution

MPO Technique	Advantage	Limitation	Application for TPO
Taguchi	Saves time and materials	Time-intensive	Not suitable
RSM	Reduces time and cost	Time-intensive	Not Suitable
MST	Simple and accurate	Time-intensive	Not suitable
SoGA	High accuracy	NA for multi-objective	Not suitable
MOEA	Solves multi-objectives	computation complexity	Not suitable
NSGA II	High accuracy	Time-intensive	Not suitable
PSO	Fast convergence	NA for multi-objective	Suitable
SA	fast convergence	No repeatability	Not suitable
ABC	Solves multi-objective	Slow convergence	Not suitable
Regression	Simple and fast	Data constraint	For large dataset
ANN	Fast and robust	High overfitting	For large dataset
Fuzzy Logic	High accuracy	High complexity	Combine with ANN

It was observed that most techniques compute optimal processing parameters based on the final outcome, such as the longest tool life or the lowest wear rate. However, this methodology fails to account for the in-process evolution of failure modes and wear mechanisms, which reveal the sub-optimal cutting mechanism during face milling of Inconel 718. To overcome this, it is advisable to monitor tool wear evolution at different flank wear stages. The ideal flank wear progression comprises four stages: initial wear stage, uniform wear stage, and rapid failure stage (which can also be identified as critical and failure stages), as depicted in Figure 2.9a. For example, Figure 2.9b [9] illustrates the tool performance at various cutting speeds and flank wear rates at stages A, B, and C.

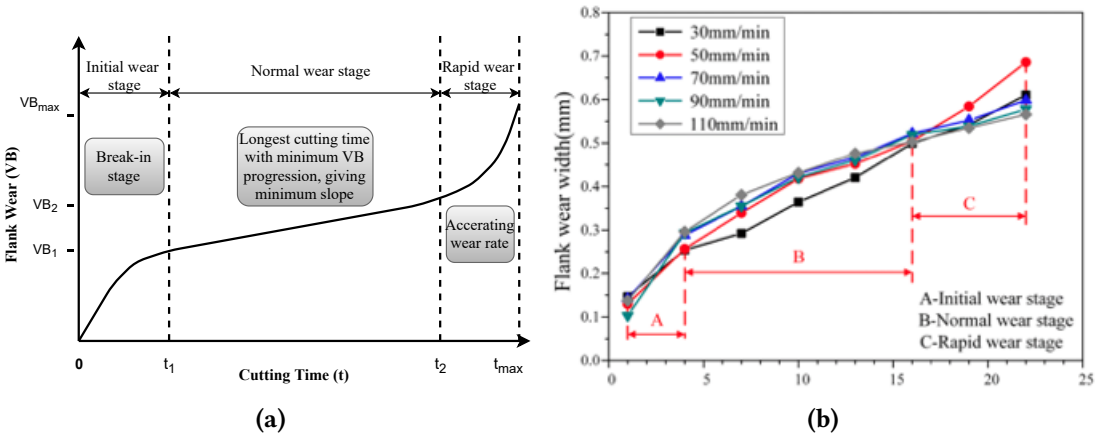

Figure 2.9: *(a) Stages of flank wear progression; (b) The VB response with the varying speed at each stage* [9]

Research indicated that the wear mechanisms tend to intensify during the rapid failure stage, where it is too late to adjust the cutting conditions to prevent rapid tool failure [2]. The steady wear stage is thus crucial for evaluating failure modes and wear mechanisms before they propagate to catastrophic failure. At this stage, the tools yield the highest economic productivity and the lowest flank wear rate [34]. Therefore, if the dominant failure modes and wear mechanisms are detected during the initial or uniform wear stages, countermeasures, such as change in process parameters, can be applied to reduce the evolution of failure modes magnitudes, thereby enhancing tool life extension during face milling of Inconel 718.

2.3 Tool Wear Monitoring Techniques

Therefore, the predictive control of tool wear evolution can be realized by two key indicators of the cutting mechanism: (1) failure modes detection and (2) VB prediction. The latter serves as a preventive measure against premature tool failure, whereas the former provides the micro-structural evolution of wear mechanisms that exacerbate the rate of flank wear evolution during machining [179]. This is why the deployment of Tool Condition Monitoring (TCM) techniques is required to monitor the evolution of VB and failure modes, enhancing the in-process TPO during face milling of Inconel 718. To improve the performance of tools, TCM was utilized to predict and control tool wear progression during machining. TCM diagnosed the magnitudes of failure modes to provide the causative mechanisms of the sub-optimal cutting mechanism. Currently, the predominant techniques employed in TCM include physics-based models, indirect methods of sensors, and direct methods of machine vision systems. Figure 2.10 illustrates a general TCM approach during the machining of Inconel 718.

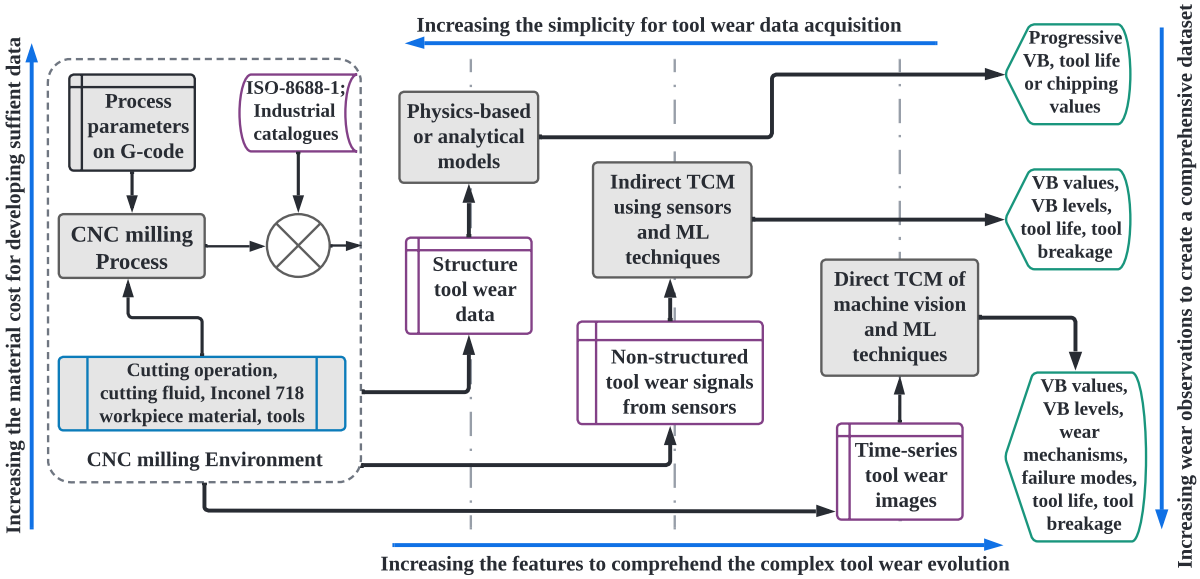

Figure 2.10: *Attributes and limitations of TCM techniques during CNC milling of Inconel 718*

2.3.1 Physics-based Models

Physics-based models apply the fundamental laws underlying the relationship between inputs and outputs. These models depict the physical behaviour of tool wear evolution based on the statistical change in the process parameters. The widely employed physics-based model is

'Taylor's tool life' [180]. It is pre-eminently utilized to anticipate tool life (T_c) by taking into account modifications in process parameters. The model is derived on the assumption that process parameters are the significant indicators of tool life, with the cutting speed (V_c) being the most critical parameter affecting tool wear progression when other input conditions are kept constant (C and n), as outlined in 2.1. In this scenario, its robustness is established based on the positive correlation between flank wear depth (VB) and cutting speed. Over time, the model was expanded to include other process parameters, such as the feed rate and depth of cut, thereby examining the synergistic impact of process parameters on tool life during machining (2.2).

$$V_c T_c^n = C \tag{2.1}$$

$$V_c T_{c(ext)}^n f_t^m a_p^r H^q = K T_{c(ref)}^n f_{t(ref)}^m a_{p(ref)}^r H_{ref}^q \tag{2.2}$$

Where $T_{(c(ext))}$ is the predicted tool life, f_t is the feed/tooth, a_p is the axial depth of cut, H is the material's hardness, and (ref) is the reference value. The values of m, r and q are exponential coefficients experimentally determined using a set of tool wear data by applying equation 2.3, which is linearly presented by logarithmic transformation using equation 2.4.

$$T_{ext} = C V^k a^m f_t^l \tag{2.3}$$

$$ln T_{c(ext)} = log\, C + k log\, V + m log\, a + l\, log\, f_t \tag{2.4}$$

Where V_c, a_p, and f_t are cutting speed, depth of cut, and feed/tooth. Although Taylor's model primarily focused on cutting speed, other physics-based models indicate the depth of cut and tool geometry as crucial parameters that can predict tool wear progression during machining. For instance, Lu et al. [181] employed a FEM using Usui's model, in which tool geometry and axial depth of cut were pivotal indicators of tool life during the micro-milling of Inconel 718 using 2-flute, PVD-TiAlN coated tungsten carbide tools. By utilizing the features of tool geometry and axial depth of cut, the model achieved a tool life percentage error of

12.12% when measured against the conventional methods. Furthermore, the power-law model, specifically Paris law, was also utilized to model tool wear progression by monitoring crack growth and propagation to reveal the critical point of tool failure during machining [21, 105, 182]. However, these models do not consider the synergistic impact of process parameters on wear mechanisms when predicting tool life during machining.

To address these constraints, statistical methods were developed by considering the impact of interaction terms on tool wear evolution. One such technique is Response Surface Methodology (RSM) [164], a TPO technique, which utilizes the combinations of critical process parameters through the regression equivalence of input-output relationships to express tool wear progression as a second-order polynomial function. However, the efficacy of such modeling techniques is contingent upon the knowledge of the absolute VB curvature, which is derived from a known correlation between the flank wear and process parameters [163]. However, if the VB profile is not well-defined due to high complexity in wear mechanisms and failure modes evolution, the development of such models becomes more challenging. As a result, physics-based or analytical models, whose coefficients are restricted by specific ranges of process parameters, may not accurately extrapolate the VB profile under the unknown cutting conditions. This limitation renders them unreliable for real-time prediction of tool wear evolution during face milling of Inconel 718 as the key parameters are not easily defined due to complex flank wear morphology.

Although physics-based models necessitated the utilization of limited dataset, the coefficients derived from these models are only valid within the vicinity of the training dataset [21]. As a result, these coefficients are not robust enough to extrapolate the VB profile under unknown cutting conditions. Additionally, the rapid evolution of failure modes, which cause stochastic tool wear evolution, may result in an uncontrollable input feature, which may not accurately predict tool life during machining [20]. Hence, there is a need to utilize data-driven models in TCM, which are derived from empirical observations made during the physical experiment. These techniques can be applied indirectly by using sensors or directly by using machine vision systems.

2.3.2 Indirect Sensor-based Technique

Indirect TCM methods utilize force, vibration, acoustic emission, current, power, and sound signals to monitor the progression of tool wear during machining operations. Research has established a positive correlation between changes in sensor signals and the evolution of tool wear [183].

Vibration

Vibration signals are captured using accelerometers that detect changes in the time-domain and frequency-domain responses caused by tool wear progression during machining. For instance, an accelerometer was affixed to the tool holder to gather time-domain responses, which were utilized to predict tool wear progression during machining [184]. Unlike frequency-domain features, it was discovered that time-domain features were more vulnerable to cutting conditions such as variations in speed or feed rate, rather than tool wear evolution [185]. Because of this, time-domain signals are converted to frequency-domain using either the Fourier transform spectrum or the Hilbert-Huang transform, in order to identify reliable signatures that correlate with tool wear progression [186]. A sharp increase in frequency amplitude indicated a rapid increase in the wear rate [187]. However, accelerometers are limited to a specific range of cutting speeds due to their sensitivity to high frequency amplitudes, and are susceptible to noise signals originating from material properties, background noise, CNC environments, such as flood coolant, and sensor position [188, 189].

In addition to accelerometers, vibrometers and microphones have also been utilized to assess the continuous change in vibration signals due to tool wear evolution during machining. For instance, Rao et al. [190] employed a Laser Doppler Vibrometer (LDV) to quantify the variations in frequency amplitudes that positively correlated with the progression of tool wear during the turning of AISI1040 steel. Similarly, Weingaertner et al. [191] utilized a PCB 377A02 microphone to identify real-time changes in the acoustic signals that were correlated with tool wear evolution during machining. Unlike accelerometers and vibrometers, the microphone's audio frequency range was deemed more reliable in detecting vibration signals under dry cutting conditions.

Force

The cutting force signals can be obtained through the use of dynamometers [192], and processed to identify feature attributes that are correlated with tool wear progression during machining [193]. However, the integration of dynamometers in a production line is challenging and not cost-effective, restricting their applications for most machining operations. In addition to dynamometers, magnetic sensors have been employed to measure the change in the torque signals of a rotating spindle, in correlation with tool wear progression during machining [194]. Nonetheless, the deployment of torque sensors often results in elevated heat, which negatively impacts their sensitivity during data acquisition. To mitigate this issue, the compensation of heat can be accomplished, enabling the extraction of the desired features from signals through the utilization of alternative methods, such as strain gauges, which specifically target stationary tools in turning operations [195].

Furthermore, the utilization of internal sensors for monitoring force signals that correspond with tool wear progression during machining is widely used in TCM. This method employs the integration of servo motors with current sensors for load regulation, wherein the cutting force and torque signals are computed by analyzing the armature current within the spindle motor. An illustration of this is demonstrated by Altintas et al. [196], who analyzed tool wear progression through the examination of current signals and determined that it is the most cost-effective technique of monitoring tool wear progression, as it requires no external connections for acquiring signals. Furthermore, in certain modern CNC machines, the load of the spindle is depicted on the control panel, thus streamlining the signal acquisition process. Nevertheless, it was established that integrating torque with other sensors signals is more effective as compared to the single-sensor TCM approach. For instance, the combination of torque and vibration signals enhances the prediction accuracy, although it necessitates the deployment of complex data processing techniques for extracting relevant features that correspond with tool wear progression [197].

Apart from dynamometers and torque signals, the utilization of cutting power to monitor tool wear progression during machining has been widely studied and implemented in the field of TCM. The cutting power, being proportional to the shear force applied by the tool on the primary and secondary shear zones, serves as a direct indicator of the tool performance and

provides valuable insight into the cutting operation [198, 199]. Furthermore, the power source in most cases is integrated into the CNC machine, such as the generator, power panel, or control unit, thereby simplifying the process of acquiring tool wear signals [200]. However, it is noteworthy that the extraction of cutting force from power signals is more susceptible to variations in process parameters as compared to direct force obtained from dynamometers or torque sensors [201]. Consequently, the cutting power is typically used for detecting tool breakage under constant process parameters [202].

Sound and Acoustic Emission

Acoustic Emission (AE) is the propagation of sound waves in three zones of the machining process: the primary shear zone (resulting from chip formation), the secondary shear zone (resulting from friction between the cutting tool and chips), and the tertiary shear zone (resulting from friction between the flank face and workpiece material) [203]. AE boasts a superior signal-to-noise ratio at low depths of cut, making it a superior method for online TCM [204]. Additionally, AE provides highly precise feedback of tool wear signals, making it a viable option in micro-milling applications, particularly when compared to force and vibration sensors [205, 206]. However, AE's strong signal-to-noise ratio also leads to signal errors during tool wear analysis, necessitating a complex feature extraction process [60, 66]. To overcome this challenge, researchers have utilized microphones with high-frequency capability to capture changes in tool wear signals during machining. For instance, a BK 4165 microphone was used to detect AE signals related to tool wear progression during turning of AISI 8620 steel [207]. A 12-bit data acquisition board with a 100kHz sampling rate was used to collect the necessary tool wear signals. Furthermore, the microphone's high sensitivity to chatter allowed it to monitor tool wear progression during high-speed milling, as it detected large frequency amplitudes in comparison to vibration signals.

AE can also be scrutinized through the medium of acoustic waves. As demonstrated by Tekner et al. [208], the machinability of AISI 304 stainless steel was assessed through the examination of tool wear progression via acoustic waves. However, a decrease in sound pressure was observed to amplify noise signals, necessitating the deployment of sophisticated filtration methods to extract valid features that were congruent with tool wear progression.

In this regard, it was observed that methods such as Singular Value Decomposition (SVD), Fast Fourier Transform (FFT), and Hidden Markov Model (HMM) could be utilized for feature selection and dimensional reduction, as highlighted in works by Lu et al. [209] and Prakash et al. [210]. Except for SVD, the FFT and HMM techniques were used to extracted features from tool wear signals acquired above 10kHz frequency [88] with noise frequency below 2kHz. Thus, it can be inferred that acoustic signals are not as trustworthy as force, vibration or AE sensors in extrapolating tool wear progression.

Recent challenges while using the indirect methods of sensors

Despite their ability to provide continuous and adaptive monitoring of tool wear progression through real-time data acquisition, sensors face a substantial challenge in detecting unstable wear mechanisms and failure modes, which are crucial indicators of suboptimal tool performance. Additionally, indirect TCM necessitates convoluted data processing techniques, thereby restricting their feasibility for simple diagnostic analysis, such as identifying tool breakage and VB levels. Hence, there is a need to implement methods that can both predict flank wear evolution and detect the magnitudes of multiple failure modes during machining. Tool wear images have the potential to furnish such vital information, thus making machine vision systems indispensable in TCM.

2.3.3 Traditional Methods of Machine Vision TCM

The limitations of both physics- and sensor-based TCM prompted the implementation of machine vision systems. While these techniques may not be suitable for ”real-time” applications, they offer a more accurate method of diagnosing wear mechanisms, failure modes, and flank wear rate. Given the paramount importance of achieving the predictive control of tool performance during TCM, the significance of utilizing machine vision is underscored due to its high accuracy in achieving the qualitative and quantitative understanding of the mechanical and microstructural features that attribute to flank wear evolution during machining. It is achieved by monitoring the evolution of dominant wear mechanisms, failure modes, and flank wear rate with a high degree of precision and accuracy. By understanding the evolution of these diverse features, machine vision is imperative in identifying the causative mecha-

nisms that offer insightful solutions to minimize the risk of uncontrolled tool failure during CNC milling of Inconel 718 [211, 212].

Additionally, by measuring the progressive VB using optical microscopes and Toolmaker, just to mention a few, machine vision predicts the failure criteria and Remaining Useful Life (RUL) prior to tool replacement, as specified by the ISO-8688-1 standard [12], also depicted in Figure 2.2. To implement this, the machining process is temporarily interrupted, and the tools are detached from the cutter for subsequent diagnosis via Scanning Electron Microscopy (SEM) and Energy-Dispersive Spectroscopy (EDS) to identify the dominant wear mechanisms and failure modes [2]. According to previous studies, scanning through SEM/EDS revealed abrasion, adhesion, diffusion, attrition, and oxidation as prevalent wear mechanisms that accelerate flank wear during machining [34, 213]. These wear mechanisms give rise to uncontrolled failure modes, which can as well be observed using SEM/EDS, Optical Microscopes (OM), and X-ray Diffraction (XRD) techniques, as depicted in Table 2.2.

In addition, tool-maker, and optical microscopes are deployed to measure the magnitudes of various failure modes, such as flank wear depth (VB), chipping width, and crater depth, thereby establishing the criteria for tool failure during machining [12]. As a result of their precision in detecting and estimating the magnitudes of failure modes, they are frequently utilized in conjunction with various Tool Performance Optimization (TPO) techniques to determine the optimal cutting parameters during machining processes. For instance, SEM was utilized to diagnose tool wear mechanisms, supplementing Response Surface Methodology (RSM) in determining potential process parameters that improved tool performance during machining operations [225]. Additionally, the literature has established various cutting solutions that can effectively mitigate the rapid evolution of wear mechanisms and failure modes across a wide range of machining applications [211, 212].

However, despite their ability to extract essential features, conventional methods are plagued with a high processing time, reliance on human observation, and an elevated cost of tool wear inspection. To avoid excessive time and costlier determinants, these methods are applied at the end of tool life and not during the machining process, thus providing insufficient information regarding wear mechanisms and failure modes evolution. Additionally, the high dependence on human expertise in tool wear characterization limits the application of

Table 2.2: Summary of techniques used to inspect failure modes and tool wear mechanisms on various tools

Citation	MV-Technique	Tool/workpiece	TWM	Failure mode	TPO remarks
[213]	SEM; EDX; OM	carbide inserts/AISI 4340	AD, Att, AB, DF	FW, CW, CF, CP, FL, CD	Optimise V, F, ADOC
[214]	SEM; EDS; OM	Carbide inserts/TC6 alloy	AD, AB	CP, BR, TC, PD	Optimising parameters
[215]	SEM; EDX	Cemented carbide/Ti-alloy	AD, Att	FW, CP, TC, CD	Optimise V
[136]	SEM	Tungsten carbide/N-155	AD	CW, BUE, CP, FL	Optimise V, F
[216]	SEM	carbide inserts/AISI 4340	AD, AB	FW, CW	Optimise V, F, ADOC
[217]	XRD, SEM; EDS	CVD inserts/stainless steel	AD, AB, DF	FW, PD, CF, NSW	Optimise V
[218]	SEM	Tungsten carbide/Ti-6Al4V	NA	FW, CW, PD, CP, NW	Optimise V
[219]	SEM; EDS	carbide inserts/20CrMnTi	AD, OXD	CP, FL, FC	Optimise V, F, ADOC
[179]	SEM; EDS	PVD; CVD/TC11 alloy	AD, OXD, DF, AB	BR, CD, CP,	Optimise cutting fliuds
[220]	SEM; EDX	carbide inserts/AISI 304	AD, AB	CW, BUE, CP, FW, FC	Optimise V
[221]	SEM; EDX; OM	carbide inserts/Ti-6Al-4V	AB, AD, OXD	CP, CD, FL	Optimise V
[222]	SEM; EDX; TMM	cermet inserts/AISI 1045	AD, Att, AB, OXD	NW, CP, TC, PW	Optimise cutting fluids
[223]	SEM; EDX; OM	Tungsten carbide/Ti–6Al–4V	AD, OXD, AB, DF	FW, CW, CF, CP, FL, BUE	Optimise parameters
[224]	SEM; EDX; OM	Sialon ceramic/superalloy FGH96	AD, DF	CP, FL, NW	Optimise parameters

V- Cutting speed; F- Feed rate; ADOC- Axial Depth of Cut; CP-Chipping; CD-Coating Delamination; FW-Flank wear; CW-Crater wear; BR-Breakage; FW-Fracture wear; NSW-Nose wear; NW-Notch wear; AB-Abrasion; AD-Adhesion; DF-Diffusion; OXD-Oxidation; Att-Attrition; BUE-Built/Up Edge; TC-Thermal cracks; FC-Fatigue cracks; PD-Plastic deformation

these methods to unskilled machinists. However, with advances in computer vision technology, high-speed industrial cameras, and artificial intelligence, the implementation of cyber-physical Machine Vision-based Tool Condition Monitoring (MV-TCM) systems can mitigate the challenges posed by conventional methods, as demonstrated by several studies, including [25, 50, 226–231]. Moreover, the deployment of AI in MV-TCM can simplify tool wear characterization for non-skilled personnel during machining operations.

2.3.4 On-Machine Vision-based TCM (MV-TCM)

The online MV-TCM system comprises three key components: image acquisition, features extraction, and tool wear analysis [232, 233].

Tool Wear Image Acquisition

Image acquisition is executed through the deployment of CCD or CMOS cameras within the CNC milling environment, as illustrated in Figure 1.1. An overview of the existing literature pertaining to the image acquisition process can be found in Table 2.3. It was noted that the implementation of industrial cameras is challenging due to the presence of coolant splashes and swarf, which constrain the potential installation areas of cameras within the CNC milling environment [234]. If the camera is installed on a wrong position, the resultant images contain excessive blurriness, distracting the spatial resolution of features critical to the failure modes detection during MV-TCM [25]. To mitigate the impact of smearing, researchers have resorted to either dry cutting or minimum quantity lubrication, as indicated in Table 2.3. However, the utilization of dry cutting during milling of Inconel 718 is not a viable option due to the excessive heat, friction, and thermal wear mechanisms, which accelerate tool degradation. Thus, there is a need to develop an imperative MV-TCM system capable of resisting the deluge cooling conditions encountered during CNC milling of Inconel 718.

Features Extraction

After data acquisition, the extraction of features is as well a crucial aspect of the MV-TCM system, as it facilitates the dimensionality reduction and selection of robust features, which correlate with tool wear progression during machining. This stage involves the implementa-

Table 2.3: Summary of recent MV-TCM systems

Reference	Machining Process	tool Material	Material	Camera	Lens	TCM Analysis
[25]	Dry Milling	Tungsten Carbide	AISI 1045 Steel	CMOS	Telecentric Lens	Flank wear measurement
[39]	Dry Milling	coated tungsten carbide	GH4169 Nickel	CCD	M0814 MP2FA	Flank wear measurement
[235]	Dry Milling	NA	NA	CMOS	Telecentric Lens	tool wear measurement
[50]	Dry Milling	High speed steel	Mild Steel	NA	NA	Tool wear prediction
[236]	Dry Turning	Coated Carbide tools	Inconel 718	CMOS	NA	Tool wear monitoring
[236]	Dry Turning	coated Carbide Inserts	Nimonic 75	NA	NA	tool wear measurement
[237]	Dry Milling	NA	NA	CCD	Fixed focal length	Tool wear measurement
[238]	Dry Milling	TiAlN-Tungsten carbide	Steel T4	CCD	Telecentric Lens	tool wear measurement
[239]	Dry Turning	carbide inserts	AISI1050 steel	CMOS	Macro zoom lens	Flank wear prediction
[240]	Dry Turning	carbide inserts	AISI1050 Steel	NA	Macro zoom lens	tool wear prediction
[241]	Dry Turning	carbide tool T15	40 Cr	CCD	NA	tool wear measurement
[227]	Broaching	Broach	NA	CCD	Telecentric Lens	Tool wear characterization
[230]	Dry Turning	carbide inserts	C 50 steel	CCD	Macro zoom lens	flank wear detection
[242]	Dry Milling	cemented carbides tool	Stainless steel	CCD	Telecentric lens	Tool wear measurement
[243]	Dry Turning	Coated Cemented Carbide	AISI 304 steel	CCD	Fixed Focal Length	flank wear measurement
[244]	Dry Drilling	TiN/TiCN/TiAlN	NA	CCD	Fixed focal length	flank wear measurement

Table 2.4: Summary of image processing techniques applied in MV-TCM

Reference	Extraction Technique	Illumination Unit	TCM Analysis	Limitations
[245]	GLCM and fractal	White light	Tool wear measurement	Less very accurate
[246]	Illumination controlled	LED ring light	Flank wear measurement	Not optimised for all tools
[247]	laser resolution	lighting with Laser	Tool wear measurement	No images filtering
[248]	Median, statistical filter	NA	Flank wear measurement	Offline measurement
[249]	Interferometry technique	White light	Detection of crater wear	did not measure crater depth
[250]	image processing software	Halogen light	VB, crater measurement	Offline and manual
[251]	GLCM; Fourier; Fractal	White ring light	Flank wear analysis	Did not measure VB
[252]	Accurate edge detection	Circular lighting	Flank wear detection	Not applicable on smeared tool
[253]	Segmentation, Linear discriminant	DC regulated light	Tool wear classification	No tool wear measurement
[254]	Canny, kNN and MLPNN	DC regulated light	Tool wear classification	Only 2 levels classified
[255]	Level set contour	LED light	Flank wear measurement	offline measurement
[256]	Level set segmentation	Fluorescent light	Extracting wear area	Did not measure VB
[257]	Canny, Active Contour	Side, Ring light	Flank wear measurement	Offline measurement
[258]	Otsu, Sobel edge detection	NA	Tool wear classification	Did not measure VB
[259]	ANN classifier	No light	Edge detection	limited to bi-modal images
[37]	Otsu, median filter, CED	LED light	VB measurement	Offline measurement

tion of image processing techniques to eliminate noise and extract features that quantify the progressive change in tool wear during machining. For instance, Duan et al. [255] integrated the level set and histogram contour segmentation to effectively eliminate extraneous noise resulting from smearing during machining. Furthermore, alternative methods such as morphological reconstruction, canny edge detection, and variation level-set segmentation were found to be effective in extracting geometric features, including area, average width, and perimeter of the wear region, to represent the progression of flank wear during machining [37, 256]. A synopsis of the image processing and feature extraction techniques used in MV-TCM can be found in Table 2.4.

Furthermore, the triangulation Stereography was employed for the extraction of features correlating with the progressive change in flank wear and crater depth [245]. The method proved inadequate in quantifying the tool wear progression of grooved inserts, particularly with regard to varying flank and crater wear depths. To address this limitation, interpolation and search techniques were implemented to enhance image focus at various wear depths and extract robust features, thereby increasing the accuracy of the predicting the progressive VB and crater wear during MV-TCM analysis [260]. Nevertheless, the majority of research utilized threshold segmentation for feature extraction, which presumes a bimodal characteristic of the image, comprising two separate regions demarcated by a definite boundary [261]. However, real-time tool wear images often contain more than two regions, particularly during machining of Inconel 718 where failure modes such as chipping, notching, BUE, and flaking complicate feature patterns [262, 263].

Subsequently, the utilization of textural, fractal, and Fourier transform analysis circumvents the complexity posed by the multi-modal characteristic of tool wear images. For instance, Kerr et al. [251] employed histograms, the Gray Level Co-occurrence Matrix (GLCM), fractal analysis, and Fourier spectral analysis to extract textural descriptors of tool wear progression in end milling operations. Additionally, Li et al. [241] employed the GLCM, watershed transform, and Markov random field segmentation techniques to extract entropy and average grey-level pixel values from small wear regions to evaluate tool wear progression during machining. However, the consistency of GLCM features can be influenced by the extent of failure depths, which create complex textural properties in the wear region. Consequently, research

has highlighted the significance of considering a variation in wear depths when extracting textural features for tool wear analysis [249]. It was discovered that image processing techniques like singular value decomposition, tensor decomposition, principal component analysis, fractal analysis, and deep learning, which simplify the reduction of dimensionality, filtering of noise, and extraction of features, can be fully leveraged by most MV-TCM techniques. *Hence, further research is needed to assess the viability and suitability of these techniques in MV-TCM.*

Tool Wear Analysis and Prediction

Meanwhile, the extracted features are subjected to machine learning-based analysis, including the utilization of artificial neural networks (ANNs), support vector machines, fuzzy logic algorithms, and regression models, with the aim of predicting the progression of tool wear evolution during machining. These algorithms are contingent upon numerical features to predict the extent of failure modes, such as progressive VB, build-up edge (BUE), chipping width, and crater depth, as depicted in Figure 2.11. The implementation of machine learning-based MV-TCM has emerged as a crucial aspect in optimizing tool wear due to its efficient predictive capacity. As an illustration, a Wavelet Neural Network (WNN) was implemented in a study by Ong et al. [50], combining the multi-scale wavelet transform and ANN to predict flank wear during end milling operation. It utilized parameters such as speed, feed, depth of cut, and image features to exhibit superior accuracy as compared to Deep Multi-Layer Neural Network (DMLNN), Radial Basis Function Neural Network (RBFNN), and RSM. However, the authors recommended that optimizing the illumination conditions of the MV-TCM system could improve the image focus during acquisition, as well as features extraction.

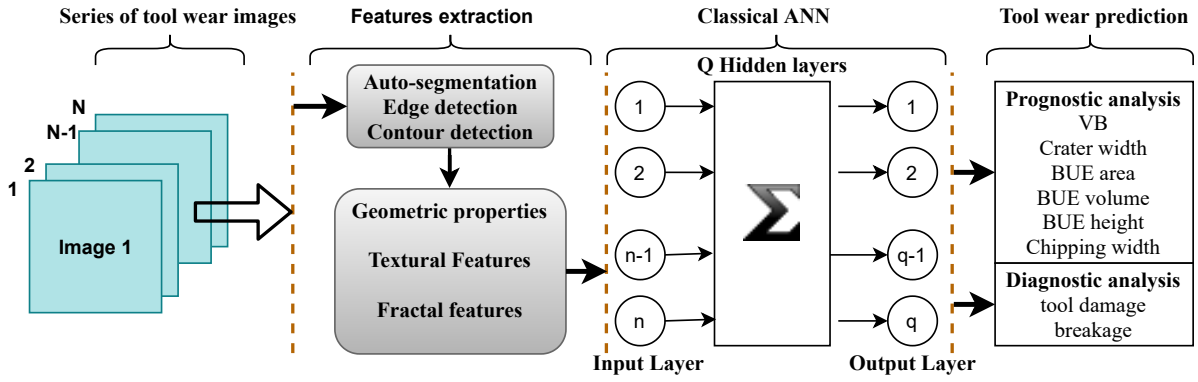

Figure 2.11: *Tool wear prediction using image processing and classical neural networks*

Furthermore, Chethan et al. [264] established a correlation between AE signals and image features, with the aim of evaluating the impact of machining parameters on the progression of flank wear. In their approach, they employed the AE_{RSM}, AE_{COUNT}, wear area, and perimeter as the descriptors of tool wear. The Taguchi methodology was then employed to determine the optimum cutting speed, feed, and depth of cut that minimized the flank wear progression. Some researchers also posited that the MV-TCM affords a more precise prediction of tool wear evolution as compared to conventional methods. For instance, Zhang et al. [242] noted that the detection of wear edge points in a ball-end milling through the extraction of sub-pixels from the cutting edge of the tool was more accurate than the traditional SEM measurement.

In another research, Ponce et al. [38] applied an MV-TCM system to detect the evolution of failure modes via automatic segmentation, thereby predicting the changes in area, thickness, and volume of the BUE, as depicted in Figures 2.12a and 2.12b. Among the all, the BUE thickness decreased with an increase in cutting speed for all values of ADOC (Figure 2.13a). As such, there was no correlation between the progressive wear area or BUE volume with cutting speed and feed rate (Figures 2.13b and 2.13c). Therefore, the best cutting speed was selected based on the BUE thickness, rendering it one of the critical metrics of tool performance during machining. Nonetheless, the issue of MV-TCM not being enhanced to predict the magnitudes of multiple failure modes still persist. As depicted in Table 2.2, the multiple occurrence of failure modes is a crucial indicator of sub-optimal tool performance, and can be utilized to generate informed decisions on the choice of process parameters and tool grades, particularly when milling Inconel 718 [112].

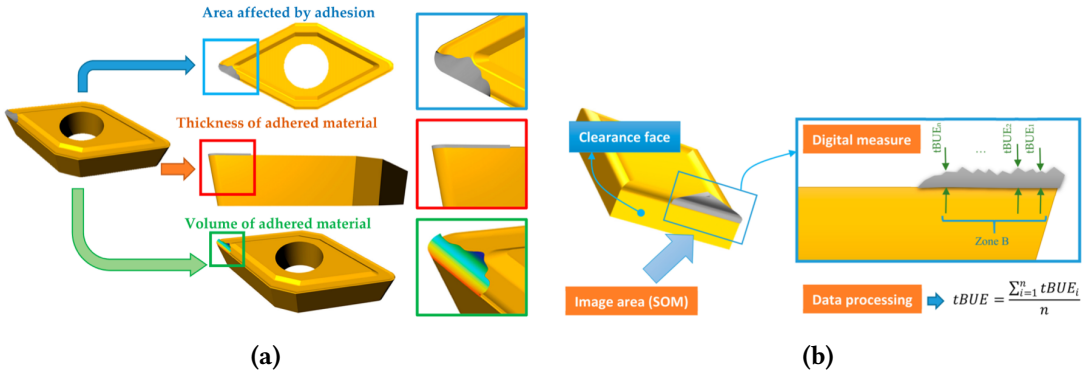

Figure 2.12: *Presentation of adhesion wear: (a) different tool orientation; (b) digital measurement of tBUE* [38]

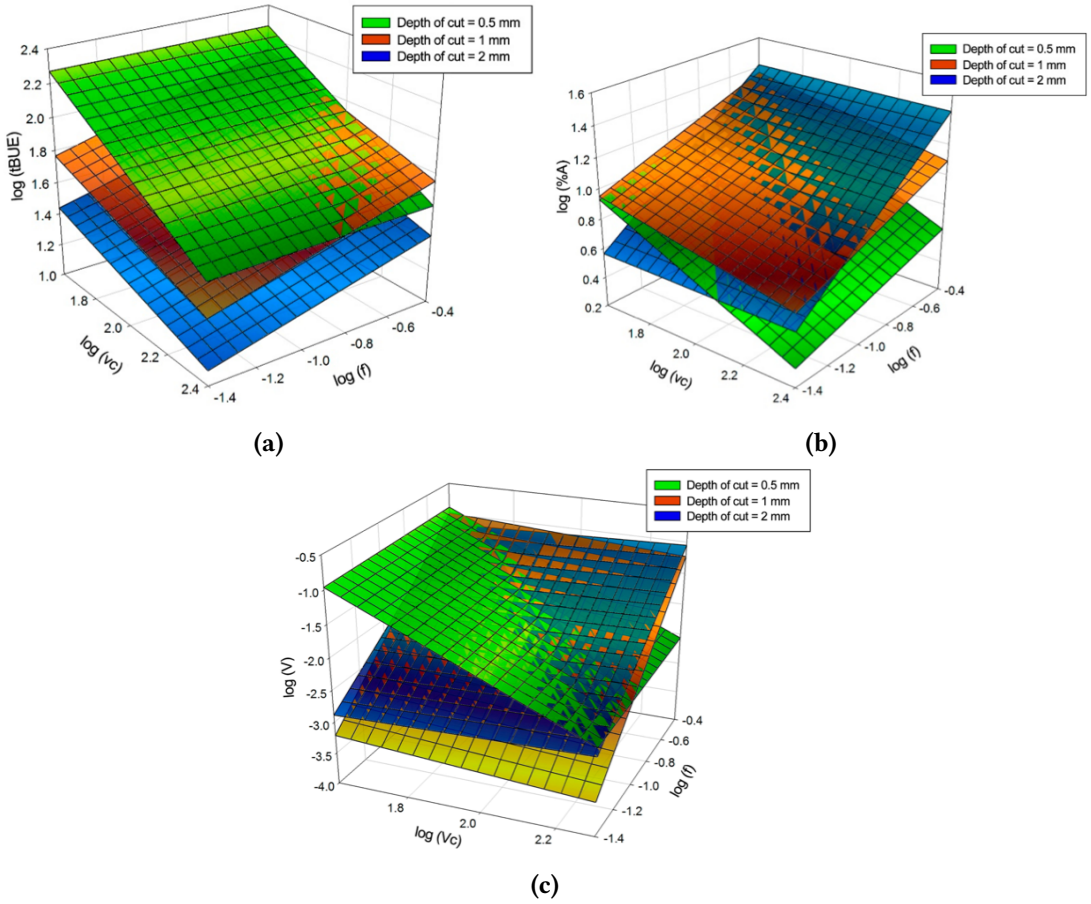

Figure 2.13: *The graphical modelling of abrasion particles prediction: (a) tBUE; (b) Area; (c) Volume* [38]

Recent challenges faced by MV-TCM and the proposed solution

As demonstrated by Tables 2.3 and 2.4, MV-TCM is still in its fledgling stage, relying on classical image processing techniques to extract geometric and textural features. However, these techniques are unreliable in the presence of multiple failure modes due to multi-modal characteristic and poor spatial resolution of tool wear images [25]. Therefore, there is a need to augment MV-TCM through feature engineering and deep learning techniques. Feature engineering encompasses advanced noise filtering methods, dimensionality reduction, and features selection, which can be leveraged to predict progressive VB. Deep Learning (DL), on the other hand, emphasizes on image super-resolution to extract high-level.

2.3.5 Enhancing MV-TCM with Feature Engineering

The application of classical image processing techniques, such as segmentation and edge detection, is predicated upon the bi-modal characteristic of the images, assuming the presence of

two distinct regions (wear region and background). However, the configuration of online tool wear images is often more complex, particularly during dry cutting superalloys, where heat, chipping, notching, BUE, catastrophic failure, and flaking can disrupt the wear region's pixel distribution and feature patterns. To mitigate this complexity, textural, fractal, and Fourier transform analysis were utilized to provide spatial variation of the pixel distribution, regardless of the multi-modal characteristic of tool wear images. Despite the promise of these techniques, their full utilization in in-process MV-TCM was limited by the high computational cost, which is time-intensive for real-time application.

In response, online MV-TCM can utilize alternative pattern recognition and feature extraction techniques, such as Principal Component Analysis (PCA), Singular Value Decomposition (SVD), and tensor decomposition, to avoid the complexity of textural analysis and automatic segmentation on multi-modal tool wear images. PCA, for example, is a feature mining technique that can be used for dimensionality reduction and was utilized for pattern recognition in face detection and image compression [157, 265], with the advantage of low sensitivity to noise, low capacity, and low memory usage during online deployment [266]. Additionally, PCA utilizes an unsupervised learning technique [267, 268], which can eliminate human involvement in the selection of reliable feature attributes, making it an ideal candidate for MV-TCM. SVD, on the other hand, considers an image as a 2-D matrix and factorizes the matrix into a left singular matrix, a right singular matrix, and singular values [269]. It isolates the noise component orthogonal to the data signal subspace by reconstructing the dominant features of an image [270, 271], enhancing the resolution of tool wear images and enabling the extraction of reliable feature attributes for tool wear prediction during MV-TCM, as illustrated in Figure 2.14 (a).

Furthermore, a series of tool wear images during in-process MV-TCM forms a 3-D tensor, representing time-series image data of tool wear progression [242]. In such cases, tensor decomposition, in the form of Higher-Order SVD (HOSVD), can be used to accelerate the features extraction process on time-series image datasets during MV-TCM. HOSVD applies the same principles of SVD, but this time, the singular values are presented as a 3-D core tensor, as shown in Figure 2.14 (b), and can be utilized to denoise and watermark tool wear images, filtering noise to enhance the resolution of the wear region. In conclusion, PCA, SVD, and

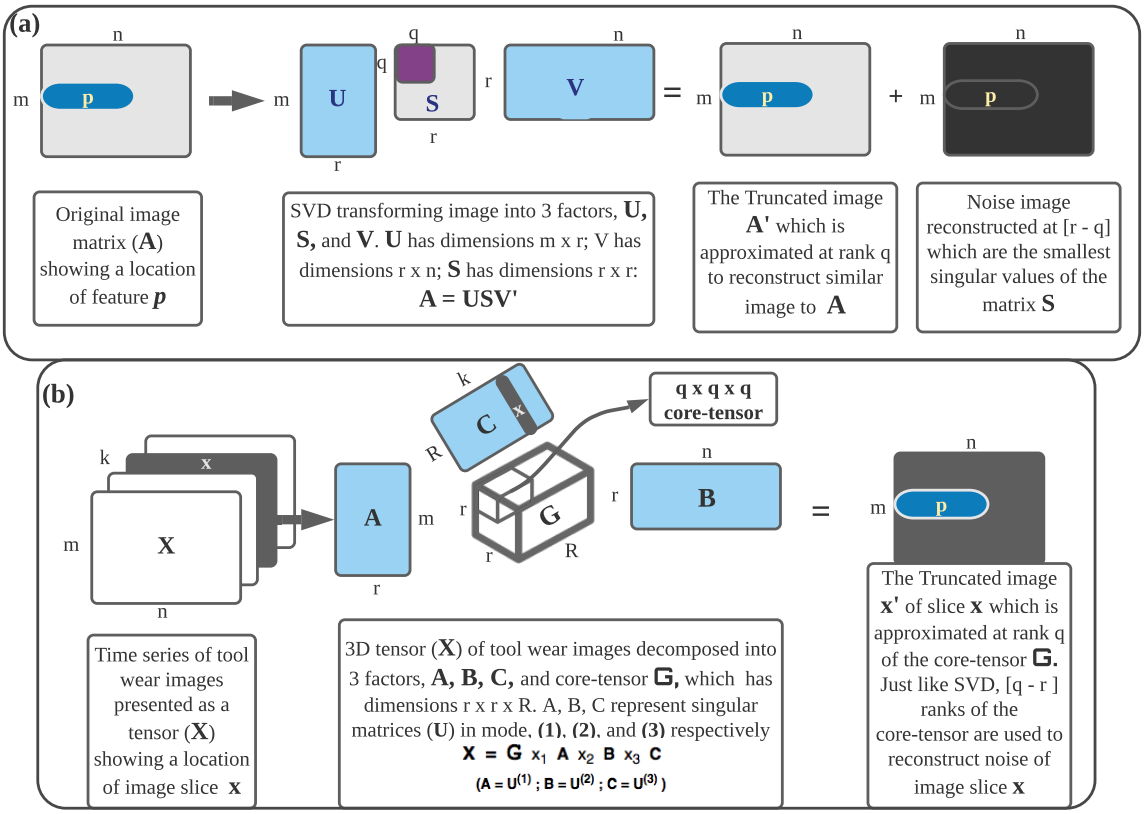

Figure 2.14: *Image decomposition using (a) SVD and (b) HOSVD (Tucker) to extract feature patterns during MV-TCM analysis*

tensor decomposition can be utilized to extract statistical features from tool wear images to train machine learning models for more accurate flank wear prediction with limited datasets during MV-TCM.

2.3.6 Enhancing MV-TCM with Deep Learning

The advent of Deep Learning (DL) provides a solution for handling big data in various applications, including computer vision [272]. Due to its robust architecture, it was widely utilized for facial recognition, object detection, and image super-resolution enhancement. The architecture of DL enables the use of built-in convolution layers for feature extraction from input images [272], thus reducing the complexity of selecting prevalent features for MV-TCM application. Serin et al. [29] posited the utilization of big data obtained from sensors in the implementation of Deep Learning (DL) architectures, encompassing CNN, Deep Multi-Layer Neural Networks (DMLNNs), and Recurrent Neural Networks (RNNs), for TCM application.

Nonetheless, the present corpus of research concentrates on the utilization of DL in MV-TCM, a facet that has not been thoroughly reviewed since the evolution of new DL architectures for computer vision application. The various DL techniques that have been applied to computer vision applications are summarized in Table 2.5.

Among the DL architectures, the CNN is highly effective in carrying out computer vision tasks, particularly in the areas of object detection and classification [293]. However, their robustness is contingent upon having large data, which can pose a challenge in the context of in-process MV-TCM, where the availability of tool wear datasets is limited. To address this, researchers have devised a way to leverage the strengths of CNNs by implementing transfer learning, which involves utilizing pre-trained CNNs to extract high-level features for training smaller ML models, such as regression models, classical ANN, and SVM. A study that is pertinent to this context employed convolution auto-encoders to extract high-level features from tool wear dataset for the purpose of classifying types of wear observed on PVD and CVD-coated carbide inserts during CNC milling of Inconel 718 [46]. Although this model demonstrated an average precision of 96.2% for classifying different types of tool wear, such as flank wear, rake face wear, tool breakage, and adhesion wear, its performance was lower than that of VggNet-16, which was deemed efficient for MV-TCM applications. However, the model was not equipped to detect multiple failure modes on the same flank wear region.

when machining Inconel 718, research has indicated that the flank wear region is a dominant determinant of tool failure [294]. In this scenario, it is imperative to localize multiple failure modes on the flank wear region before applying DNN, and certain obstacles must be addressed in the process. The foremost challenge is acquiring a sufficient quantity of flank wear images with a diverse array of failure modes on the flank wear region. Adequacy is contingent on two factors: (1) the diversity of failure modes to ensure the quality of the dataset and (2) the size of the dataset. The former can be resolved through appropriate selection of cutting tools. Selecting tools with exceptional properties, such as high hardness, toughness, thermal stability, and chemical stability, may not necessarily be the optimal strategy as the dataset could be unduly biased towards a single type of failure mode, such as uniform flank wear. Thus, the ability to encounter different wear mechanisms under the combined effect of various processing conditions is the ideal criterion for selecting cutting tools. The complexity

Table 2.5: Summary of DNNs applied in computer vision and proposed applications in MV-TCM

Computer vision task	DNN technique	Proposed In-process TPO application
Resolution enhancement	GAN [273], LapSRN [274]	Improve online wear images resolution
SDS	FCN [275], DeepLab-LargeFOV [276], R-CNN [277]	Detect failure modes, segment wear
Image classification	DCNN [278–280]	Classification of dominant wear
Object localisation and detection	R-CNN [47, 281–285]	Detection, classification of failure modes
Image reconstruction	PatchMatch [286], RNN [287], CNN [287, 288], PCL [289]	Filtering smeared tool wear images
Image synthesis	GAN [290], PixelCNN encoders [287]	Generating dataset of images
Knowledge extraction	GNN [291], R-CNN/GNN [292]	Inductive reasoning in MV-TCM

-

PCL- Partial Convolutional layer; LapSRN- Laplacian Pyramid Super-Resolution Network; SDS-Simultaneous Detection and Segmentation;

-

DCNN variants- DRL, DenseNet121, AlexNet, InceptionV3, VGG16, VGG19, Xception, ResNet50, and InceptionResNetV2;
R-CNN variants- Fast R-CNN, Faster R-CNN, SSD, YOLOv3, YOLOv4, YOLOv5;
FCN variants- Adapted AlexNet, LeNet, VGG16, GoogleNet;
GAN variants- Deep Convolutional Generative Adversarial Networks (DCGANs), Unpaired Image-to-Image Translation GAN;
GNN variants- Graphical Concolution Network (GCN), Gated Graphical Convolutional Neural Network (GGCNN)

-

Resolution enhancement- Image restoration to enhance high quality resolution; SDS- Identifying each object in ROI, segment each bounding box, interpolate the segmented ROIs to produce one single segment, and detect the object with B-boxes; Image classification- Binary: Assigning a label to an image as an object or not, Multi-class: Assigning different class labels to images as objects; Object localisation and detection, Label each object using a B-box, Detect each object using B-box, Classify each object by a B-Box; Image reconstruction Image filtering and inpainting, filling corrupt parts of an image; Image synthesis Changing style of objects in images, adding new objects in an image, generating new images similar to existing one; Knowledge extraction Creating knowledge graphs from objects relations in an image.

of failure modes within the training dataset can enhance the robustness of DNN models.

On the other hand, the creation of large datasets for MV-TCM poses a significant challenge. To generate such a diverse dataset, various cutting conditions must be implemented during the experiment. This approach entails a significant losses in terms of material cost and duration of the experiment. To mitigate this challenge, the application of Generative Adversarial Networks (GANs) presents a viable alternative. GAN leverages the power of unsupervised learning to analyze the failure patterns in a dataset, enabling the creation of additional images with similar features [290]. It is composed of two key components: the generator and the discriminator. The generator is responsible for producing the images, while the discriminator classifies these images as either genuine or fake by comparing them to the original dataset [44], as shown in Figure 2.15. As the generator continues to optimize its performance to minimize the dissimilarities between the generated and real images, the discriminator improves its capacity to distinguish them. This persistent adversarial game can propel the GAN to learn and generate high-resolution images of tool wear data. In this manner, GANs can present a feasible solution for expanding small datasets in MV-TCM, thereby streamlining the time for experiments while conserving resources.

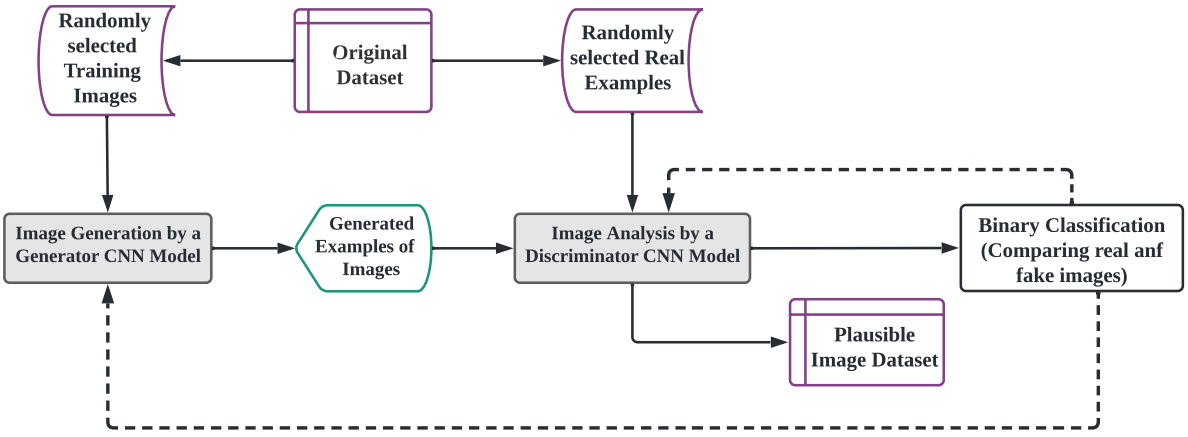

Figure 2.15: *The architecture of GAN which can generate image examples*

The principal challenge encountered by the online MV-TCM pertains to the detection of failure modes in the same flank wear region, which encompasses three critical aspects, namely localization, classification [295], and human evaluation capability [296]. Thus, the overarching objective of tool wear detection is to locate the failure mode within an image (localization), categorize it based on its predominant features (classification), and accurately label its class

(human evaluation capability). However, this pursuit is beset by several complications, including variations in wear depth, poor resolution of tool wear images, and changes in failure patterns during CNC milling of Inconel 718.

In this case, Regional-based Convolution Neural Network (R-CNN) exhibits a remarkable aptitude for learning complex features from Regions of Interest (ROI), as demonstrated in [272], making it a credible solution for MV-TCM failure modes detection. By delineating a bounding box around each failure mode, R-CNN can extract and evaluate the scores of each feature map [295]. Subsequently, a non-maximum suppression can be utilized to eliminate the class labels with low scoring metrics below predetermined threshold values [297]. More details of R-CNN techniques are presented in section 2.3.7. Meanwhile, some of the popularly known R-CNN architectures include fast R-CNN [47], faster R-CNN [292], and You Only Look Once (YOLO) [298]. It is crucial to note, however, that the reliability of R-CNN is contingent on the size of the training dataset, hence its ability to extrapolate failure modes beyond the features scope in the training data may be limited.

To address this deficiency, an alternative architecture known as Reinforcement Learning (RL) can be employed to detect failure modes during machining. Deep Reinforcement Learning (DRL) leverages CNN structures to generate feature maps, which are utilized to train an RL [299]. This combines the DL perception and the sophisticated automation of RL to create an AI system that mimics human ability to learn, predict, and make decisions in a complex machining environment [300]. DRL was utilized to determine the precise location of objects in an image [301], which can be applied to detect the exact location of failure modes on the flank wear region. It can also enhance object segmentation by directing an agent to follow the contour edge around the wear region [302]. While the task of detecting failure modes in MV-TCM may pose significant challenges, the capabilities of DRL can be harnessed to automate wear region segmentation and provide real-time detection of failure modes even with varying processing conditions.

The final challenge pertains to the inductive reasoning aspect, which deciphers the interrelationships between synergistic failure modes and wear mechanisms. As previously outlined in Table 2.2, the predominant failure modes can be used to determine the wear mechanisms during machining. In this context, MV-TCM can make use of the inductive reasoning capabil-

ities of ML to streamline decision-making for non-expert machinists during in-process wear characterization phase. The current state-of-the-art architecture for inductive reasoning is the Graphical Neural Network (GNN). It can exploit the existing relationships between failure modes to predict concealed information, such as tool wear mechanisms or other causes of rapid tool failure [303].

Recently, a Graphical Convolution Network (GCN) was employed to build a knowledge graph of a framework position and speed-dependent dynamics of tool-tips based on vibration signals [291]. A multilayer perceptron (MLP) was utilized to learn the adjacent matrix of the knowledge graph. By leveraging features and graph networks, a semi-supervised GCN was trained to propagate crucial features from labeled to unlabeled samples, thus enabling the prediction of tool-tip dynamics. Although this research was not specifically focused on MV-TCM, it exemplified the applicability of the GNN model for real-time tool wear detection during machining. Similarly, failure modes can also be presented in a graph network as nodes connected by their respective attributes, such as location, neighboring edges, boundaries, and colour, as shown in Figure 2.16. Such an idea can be enhanced by precisely defining the super-subordinate, positive, and negative relations that transmit significant information between related nodes [304]. Other ML techniques like Faster R-CNN can then be used to extract and propagate different features between the nodes [292], which can then be aggregated by the Point-GNN to create a knowledge graph for MV-TCM application.

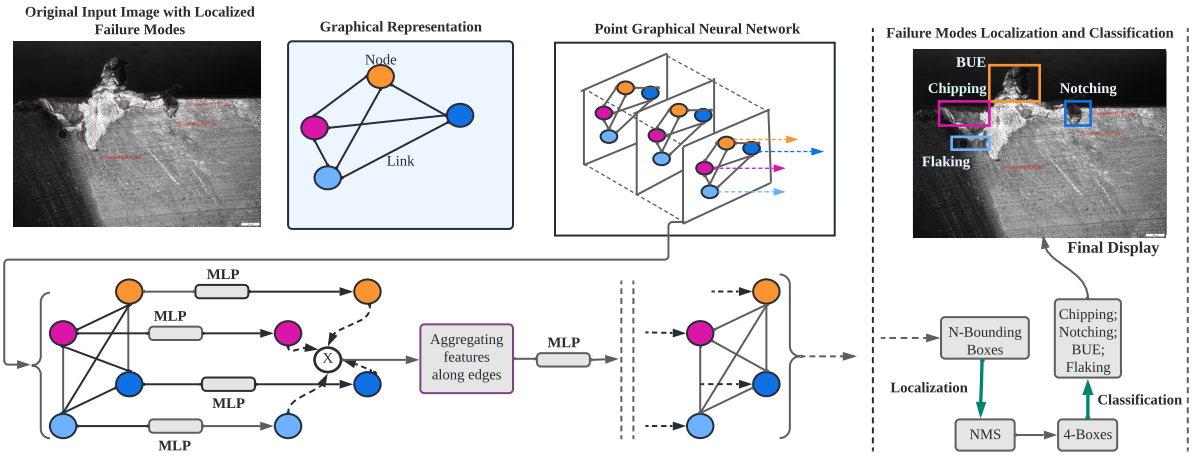

Figure 2.16: *An example of a trained GNN model that can predict failure modes*

However, it was observed that developing the semantic relationships of diverse failure modes requires the utilization of different workpiece materials and cutting tools. For instance,

coating grades of most cutting inserts, such as PVD, CVD and ceramics, possess diverse configurations and color, which are also salient features extracted in the first layers of CNN architectures [305]. On the other hand, the metallurgical attributes of the workpiece material can impact the type of failure modes during machining. For example, when processing ductile metals, including Aluminium and low-alloy steel, most tools predominantly exhibit Built-Up Edge and uniform flank wear [37, 259], whose features can easily be discerned at the tool's flank face. Nevertheless, identifying features that differentiate failure modes during processing of high-performance alloys is onerous [224].

When machining superalloys such as Inconel 718, tools are prone to complex failure modes, including progressive chipping, flaking, notching, coating delamination, and others [223]. These features are difficult to identify on the tool's cutting edge and necessitate the expertise with extensive knowledge in tool wear characterization. However, if the training dataset contains ample examples of features associated with each failure mode, the model can be trained to predict multiple failure modes on the same flank wear region. Therefore, by incorporating well trained R-CNN variants in MV-TCM, the system is adept at detecting the magnitudes of failure modes that attribute to rapid flank wear rate during face milling of Inconel 718.

2.3.7 Enhancing MV-TCM with Real-Time Detection Networks

In the meantime, CNN serves as a preeminent paradigm for features extraction, showing a more remarkable precision as compared to its antecedents, such as Gray Level Co-occurrence Matrix, Voronoi Tessellation, and Support Vector Machine (SVM) [306]. Nevertheless, the classical CNN models are deficient in encoding the spatial location of objects within the same region, thereby restricting its application to single-object classification, such as tool breakage, region-based failure modes, and VB levels. As of 2023, there appears to be no instance of in-process detection of magnitudes of multiple failure modes on the same flank wear region to reveal the extent of wear severity during face milling of Inconel 718. To achieve this, the R-CNN variants can be implemented for MV-TCM application. Figure 2.17 exemplifies how R-CNN can be employed for the real-time detection of failure modes.

Regional-based Convolution Neural Network (R-CNN) demarcates regions within an im-

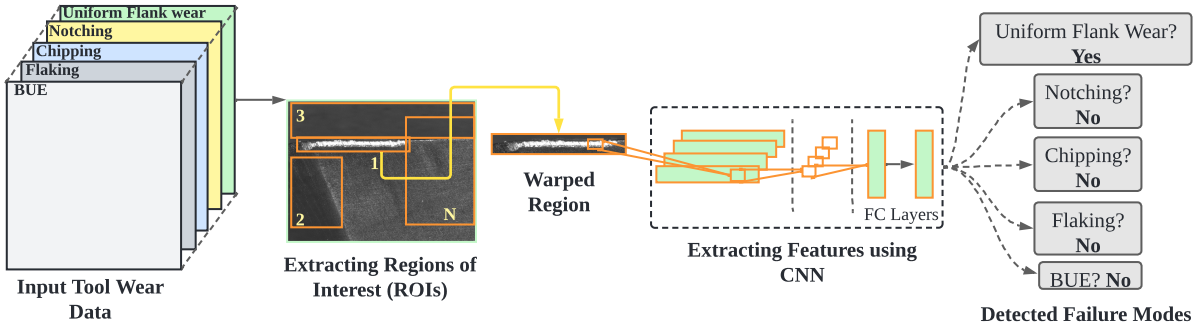

Figure 2.17: *An illustration of Failure modes detection using R-CNN architecture during CNC milling of Inconel 718*

age based on predefined kernels and then utilize convolution layers to extract high-level features from each sub-region. These features are then leveraged to detect objects present within the regions. However, generating and convolving feature maps within sub-regions of the entire image requires a substantial amount of computational power and processing time, rendering classical R-CNNs unsuitable for MV-TCM applications. To address this issue, Fast and Faster R-CNN models were developed, whose network architectures were reconfigured to compress the image prior to generating sub-regions, thus reducing the overall processing time [47]. For instance, Fast R-CNN was utilized in the real-time detection of pedestrians with a processing time of 3s [307]. On the other hand, Faster R-CNN was employed in the detection of apples in dense-foliage fruiting wall trees, achieving an accuracy of 87% with a processing time of 0.182s [308]. Although Fast and Faster R-CNNs improved processing speed, computational complexity still posed a challenge. To address this, a Single-Shot Detector (SSD) was developed, which employs grid cells instead of sub-regions, thereby simplifying the network architecture and reducing computational power during real-time detection [309]. However, this approach is limited in detecting large objects with anchor box-scales greater than [0.1, 0.2, 0.5, 1.0] or image size of at least 300×300 pixels, which is a potential limitation for small scale objects, such as failure modes detection during MV-TCM.

The challenge of detecting small objects was addressed by introducing a novel R-CNN variant called You Only Look Once (YOLO). Despite having a network architecture comparable to Faster R-CNN, it can traverse an image without dividing it into sub-regions, at the same time assigning coordinates to bounding boxes to localize and classify them into distinct categories [282]. This capability results in a substantial decrease in computational power and processing

time, rendering YOLO more dependable than other R-CNNs and reducing the likelihood of system failures and downtime during MV-TCM applications.

The YOLO network has undergone several upgrades to overcome the limitations encountered by its predecessors. YOLOv1, which utilizes DarkNet as its feature extraction network, is suitable for detecting large objects and thus may not be appropriate for identifying failure modes with microscopic features on the cutting edge of a tool [310]. YOLOv2, on the other hand, incorporates Batch Normalization to enhance network stability and employed anchor boxes for localization and classification of small objects [311]. However, it has a limitation of predicting only a single object in an image, rendering it unreliable for multiple failure modes on the same flank wear region. The last official network, YOLOv3 represents a marked improvement over its predecessors and eliminates almost all known limitations during real-time object detection. Additionally, it assigns each object within a bounding box a score to predict a particular location, enabling it to learn and predict multiple features at a faster rate [49, 311]. This was proven by comparing various R-CNNs during fire detection, where YOLOv3 achieved the highest accuracy of 83.7% with the fastest detection rate as compared to Faster R-CNN, R-FCN, and SSD [48].

After YOLOv3, other variants have been devised recently, including YOLOv4 and YOLOv5, just to mention a few. YOLOv4 constitutes a sophisticated architecture compared to its predecessor, YOLOv3. The network incorporates a novel ”reward” system for its learning algorithm by integrating the concepts of Bag of Freebies (BoF) and Bag of Specials (BoS) into its architecture. BoF and BoS represent performance metrics that bolster the network's ability to learn more efficiently and make autonomous decisions [312, 313]. However, BoS also poses a potential threat to the network's stability as it might lead to the mislabeling of features, resulting in an abrupt drop in learning performance, thus compromising the system's reliability to identify features that distinguish different failure modes during MV-TCM. To enhance the learning process, YOLOv5 replaces the DarkNet feature extraction network with Pytorch, incorporating mosaic data augmentation and auto-learning bounding box anchors to improve the detection accuracy [314]. Nonetheless, the YOLOv5 and other renown networks are still under development and can show instability under unoptimized hyper-parameters conditions.

Summary of MV-TCM Enhancement with Deep Learning

Despite YOLOv3 not being employed during MV-TCM, it demonstrates exceptional predictive efficiency, which can be leveraged to identify multiple failure modes with high mean Average Precision (mAP) and low computational cost. As opposed to previous systems, the YOLOv3 has the potential to enhance the extraction of multiple failure modes on different VB stages, thus enhancing diverse features for predicting and controlling flank wear evolution during machining.

2.4 Research Gaps

Despite the previous sections highlighting several shortcomings, the knowledge gaps can be summarized into two principle aspects: (1) The machinability of Inconel 718, and (2) the application of machine learning and artificial intelligence in MV-TCM. In the former case, previous studies have demonstrated inadequate empirical correlation between the process parameters and real-time evolution of flank wear attributes, such as wear mechanisms, failure modes, and chip morphology, during interrupted CNC milling of Inconel 718 under flood cooling condition. This prohibits the development of credible dataset that could accurately represent the underlying physical, thermal, mechanical, chemical, and microstructural changes in diverse features that attribute to the rapid flank wear rate. As a result, most custom datasets developed by such incoherent features cannot combat the current ubiquitous pitfall of ”garbage in, garbage out,” encountered by the predictive models during MV-TCM. Therefore, a comprehensive dataset has to be developed and established from the empirical observations made during the physical experiment via the utilization of conventional methods, machining industrial standards, and data reported by relevant literature. Furthermore, previous conventional, evolutionary, and soft-computing methods focused on one-time selection of process parameters using a quantitative correlation of inputs and outputs when optimising tool performance during machining. Unfortunately, such methods are not informed by real-time evolution of the wear mechanisms and failure modes at different wear stages when selecting optimum processing conditions to enhance the in-process tool wear control, and optimisation.

In the latter case, despite the established nature of MV-TCM, it was observed that in-

tegrating this system with advanced ML techniques is still on a developmental stage. The capability to extract diverse features from imagery signals with smeared noise, which can extrapolate complex VB profile under the limited dataset still remains a topic of discussion in TCM. Furthermore, the successful implementation of deep learning techniques in detecting the real-time evolution of failure modes and wear mechanisms during CNC milling of superalloys is still on its infancy stage. This hinders the real-time adjustment of process parameters to alleviate the synergistic impact of wear mechanisms on tools performance and overall cutting efficiency. While the pattern recognition and deep learning techniques can play a critical role in reducing the dimension and selecting diverse features from imagery signals, there is no proven evidence that these techniques were utilized by MV-TCM for online detection and control of wear mechanisms and failure modes for the PVD-coated carbide inserts during CNC milling of Inconel 718 under flood cooling condition. In particular, the MV-TCM system did not fully utilize techniques, such as Singular Value Decomposition (SVD) and R-CNN variants for the purpose of reducing the dimensions of imagery data and select diverse features that can predict the VB profile under complex flank wear morphology. In addition, the ML-based MV-TCM system was not successfully utilized for in-process tool wear prediction and control due to the absence of an inductive-reasoning algorithm. By utilizing deep learning along with the inductive-reasoning algorithms, the MV-TCM can be enhanced to predict the actual causative mechanisms of rapid flank wear rate and inefficient cutting mechanism in the early cutting stage. Therefore, the successful implementation of ML-based MV-TCM can enhance in-process adjustment of cutting conditions to improve the online performance of PVD-coated carbide inserts during CNC milling of Inconel 718.

Chapter 3

Methodology

The methodology was divided into three main sections corresponding to the main objectives of this research: (1) Experimental investigation (Section 3.1); (2) Developing ML models (Section 3.2); and (3) Developing the ML-based MV-TCM system (Section 3.3). Figure 3.1 shows the general methodology of this research, including principle elements of physical and virtual environments.

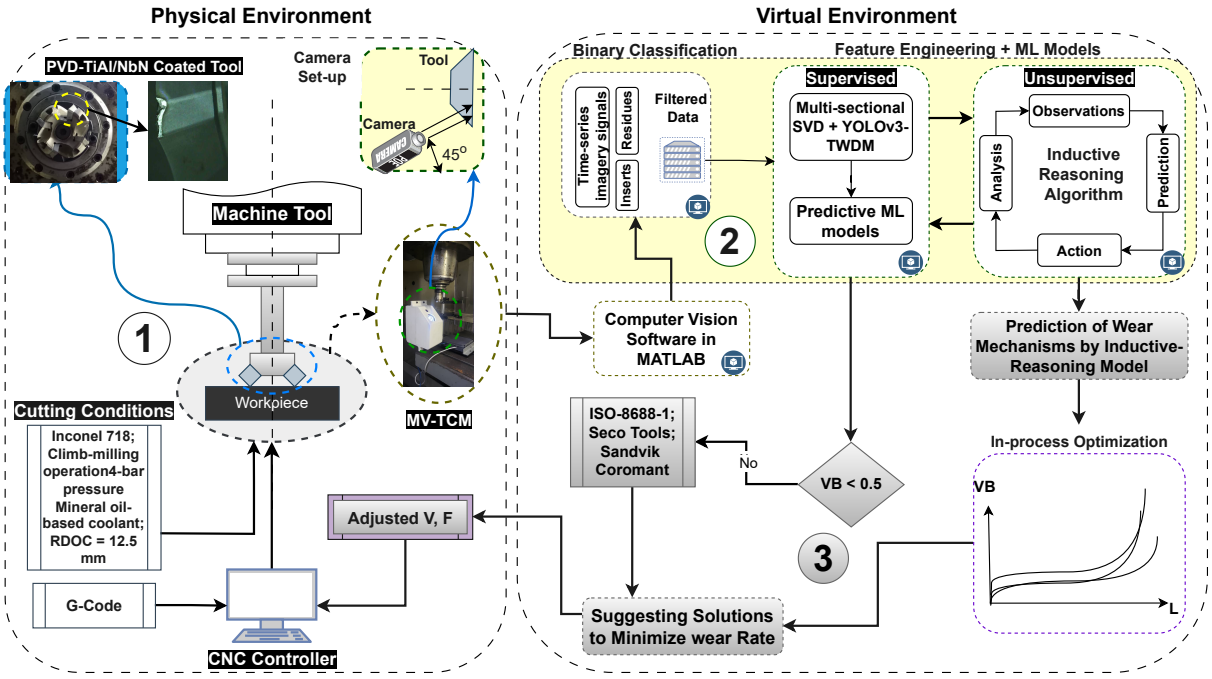

Figure 3.1: *Methodology illustrating the principle elements of the research methodology*

3.1 Experimental Investigation of Tool Wear Evolution

The experiment serves as a fundamental building block of developing feature engineering and ML models. It accentuates the crucial elements, such as the materials, process conditions, and practical methods of characterizing the wear mechanisms, failure modes, progressive VB, and chip morphology. The procedure is summarized in Figure 3.2.

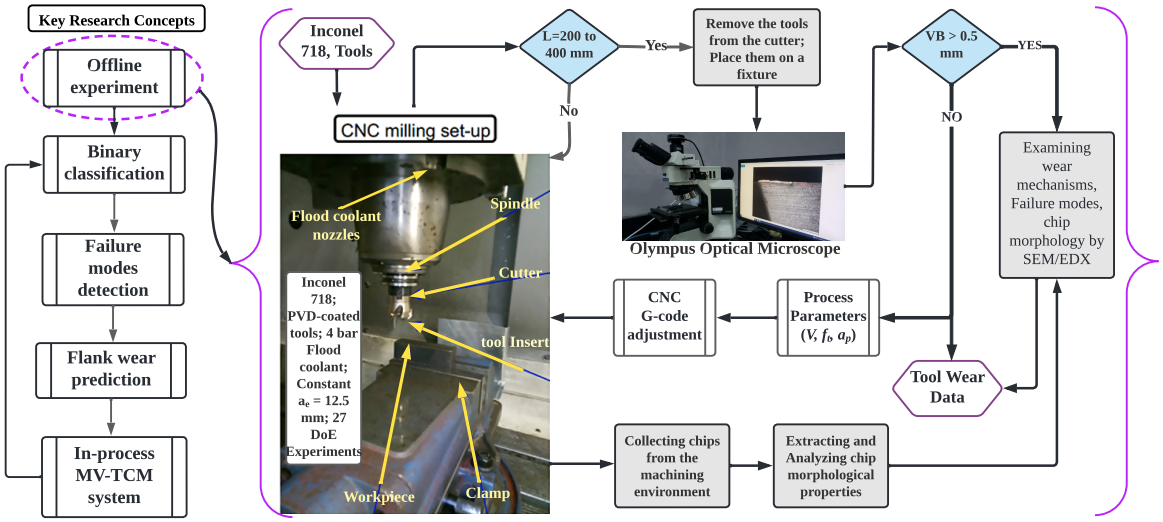

Figure 3.2: *The experimental methodology illustrating the inputs, observed features and output features*

The significant contribution during experiment was a unique synthesis of the correlation between processing inputs, failure modes, wear mechanisms, and progressive VB. Unlike previous studies, the strategic approach to the experiment in this study facilitated the development of a coherent dataset with a range of volatile features that adeptly adapt to changes in processing conditions, thus fulfilling the first question and objective of this study. This not only enhances our understanding of the wear complexity but also sets a new standard for the development of adaptable datasets for training feature engineering and ML models, marking a substantial advancement in MV-TCM.

3.1.1 Justification of Process Conditions

Tool selection was predicated upon two principle determinants: the capability to cut superalloys and to form disparate failure modes under different processing conditions. The goal was to achieve diverse flank wear features to bolster the robustness of the ML models, even with

limited data repository. To attain this, the present study selected multi-layer PVD-TiAlN/NbN coated cemented carbide inserts, which are designed to cut superalloys, as stated in the SECO tools catalogue [212]. Tungsten and carbon are the constituents of the tool's substrate, while TiAlN and NbN are the first and second coating layers, respectively. The stability of the NbN phase renders the tool's outer layer impervious to severe abrasions and chemical wear [61]. Literature has established that this also endows the tools with the ability to withstand thermal degradation at high cutting temperatures [315–317]. Furthermore, the tool has a finite cutting edge, which increases friction in the tool-workpiece interface, leading to thermally-induced wear mechanisms at moderate to high cutting speeds [318]. Given that Inconel 718 exhibits complex metallurgical properties during machining, these tools were capable of displaying disparate wear mechanisms and failure modes, at varying process conditions, thereby creating a more exhaustive data repository for developing the robust ML models. The micro-mechanical properties of tool coatings are shown in Table 3.1. The tool had an approach angle (KAPR) of 45°, the rake angle of 18°, and radial rake angle of 8°. Figure 3.3 and Table 3.2 show the geometry of tool inserts.

Table 3.1: The micro-mechanical properties of PVD-TiAlN-NbN coated carbide inserts

Hardness	T_{OXD} °C	μ_f	Thickness (μm)	Ra (μm)	Composition (EDS)
2800	800	70	2-4	2.105	N(69.6), Nb(28), Ti(1.5), Al(0.82)

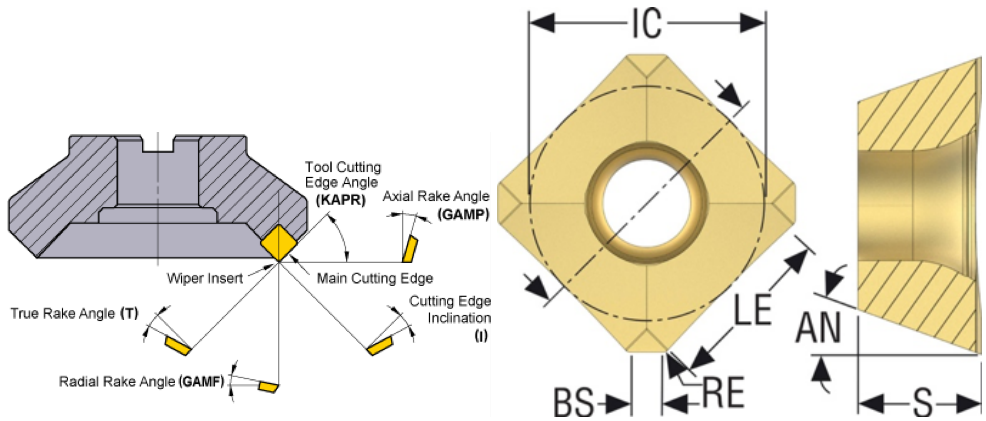

Figure 3.3: *Tool geometry of PVD coated MS2050 inserts: (a) angles and (a) sides of PVD coated inserts* [212]

On the other hand, the selection of process parameters is equally important in this research. According to [101], choosing optimal process parameters for CNC milling of Inconel

Table 3.2: The geometry of TiAlN-NbN coated carbide inserts (MS2050)

AN (mm)	RE (mm)	BS (mm)	IC (mm)	KAPR (°)	LE (mm)	S (mm)
20	0.3	1.5	9.53	45	7.4	3.97

718 is a complex task. Nevertheless, this study deemed cutting speed, feed rate, and ADOC as crucial parameters that influenced the performance of PVD-coated carbide inserts [18]. The determination of process parameters for the designated tools was achieved through the synchronization of the SECO tools catalog and relevant data obtained from literature, pertaining to similar cutting conditions. It was advised that the tool entry angle should surpass $90°$ when measured relative to the negative x-axis of the milling center to preserve a ratio of a_e/D_c less than 0.5 [319], where D_c represents the effective cutter diameter of 32 mm. Even though the calculated ratio was 0.39 at a fixed a_e of 12.5 mm, a perusal of the R220.53 - 0032 - 09 - 4A, S13, and MS2050 sections of the SECO tool catalog revealed that the closest achievable ratio was 30%. This corresponded to a medium cutting speed of 60 m/min, minimum feed of 0.07 mm/tooth, and an ADOC of 1.6 mm. These specifications, however, were not exclusively applicable to Inconel 718, thus the parameters were subject to further validation by used cases in literature.

Despite the subjective nature of the process conditions obtained from other sources, the literature utilized cutting speeds ranging between 40 to 80 m/min during the face milling of Inconel 718 [61, 320–322]. A minimum speed of 40 m/min was also utilized to characterize the micro-mechanical properties of PVD-TiAlN/NbN coated carbide inserts [61]. The maximum feed rate employed in the literature was 0.2 mm/tooth [323], with an ADOC (Axial Depth of Cut) ranging from 0.2 to 0.8 mm [10, 54, 320, 324]. Hence, a maximum ADOC of 1 mm, consistent with a fixed value reported in [321, 322], was chosen in this study. In summary, cutting speeds of 40, 60, and 80 m/min, feeds of 0.7, 0.1, and 0.13 mm/tooth, and ADOC of 0.5, 0.75, and 1 mm fulfilled the minimum requirements of SECO tools, without deviating from the data reported by the literature.

Furthermore, the choice of the cutting fluid helps to optimize tool performance by controlling heat and friction during CNC milling of Inconel 718. In this case, an experiment was conducted to compare the wear mechanisms and failure modes during face milling of Inconel

718 with different cutting fluids. The findings showed that a mineral oil-based cutting fluid was more efficient due to its exceptional lubrication properties, which reduced friction at low to medium cutting speeds as compared to synthetic coolant and dry cutting, and this was consistent with the literature findings in [120, 325]. Moreover, it had a greater ease of refilling and a cost-performance advantage as compared to alternative bio-oils, synthetic fluids, and nano-fluids, rendering it economically sound in the context of flood cooling conditions [326]. Therefore, the study utilized a mineral oil-based cutting fluid to investigate the synergistic effect of the cutting speed, feed per tooth, and ADOC on flank wear evolution during the CNC milling of Inconel 718.

3.1.2 Down-milling Operation for Data Collection

To collect tool wear data, a down milling experiment of a 100 × 50 × 25 mm Inconel 718 block (purchased from Jiangsu DZX Technology Co., Ltd, China) was carried out on a 3-axis 14kW DMC 835V-DECKEL MAHO CNC vertical milling machine using PVD-TiAlN/NbN coated carbide inserts (purchased from SECO tools, Sweden) with a fly-cutter designation of R220.53-0032-09-4A, arbor mounting, which was designed to take 4 inserts at a time. According to the manufacturers, Inconel 718 was made for cryogenic temperatures up to 650°C. Apart from titanium and aluminum, which enhanced the strength, Niobium and molybdenum were added to stiffen the alloy matrix, even without strengthening it by heat-treatment, thus it was specifically made to be used in aerospace and other industries. The properties of Inconel 718 block are shown in Tables 3.3 and 3.4. A full factorial Design of Experiment (DoE) (Table 3.5) was then developed from the levels of process parameters indicated in Table 3.6 using Minitab 19.

Table 3.3: Physical and Mechanical Properties of Inconel 718

Specific Density	Thermal Conductivity	Hardness	σ_y	σ_{UTS}	% Elongation
8.22 (aged)	6.5 w/m.K	36 HRC	725 MPa	1035 MPa	30 (min)

Table 3.4: Chemical composition of Inconel 718

Chemical	C	Cr	Mo	Ti	Ni	Nb	Al	Cu	Si	Fe
Weight(%)	0.08	21	3.3	1.15	55	5.5	0.8	0.3	0.1	12.8

Table 3.5: experimental factors and levels

Levels	V (m/min)	f (mm/tooth)	ADOC (mm)
-1	40	0.07	0.5
0	60	0.1	0.75
1	80	0.13	1

Table 3.6: Full factorial design of experiment for speed, feed, ADOC

Run	Treatment	V (m/min)	f (mm/tooth)	ADOC
1	(-1, -1, -1)	40	0.07	0.5
2	(-1, -1, 0)	40	0.07	0.75
3	(-1, -1, 1)	40	0.07	1
4	(-1, 0, -1)	40	0.1	0.5
5	(-1, 0, 0)	40	0.1	0.75
6	(-1, 0, 1)	40	0.1	1
7	(-1, 1, -1)	40	0.13	0.5
8	(-1, 1, 0)	40	0.13	0.75
9	(-1, 1, 1)	40	0.13	1
10	(0, -1, -1)	60	0.07	0.5
11	(0, -1, 0)	60	0.07	0.75
12	(0, -1, 1)	60	0.07	1
13	(0, 0, -1)	60	0.1	0.5
14	(0, 0, 0)	60	0.1	0.75
15	(0, 0, 1)	60	0.1	1
16	(0, 1, -1)	60	0.13	0.5
17	(0, 1, 0)	60	0.13	0.75
18	(0, 1, 1)	60	0.13	1
19	(1, -1, -1)	80	0.1	0.5
20	(1, -1, 0)	80	0.1	0.75
21	(1, -1, 1)	80	0.1	1
22	(1, 0, -1)	80	0.1	0.5
23	(1, 0, 0)	80	0.1	0.75
24	(1, 0, 1)	80	0.1	1
25	(1, 1, -1)	80	0.13	0.5
26	(1, 1, 0)	80	0.13	0.75
27	(1, 1, 1)	80	0.13	1

This ensured that all parameters were synergistically investigated to create an inherent understanding of wear mechanisms, failure modes, and flank wear evolution during machining. It should also be noted that during CNC milling, the speed in m/min was converted to rev/min using equation (3.1) and the f_t/tooth was also changed to feed/min using equation (3.2). The tool wear data was collected at intervals of 200 or 400 mm cutting length, contingent on the synergistic cutting conditions, until the failure criteria was reached or exceeded.

$$Nrev/min = \frac{V \times 1000}{D_c \times \pi} \tag{3.1}$$

$$f/min = 4 \times f_t \times N \tag{3.2}$$

3.1.3 Flank Wear Measurement

Tool wear was characterized by the progressive VB, failure modes and wear mechanisms. Tool wear images were captured via optical microscopy (using an Olympus U-MSSP4, BX53M, with 1000× magnification), at a magnification of $50\times$, consistence with the minimum standard established by the ISO-8688-1 [12]. To assess the impact of these failure modes, the magnitude of flank wear depth (VB) was measured at every 200 to 400 mm cutting length until a maximum VB of 500 µm was reached or exceeded, as shown in Figure 3.4. The largest VB criteria ensured that the time-series data encapsulated a wide range of wear mechanisms and failure modes, thereby providing diverse features that described sub-optimal tool performance for the purpose of developing ML models. Table 3.7 shows the failure criteria, as established by the ISO 8688-1 standard. Due to different cutting conditions, this study utilized the rest of the criteria except for notching and chipping criteria.

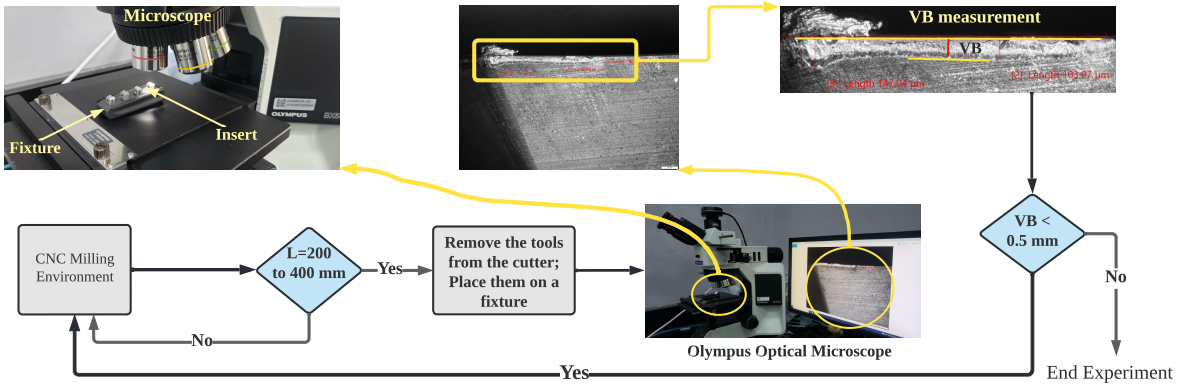

Figure 3.4: *Flank wear measurement through a digital microscope*

To understand the significance of the synergistic impact of process parameters on the progression of flank wear depth (VB) during face milling of Inconel 718, a 2-way Analysis of Variance (ANOVA) was employed for data analysis. This analysis not only helped identify significant process parameters but also suggested the optimal levels of speed, feed, and ADOC

Table 3.7: ISO-8688-1 tool life criteria during face milling of Inconel 718 using ISO 8688-1

Tool deterioration	Description criteria	small	normal	Large
Uniform flank	Regular wear depth	0.2	0.3	0.5
Non-uniform flank	Irregular wear depth	0.9	1.2	1.5
Localised flank	Notch wear depth	0.8	1	1.2
Micro-chipping	Minor Chipping width	L=0.2	L=0.25	L=0.3
Macro-chipping	Chipping width	L=0.25	L=0.4	L=0.5
Catastrophic failure	Sudden mechanical failure	-	-	-
Cracks	Fracture without material loss	-	-	-
Flakes	Loss of tool fragments	-	-	-

that minimized VB rate. In this study, progressive VB served as the dependent variable, while the independent factors were cutting speed (V_c), feed rate (f_t), and ADOC (a_p), each with three levels (-1, 0, 1) as detailed in Table 3.5. The interaction between these factors unveiled the synergistic impact of process parameters on VB progression. The 2-way ANOVA is a statistical approach, which employed a significance level criterion by setting a threshold of p-value less than 0.05 to assess the impact of the factors and their interactions on tool wear evolution. However, it is worth noting that this analysis did not provide the in-depth correlation of the process parameters and various causative mechanisms that attributed to rapid VB rate during face milling of Inconel 718. As a result, further qualitative study was conducted to understand the synergistic effects of process parameters on the wear mechanisms and failures that contribute to the rapid VB rate during face milling of Inconel 718.

3.1.4 Characterizing Wear Mechanisms And Failure Modes

The Olympus optical microscope was also used to observe failure modes, including flank wear, notching, chipping, flaking, Built-Up Edge (BUE), Built-Up Layer (BUL), coating delamination, and galling. This was done together with VB measurement at every 400 mm incremental length. After finishing the experiment, the wear inserts were removed from the cutter and soaked in heated hydro-chloric acid (30% of HCL and 70% of water) [327] and placed in a ultrasonic bath for 15 minutes to remove the Inconel 718 adhesive particles and wear debris. Then they were soaked again in acetone and placed in the ultrasonic bath for 10 minutes to remove the residual acid on the tool's cutting edge. Tool samples were mounted on metal stubs with carbon adhesive tapes before putting them inside the chamber for tool wear inspection.

Field Emission Scanning Electron Microscope (FESEM, FEI Quanta 400 F, USA) was used to observe the wear mechanisms, as shown in Figure 3.5. FESEM uses a vacuum to scan the tool wear surfaces and produce the high-resolution micrographs, which varied from 20 - 300000 $\times$ magnification. The micro-graphs at $20kV$ with magnifications of $500\times$ were used to identify the thermal and mechanical cracks. In addition, the BUL or BUE revealed the adhesion wear of Inconel 718 on the tools. The abrasive marks on both flank and rake face revealed abrasion wear. The cavities on the cutting edge associated with small adhesive particles revealed the attrition wear, whereas the galled BUE revealed asperities deformation.

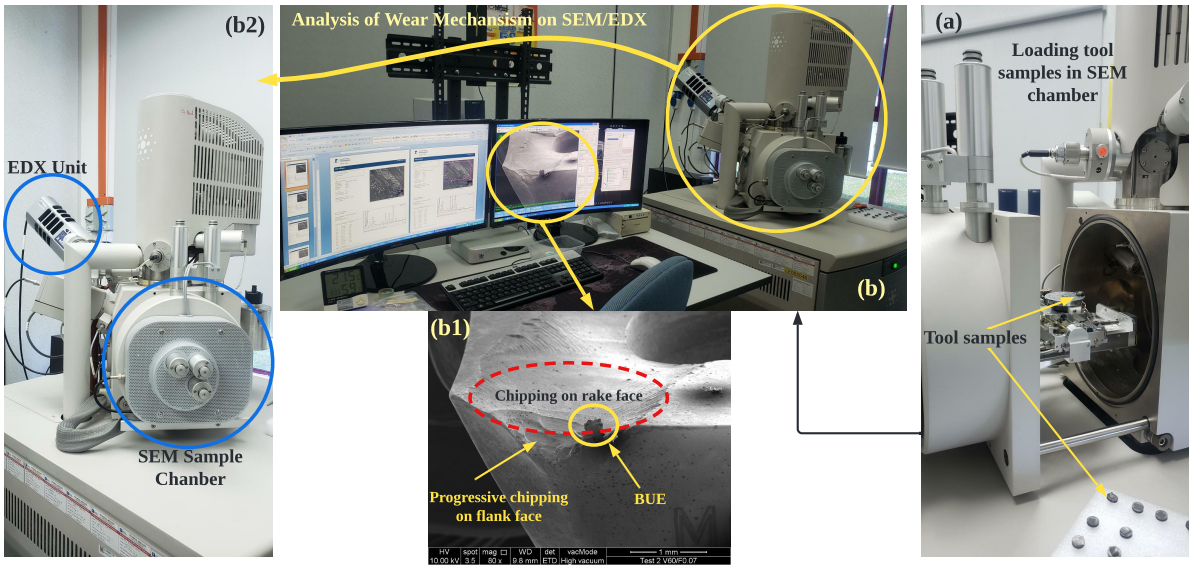

Figure 3.5: *Characterization of the wear mechanisms using FESEM/EDX analysis*

Furthermore, EDS was used to map the atomic percentage to show the external substituents that revealed the diffusion and oxidation wear mechanisms on the chips or the tool's cutting edge. The EDS measured the emitted beam of electrons against energy using a solid-state device called lithium-drifted silicon. The incident ray created a charge pulse proportional to the x-ray energy, where a charge-sensitive amplifier converted it to a voltage pulse. The multi-channel analyzer sorted the voltage pulse whose energy was transmitted to the computer for evaluation. The spectrum of this energy gave the compositions of elements on the tools or chips. The EDS mapping was taken at $500\times$ magnification. If the mapping showed the concentration of Ni, Fe, and Mo particles on the tool's cutting edge, it signified the presence of indirect diffusion wear. Whereas, the direct diffusion was revealed by mapping the substrate constituents (W and Co) on the surface of the chips. Since the SEM/EDS was con-

ducted in vacuum, the presence of oxygen on the tool's cutting edge revealed the chemical wear by oxidation. In summary, tool wear mechanisms, including adhesion and abrasion, were characterized through direct observation in the FESEM micrographs. On the other hand, oxidation and diffusion were identified through EDX analysis. For failure modes, thermal and mechanical cracks were characterized using FESEM, while BUE, notching, flaking, chipping, and uniform flank wear were identified through optical microscopy before ultrasonic bath.

3.1.5 Evaluation of Chip Morphology

Obtaining optimal process conditions still remains a challenge when face milling Inconel 718. While tool wear evolution was a significant indicator of tool performance, the chip geometry can be correlated with the process parameters to evaluate the desirable condition for chip disposal and optimize the heat dissipation capacity of the tools during machining [328]. To achieve this, Inconel 718 chips were collected from the CNC milling environment at the start and end of each experiment. Then, the chips were preprocessed before extracting their morphological profiles. Figure 3.6 shows the methodology that was used to evaluate the chip morphology during face milling of Inconel 718.

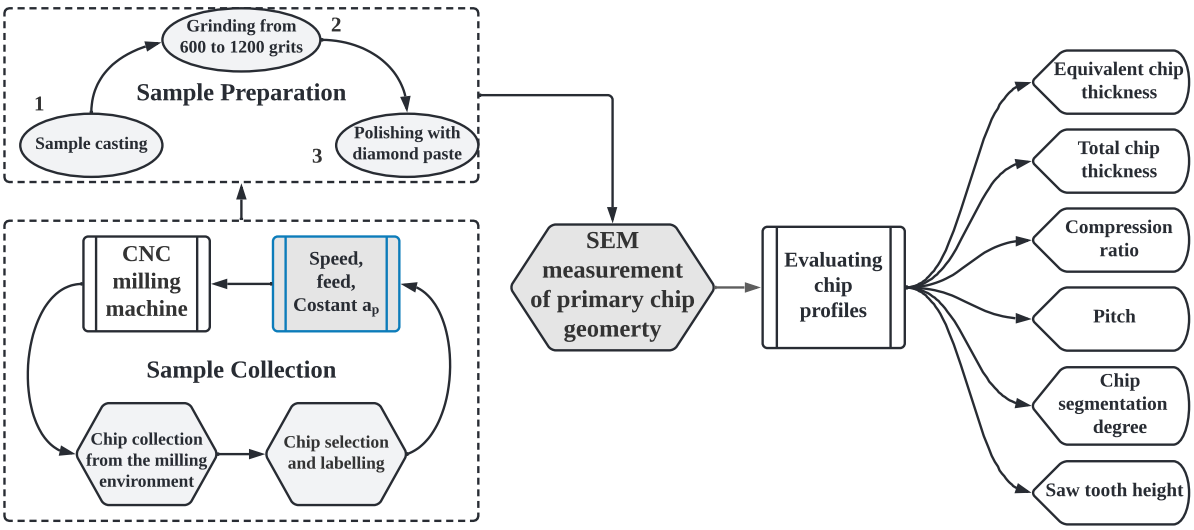

Figure 3.6: *Analyzing chi morphology during face milling of Inconel 718*

The selected samples were first placed upright on a dish, located by double-sided tape, and then cast in an epoxy resin. The epoxy resin was mixed with a hardener using a ratio of 3:1. It was stirred gently to avoid bubbles in the medium before pouring in the mould to cure

for about 48 hours. After that, it was ground and polished sequentially with a 120, 400, 800, and 1200 SiC sandpaper grit before polishing it with a Texpan cloth by a 1.0 μm polycrystalline diamond and 0.5 μm alumina solution to obtain a mirror surface finish. After polishing, the samples were ready for chemical etching using Kroll's reagent to reveal fine chip profile. The finished samples were observed under SEM to extract the micrographs and measure the valley and overall chip thickness.

The first property was the equivalent chip thickness. It was taken from the middle of the undeformed or uncut chip ($h_{eq} = f_z sin(k)$ or h_{cu}), as shown in Figure 3.7. The second property was the chip reduction coefficient (also known as chip compression ratio), which was used to measure the plastic deformation of the chips. It was presented as t_c/t_{cu}, where t_c and t_{cu} are the deformed and undeformed chip thicknesses. The third characteristic was the chip segmentation, which showed that the chip was not homogeneously deformed, but serrated. It was a ratio of valley height to overall chip thickness. The fourth property was the pitch (p), which measured the radial position of the tool. The pitch and the effective cutter diameter (D_c or d) were used to compute the engagement angle during machining, as shown in 3.3. The uncut length (l_0 or l_{cu}), width (b_0 or b_{cu}), and cross-section area (A_0 or A_{cu}) are given by equations 3.4, 3.5, and 3.6, respectively. The notations of chip profile used in this research were adopted from [329], where Φ_0, F_c, F_{cn}, and F_p are the engagement angle, chip load, normal cutting force, and tangential cutting force, respectively.

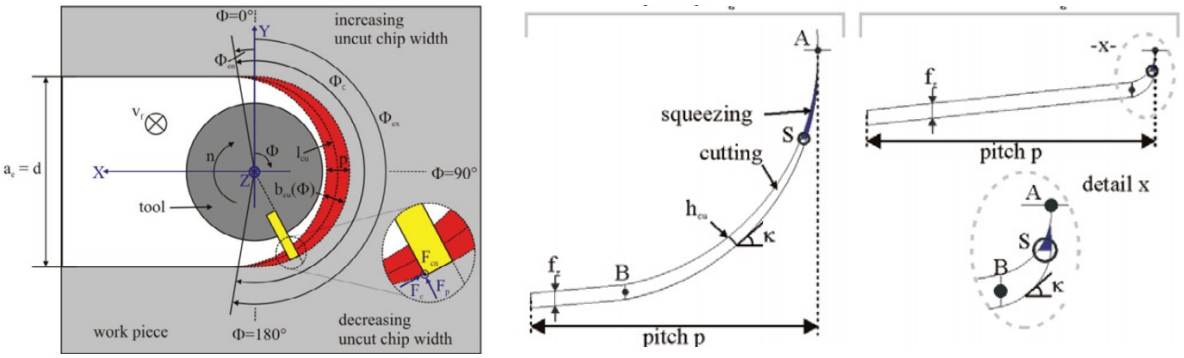

Figure 3.7: *Chip properties during the machining process* [329]

$$\Phi_0 = 180° + 2 \times [-sin^{-1}(p/D_c)] \tag{3.3}$$

$$l_0 = \frac{\pi \times D_c}{360^\circ} \times \phi_0 \tag{3.4}$$

$$b_0(\phi) = \frac{D_c}{2} + p \times sin\phi_0 - \sqrt{\frac{D_c}{2}^2 - (p \times cos\phi_0)^2} \tag{3.5}$$

$$A_0(\Phi) = b_c(\phi_0) \times h_{eq} \tag{3.6}$$

3.1.6 Formulating a Diverse Feature Synthesis Vector (DFSV)

Following tool wear characterization at various processing , the correlations were made to generate the dataset by formulating a Diverse Feature Synthesis Vector (DFSV). The feature vector was used to train the feature engineering and ML models, which were applied for the predictive control of tool wear evolution during MV-TCM. The DFSV had two types of features: primary features, comprising sets of processing parameters, and secondary features derived from the time-series flank wear images. The secondary or observed features include the magnitude of energy layers (F_i) and dominant failure modes (FW - Flank Wear; CW - Chipping Wear; NW - Notch Wear; BUE; and FLW - Flaking Wear), which were extracted from the wear region using feature engineering and ML techniques. Equation 3.7 delineates the significant features of the DFSV derived from the experimental findings to train the ML models.

$$DFSV = [V_c, f_t, a_p, L, F_i, FW, CW, NW, BUE, FLW] \tag{3.7}$$

The DFSV was used to design a systematic approach to predictive control of tool wear evolution during face milling of Inconel 718. As previously stated, most manufacturing industries regulate process conditions to reduce the impact of prevalent wear mechanisms and failure modes in order to improve tool performance during machining [212, 330]. Although the conventional, evolutionary, and soft-computing methods were found effective for most cutting operations, they cannot be applied for in-process tool performance optimization due to their time-intensiveness, data-hungry nature, computational complexity, and operational cost.

In addition, lack of in-process predictive control of failure modes evolution makes it difficult to select proper levels of optimal speed and feed during face milling of Inconel 718. Hence, there was a need to train the ML models using the data established through the experimental findings. The ML models should predict and control the in-process tool wear progression to ensure the overall cutting efficiency during face milling of Inconel 718. In this case, the proposed ML models were further utilized to regulate the speed and feed, designing the promising cutting condition that optimized tool performance at different VB levels (early, uniform, critical, and failure stages) during machining. This was validated with the conventional and soft-computing methods to ensure high efficacy in predicting and controlling tool wear evolution during face milling of Inconel 718.

3.2 Developing ML Models for Tool Wear Prediction

The term ”Machine Learning (ML)” refers data-driven computational methods that leverages algorithms and statistical approach to analyze and interpret complex features within the data generated, aiming at developing predictive models that discern tool's failure states based on various input conditions. In this research, it referred to the soft computing techniques that predict and control tool wear evolution during face milling of Inconel 718. The ML was devised from the stimuli-response of features derived from the empirical observations during physical experiment. In this case, feature extraction techniques played a substantial role in transforming raw data to latent features that described the underlying physical, mechanical, and microstructural behaviour of the flank wear region. Despite limited hyper-parameters, the models' robustness was enhanced by diversifying the features to represent the complex flank wear morphology, thus addressing the second question and objective of this research. Therefore, the main contributions in this section are:

- The introduction of new feature engineering techniques (multi-sectional SVD – enhanced by a newly developed multi-sectioning algorithm; and YOLOv3-TWDM — enhanced by an improved detection model, newly developed data transfer and image processing algorithms);
- The Machine Learning (ML) models (DFSV-ML and SBF–ML: Both enhanced by new

feature vectors [Diverse Feature Synthesis Vector (DFSV) and Spatial Binary Features (SBF)] and image processing algorithms); and

- Induction-reasoning algorithm (a new algorithm developed in this research to improve decision-making during MV-TCM).

Previous studies have shown that the wear region grows with the cutting length, and it can be extracted to represent the progressive change in flank wear depth (VB) [46, 331]. In this case, pattern recognition techniques statistically quantified the magnitudes of energy layers (F_i) as time-varying features of the flank wear region. This was achieved by leveraging the strength of singular values [45] to separate the dominant energy layers from the smeared noise component of the wear region [269, 270]. The present study further enhanced this technique by developing a multi-sectioning algorithm, wherein small sections of the wear region were generated and the section that exhibited the highest luminosity along the cutting edge was selected to represent the entire row. The synergy of these retained sections resulted in a thin and tall column matrix that predicted the highest energy layer of the entire flank wear region.

The presence of low energy layers in the flank wear region revealed the sections affected by the uncontrolled failure modes, including localized chipping, Notching, and flaking, which are critical indicators of sub-optimal cutting mechanism. As such, it was crucial to include these failure modes and their magnitudes as essential features of the flank wear region. To achieve this, it was imperative to locate and identify multiple failure modes in the same flank wear region. In this regard, YOLOv3, a highly efficient R-CNN architecture for real-time object detection [332], was utilized in conjunction with SqueezeNet, a highly compressed CNN variant [333], to detect the evolution of failure modes during machining. By utilizing SqueezeNet as a feature extraction network, the YOLOv3 Tool Wear Detection Model (YOLOv3-TWDM) exhibited low computational time, a high detection rate and mean Average Precision (mAP). Furthermore, all the models were implemented using MATLAB, owing to its superiority in parallel computing, debugging, recompilation, software customization, and the auto-generation of Graphical User Interfaces (GUI).

3.2.1 Multi-sectional SVD

Singular Value Decomposition (SVD) was used to compress images by mapping them into a new sub-space (r) [270, 334]. Research has shown that SVD shares a fundamental similarity with the Fourier Transform, in that both processes entail unitary transforms or a change in basis vectors, and have the capacity to approximate reduced-rank images. However, SVD outperformed the standard Fourier Transform in capturing the basis vectors of an image, making it a valuable tool to capture feature patterns of the flank wear region during MV-TCM. It is based on the hypothesis of linear algebra that a 2-d image matrix can be factorized into three parts: an orthogonal matrix (U), a diagonal matrix (S) containing singular values (SVs), and a transposed orthogonal matrix (V). It utilizes the strength of SVs to restore energy layers and localize the noise component orthogonal to the data signal subspace. Such a characteristic can be used to separate the smeared noise from the prevalent features of tool wear images.

Dimensionality Reduction and Features Extraction

The multi-sectional SVD approach was used to reduce the dimensions of tool wear images and extract the time-varying SV magnitudes to quantify the evolution of the wear region. Unlike the previous features extraction techniques, the multi-sectional SVD in this research extract features from the region of interest (ROI). Apart from the computational complexity, the ROI was found to be more effective in extracting the feature embeddings of the wear region than using the entire image [335]. In this study, the ROI was located slightly above the cutting edge to minimize the impact of the Built-up Edge (BUE) that protrudes above the cutting edge. This assumption was incorporated based on the argument that the average flank wear depth (VB) is measured from the main cutting edge line, which excludes the BUE. To effectively extract the ROI, the flank wear image was divided into 160 slices ($A1B1, A2B1, ...A20B8$), and 40 slices, which encompassed the maximum flank wear depth and width, were selected. It is also worth noting that the number of slices (sections) were selected by try and error. This resulted in a 75% dimensionality reduction. The ROI was defined by 4 rows ($B3 - B6$) and 10 columns ($A3 - A12$). Each slice $AB \in \mathbb{R}^{m \times n}$ was decomposed into three factors: (1) U_{AB}, (2) S_{AB} and (3) V_{AB}, as shown in Figure 3.8, and $S_{AB} \in \mathbb{R}^{r \times r}$ was reserved for further processing.

The matrix $S_{AB} \in \mathbb{R}^{r \times r}$ contained the singular values of the slice AB, which represented

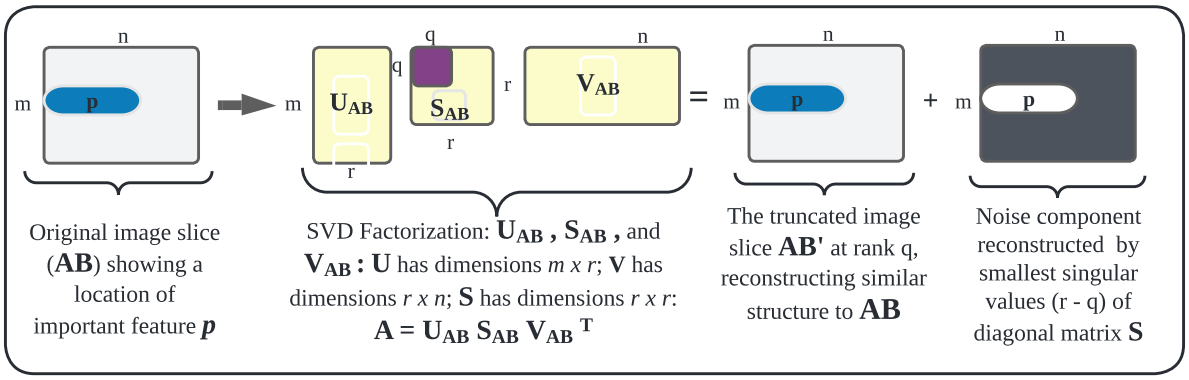

Figure 3.8: *Methodology for multi-sectional SVD*

the unique luminance layer of the flank wear region. The u_{ji} and v_{ij} are the left and right eigenvalues, and S_{AB} contains singular values $[\sigma_{11}, \sigma_{22}, ...\sigma_{rr} = \sqrt{\lambda_{11}}, \sqrt{\lambda_{22}}, ...\sqrt{\lambda_{rr}}]$, arranged in descending order. The singular values represented the strength of different energy layers on the wear region, as explained in [45]. As such, an L2-norm, derived from these singular values, was used to measure the magnitude of features in this research, as well as in other applications [334]. Therefore, the magnitudes ($M(i,j)$) of singular values were calculated using the L2-norm of the S-diagonal vector (S_{AB}) (3.8) to statistically quantify the progressive change in the flank wear region.

$$M(i,j) = \sum_{(r=1)}^{q} \|\mathbf{S_{AiBj}}\|_2 \tag{3.8}$$

For integer values of i ranging from 3 to 12 and j ranging from 3 to 6, the maximum values of $M(i,j)$ were selected from rows ($B3 - B6$) that were parallel to the main cutting edge by discarding sections with lowest SV magnitudes. The cumulative sum of the identified maximum M values generated the final feature, F_i, which represented the sector exhibiting the utmost energy in the entire flank wear domain, thus eliminating the localized noise associated with uncontrolled failure modes. The efficacy of this methodology was established by correlating the incremental change in F_i with the experimentally determined VB values under varying process parameters. Figure 3.9 illustrates the application of multi-sectional SVD for extracting F_i magnitude from grayscale tool wear image obtained using an optical microscope during face milling of Inconel 718.

It was observed that the first $5\,SVs$ harbored high energy layers that retained the gen-

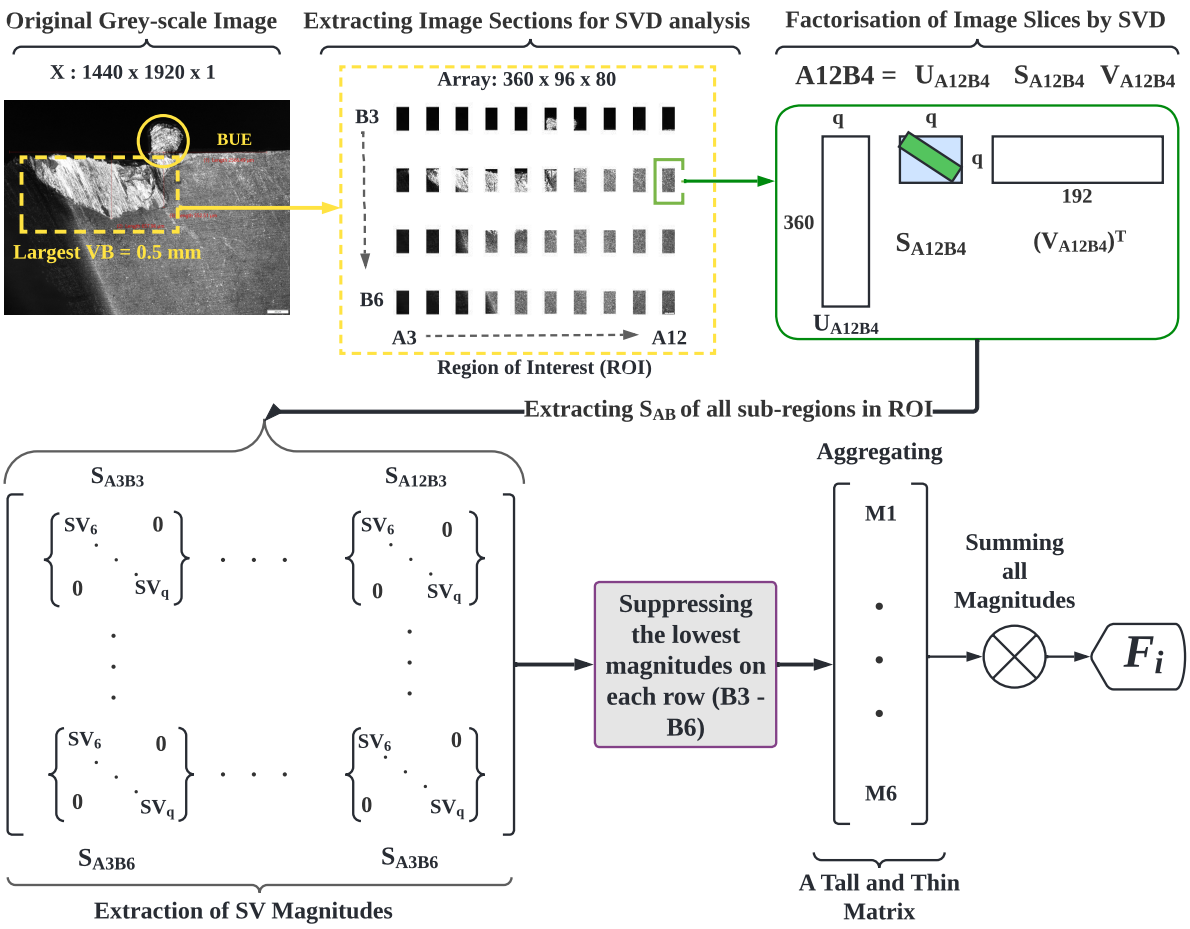

Figure 3.9: *Dimensionality reduction and extraction of SV magnitudes using the multi-sectional SVD*

eral quality of the flank wear region, however, the distinct features that differentiated failure patterns in various sub-regions were not yet discernible. Again, singular values below $r = 60$ were deemed insignificant, as they contained image noise that was inconsequential for the intended purpose. Distinct features began to emerge at rank $q-5$, where $q = 60$ represented the effective rank during truncation. Hence, this study employed the middle SVs ($5 < q < 60$), as they stored significant feature embeddings that could differentiate the time-varying flank wear regions, similar to the approach described in [45]. As a result, 55 SVs were utilized to compute the time-varying magnitudes ($M(i, j)$), while the remaining $[r - 60]\, SVs$ were employed to reconstitute the noise component, with r denoting as the maximum rank during image decomposition. The multi-sectional SVD procedure implemented in this research is summarized by the pseudocode 1.

Evaluating the Performance of Multi-sectional SVD

The performance of the multi-sectional SVD was evaluated using compression ratio (R) (3.9), Peak Signal to Noise Ratio ($PSNR$) (3.11), Mean Square Error (MSE) (3.10), and Structural Similarity Index Measure ($SSIM$) (3.12), as described in [270, 334]. The compression ratio quantified the percentage reduction of the sub-regions during truncation. Upon decomposition, if the rank q was equal to the width of the image (n), then the dimensions of matrix U_{AB} were congruent to those of AB, while if q was equal to the height of the image (m), then the dimensions of matrix V_{AB} were equivalent to those of AB. Hence, the image was only compressed if q was less than m and n, as previously stated ($5 < q < r$).

Algorithm 1 Multi-section SVD

$compressionratio(r) \leftarrow m * n/(r * (m + n + 1))$

function LOOP([ ])

  $X(:,:,1) \leftarrow inputimage$

  $[AB] \leftarrow X(:,:,1:160)$

  $Rank_{max} \leftarrow 5:60$

  $[U_{AB}(:,:,e), S_{AB}(:,:,e), V_{AB}(:,:,e)'] \leftarrow svd(AB(:,:,e))$

  for $e \leftarrow 0$ to $Rank_{max}$ **do**

    $[ca(:,:,e)] \leftarrow deal(U_{AB}(:,1:q,e) * S_{AB}(1:q,1:q,e) * V_{AB}(1:q,:,e)')$

    $RMSE(q,e) \leftarrow \sqrt{(AB(:,:,e) - ca(:,:,e))^2}$

    $[PSNR] \leftarrow psnr(ca(:,:,e), AB(:,:,e))$

    $[SSIMval(q,e), SSIMmap(q,e)] \leftarrow ssim(ca(:,:,e), AB(:,:,e));$

    $[\sigma_{AB}] \leftarrow$ S(q+1,e)

  return $[M(i,j)] \leftarrow norm(\lambda(:,:,e))$

  return $[F_i] \leftarrow \sum M(i,j)$

On the other hand, the $PSNR$ served as a logarithmic gauge of the quality of a reconstructed image following compression, guaranteeing that the predominant features were fully reinstated within the wear region. The $PSNR$ was calculated based on the Mean Square Error (MSE) between the original AB and the reconstructed slice AB'. The R and $PSNR$ described the signal error of the image reconstruction, while the $SSIM$ verified the capability

of the multi-sectional SVD in recreating the structural interdependence of pixel distribution between AB and AB'. The $SSIM$ combined the measures of central tendency and dispersion. It was validated through the use of small windows of 11×11 pixels (window ab for AB and ab' for AB'), with windows exhibiting larger $SSIM$ values approaching 1 indicating higher structural similarity. This was achieved by applying the luminance (l), contrast (c), and structure index (s) as key characteristics of an image.

$$Compressionratio = (1 - \frac{nq + q + mq}{mn}) \times 100\% \tag{3.9}$$

$$RMSE = \sqrt{\sum_{i=1}^{n}\sum_{j=1}^{m}[AB(i,j) - AB'(i,j)]^2} \tag{3.10}$$

$$PSNR(db) = 20\log_{10}\frac{MAX_{AB}}{RMSE} \tag{3.11}$$

$$SSIM_{ab,ab'} = \frac{(2\mu_{ab}\mu_{ab'} + C_1)(2\sigma_{ab,ab'} + C_2)}{(\mu_{ab}^2 + \mu_{ab'}^2 + C_1)(\sigma_{ab}^2 + \sigma_{ab'}^2 + C_2)} \tag{3.12}$$

where: $C_1 = (a_1 L)^2$; $C_2 = (a_2 L)^2$; $a_1 = 0.01$; $a_2 = 0.03$; L=dynamic range; MAX_{AB} is the maximum pixel value of the original image AB; μ_{ab} and $\mu_{ab'}$ are mean values of window ab and window ab' respectively;σ_{ab}, $\sigma_{ab'}$ and $\sigma_{ab,ab'}$ are standard deviations of window x, window g and covariance of x and g respectively.C_1 and C_2 are constants for luminance and contrast.

3.2.2 YOLOv3-Tool Wear Detection Model

The flank wear region experienced multiple failure modes during CNC milling of Inconel 718. Therefore, apart from the process parameters and F_i magnitudes, the multiple failure modes also contributed to the rate of change of the flank wear region during machining. For example, at the highest cutting speed and feed rate, the flank wear region predominantly experienced progressive chipping and flaking, which caused rapid VB progression. Thus, the magnitudes of failure modes were among the key flank wear features during face milling of Inconel 718. To achieve this, the YOLOv3-Tool Wear Detection Model (YOLOv3-TWDM) was proposed to detect the magnitudes of failure modes on the wear region. The YOLOv3-TWDM architecture

comprised two essential sections, as depicted in Figure 3.10: (1) feature extraction through the SqueezeNet architecture, and (2) decision-making through the trained YOLOv3-TWDM. The determination of the feature extraction architecture was of utmost significance. This procedure entailed a compromise between the detection speed and precision. An enhancement in precision was realized by augmenting the number of convolution layers and model parameters, however, this created a complex architecture, which posed a terminal challenge of high computational cost.

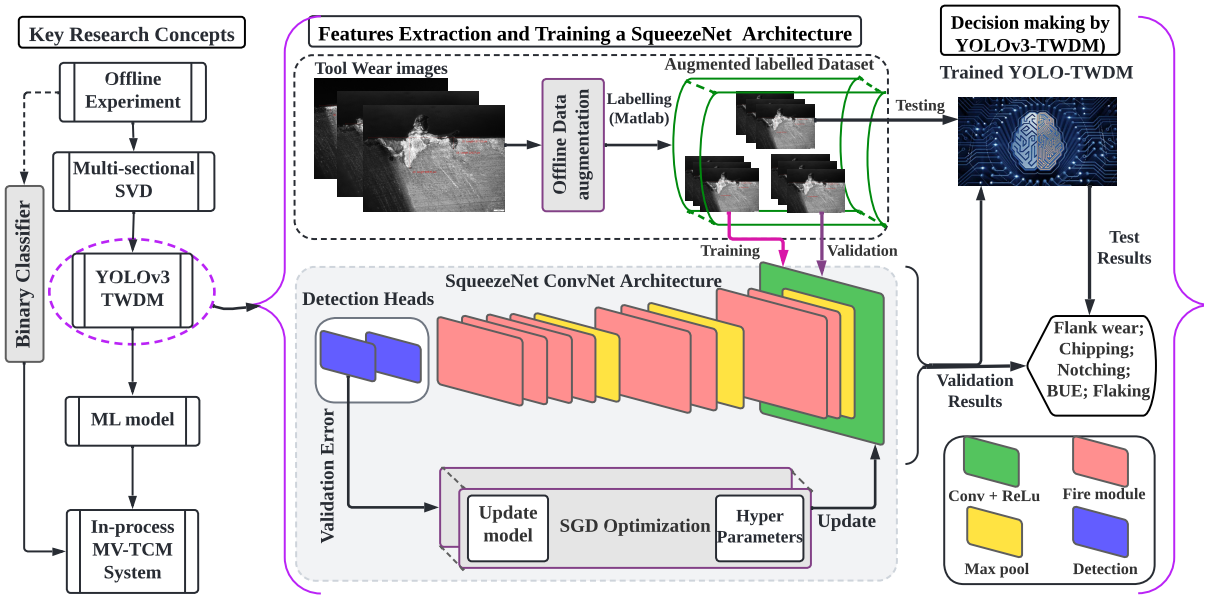

Figure 3.10: *Applying the YOLOv3-TWDM for failure modes detection*

Features Extraction by the YOLOv3-TWDM

Despite these limitations, there was a requirement to attain an equilibrium between speed and precision, to prevent both the excessive processing time and false detections. Inspired by [336], the SqueezeNet architecture was selected in this study to extract high-level features from time-series images. This architecture distinguished itself from other CNN variants by being designed to reduce the model's parameters and size through three main strategies, including the transformation of 3×3 filters into a fire module, thereby compressing the filters from 3×3 to a squeeze s (1×1) and expand (e) structure $[(3 \times 3)$ and $(1 \times 1)]$, as depicted in Figure 3.11.

The input parameters to the subsequent 3×3 filters were reduced. Lastly, late downsampling was employed to increase the activation maps. These three strategies were executed to sustain accuracy whilst utilizing a limited number of input hyper-parameters, which were

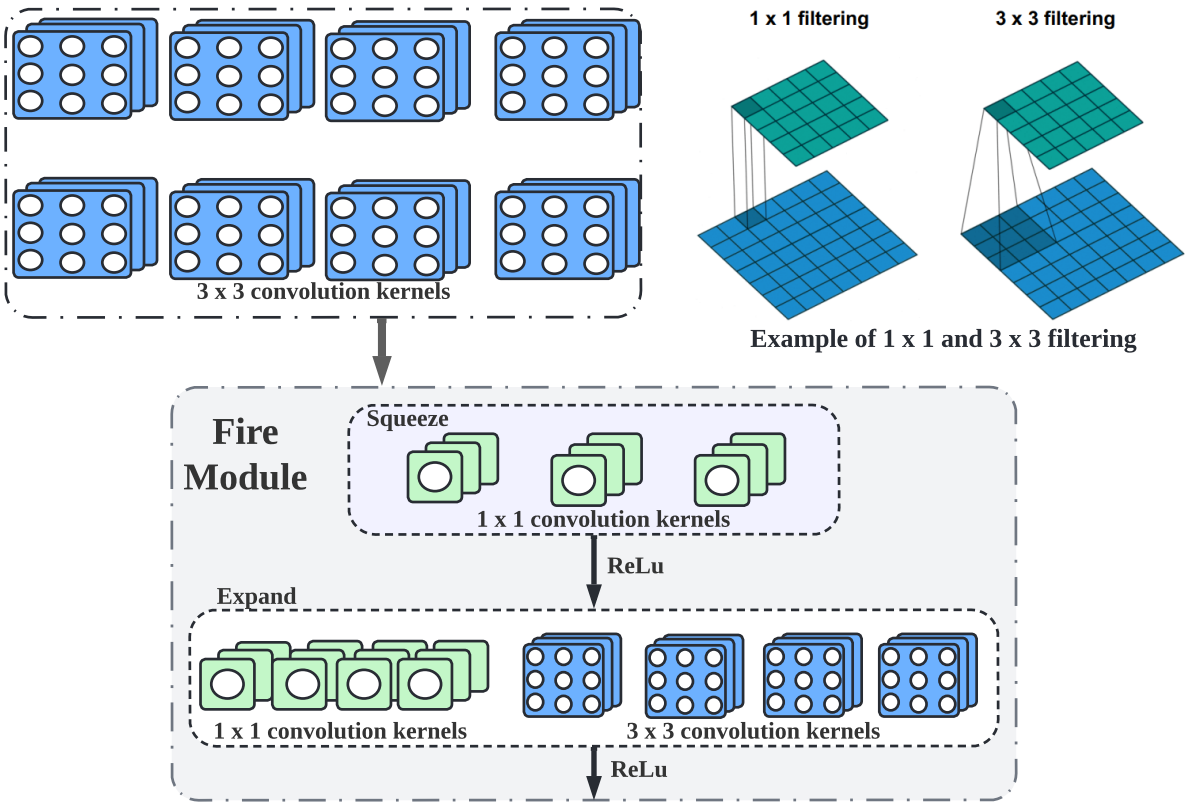

Figure 3.11: *Converting* 3×3 *filters to a fire modules:* $s_{1\times1}$ *= 3 ;* $e_{1\times1}$ *= 4 and* $e_{3\times3}$ *= 4*

$50\times$ fewer than 60 million hyperparameters for the original AlexNet architecture [337]. As a result of these modifications, the architecture was compressed by a factor of $510\times$ to achieve comparable accuracy to that of AlexNet [333]. The 1×1 filters from the squeeze layer facilitated the transfer of features to the expand layer, which incorporated both 1×1 and 3×3 kernels. To optimize the weight parameters, three variables were fine-tuned during the training process: (1) the number of 1×1 kernels in the squeeze layer ($s_{1\times1}$), (2) the number of 1×1 kernels in the expand layer ($e_{1\times1}$), and (3) the number of 3×3 filters in the expand layer ($e_{3\times3}$). The input channels to the 3×3 filters were restricted if the value of $s_{1\times1}$ was greater than $(e_{1\times1} + e_{3\times3})$.

The input to the SqueezeNet architecture was set to $227 \times 227 \times 3$, with the dimensions of $277 \times 227 \times 3$ representing the RGB tool wear images. A 3×3 maximum pooling layer with a stride of 2 was employed to reduce the size of the feature maps. Subsequently, the feature maps were convolved through a series of fire modules (Fire 2 to Fire 8), and the resulting last feature map in Fire Module 9 (Fire 9) had dimensions of $14\times14\times512$. Literature has indicated that larger feature maps are better suited for detecting small objects as compared to smaller feature maps [309]. As the failure modes in this research were considered micro-features, the

$14 \times 14 \times 512$ feature map was transformed through a 1×1 convolution layer (Conv10) with 1000 channels to obtain a larger feature map of dimensions $14 \times 14 \times 1000$. The number of 1×1 kernels in each fire module was greater as compared to the number of 3×3 kernels. This compression of the overall network was achieved without sacrificing the feature patterns in the wear region, thereby observing the SqueezeNet theory proposed by Iandola in [333].

Detecting Failure Modes by the YOLOv3-TWDM

Inspired by the findings reported in [49], the present study proposed a novel implementation of the YOLOv3, which leveraged a series of detection heads integrated into a SqueezeNet architecture, as depicted in Figure 3.10. The second detection head was twice the size of the first, thereby augmenting the size of the feature map and enabling the detection of smaller objects, as indicated in [309]. However, it was observed that the process of determining the optimal input feature source for the detection network was a trial-and-error process. As such, this research successfully utilized the output feature maps from the 5^{th} and 9^{th} Fire modules of the SqueezeNet architecture, a technique that was also employed in [332]. The low-level features from the 5^{th} Fire module and high-level features from the 9^{th} Fire module were fused in the classification layer to yield improved detection accuracy. The first detection head utilized a 3×3 kernel of the first convolution layer (Conv10), a rectified linear unit activation function (ReLu10), and a 1×1 filter of the second convolution layer (Conv11) to convolve the overall feature map. Whereas, the second detection head, in turn, convolved the features using a 3×3 filter of the first convolution layer (Conv12), a rectified linear unit activation function (ReLu12), and a 1×1 filter of the second convolution layer (Conv13).

The detection heads of the YOLOv3 algorithm were initialized with the same weight initialization scheme (HE). HE, named after its creator, Kaiming He, is similar to the commonly used "Xavier" initializer, and is commonly used for layers with the ReLU activation function. The output produced by the YOLOv3-TWDM was a list of Bounding Boxes (B-Boxes) with associated predicted classes, extracted from the detection layers of the network. Each B-Box was represented by a set of four parameters: (1) the probability of the B-Box containing a specific class (P_c), (2) the x and y coordinates of the B-Box centroid (b_x, b_y), (3) the width and height of the B-Box (b_w, b_h), and (4) the probability of a cell containing a failure mode (C). For a single

cell, the detection heads predicted a feature vector y = [P_c, b_x, b_y, b_h, h_w, C_1, C_2, C_3, C_4, C_5], with locations denoted by five labels: "chipping," "flaking," "uniform flank wear," "BUE," and "Notching". At each location, an output was produced with a score s_c relative to the bounding box, and the confidence of each predicted class ($C(s_c)$) was computed by 3.13 [336].

$$C(s_c) = \frac{e^{s_c}}{\sum_c^{e^{s_c}}} \tag{3.13}$$

Evaluating the Performance of YOLOv3-TWDM

The Regions of Interest (ROIs), identified through these failure modes, resulted in a final feature map of $(5B + 5)$ items, Where B represented the number of bounding boxes each cell predicted. The input image was divided into numerous grids to ensure each cell detected a solitary class label, as depicted in Figure 3.12. However, the predicted and ground truth B-boxes sometimes varied in their coordinates during detection. Thus, the features localization was evaluated by determining the area of overlap between the ground truth and predicted B-Boxes, thus introducing the Intersection over Union (IoU) metric, with a perfect localization being identified by an IoU of 1. Nevertheless, some redundant boxes still persisted. As such, Non-Maxima Suppression (NMS) was employed to eliminate them by: (1) identifying boxes with the highest confidence levels, (2) selecting boxes with an IoU above a specified threshold, and (3) suppressing boxes with an IoU below the threshold. Figure 3.13 exemplifies the utilization of IoU to assess the performance of YOLOv3-TWDM.

In addition to the IoU metric, the Precision-Recall curve (PR-curve) was employed to evaluate the performance due to its ability to accurately interpret specificity in the presence of an imbalanced dataset [338]. Precision reflected the model's efficiency in predicting the correct failure mode while recall captured the number of failure modes correctly classified [339]. The values of precision and recall were calculated through equations (3.14) and (3.15), respectively. The Area Under the PR-Curve (AUC) was used to evaluate the model's ability to distinguish between positive and negative detections. The AUC ranged between 0 and 1, where 1 represents a perfect detection, whereas 0.5 represents a random detection. AUC is widely used due to its robustness in detecting imbalanced tool wear dataset by providing a scalar value that summarizes a model's performance across all thresholds. This was used to

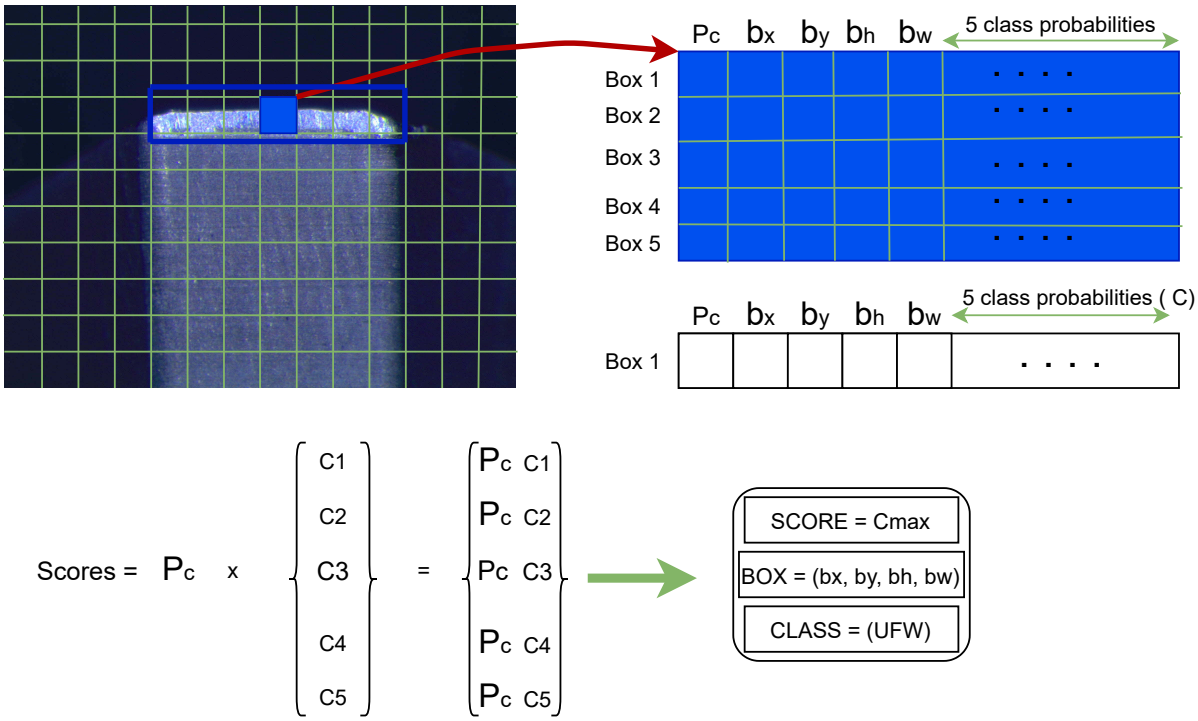

Figure 3.12: *Detecting and classifying failure modes using YOLOv3-TWDM*

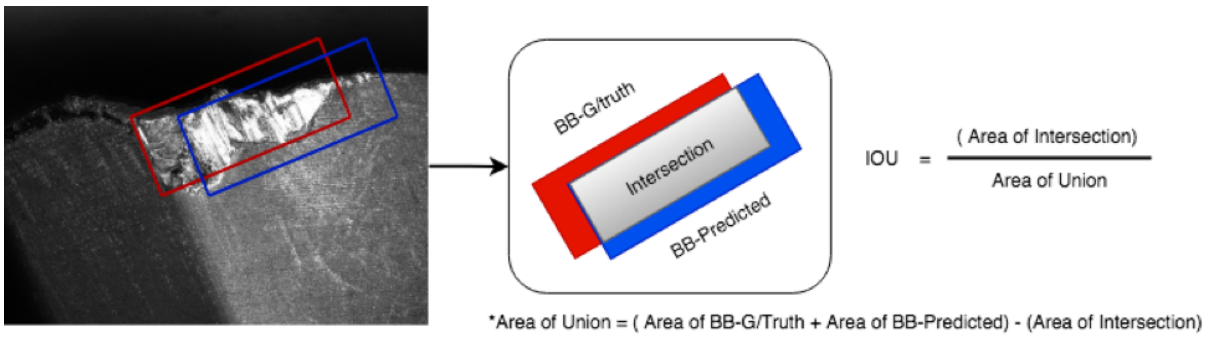

Figure 3.13: *Evaluating the YOLOv3-TWDM using IoU*

assess the model's proficiency in detecting individual failure modes during MV-TCM.

$$Precision = \frac{True\ Positive(TP)}{True\ Positive(TP) + False\ Positive(FP)} \tag{3.14}$$

$$Recall = \frac{True\ Positive(TP)}{True\ Positive(TP) + False\ Negative(FN)} \tag{3.15}$$

The objective was to attain the highest AUC for all 5 failure modes. To realize this, the YOLOv3-TWDM was engineered to reduce the losses incurred during failure modes detection. These losses were denoted as the localization loss ($Loss_{fail-loc}$), which occurred as a result of the missing predicted B-Box coordinates, and the confidence loss ($Loss_{fail-coff}$), which

depicted the misclassified failure modes. These losses were calculated through equations (3.16) and (3.17) respectively [336], with localization loss utilizing positive samples (ps) only, and the confidence loss incorporating both positive and negative samples (ps and ng).

$$Loss_{fail-loc} = \sum_{i \in ps}^{N} \sum_{k \in (x,y,w,h)} x_{i,j}^{q} smooth_{L1}(p_i^k - g_j^k) \tag{3.16}$$

$$Loss_{fail-coff} = (\sum_{i \in ps}^{N} x_{i,j}^{c} log(C(s_{ci}^{c})) + \sum_{i \in ng}^{N} log(C(s_{ci}^{0}))) \tag{3.17}$$

If the combined losses were high, the YOLOv3-TWDM would not accurately detect and categorize the failure modes. The value $x_{i,j}^{c} = 1$ signifies a correspondence between the i^{th} predicted and the j^{th} ground truth B-Boxes in the context of a particular failure detection. Conversely, a value of $x_{i,j}^{c} = 0$ indicates the absence of said correspondence. The confidence metric C_i^c quantified the certainty of the failure mode c.

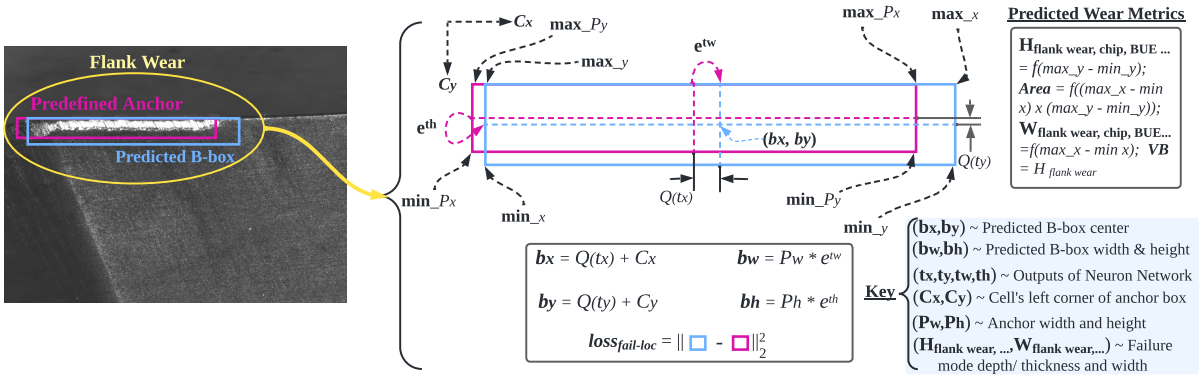

Figure 3.14: *Correlating flank wear with the B-box coordinates in YOLOv3-TWDM*

It should also be noted that YOLOv3-TWDM applied in this research predicted both the presence of failure modes and their respective magnitudes by analysing the geometry of the predicted B-Boxes. It was noted that the dimensions of the B-Box (b_h, b_w) were proportional to the magnitudes of the multiple failure modes, as illustrated in Figures 3.14 and 3.15. This information was then utilized to enhance the F_i magnitudes in predicting and optimizing the flank wear evolution.

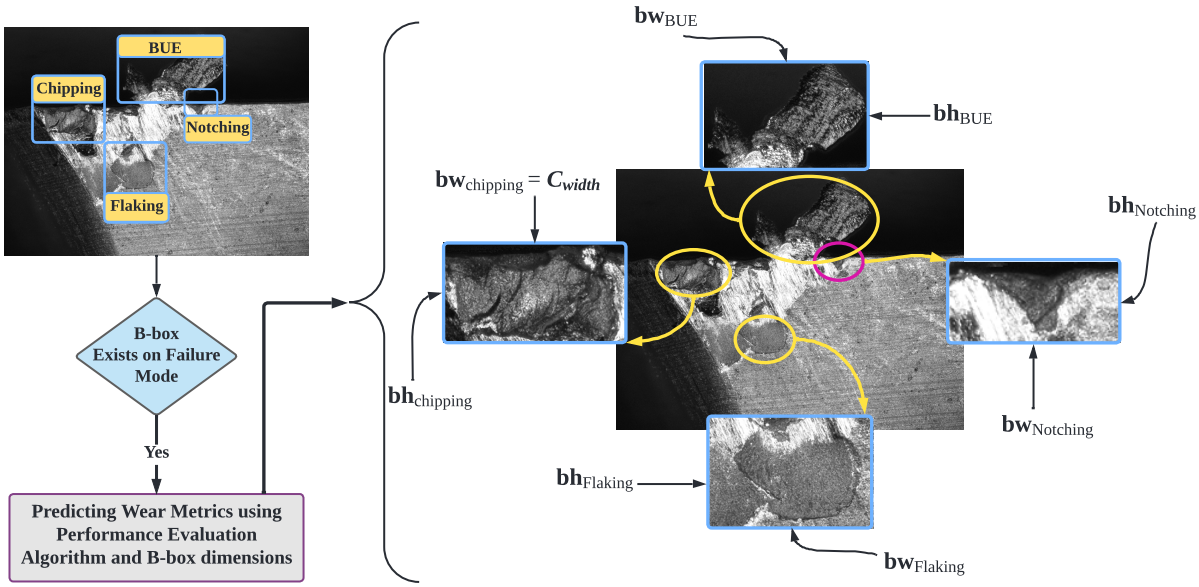

Figure 3.15: *Estimating the magnitudes of failure modes using B-boxes predicted by YOLOv3-TWDM*

Training the YOLOv3-TWDM

During training, it was observed that the wear region exhibited some noise due to smearing, and this necessitated pre-processing of the images prior to features extraction by the squeezeNet architecture. In this case, the Contrast Limited Adaptive Histogram Equalisation (CLAHE) was applied to improve the contrast of tool wear images. The rationale behind CLAHE was to repair irregularities across borders while performing histogram equalization of non-overlapping sub-areas of tool wear images [340]. The Clip Limit (CL) and Number of Tiles (NT) were hyper-parameters applied during CLAHE. The NT controlled the size of sub-regions while the CL limited the noise for each sub-region during contrast equalization. The values of CL and NT that optimized CLAHE were 0.005 and [20, 20]. In this case, the original image, $1440 \times 1920 \times 3$, was divided into 6912 sub-regions. Then, CLAHE was applied to each sub-histogram of 6912 sub-areas to create sub-histograms, which were redistributed to ensure the height did not exceed a CL of 0.005. After that, a cumulative histogram was generated by interpolating the equalized 6912 sub-histograms [341].

After enhancing the contrast, 404 images (80% of total dataset of 506 images) was used to create ground truth bounding boxes by labelling the failure modes in each image as regions of interest (ROIs) using MATLAB image labeller application, as shown in Figure 3.16. The failure modes were identified by following the ISO-8688-1 face milling standard [12] and relevant lit-

erature findings [10, 69]. The flank wear was identified as the entire wear region, extending uniformly along the main cutting edge. In contrast, chipping was saw-tooth profile along the cutting edge, and was characterized by its location, color, and shape. BUE was identified as adhesive particles that projected above the main cutting edge, whereas flaking was a localized fracture beneath the main cutting edge. Like chipping, flaking exposed the low-energy layers of the tool's substrate, but it was distinguished from chipping by its location and shape. Notching was a deep groove at the tool entry into the workpiece. After labelling the failure modes, the training dataset was augmented to combat the powerful fitting ability of SqueezeNet features extraction network [33]. During this process, it was transformed by jittering the contrast ratio of 0.1, a hue of 0.1, saturation and brightness of 0.2; flipping by a reflection scale of [1, 1.1]; and clipping the region outside the overlap of 0.25. After augmentation the dataset, 80% was used for training, and 20% for testing.

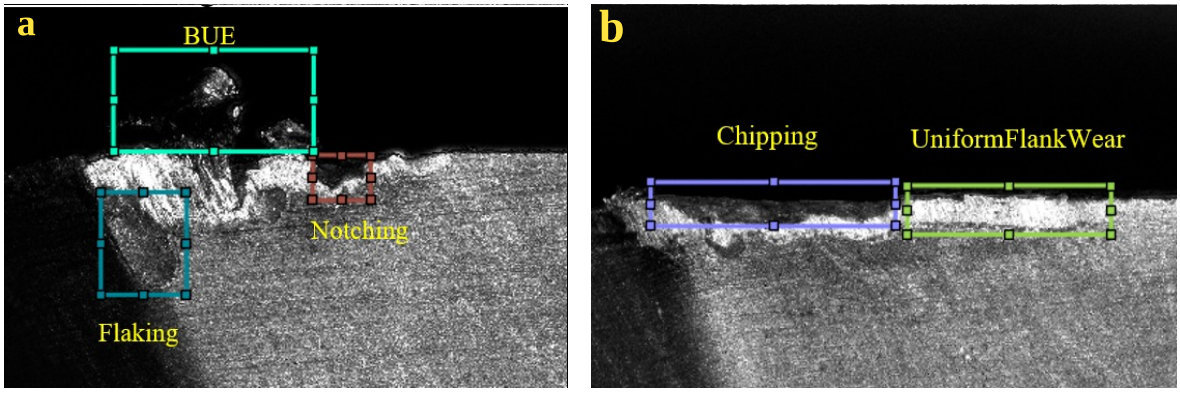

Figure 3.16: *Labelling failure modes using MATLAB image labeler application*

After transforming the labelled dataset, SqueezeNet was applied to extract features through transfer learning. During this process, YOLOv3-TWDM was optimized by tuning the hyper-parameters using stochastic gradient descent algorithm. The hyper-parameters were adopted from [332], including the number of epoch, mini-batch size, learning rate, L2regularization, and penalty threshold. The hyperparameters as described as follow:

- The number of epochs denoted number of iterations that ensured a complete training and minimum losses.
- MinibatchSize represented the number of images processed per iteration, signifying the speed and duration of the training process.

- Learning Rate signified the rate at which the training response changes in relation to the estimated error, balancing both accuracy and speed.
- L2Regularization is a mathematical variable employed to penalise errors, enabling the achievement of minimum losses and high precision.
- The Penalty Threshold was defined as the penalty applied to specific detections that scored below a specified threshold, returning only detections of the highest confidence.

The predicted failure modes were compared with the ground truth data to assess the mean Average Precision (mAP) during training. After training and evaluating the performance of the multi-sectional SVD and YOLOv3-TWDM, the extracted features were combined with process parameters to formulate a Diverse Feature Synthesis Vector (DFSV). Thus, the DFSV consisted of process parameters, Fi, and failure modes (categorical features). The DFSV was used to train an ML model for average VB prediction and control during face milling of Inconel 718. However, considering that previous studies utilized geometric and textural features to predict tool wear evolution, the DFSV was compared with the Spatial Binary Features (SBF) (which is a combination of the geometric and fractal properties of the flank wear region) to validate its feasibility in representing the complex wear morphology during face milling of Inconel 718. The training and optimization process of YOLOv3-TWDM is outlined in Algorithm 2.

Algorithm 2 Training of SqueezeNet-Based YOLOv3-TWDM

Inputs: Tool Wear Images

Outputs: Weight parameters of YOLOv3-TWDM

Global Parameters:

1. $Groundtruth\, BBoxes \leftarrow input\, images\, ISO\, 8688-1\, labels$
2. $Number\, of\, Predicted\, BBoxes$
3. $ps, ng \leftarrow Evaluate\, Positive\, and\, Negative\, samples$
4. $Weight\, parameters$

function LOOP([ ])

$Groundtruth \leftarrow 80\%\, input\, dataset$

$Feature\, map \leftarrow SqueezeNet\, Fire9 + Fire5$

$Final\, Feature\, map \leftarrow Detection\, Heads$

$Predicted\, BBoxes \leftarrow Detection\, TOLOv3\, Network$

for $i \leftarrow 1$ to $number\, of\, test\, set$ **do**

$ps\, BBoxes \leftarrow IoU \leq 0.65$

$ng\, BBoxes \leftarrow IoU \geq 0.65$

$Calculate\, Total\, loss$

$Minimize\, loss \leftarrow Optimize\, Hyperparameters$

$Detected\, failure\, modes \leftarrow 20\%\, test\, dataset$

$Detected\, failure\, modes \leftarrow Non-Maxima\, Suppression\, (NMS)$

$Precision,\, Recall \leftarrow Evaluate\, TP\, FP,\, TN\, FN$

$mAP \leftarrow Precision,\, Recall$

return $Failure\, modes,\, Precision,\, Recall,\, mAP \leftarrow YOLOv3-TWDM$

return $Magnitudes\, of\, failure\, modes \leftarrow Predicted\, BBoxes\, Dimensions$

3.2.3 Extracting Spatial Binary feature (SBF)

Unlike the Diverse Feature Synthesis Vector (DFSV) approach, this technique improved the effectiveness of features representation by extracting the geometric and fractal properties from the side cutting edge of the wear inserts to circumvent the uncontrolled failure modes on the

main cutting edge. Figure 3.18 shows the methodology used to process images and extract spatial binary features for VB prediction during machining. Before extracting the spatial binary features, the Contrast Limited Adaptive Histogram Equalization (CLAHE) was used to improve the contrast ratio of tool wear images. The results of CLAHE technique applied in SBF approach is shown in Figure 3.17 (b). The Morphological Reconstruction Technique (MRT) was enhanced in this research by integrating it with CLAHE to generate binary images. The Enhanced MRT (EMRT) performed segmentation through thresholding, dilation, filling of voids, masking the binary image with the original grayscale image, and removal of peripheral edges [342].

Figure 3.17: *Image processing during extraction of spatial binary features (SBF)*

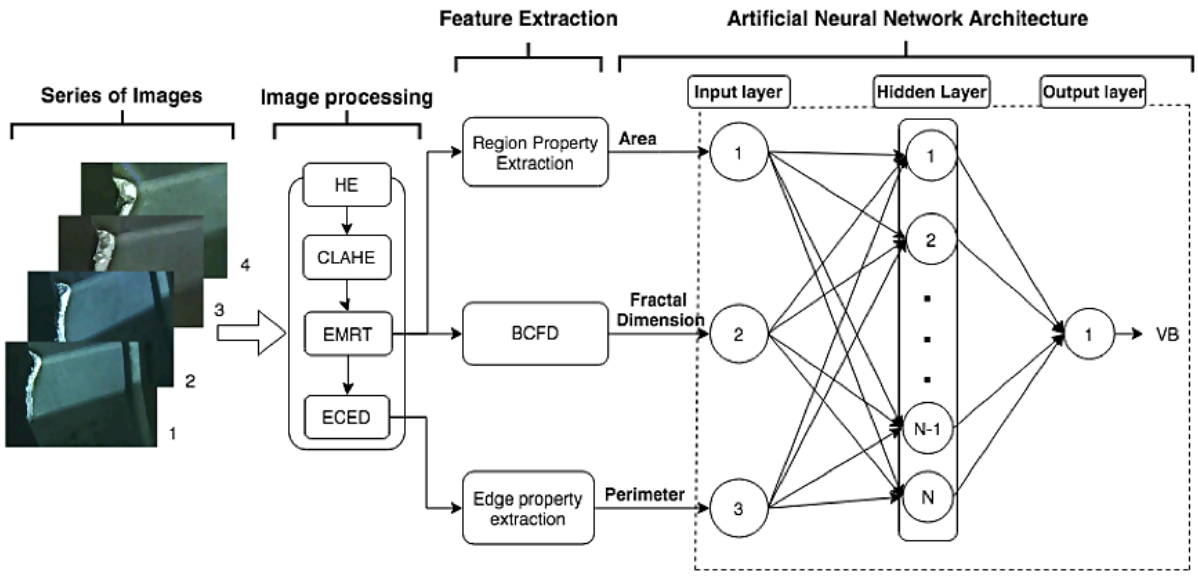

Figure 3.18: *Predicting VB progression using spatial binary properties and MLPNN*

The assumption was that tool wear images extracted from the side cutting edge were bimodal as they comprised a single region (wear region) that was to be extracted and binalized. The global thresholding aimed to identify a gradient value that would completely binarize the tool wear image [261]. Subsequently, the MRT filled all the edges, boundaries, and voids

to form a dilated and continuous flank wear region. The original grayscale image masked the binary image to ensure that the wear region did not surpass the original size. Finally, EMRT eradicated all minor edges to yield two distinct segments, namely the flank wear region (represented by white pixels) and the background (represented by black pixels), as shown in Figure 3.17 (c). In addition to EMRT, Canny edge detection [343] was employed and enhanced by EMRT to produce a thin ridge around the wear region. The first step of the Enhanced Canny Edge Detection (ECED) computed the gradient (M(x,y)) using 3.18, which leveraged the Robert operator along the gradient direction θ (3.19).

$$M(x,y) = \sqrt{(g_x^2(x,y) + g_y^2(x,y))} \tag{3.18}$$

$$\theta = tan^{-1}\frac{(g_y(x,y)}{(g_x(x,y)} \tag{3.19}$$

Where $g_y(x,y)$ and $g_x(x,y)$ are the gradients of a Gaussian function $g(x,y)$. The second phase applied the gradient magnitude ($M(m,n)$) to determine a threshold value that would preserve the contours of the wear region while eliminating extraneous noise along the perimeter. The dilatory aspect of EMRT induced an inconsistent width of the edge surrounding the wear region. To rectify this, the third stage implemented a non-maximum suppression to eliminate pixels outside the wear region and establish a narrow ridge. Finally, a continuous outline was formed by identifying the nearest neighboring pixels along the slender ridge, resulting in a contiguous perimeter that circumscribed the wear region, as shown in Figure 3.17 (d). After applying image processing techniques, the binary image was transformed into quantifiable metrics, such as area, perimeter, and fractal dimension.

The area was defined as the aggregate of pixels constituting the boundary of the flank wear region in a binary image [37] (Figure 3.17 (b)), and was hypothesised to increase with the progressive VB, owing to an expansion of the wear region during machining. The perimeter constituted the sum of pixels circumscribing a narrow ridge of the wear region, as depicted in Figure 3.17 (d), and was similarly anticipated to increase with the progressive VB. The third feature proposed in this research is the self-similarity of the flank wear region, referred to as the fractal dimension (D), which was derived from the EMRT image (Figure 3.17 (b)). D was

introduced to decipher the flank wear geometry by providing a statistical index of complexity, comparing the intricacy of the evolving wear pattern at a measured VB scale. Thus, D characterized the fractal patterns by quantifying the complexity of the wear region as the ratio of change in intricacy to the change in the wear region. It was observed that evolution of D played a crucial role in identifying the uncontrolled failure patterns of a highly complex flank wear morphology. Therefore, it was employed to augment the area and perimeter in predicting the VB profile during face milling of Inconel 718.

The value of D was assessed through the conventional box-counting technique (BCFD) [344]. It is an exponent ranging from 1 to 2, which increased with a contiguous wear region. During BCFD, various values of N were determined by reducing the value of r until the best line of fit satisfied the least-squares linear regression equation, $Y = DX + E$, where D represents the fractal dimension and E represents the y-intercept, as illustrated by the graph-line of equation 3.20. Figure 3.19a illustrates the BCFD technique employed to determine the values of N and r. Only the boxes encompassing the wear region were counted to compute N relative to the value of r. A contour plot generated in MATLAB, shown in Figure 3.17 (b), depicts the results of least-squares analysis utilized to determine the value of D (1.24). The correlation coefficient of the logarithmic N to logarithmic r is 0.95, indicating the strong correlation of fractal data obtained from the wear geometry.

$$D = \frac{\log N}{\log r} \tag{3.20}$$

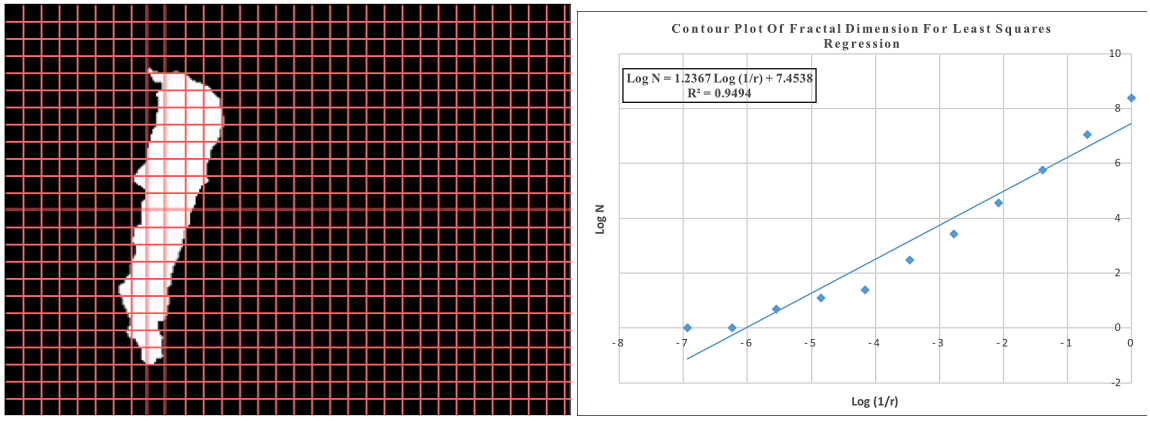

(a) **(b)**

Figure 3.19: *Computing fractal dimension: (a) Box-counting method; (b) contour plot for least squares regression*

3.2.4 Multi-layer Perceptron Neural Network for VB Prediction

After extracting the features (DFSV and SBF) from the training images, they were combined with process parameters to train a Multi-layer Perceptron Neural Network (MLPNN) in MATLAB R2021b. During this process, the features were normalized by standardization to equalize the predictive strength during MLPNN training. Given the case of multicollinear data, the MLPNN architecture was attuned to grasp the intricate relationship between nominal and numerical features, thus augmenting its versatility to predict VB progression under complex flank wear morphology. Despite the requirement of large datasets to prevent under-fitting issues [171], the MLPNN was optimized by updating the features' weights and biases to fit a regression model, thus implementing the adaptive learning to predict the prevailing VB profile at varying processing conditions [166].

The MLPNN was evaluated by the mean squared error (MSE) loss function (3.21)[345]. The backpropagation (3.23) was used to compute the partial derivative to minimize the loss function. A purelin transfer function (f) was used because the model applied regression analysis to compute the VB output (3.22). The number of neurons in the input layer was corresponding to the features, whereas the output layer had one neuron representing VB output. The optimal number of neurons in the hidden layer was determined by conducting several iterations.

$$MSE_{VB} = 1/n \sum_{i=1}^{n} (VB_t - VB_y)^2 = 1/n \sum_{i=1}^{n} \epsilon_{VB}^2 \tag{3.21}$$

$$y_j = f(b + \sum_{k=1}^{N} w_{kj} - x_k) \tag{3.22}$$

$$\frac{d\epsilon}{dw_{kj}} = \frac{d\epsilon.(dy_j)}{(dy_j)(dw_{kj})} = \frac{d\epsilon.(dy_j)}{(dy_j).d(\sum_{k=1}^{N} w_{kj} - x_k)} . \frac{d(\sum_{k=1}^{N} w_{kj} - x_k)}{dw_{kj}} \tag{3.23}$$

where f is a purelin transfer function, b is the bias, x_k is the input to a neuron, ϵ is the error, w_{kj} is the weight between neuron k of previous layer and j of the current layer, y_j is the output of j^{th} neuron. The training and test performance was further evaluated by Root Mean Square Error (RMSE), box plots, and correlation coefficient (R^2) metrics. After training, evaluating, and validating the MLPNN using DFSV and SBF, the ML models (DFSV-ML and

SBF-ML) models were created. The models were further evaluated and compared using test dataset to select the best ML for in-process utilization. This dataset was extracted from the speed of 40 m/min, feed of 0.13 mm/tooth, and ADOC of 1 mm, a condition outside the vicinity of the training parameters and images. Thus, the selected ML was integrated with an MV-TCM system for in-process predictive control of tool wear evolution during face milling of Inconel 718. The outcome of such integration was an ML-based MV-TCM system.

3.3 Developing ML-based MV-TCM for Predicting Tool Wear Evolution

It was reported that tool replacement in CNC milling operations constitutes more than 20% of the total machine downtime [237]. The ISO 8688-1 standard stipulates that tools should be replaced once they reach a maximum failure criteria, which is determined by the magnitude of failure modes. However, these magnitudes are typically measured offline using digital microscopes. This process is time-consuming, hazardous (due to the use of chemicals during cleaning), expensive (as most microscopes are costly, especially when inspecting a large sample size), and requires skilled experts to carry out the tool wear characterization. Therefore, there is a need to address these limitations by implementing a cyber-physical MV-TCM system that can predict or measure the magnitudes of failure modes to determine the failure criteria and actual time for tool replacement. To achieve this, an ML-based on-machine vision system was employed in this research to predict and control in-process tool wear evolution, thus, addressing the third question and objective of this research. Figure 3.20 summarizes the methodology of applying ML-based MV-TCM system during face milling of Inconel 718.

The main contributions of this method to the field of MV-TCM is:

- The structural design of the MV-TCM exhibits exceptional properties, streamlining in-process data acquisition, processing, and transfer within challenging CNC machining domains.
- The newly proposed integrated system, featuring an ML-based MV-TCM, not only predicts and controls but also enhances informed decision-making for real-time tool per-

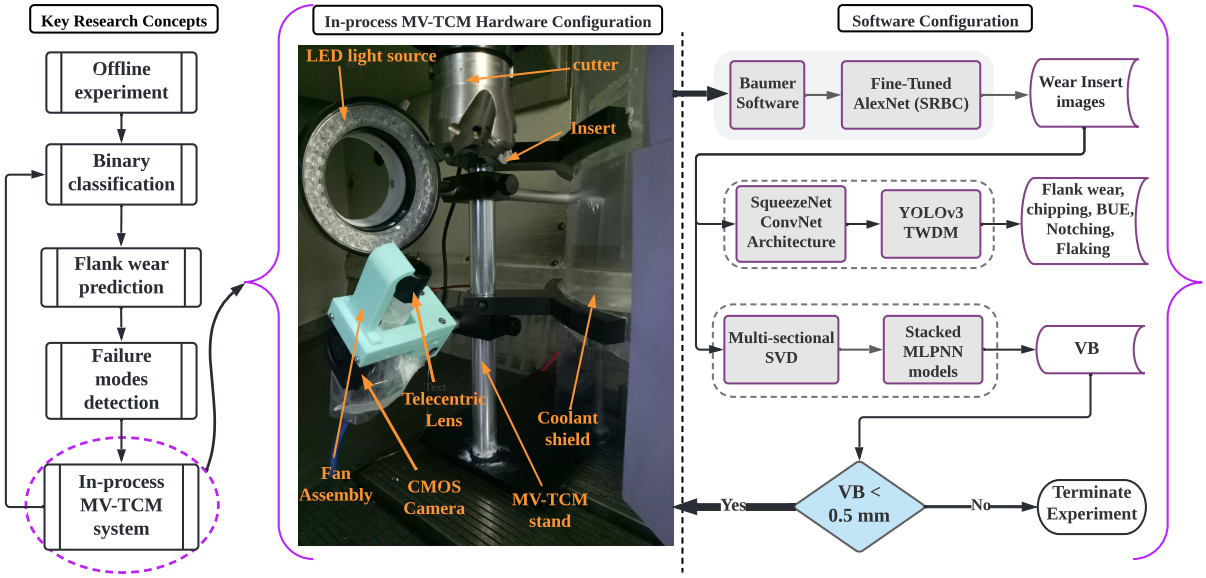

Figure 3.20: *ML-based MV-TCM for tool wear prediction and control*

formance optimization, particularly under dynamic and varying processing conditions.

These contributions showcase a paradigm shift in MV-TCM structural design, an innovative approach that offers a streamlined data management, heralding a new era in real-time tool performance control and optimization under varying processing conditions.

3.3.1 Developing an MV-TCM Structure

In machine vision technology, *CMOS cameras* have advanced over the years, where high price-to-performance ratio has facilitated their deployment in TCM applications [346]. The high speed, sensitivity, and low power consumption, make them indispensable in acquiring time-series data during machining [347]. However, capturing high-resolution images with varying flank wear depths still remains a challenge for most CMOS cameras. To overcome this, auxiliary components such as telecentric lens and LED ring light were employed to enhance the data acquisition. The telecentric lens, unlike a fixed focal length, improved the magnification with varying flank wear depths [346]. The LED ring light, with its unique flexibility, output stability, and longevity, facilitated the matching of the source's spectral output with the sensitivity of the CMOS camera. The polypropylene plastic shielded the camera, lens, auto-capturing system, and LED light source, thereby thwarting any potential ingress of coolant droplets and swarf onto the system. Figure 3.21 shows the main structural components of the

MV-TCM.

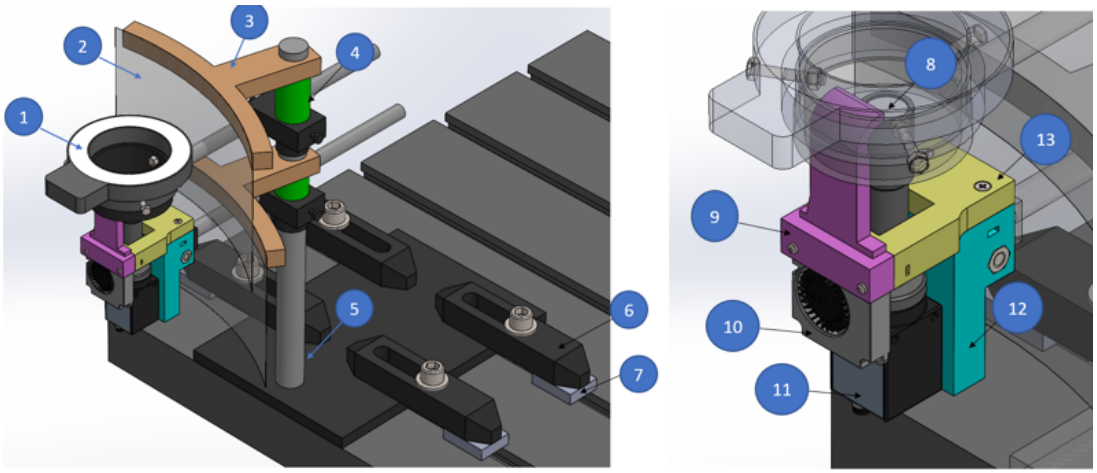

(a) (b)

Figure 3.21: *The main structure: 1.LED light, 2.Plastic films, 3.Plastic film holder, 4.Holder support, 5.Table stand, 6.Clamps, 7.Blocks, 8.Telecentric lens, 9.Cooling fan duct, 10.Cooling fan, 11.Camera, 12.Camera fixture, 13.Cooling fan fixture*

Furthermore, the processing time was minimized by integrating an auto-capturing system, which instantaneously detected the cutter as it approached the focal coordinate, thereby activating the camera's shutter to capture tool wear images. To achieve this, an infrared photoelectric proximity sensor (SN-E18-B03N1, diffuse reflective type, NPN output, $1.6cm(Diameter) \times 6.7cm(Length)$) was reliable for a close-range MV-TCM installation. It had a maximum detection distance of 14 cm, sufficient to encompass the camera's working distance of 65 mm. In addition, the cutter detection also considered an average delay before tools were registered on the focal coordinate of the camera. A design of such helped to estimate the actual time to turn on the camera. To synchronise the entire auto-capturing system, an Arduino Uno microcontroller was programmed with MATLAB to control the camera and infrared photoelectric proximity sensor.

During image acquisition, an industrial camera (Baumer, VCXU-65M.R, 1/1.8" CMOS sensor, 3072 × 2048 resolution, 47 fps, purchased from Vitals Vision Technology, Singapore) and a telecentric lens (APT08-65, $0.8\times$, 1/1.8", also purchased from Vitals Vision Technology, Singapore) were oriented at 45°relative to the CNC spindle axis at a working distance (WD) of 65 mm with a $6.9 \times 8.9mm$ field of view and a maximum distortion of 0.03%. The camera and lens specifications are shown in Table 3.8 and 3.9, respectively. The camera system was securely affixed to the MV-TCM stand, which was supported by 4 magnet discs (HD-MAG-2003, Strong

N52, $\phi = 20mm \times H = 3mm$) and vibration pads to prevent any extraneous motion induced by high vibrations when cutting Inconel 718.

To optimize the resolution of the images, the camera and lens were calibrated to optimal settings, including 30 fps, a gain of 10, and an exposure time of 400. In addition, other parameters were computed, including Angular Field of View (AFV), Horizontal Field of View (HFoV), Depth of View (DoV), and image resolution by using the image height of 1920 pixels, minimum detectable size of 2 pixels, working $fnumber$ of 9.6, and working distance (WD) of 65 mm. Therefore, the Angular Field of View ($AFOV$) and Horizontal Field of View ($HFOV$) were 22.93° and 26.77 mm, respectively. The aspect ratio of the image was 1:1, thus rendering the Vertical Field of View ($VFOV$) congruent with the $HFOV$.

Table 3.8: The specifications of Baumer VCXU-65M.R Camera

Sensor	Resolution	Frame Rate
1/1.8" CMOS	3072 (H) x 2048 (V)	47 fps

Table 3.9: The specifications of VST APT08-65 Telecentric Lens

Working Distance (WD)	Field of View (FOV)	Distortion (Max)
66mm	6.9 x 8.9 mm	0.03%

The geometry of the PVD-TiAlN/NbN coated cemented carbide inserts, as outlined in Table 3.2, indicated that the effective length of the main cutting edge for the maximum ADOC of 1 mm and 45°leading angle was 1.4 mm, thereby rendering the Field of View ($FoV = 9.6$) sufficient to focus the entire flank wear region. The maximum Depth of View (DoV) was determined to be 0.54 mm, which was deemed adequate to capture the maximum flank wear depth incurred during the milling of Inconel 718. The minimum detectable size was calculated to be $26\mu m$, which resulted in approximately 20 salient sub-regions within a $500\mu m$ of maximum VB, thus providing ample focus on the 5 potential failure modes on the tool's cutting edge. Nevertheless, the resolution was further augmented through image processing techniques, resulting in an improved pixel distribution and contrast ratio within the flank wear region.

The MV-TCM was further enhanced to overcome the vibrations, which had a detrimental impact on the sensitivity of camera and photo-electric sensors, as well as the stability of the

LED light source. As a result, the MV-TCM base was enhanced with vibration pads as shock absorbers. To arrive at this decision, the main structure of the MV-TCM system was first modelled in SOLIDWORKS, as depicted in Figure 3.21. The detailed and assembly drawings of the whole system is shown in *Appendices E.1 to E.6*. The arms were fabricated from aluminium with the ultimate, yield, and fatigue strength of 310 MPa, 280 MPa, and 130 MPa, respectively. The arms that supported the camera and LED light assemblies weighed 2.4545 N and 0.981 N. Thus, the structure was tailored to withstand the bending stresses along these arms. Furthermore, a fatigue analysis was performed to evaluate the maximum life and damage of the structural components, which could result in an unprecedented failure of the critical components. Additionally, the total deformation was analyzed to assess the deviation of the camera assembly from the focal coordinate, x_{camera} and y_{camera} position of the CNC G-code, ensuring the minimum deviation of the DoV, $VFoV$ and $HFoV$.

The MV-TCM system was designed to withstand the random vibration resulting from high-frequency response, particularly at the end of tool life when tools were subjected to chatter due to rapid wear evolution. Random vibrations entailed the probabilistic computation of the structural response associated with statistical inputs, such as displacement. Hence, the arbitrary loading condition of the CNC milling environment was simulated to examine the stability and service life of the arms. To achieve this, the model was simulated by the ANSYS 2021 R2 with all components connected through friction-contact to facilitate stress transmission from the joints. The entire geometry was meshed with triangular elements, with increased refinement in regions of stress concentration, such as the arm joints, base joint, chamfers, and fillets. The base was fixed to simulate physical clamping on the CNC worktable. During simulation, PSD was applied at the base, and the loads of the arms were loaded into the static structure to provide the pre-stress conditions for the modal analysis. The natural frequencies and mode shapes were obtained through modal analysis. The displacement excitation was then implemented at all friction-based supports, also known as boundary conditions, enabling the random load to propagate throughout the entire structure. Figure 3.22 shows the simulation procedure using ANSYS workbench.

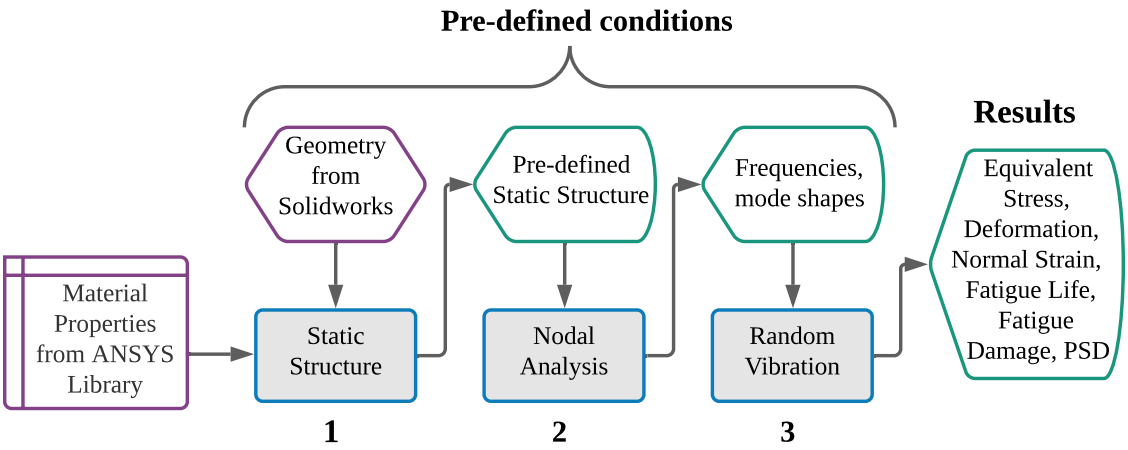

Figure 3.22: *Methodology for structural analysis in ANSYS 2021 R2*

3.3.2 A Binary Classifier for Separating Wear Inserts

To facilitate efficient online data processing, an ML model was developed to separate the wear inserts from the residues. This process controlled and filtered the number of images for tool wear analysis, thus, improving the computational cost and time required to analyze and predict tool wear progression. However, tool wear images and residues shared similar characteristics, making it challenging to separate them using simple binary classifiers, as depicted in Figure 3.23. Therefore, this study extracted high level features to distinguish the wear inserts from the residues by using a pre-trained CNN. This technique was also successfully implemented in [348, 349].

Inspired by the transfer learning technique in [348], the pre-trained AlexNet was used in this research. The feature map from a Fully Connected layer (FC-7) of a pre-trained AlexNet was then transferred to a softmax regression model for binary classification [305, 350]. During training, the hyper-parameters were optimised by stochastic gradient descent (SGD) to tune the weights and bias. Thus, the binary classifier was divided into: (1) pre-trained AlexNet and (2) softmax regression model. The methodology of the binary classifier is shown in Figure 3.24. The input size of AlexNet was $227 \times 227 \times 3$. It should also be noted that the AlexNet architecture contains eight layers, 5 convolution and three fully-connected layers.

According to [305, 350], Alexnet can classify 1000 labels with an error of 15.3%. It divides the tool wear image into small patches called samples. By extracting the colour, edge, pixel distribution, and failure patterns, it convolves the features to obtain the activation values,

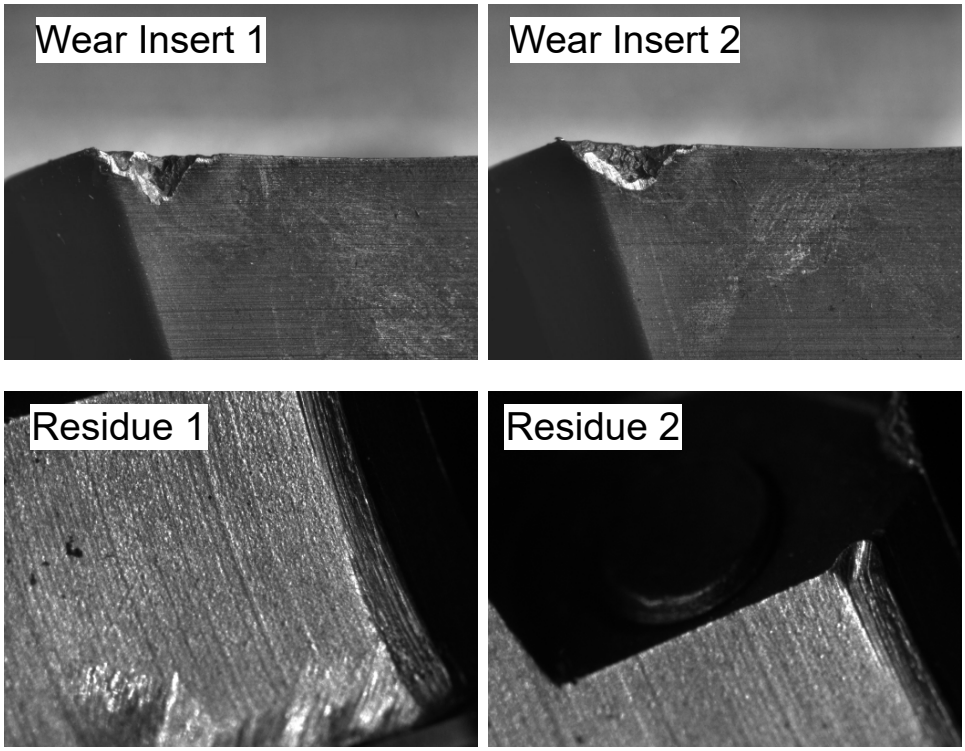

Figure 3.23: *Examples of tool wear inserts and residual images*

which are applied to the entire image [351]. Given $r \times c$ images, small $a \times b$ patch with an x_s small image sample and $k^{th} filter$, the function of the learned $k^{th} features$ is given by $f = \delta(W(1)x_s + b(1))$, which convolves by $f_{conv}, k \times (r - a + 1) \times (c - b + 1)$ into a new feature map. The maximum pooling is used to scan the largest feature on each small sample and form another feature map. The process iterates five times (in 5 convolution layers) with different filters until a final feature vector is formed. The whole feature extraction process of AlexNet is described in [305]. During features extraction, backpropagation was used to update weights, $W^{(1)}$, by applying the derivative of the cost function. If δ^{l+1} is the error for $(l + 1)$ layer with a cost of $J(W, b; x, y)$ where (W, b) and (x, y) are parameters, (x is the input data and y is the output labels. Error was computed by (3.24) [305].

$$\epsilon^{(l)} = \left((W^{(l)})^T \delta^{(l+1)}\right) \bullet f'(z^{(l)}) \tag{3.24}$$

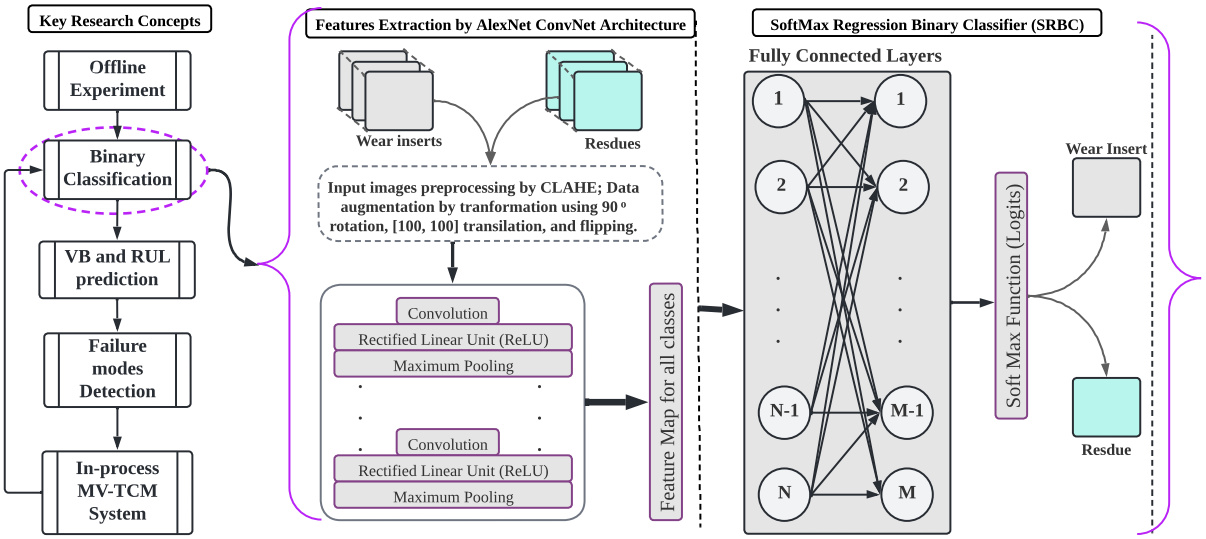

Figure 3.24: *Wear inserts identification using a binary classifier*

And the corresponding gradient becomes (3.25, 3.26) [305]:

$$\nabla_{W^{(l)}} J(W, b; x, y) = \delta^{(l+1)} (a^{(l)})^T, \tag{3.25}$$

$$\nabla_{b^{(l)}} J(W, b; x, y) = \delta^{(l+1)}. \tag{3.26}$$

Then the error in convolution layer can be propagated by (3.27) [305]:

$$\delta_k^{(l)} = \text{upsample}\left((W_k^{(l)})^T \delta_k^{(l+1)}\right) \bullet f'(z_k^{(l)}) \tag{3.27}$$

Where k is the filter number and $f'(z_k^l)$ is the derivative of the activation function. The next errors are computed by pooling layer. A gradient that maps on $a^(l)$ input to $i^{th} layer$ with respect to $k^{th} filter$ can be found by 3.28 and 3.29 [305].

$$\nabla_{W_k^{(l)}} J(W, b; x, y) = \sum_{i=1}^{m} (a_i^{(l)}) * \text{rot90}(\delta_k^{(l+1)}, 2) \tag{3.28}$$

$$\nabla_{b_k^{(l)}} J(W, b; x, y) = \sum_{a,b} (\delta_k^{(l+1)})_{a,b}. \tag{3.29}$$

The FC-7 (a softmax layer in AlexNet) was modified from 1000 to 2 classes to synchronise the number of outputs (wear inserts and residues). During training, hyper-parameters such as batch size, learning rate, epochs, momentum, regularisation, and normalisation were opti-

mised using stochastic gradient descent algorithm (SGD). The training features were (x(1),y(1)) and (x(m),y(m))], where y(i)$\epsilon 1, 2, \ldots, K$ for k classes (where k is 2 as described above). Given input x, a probability, $P(y = k|x)$, was computed for each class (wear inserts or residues) to create a vector of probabilities $h_\theta(x)$. The k-dimensional vector had k-probabilities whose sum of elements was 1.

$$h_\theta(x) = \begin{bmatrix} P(y=1|x;\theta^1) \\ P(y=2|x;\theta^2) \\ \vdots \\ P(y=K|x;\theta^K) \end{bmatrix} = \frac{1}{\sum_{j=1}^{K} \exp(\theta^{(j)\top} x)} \begin{bmatrix} \exp(\theta^{(1)\top} x) \\ \exp(\theta^{(2)\top} x) \\ \vdots \\ \exp(\theta^{(K)\top} x) \end{bmatrix} \tag{3.30}$$

$\theta^{(1)}, \theta^{(2)}, \ldots, \theta^{(K)} \in \Re^n$ are model parameters and $\frac{1}{\sum_{j=1}^{K} \exp(\theta^{(j)\top} x)}$ is the normalization function. θ represents all parameters of the model which is a matrix of column vectors after concatenating $\theta^{(1)}, \theta^{(2)}, \ldots, \theta^{(K)}$. That yields (3.31) [352]:

$$\theta = \begin{bmatrix} | & | & | & | \\ \theta^{(1)} & \theta^{(2)} & \ldots & \theta^{(K)} \\ | & | & | & | \end{bmatrix}. \tag{3.31}$$

Whose cost function is (3.32) [352]:

$$P(y^{(i)} = k|x^{(i)};\theta) = \frac{\exp(\theta^{(k)\top} x^{(i)})}{\sum_{j=1}^{K} \exp(\theta^{(j)\top} x^{(i)})} \tag{3.32}$$

And the gradient can be computed iteratively by (3.33) [352]:

$$\nabla_{\theta^{(k)}} J(\theta) = -\sum_{i=1}^{m} \left[x^{(i)} \left(1\{y^{(i)} = k\} - P(y^{(i)} = k|x^{(i)};\theta) \right) \right] \tag{3.33}$$

Just like the YOLOv3-TWDM, the performance of the binary classifier was evaluated by True Positives (TP), True Negatives (TN), False Positives (FP), and False Negatives (FN) were used to evaluate the recall, precision, relative accuracy, and overall accuracy. In this case, the TP described the correct prediction of the wear inserts while FP describes the residue image

classified as a wear insert. The TN defined the correct predictions of the residue image, whereas FN described the wear inserts classified as residues. The precision described how correct the model classified the image as wear insert of residue (a measure of accuracy by quality), whereas recall was characterized by the number of correctly classified images (a measure of accuracy by quantity). The Average Precision (AP) was then calculated from plotting the graph of Precision against Recall, and then obtaining the Area under the curve. The specific accuracy was the number of wear inserts correctly classified against the total number of images for each class during data acquisition.

3.3.3 Validating In-process Performance of ML-based MV-TCM

After developing the MV-TCM hardware, it was integrated with the trained ML models to create an ***ML-based MV-TCM system***. An experiment was conducted to validate this system in terms of flank wear prediction and control. The experiment was carried out under unknown cutting condition by utilizing a speed of 40 m/min, a feed rate of 0.08 mm/tooth, and an axial depth of cut (ADOC) of 0.9 mm. This condition was selected using a Gaussian Kernel Ridge Regression Model (GKRR) (Appendix C.7) in Chapter 6. This ensured that the validation data was different from the training dataset to test the reliability of the system in extracting features and predicting VB progression for real-life scenarios. At this point, the conventional methods were also used to observe the actual failure modes and measure VB at each incremental length of 400 mm. The CNC spindle was rotated at 5000 rpm while moving upwards at a feed of 1000 mm/min to remove any residual coolant droplets on the tool's surface by centrifugal force. Then it was moved towards the camera position, where it rotated at 10 rpm (lowest CNC setting). A mini fan was installed to blow the camera lens, drying any humid contaminants that could reduce the resolution of flank wear images during capturing. Upon arrival, the cutter was detected by the photoelectric proximity sensor to trigger the camera's shutter for image acquisition.

The time-series flank wear images were acquired by a Baumer camera via a webcam, and a total of 180 images (1 image per 2° of 360° revolution) were obtained at each incremental length. Another program was devised to save the data file with the associated date and time for easy retrieval in the directory. Thereafter, a binary classifier was used to separate the wear

inserts from the residues. After separating the wear inserts, a Contrast Limited Adaptive Histogram Equalization (CLAHE) was applied to improve the pixel distribution and luminosity, thus enhancing the resolution of flank wear images for easy identification of failure modes on the tool's cutting edge. The processed images were further transformed by rotating through 180°, resizing them to [227, 227, 3], and cropping them to [900, 1000], as per the specifications of the YOLOv3-TWDN training data (ground-truths). Subsequently, the trained multi-sectional SVD and YOLOv3-TWDM were utilized to detect the DFSV. In cases where the uncontrolled failure modes were detected, an induction-reasoning algorithm was also used to configure the underlying wear mechanisms and suggest the credible levels of process parameters that could minimize the tool's failure rate. By doing this, the system was utilized to design the optimum speed and feed, which minimized the evolution of VB and improve the cutting efficiency. Finally, the ML-based MV-TCM efficacy was validated and compared with known conventional and soft computing methods (GKRR) for the predictive control of tool wear evolution during face milling of Inconel 718.

3.3.4 In-process Control of Tool Wear Evolution

Therefore, this study enhanced the ML model with an inductive-reasoning algorithm to detect flank wear and chipping magnitudes of the PVD-TiAlN/NbN coated carbide inserts during face milling of Inconel 718. The decision-making algorithm was designed by harmoniously blending the experimental findings, SECO tool's recommendations, and ISO-8688-1 face-milling standard to ensure its practical use in the real manufacturing industry. Unlike the previous TCM methods, it was observed that the decision-making algorithm in this study was able to decipher the underlying wear mechanisms based on the failure modes detected by the YOLOv3-TWDM to determine the significant levels of speed and feed/tooth, which optimized the rate of VB and chipping evolution during machining. In so doing, the system helped in designing the promising cutting condition that improved the life of PVD-coated carbide inserts during face milling of Inconel 718.

After detecting the type of failure modes, the YOLOv3-TWDM was utilized to detect the magnitudes of failure modes directly from tool wear images to further demonstrate the complexity of wear evolution on the tool's cutting edge during face milling of Inconel 718. These

magnitudes were correlated with process parameters to determine the optimal speed, feed, and ADOC that minimized the wear rate during machining. This was achieved by plotting the graphs to study the flank wear and chipping evolution at various processing parameters to determine the promising cutting condition that minimized F_i, Bh_{FW}, $Bh_{chipping}$, and $Bw_{chipping}$ rate. From such a correlation, the thresholds were derived by mapping the values of the magnitudes against the ISO-8688-1 designated wear values on the promising cutting condition. Considering that it was not feasible to always remove the tools and measure the actual VB to determine failure criteria, these thresholds were then used to enhance the decision-making algorithm by determining the stopping criteria at various VB levels during the machining process. As a result, the inductive-reasoning algorithm was built to achieve two principal functions: (1) determination of the Limiting Threshold Values (LTVs) at various wear levels (early, uniform, critical, and failure stages) and (2) determination of levels of speed and feed using the predicted failure modes and wear mechanisms as indicated in Figure 3.25.

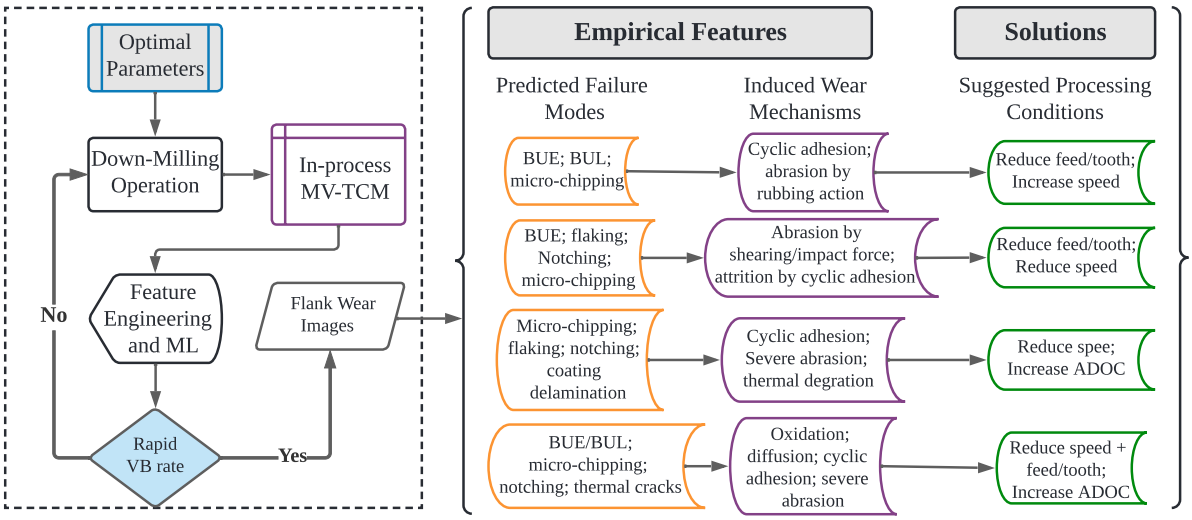

Figure 3.25: *A strategy used for in-process tool performance control and optimization*

The first decision was achieved after correlating the magnitudes of the flank wear features with the actual VB to determine their equivalence according to ISO-8688-1 face milling standard. Thus, features were divided into four distinct values, corresponding to $LTV_{VB=0.1mm}$ (early rapid wear), $LTV_{VB=0.2mm}$ (uniform wear), $LTV_{VB=0.3mm}$ (critical wear), and $LTV_{VB=0.5mm}$ (failure). The LTV equivalence were presented by equations 3.34.

$$LTV_{VB-level} = max[\phi(F_i), \alpha(Bh_{FW}), \gamma(Bh_{chipping}), \delta(Bw_{chipping})] \tag{3.34}$$

Where, ϕ, α, γ, and δ are coefficients that normalize the F_i, Bh_{FW}, $Bh_{chipping}$ and $Bw_{chipping}$ to standardize their influence in selecting the maximum threshold value for each flank wear level. Except for F_i and Bh_{FW}, which were consistent in the early and uniform wear stages, the $Bh_{chipping}$ and $Bw_{chipping}$ magnitudes normally evolved in the critical and failure regions. Therefore, threshold values of $Bh_{chipping}$ and $Bw_{chipping}$ were mostly utilized in the critical and failure regions, where the evolution of F_i and Bh_{FW} was noticed to fluctuate under uneven pixel distribution and complex flank wear morphology. This decision was made by considering that the critical and failure regions experienced the synergistic wear mechanisms, which exacerbated the rapid evolution of failure modes, such as BUE and chipping magnitudes. However, these failure modes also posed a terminal challenging of mutilating the pixel distribution and energy layers, affecting the consistency of the Bh_FW and F_i, thus, making them unreliable for detecting the LTV in the critical and failure regions. According to the experimental findings in Chapters 5 and 6, the $Bh_{chipping}$ and $Bw_{chipping}$ emerged in the critical and failure region due to the synergistic wear mechanisms at the end of tool life. As a result, the presence of chipping magnitudes in the early and uniform wear regions signified rapid VB rate, sub-optimal process parameters, and inefficient cutting mechanism.

The second decision was achieved by evaluating the failure modes and wear mechanisms, as shown in Figure 3.25. After detecting the dominant failure modes, they were used to reveal the causative wear mechanisms through inductive-reasoning, which was based on the experimental findings, SECO tools catalogue, and ISO-8688-1 face-milling standard. These predicted wear mechanisms revealed the sub-optimal process conditions, thus, prompting a change in speed and feed to improve the performance of the PVD-TiAlN/NbN coated carbide inserts during machining. Therefore, by regulating the speed and feed, the chipping magnitudes were controlled in the early cutting stage to minimize the wear rate. During this analysis, two techniques were applied: (1) one-time adjustment of speed and feed and (2) multi-stage adjustment of speed and feed. The former was achieved by changing the process parameters only once during the experiment, whereas the latter was achieved by adjusting the processing parameters at various VB stages to obtain the overall optimum condition that minimized the VB rate and improved tool life during face milling of Inconel 718. Algorithm 3 shows the inductive-reasoning model that enhanced YOLOv3-TWDM during MV-TCM.

Algorithm 3 In-process Predictive Control and Decision-making Algorithm

Inputs: multi-sectional SVD; YOLOv3-TWDM; Inductive Reasoning; Process Conditions
Outputs: Optimal speed and feed rate
Global Parameters:

1. $Initial\,process\,condition \leftarrow speed,\ feed\,rate$
2. $[LTV_{early}; LTV_{uniform}; LTV_{critical}; LTV_{failure}]$
3. $N \leftarrow Detected\,Failure\,Modes$

while $N \geq 0$ **do**
$[FlankWear,\ chipping,\ flaking,\ notching,\ BUE] \leftarrow YOLOv3 - TWDM$
$[Bh_{FW},\ Bh_{chipping},\ Bw_{chipping}] \leftarrow B - Box\,geometry$
$F_i \leftarrow multi - sectional\,SVD$
$LTV_{VB} \leftarrow [F_i,\ Bh_{FW},\ Bh_{chipping},\ Bw_{chipping}]$
if $LTV_{VB} \geq LTV_{early}$ **then**
$LTV_{early} \leftarrow max[\phi(F_i); \alpha(Bh_{FW}); \gamma(Bh_{chipping}); \delta(Bw_{chipping})]$
$Failure\,modes \leftarrow YOLOv3 - TWDM$ ▷ Early rapid wear
else if $LTV_{VB} \geq LTV_{uniform}$ **then**
$LTV_{uniform} \leftarrow max[\phi(F_i); \alpha(Bh_{FW}); \gamma(Bh_{chipping}); \delta(Bw_{chipping})]$
$Failure\,modes \leftarrow YOLOv3 - TWDM$ ▷ Steady wear
else if $LTV_{VB}) \geq LTV_{critical}$ **then**
$LTV_{critical} \leftarrow max[\phi(F_i); \alpha(Bh_{FW}); \gamma(Bh_{chipping}); \delta(Bw_{chipping})]$
$Failure\,modes \leftarrow YOLOv3 - TWDM$ ▷ critical wear conditions
else if $LTV_{VB}) \geq LTV_{failure}$ **then**
$LTV_{failure} \leftarrow max[\phi(F_i); \alpha(Bh_{FW}); \gamma(Bh_{chipping}); \delta(Bw_{chipping})]$
$Failure\,modes \leftarrow YOLOv3 - TWDM$ ▷ Failure region
$[Dominant\,wear\,mechanisms] \leftarrow [Inductive\,Reasoning]$
$[New\,speed,\ New\,feed\,rate] \leftarrow [Wear\,mechanisms]$

Just like the F_i and Bh_{FW}, which fluctuated in the critical and failure regions, the intermittent behaviour of $Bh_{chipping}$ and $Bw_{chipping}$ deemed it unreliable to detect the LTV_{VB} in the early and uniform wear regions. This is why all features were inherently significant when selecting the maximum LTV_{VB} at various flank wear levels. To achieve the second decision, the failure modes were categorically encoded [0, 0, 0, 0, 0] for [absence] and [1, 1, 1, 1, 1] for [presence]. To initiate the process, the experimentally determined optimal speed and feed were used at the beginning of the experiment. Finally, the techniques were validated by comparing the percentage change in tool life for the promising processing conditions, relative to the conventional and soft computing (GKRR) methods. The methodology of GKRR ML technique is presented in the proceeding section, whereas the convention method is described in section 3.1. It is also worth noting that the findings and scoring metrics of the GKRR (soft-computing technique) were used specifically to validate the proposed technique of in-process ML-based MV-TCM system as both techniques were successfully used to predict VB profile and design promising cutting conditions under limited dataset.

3.3.5 Gaussian Kernel Ridge Regression (GKRR) Model

The ML-based MV-TCM system was further validated by comparing it with the performance of the Gaussian kernel ridge regression (GKRR) model. The GKRR ML model developed in this research applied the radial based function to extrapolate VB and design optimal cutting condition during face milling of Inconel 718. The input features were cutting speed, feed rate, ADOC and in-process cutting length. The output feature was the progressive VB. The distance between feature vectors in GKRR model is described by Equation 3.35, whereas the loss function is described by 3.36.

$$k_{ij} = e^{-\gamma \|x_i - x_j\|^2} \tag{3.35}$$

$$Loss\ function = \|Y - K\beta\|_2^2 + \alpha\beta^T K\beta \tag{3.36}$$

Where γ is a hyper-parameter that represents the length scale between two given features, $x_i\, and\, x_j$, Y is the target feature, K is the Gaussian kernel, β is the coefficient, and α is the coefficient of L2-norm penalty used to penalize the fitting coefficients. The dataset used

in the study consisted of the measured VB data as well as the boundary condition data. The boundary condition data was introduced to catter for the anticipated VB behaviour, thereby forcing the ML model to perform better at the conditions where VB values were missing. These conditions specifically referred to the ones at zero process conditions. The total dataset was 870, including 267 experimentally determined and 603 boundary condition data. The hyper-parameters (α, γ) of the ML model were optimized using a genetic algorithm (GA) with a custom cost function taking the leave-out- (LO) group cross-validation (CV) average root-mean-square error (RMSE) as the scoring metric. A set of data with the same cutting speed, feed rate and ADOC was considered a group. In a given group, cutting length remained a variable. For instance, cutting speed = 80 m/min, feed rate = 0.07 mm/tooth, ADOC = 1 mm, and cutting length ranging from 400 to 1200 mm was one group. The model analysis and exploration were primarily performed with the MAterials Simulation Toolkit for Machine Learning (MAST-ML) [353], an open-source Python package with scikit-learn [354] library to automate ML workflows and model assessments. A 5-fold CV, and cross-plot analyses were carried out to assess the model. The 5-fold CV test was repeated 20 times in this work, and the CV RMSE was given as the average of the fold-average RMSE.

Chapter 4

Experimental Investigation of Tool Wear Evolution

The findings of the experiments demonstrate a comprehensive assessment of tool wear evolution during the face milling of Inconel 718. They yield a deeper comprehension of the diverse features that contribute to rapid flank wear rate. The empirical observation and identification of these features laid the foundation for the creation of machine learning algorithms that were used for the predictive control of flank wear evolution while utilizing the MV-TCM system. This chapter, therefore, encompasses the following aspects: the critical analysis of flank wear progression, failure modes evolution, tool wear mechanisms, chip morphology, and data synthesis by formulating the Diverse Feature Synthesis Vector (DFSV).

4.1 Flank Wear Progression

The progression of flank wear was investigated through the examination of the change in VB rate at different process parameters, as illustrated in Figure 4.1. The average VB profiles were plotted against the cutting length to determine the variations of VB rate at different cutting speeds, feed rates, and axial depth of cut. The cross-plots represented the mean VB relative to the cutting length for each cutting condition specified in Table 3.6.

It was observed that the cutting speed had a significant impact on the VB rate during face milling of Inconel 718 [18]. Figure 4.1a reveals that as the cutting speed increases, there

was rapid VB rate due to the rise in temperature, which exacerbated the thermally induced wear mechanisms, such as diffusion, oxidation, and adhesion. The highest speed of 80 m/min induced high cutting temperature, which led to a rapid tool degradation, creating an exponential VB profile and the shortest cutting length as compared to the lowest speed of 40 m/min. Additionally, the lowest speed increased the tool-workpiece contact time, enhancing coolant penetration to minimize heat and friction. At 60 m/min, the tools experienced a synergistic effect of both thermal and mechanical wear mechanisms due to moderate temperature, friction, and coolant penetration in the heat-concentrated zone.

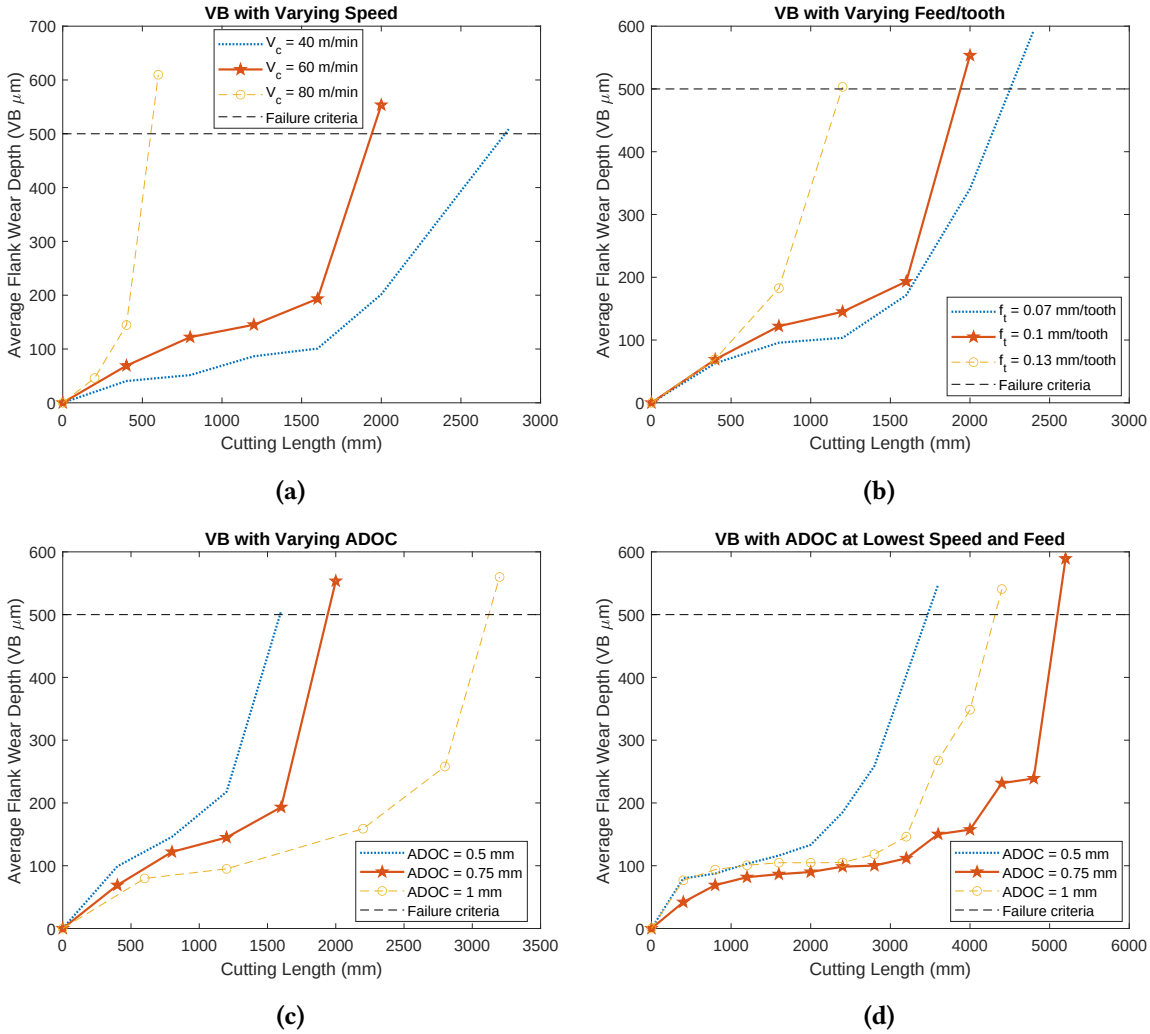

Figure 4.1: *Flank wear progression: (a) VB with speed at $f_t = 0.1mm/tooth$ and $ADOC = 0.75mm$ (b) VB with feed/tooth at $V = 60m/min$ and $ADOC = 0.75mm$ (c) VB with ADOC at $V = 60m/min$ and $f_t = 0.1mm/tooth$; and (d) VB with lowest speed and feed at $ADOC = 0.75mm$*

In addition, the VB progression was also significantly affected by the feed rate during machining. Figure 4.1b analyses the effect of feed rate on VB evolution. It was observed that

the rate of VB progression increased with the feed/tooth. From 0.07 to 0.13 mm/tooth, the chip thickness increased from 0.0647 to 0.120185 mm, resulting in large chip load, which required a higher force to shear the workpiece material. This caused high friction, which resulted in severe abrasion. In addition, the large chip load also increased adhesion wear mechanism, which exacerbated the BUE and BUL formation on the tool's cutting edge. The subsequent removal of BUE and BUL led to progressive chipping and coating delamination, thereby exposing the tool's substrate to more sub-surface deterioration and catastrophic failure. Under such conditions, tools experienced rapid VB rate as shown in Figure 4.1b. As a result, the VB profile at 0.13 mm/tooth was exponential as compared to 0.07 mm/tooth. The reduced chip load at the lowest feed rate minimized the friction and adhesion wear mechanism, leading to less BUE and BUL formation on the tool's cutting edge. Therefore, the lowest feed rate of 0.07 mm/tooth was a favourable condition that minimized adhesion wear mechanism of the PVD-TiAlN/NbN coated carbide inserts during face milling of Inconel 718.

Furthermore, the axial depth of cut (ADOC) had a substantial influence on the VB progression during face milling of Inconel 718. Figure 4.1c shows the effect of ADOC on VB progression. ADOC affected the shear force of the tool as it enters the precipitation-hardened surface layer of the workpiece material. At the medium speed and medium temperature, the moderate rate of precipitation hardening caused high shearing force, which attributed to severe friction and abrasion wear mechanism. As a result, at a small ADOC of 0.5 mm, the large percentage of the tool's cutting edge was subjected to the precipitation-hardened layer, causing localized chipping on the Depth of Cut (DOC) line. At 0.75 mm, the shearing force reduced as the larger portion of the cutting edge was subjected to the subjacent layer of the workpiece material, free from the precipitation hardening effect, thereby reducing the localized chipping on the DOC line. As the ADOC increased to 1 mm, progressive chipping was evident at a distant away from the DOC line, making the tools survive high impact forces even at the lowest and medium speed and feed rate. Although the ADOC of 1 mm attributed to a high shearing force due to the largest chip load, it minimized the localized chipping at DOC because the largest percentage of the effective cutting edge was used to machine the subjacent layers free from precipitation hardening effect.

In conclusion, the findings depicted in Figure 4.1d showed that an ADOC of 0.75 mm

exhibited the lowest rate of progressive VB at the medium speed and feed rates, while the highest ADOC of 1 mm was recommended for the lowest speed and feed rate. To further identify the most significant parameters that optimized VB evolution, a 2-way ANOVA was conducted in Minitab-19. Analysis : The P-values of the lowest magnitude in Table 4.1 indicate a robust correlation between the rate of VB and the cutting speed (V), feed (f_t), and cutting length (L). The lowest levels of VB were achieved at V = 40 m/min, f_t = 0.07 mm/tooth, and ADOC (a_p) = 0.75 mm. Furthermore, the synergistic effect of the cutting speed and feed rate was found to be more critical in affecting the VB rate during face milling of Inconel 718. On the other hand, it was also observed that the minimum VB rate occurred within the ADOC range of $0.75mm < a_p < 1mm$. Based on these findings, a 2-way ANOVA analysis summarized in Table 4.2 recommends the cutting speed of 42 m/min, feed rate of 0.08mm/tooth, and ADOC of 1 mm as the optimal process parameters that minimized VB rate during face milling of Inconel 718. However, to establish the most prominent levels of speed, feed, and ADOC, a subsequent qualitative study was conducted, correlating these process parameters with wear mechanism, failure modes, and chip morphology.

Table 4.1: Evaluation of 2-way ANOVA in Minitab-19

Source	DF	Adj SS	Adj MS	F-Value	P-Value
Linear					
V	1	1121151	1121151	70.52	0.000
f_t	1	233079	233079	14.66	0.000
a_p	1	14115	14115	0.89	0.348
L	1	1626330	1626330	102.30	0.000
2-Way Interaction					
$V \times f_t$	1	78258	78258	4.92	0.028
$V \times a_p$	1	46900	46900	2.95	0.088
$f_t \times a_p$	1	2567	2567	0.16	0.688
Error	126	2003141	15898		
Total	136	4117857			

Table 4.2: Possible desirable solutions that can optimize VB progression

Solution	V (m/min)	f_t (mm/tooth)	a_p (mm)	VB fit	Desirability (%)
1	43	0.086	1.0	38.107	0.9988
2	41	0.071	1.0	-117.916	0.9905
3	45	0.088	1.0	54.059	0.9868
4	42	0.071	0.5	-21.806	0.9799

4.2 Failure Modes Evolution

The evolution of failure modes was evaluated for all the process parameters. The results showed that all the three process parameters had a significant impact on the evolution of failure modes that contributed to the rapid VB rate during face milling of Inconel 718.

Cutting Speed (m/min): The evolution of failure modes at different speeds can be seen in Figure 4.2. At a speed of 40 m/min, the size of notching and macro-chipping was observed to increase with the BUE magnitude. Figure 4.2a portrays the BUE, which filled the chipped region and later detached as the cutting approached the failure region, as depicted in Figure 4.2b. The removal of BUE plucked away tool's aggregates with it. Consequently, the magnitude of notching and localized chipping became uncontrollable, as depicted in Figure 4.2c. With the exception of the rapid failure region, flaking of the coating layer was not predominantly observed, in comparison to the uniform flank wear and the presence of micro- or macro-chipping.

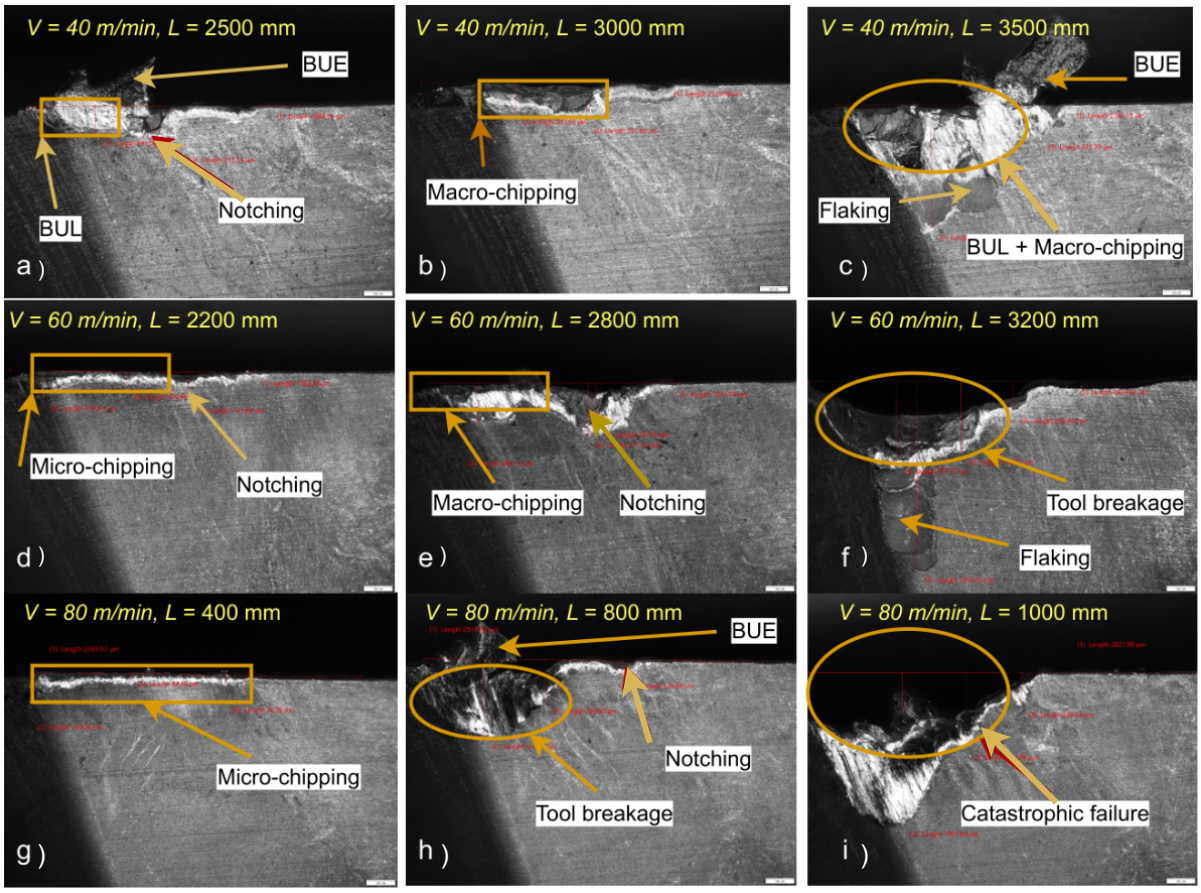

Figure 4.2: *Evolution of failure modes at various cutting speeds*

At 60 m/min, notching was increased due to the elevated cutting speed, which exacer-

bated the impact force as the cutting edge recurrently engaged the precipitation-hardened layer of the Inconel 718 workpiece. The elevated friction and failure of the hard Inconel 718 surface to absorb shock resulted in the high rate of mechanical wear mechanisms, such as severe abrasion [355]. The progression of localised chipping and notching was exacerbated by the cyclic formation of BUE, leading to failure modes such as macro-chipping and catastrophic failure, as illustrated in Figure 4.2f. The size of flaking was found to be greater at 60 m/min as compared to 40 m/min, which was attributed to the synergistic effect of elevated cutting speed and temperature, which exacerbated chemical wear by oxidation, diffusion of the tool's constituents, and absorption of the Co binder, thus, weakening the bonding strength between the tool's coating and the substrate [69]. At 80 m/min (Figure 4.2h), the premature occurrence of notching signified rapid tool's failure rate. This exacerbated the chipping magnitude, which instigated an exponential VB profile (Figure 4.1a). Nevertheless, the tool failure still took place after the VB exceeded the specified failure criteria (Figure 4.1a and 4.2i). However, the abrupt tool degradation was attributed to the increased work hardening effect of the Inconel 718 workpiece at the highest cutting speed and temperature, which exacerbated both the mechanically and thermally induced wear mechanisms, such as oxidation, diffusion, and adhesion [356]. Unlike tool fracture, which occurred after the tools reached the failure criteria, most tools at 80 m/min experienced catastrophic failure before exceeding the VB criteria.

Feed rate (mm/tooth): Figure 4.3 displays the evolution of failure modes at various feed rates. At 0.07 mm/tooth, micro-chipping and tip breakage were the predominant failure modes, which resulted in high vibration and chatter due to the high friction generated by rubbing action at the tool-workpiece contact zone. The high friction action was responsible for the severe abrasion and localized chipping along the DOC line, as illustrated in Figure 4.3c. Furthermore, the intense heat generated by the friction weakened the bonding strength between the tool's coating and the substrate [357], leading to severe flaking on the tool's cutting edge. At 0.1 mm/tooth, the dominant failure modes were notching and chipping. This wear phenomena were primarily attributed to the higher formation of BUE due to increased chip load at moderate feed/tooth. As the feed rate further increased to 0.13 mm/tooth, the magnitude of notching and chipping increased until they eventually converged, leading to sudden tool breakage, as seen in Figures 4.3e-f and 4.3h-i. This phenomenon was as well attributed to the largest chip

load at the highest feed/tooth, which resulted in the highest shear force accompanied by mechanical wear mechanisms,such as severe abrasion and attrition [358].

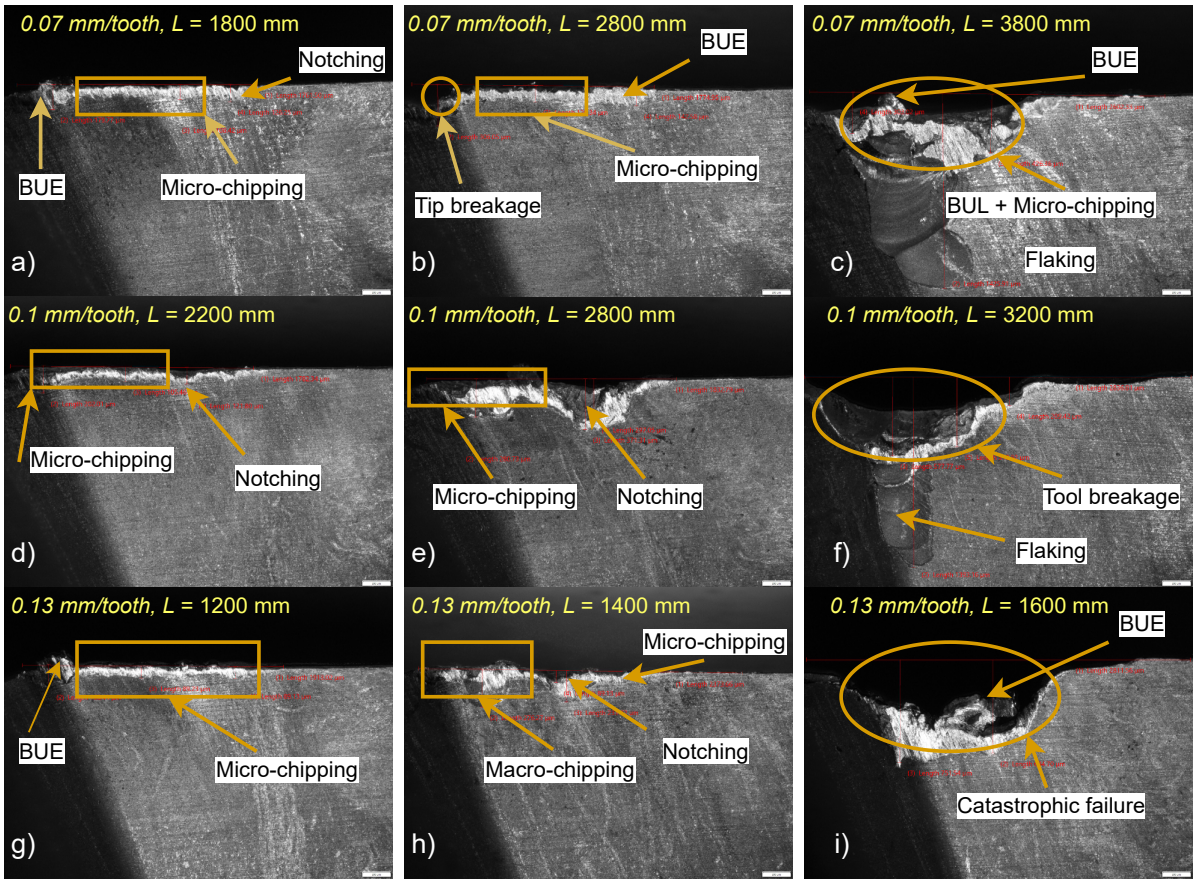

Figure 4.3: *Evolution of failure modes at various feed rate*

Axial Depth of Cut (ADOC–mm): The evolution of failure modes was also affected by the axial depth of cut (ADOC), as shown in Figure 4.4. In this research, the ADOC was studied at the lowest speed and feed to ensure a longer tool life span for thorough observation of wear mechanisms and failure modes. The axial depth of cut affects the tool-workpiece contact area. A larger ADOC had the largest contact area, which increased the chip load, shearing and friction force, leading to high heat generated on the tool's tip. This phenomenon was further exacerbated by the poor thermal conductivity of Inconel 718 chips, facilitating heat build-up on the tool's cutting edge during machining. Therefore, increase in ADOC from 0.5 to 1 mm caused a slightly higher cutting temperature on the tool's cutting edge, which potentially led to BUE and chipping formation on the tool's flank face (Figure 4.4 e, f, h, and i). In addition, the largest ADOC resulted in chatter, self-excited vibration, which caused severe chipping on the tool's flank face (Figure 4.4 h).

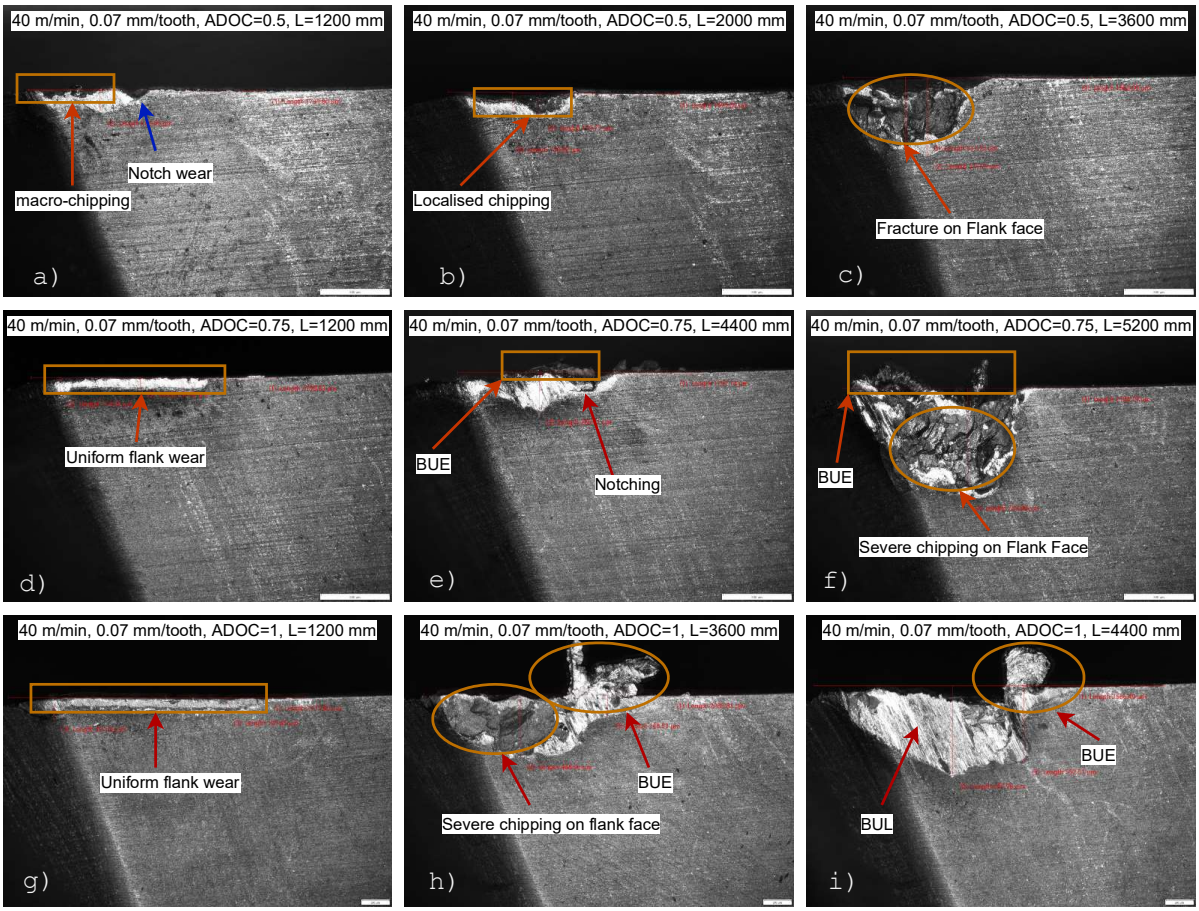

Figure 4.4: *Evolution of failure modes at various feed rate*

Furthermore, Inconel 718 experiences precipitation hardening on its surface layer, which greatly affected the chipping evolution on the tool's cutting edge, especially on the DOC line. As a result, a small depth of cut of 0.5 mm was utilized to cut a precipitation-hardened layer of Inconel 718 on the surface of the workpiece, leading to highest localized chipping and shortest tool life, as compared to 0.75 and 1 mm (Figure 4.4 c, f, and i). On the other hand, a large portion of effective cutting edge for the largest ADOC was used to cut the superjacent layers, free from precipitation-hardened effect, causing localized chipping, slightly away from DOC line. However, the synergistic impact of the large chip load, shearing force, friction, chatter, and low thermal conductivity exacerbated the abrasive wear mechanism, leading to rapid chipping formation and slightly shorter tool life, as compared to ADOC of 0.75 mm (Figure 4.4 f and i). According to the findings in this research, the ADOC larger than 0.75 mm was required to combat the effect of precipitation hardening, which exacerbated the chipping evolution, especially at the lowest cutting speed and feed rate.

4.3 Tool Wear Mechanisms

Based on the observations made during the experiment, the Axial Depth of Cut (ADOC) exhibited a small impact on abrasion and adhesion wear mechanisms, which ultimately resulting in localized chipping along the tool's cutting edge, as illustrated in Figure 4.4. The largest ADOC settings introduced high chip loads, shearing forces, and friction, thereby facilitating thermally and mechanically induced wear mechanisms, particularly small adhesion wear, as evident from the formation of BUE and BUL in Figure 4.4 h and i. While no conclusive evidence directly linking ADOC to abrasion wear mechanism was found, localized chipping was observed, potentially arising from the substantial high chip load and friction forces associated with severe abrasion of hard carbide particles. Additionally, there was no apparent influence of ADOC on oxidation and diffusion wear mechanisms. In summary, it was observed that ADOC had a minimal impact on the wear mechanisms, except for its substantial influence on the formation of localized chipping, which was attributed to factors such as chip load, chatter, high cutting force, and the precipitation hardening of the Inconel 718 surface. This observation aligns with the results of the ANOVA analysis. Therefore, the investigation of wear mechanisms was conducted at various cutting speeds and feeds, as they synergistically exerted a more significant impact on the evolution of wear mechanisms and failure modes, a notable observation that agreed with data reported by relevant literature in [18, 20, 322, 324].

4.3.1 Adhesion

The evolution of adhesion wear mechanism was affected by varying the cutting speed during face milling of Inconel 718. The adhesion wear was manifested in the forms of BUE (Built-Up Edge) and BUL (Built-Up Layer). At a cutting speed of 80 m/min, the BUL did not display a stacked profile, instead it adopted a single layer profile (Figure 4.6(a)). The temperature and stress levels were high at the highest cutting speed, thus, increasing the affinity of Inconel 718 to form BUE/BUL layers on the tool's cutting edge. However, the shortest tool-workpiece contact time attributed to high cutting speed under intense heat facilitated chip deformation, resulting in a soft layer welding onto the tool's cutting edge [359]. Despite the high stress concentration that promoted chip welding, the low shearing strength on the tools hindered

this process. Conversely, the BUL at the highest cutting speed experienced a robust work-hardening effect, which resulted in a hard and stable single layer profile along the DOC line [360].

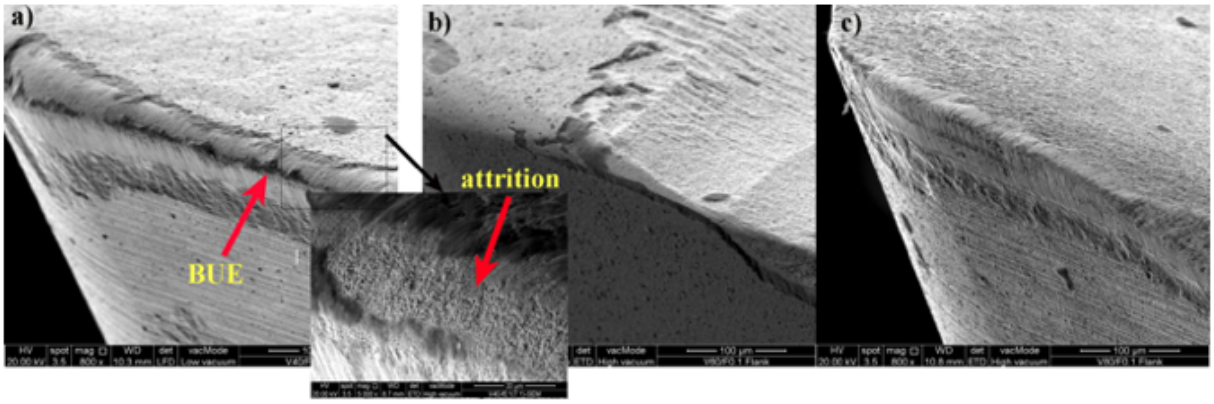

Figure 4.5: *BUE at different cutting speeds: (a) 40; (b) 60 and (c) 80 m/min*

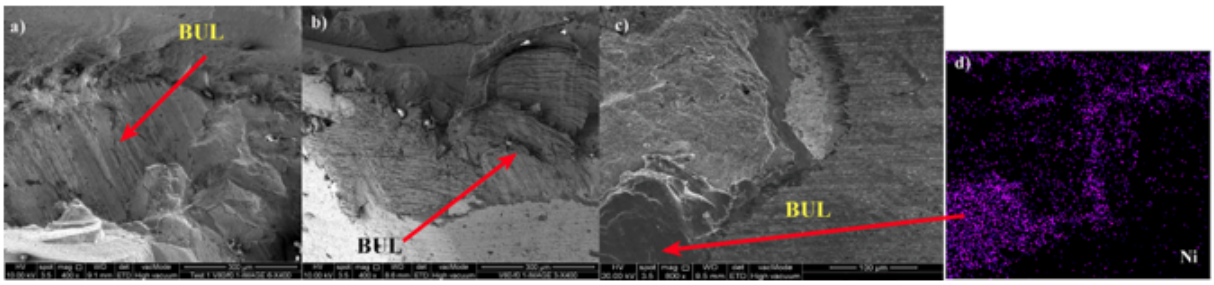

Figure 4.6: *BUL at different cutting speeds: (a) 40; (b) 60 and (c) 80 m/min*

At a medium speed of 60 m/min, the BUE magnitude was significantly reduced, as shown in Figure 4.5(b), but the density of BUL increased as shown in Figure 4.6(b). The stacked profile was attributed to the moderate temperature and stress concentration, which increased pressure on the ductile BUL layer. Besides, the formation of BUE/BUL also depended on the moderate tool-chip contact time during the cutting process [361]. The lowest speed had the longest tool-workpiece contact time. As a result, at the speed of 40 m/min, the Built-Up Edge (BUE) formation was significantly increased, as shown in Figure 4.5(a), whereas the Built-Up Layer (BUL) manifested a stacking pattern as shown in Figure 4.6(c). It was further observed that, despite the relatively low cutting temperatures and stresses at the lowest cutting speed, the longest tool-workpiece contact time was sufficient to elicit the formation of BUE/BUL layers on the tool's cutting edge. Conversely, the extent of attrition wear was found to be heavily influenced by high affinity of cyclic BUE formation [361]. This highlights that tools operating

at 40 m/min exhibited the most severe levels of attrition wear as compared to tools operating at 60 and 80 m/min, as shown in Figure 4.5(a).

Apart from the cutting speed, it was observed that the feed rate had a significant influence on the evolution of adhesion wear mechanism during face milling of Inconel 718. At the lowest feed rate of 0.07 mm/tooth, the BUE formation was less prevalent as compared to the highest feed of 0.13 mm/tooth. It was deduced from the comparison of Figures 4.7(a) and 4.7(b) that the substantial BUE formation was as a result of the increasing chip load/tooth at highest feed rate, which exacerbated the pressure welding of chips onto the surface of the tool [362]. Conversely, the BUL along the Depth of Cut (DOC) line displayed a higher density at the lowest feed/tooth.

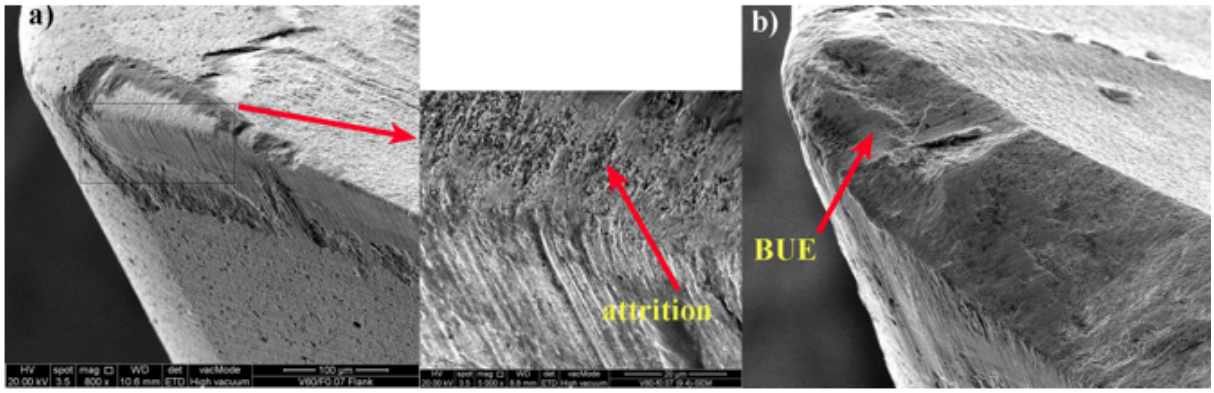

Figure 4.7: *BUE at different feed rates: (a) 0.07 and (b) 0.13 mm/tooth*

Upon comparison of Figures 4.8(a) and 4.8(b), it was observed that the BUL at a feed rate of 0.07 mm/tooth presented a stacking profile, whereas at 0.13 mm/tooth, it consisted of a solitary layer due to the substantial chip load. At the lowest feed/tooth, the rate of heat dissipation, leading to an accumulation of heat and high ductility of the BUL layer, thus, making subsequent layers piled up as they slid past each other. It can be observed from Figure 4.7(a) that the surface near the tip exhibited a severe loss in tool fragments, leading to a rough surface (attrition wear mechanism). However, there was no evidence of attrition wear at 0.13 mm/tooth due to the uncontrolled tool failure, which was ascribed to the highest chip load and shear force.

4.3.2 Abrasion

It was observed that the cutting speed had a significant impact on the abrasion wear mechanisms during face milling of Inconel 718 as it was highly dependent on both the sliding speed

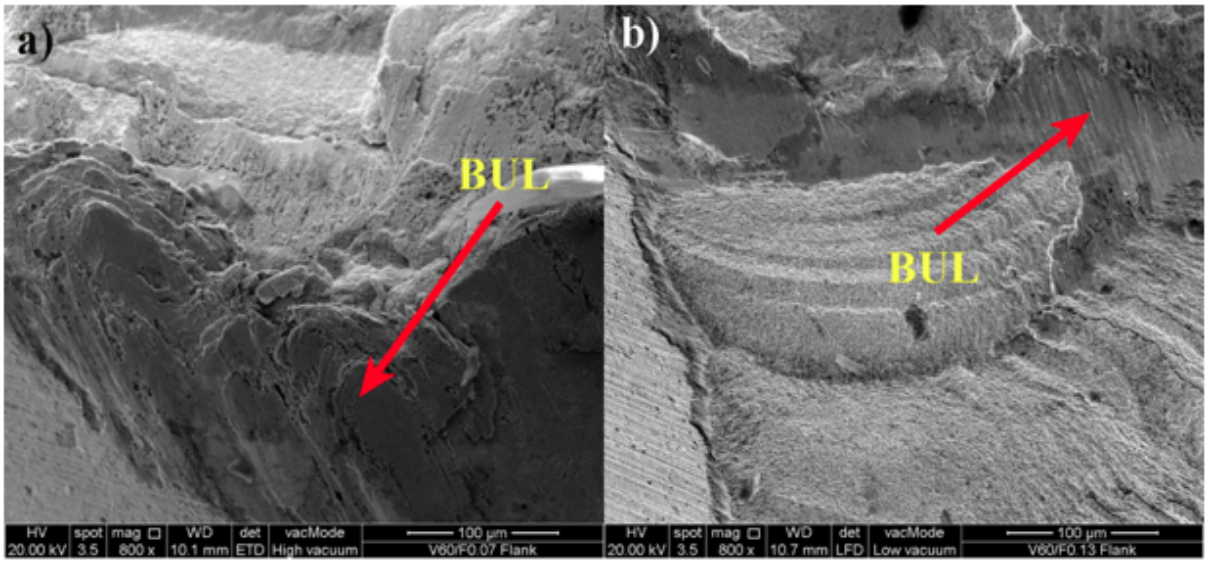

Figure 4.8: *BUL at different feed rates: (a) 0.07 and (b) 0.13 mm/tooth*

and cutting temperature. As the cutting speed increased, so did the cutting temperature and the rate of sliding action between the workpiece and the cutting edge of the tool. At 40 m/min (Figure 4.9(a)), the abrasion wear was attributed to the attrition, where tool fragments got removed by the progressive BUE or ploughed together with the chip flow, leading to abrasion on the rake or flank face, especially when the workpiece material became lodged between the workpiece and the cutting edge of the tool [64]. Abrasion wear was also caused by the hard carbide particles of the workpiece material after undergoing precipitation hardening at relatively high temperature. As the cutting speed increased to 60m/min (Figure 4.9(b)), the abrasion wear on the flank face displayed coarser contour lines along the direction of chip flow, which covered a considerable depth as compared to 40 m/min (Figure 4.9(a)).

The increased temperatures exacerbated the vulnerability of the Co-binder, causing the substrate to exhibit increased ductility and rendering it susceptible to being ploughed across a short distance by the Inconel 718 hard carbides. This abrasive action increased the free path, thus, exposing the Co-binder to further degradation such as chemical wear by oxidation [64]. On the other hand, the abrasion wear at 80 m/min (Figure 4.9c) can be characterized by the deformation of the BUE on the rake face (Figure 4.9c), as a result of the energetic sliding action of chips. This caused the deformation of both the BUE and BUL on the substrate [70]. Therefore, the presence of abrasive contours on the surface of the BUL at the DOC region, especially at the lowest speed of 40 m/min (Figure 4.9a) serves as empirical evidence for the

significance of the BUL/BUE acting as protective layers against abrasion on the tool's substrate. Therefore, a speed of 40 m/min was deemed optimal in mitigating the abrasive wear of the PVD-TiAlN/NbN coated carbide inserts during face milling of Inconel 718.

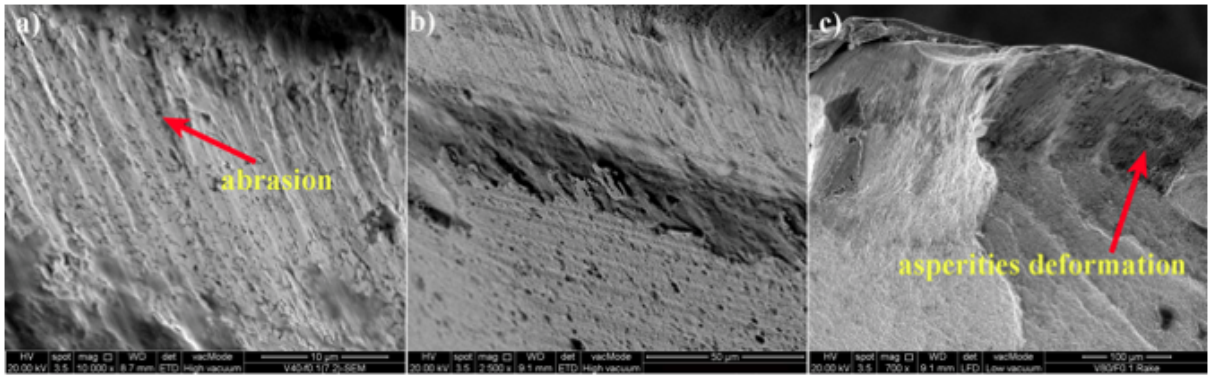

Figure 4.9: *Variation of abrasion wear with cutting speeds: (a) 40; (b) 60 and (c) 80 m/min*

Furthermore, the abrasion wear on the flank face was found to be comparatively insensitive to variations in feed rate, unlike the rake face, where the magnitude of abrasion wear was contingent upon the feed/tooth. As depicted in Figures 4.10a and 4.10b, it was established that a higher feed/tooth of 0.13 mm/tooth was accompanied by a more severe and widespread occurrence of abrasion wear, in comparison to 0.07 mm/tooth. This was attributed to the greater chip loads at the highest feed/tooth, which flowed smoothly across the rake face without experiencing substantial plastic deformation, thus, prolonging the duration and extent of tool-chip contact time and increasing the friction surface during machining. In contrast, the resilient chip thinning at the lowest feed/tooth had a tendency to bend away from the rake face, reducing the friction surface area and tool-chip contact time to mitigate the severe friction during machining.

4.3.3 Oxidation

As illustrated in Figure 4.11, the fluctuation of oxygen atoms on the flank face is proportional to the cutting speed. The flank face experienced an increase in oxidation as the cutting speed increased from 40 to 80 m/min. Nonetheless, a decrement in the atomic concentration of oxygen was observed at 80 m/min. Hence, the occurrence of chemical wear can be attributed to the high-temperature conditions at the shear zone, which caused a chemical reaction between the constituents of the tool and the atmospheric oxygen. In addition, it was also attributed

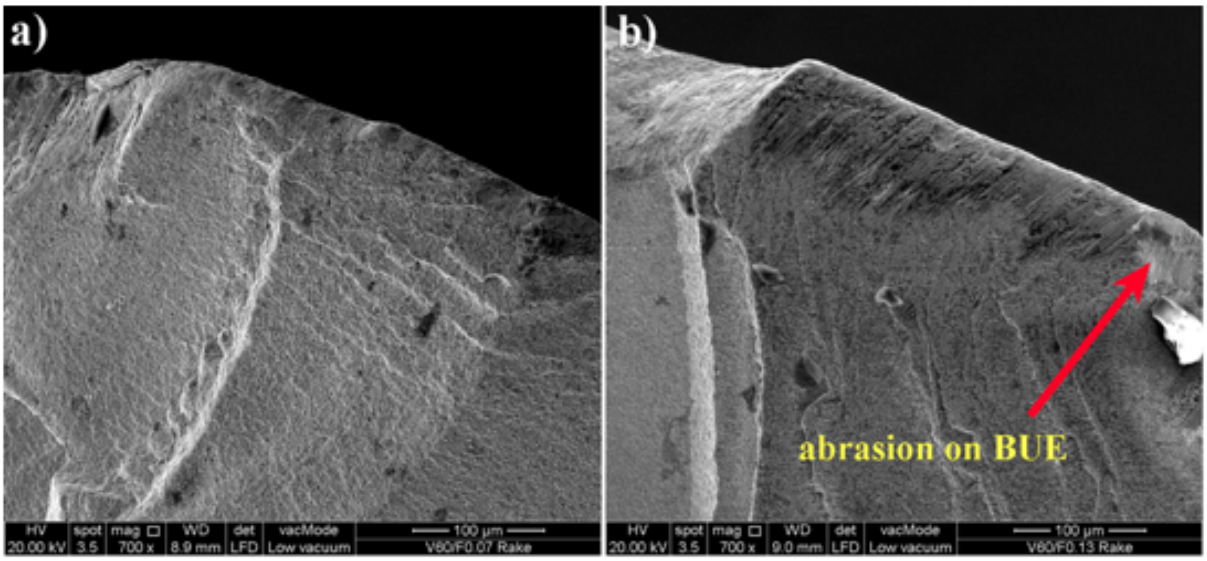

Figure 4.10: *Variation of abrasion wear with feed rates: (a) 0.07 and (b) 0.13 mm/tooth*

to the tool-workpiece contact time, which was the lowest at 80 m/min. The phenomenon of oxidation wear was a consequence of the ionization of free electrons at elevated cutting temperatures, which generated negatively charged oxygen atoms. These oxygen ions exhibited a high proclivity to diffuse into the tool and combine with positively charged Al, Ti, and Co ions.

The ensuing reaction between the tool constituents and the oxygen ions gave rise to the formation of oxides at the cutting edge of the tool [363]. The presence of free electrons at high cutting speed and temperature facilitated the oxide formation at the tool's cutting edge. Furthermore, the delamination of the coating layer due to dissolution of Co binder also exposed the tool's substrate to environmental oxygen, rendering it vulnerable to chemical degradation by oxidation (Figure 4.12a). The decline in the concentration of oxygen atoms in Figure 4.12b at the highest cutting speed was due to catastrophic failure, which eliminated the oxides on the surface of the tools. Additionally, the shifting of carbide grains in the substrate at high cutting speed exposed the Co-binder to atmospheric conditions, leading to the reaction of Co elements with oxygen to form Co_2O_3. This resulted in reduced Co concentration and hence the ductility of the tool, making it susceptible to further degradation and fracture [66].

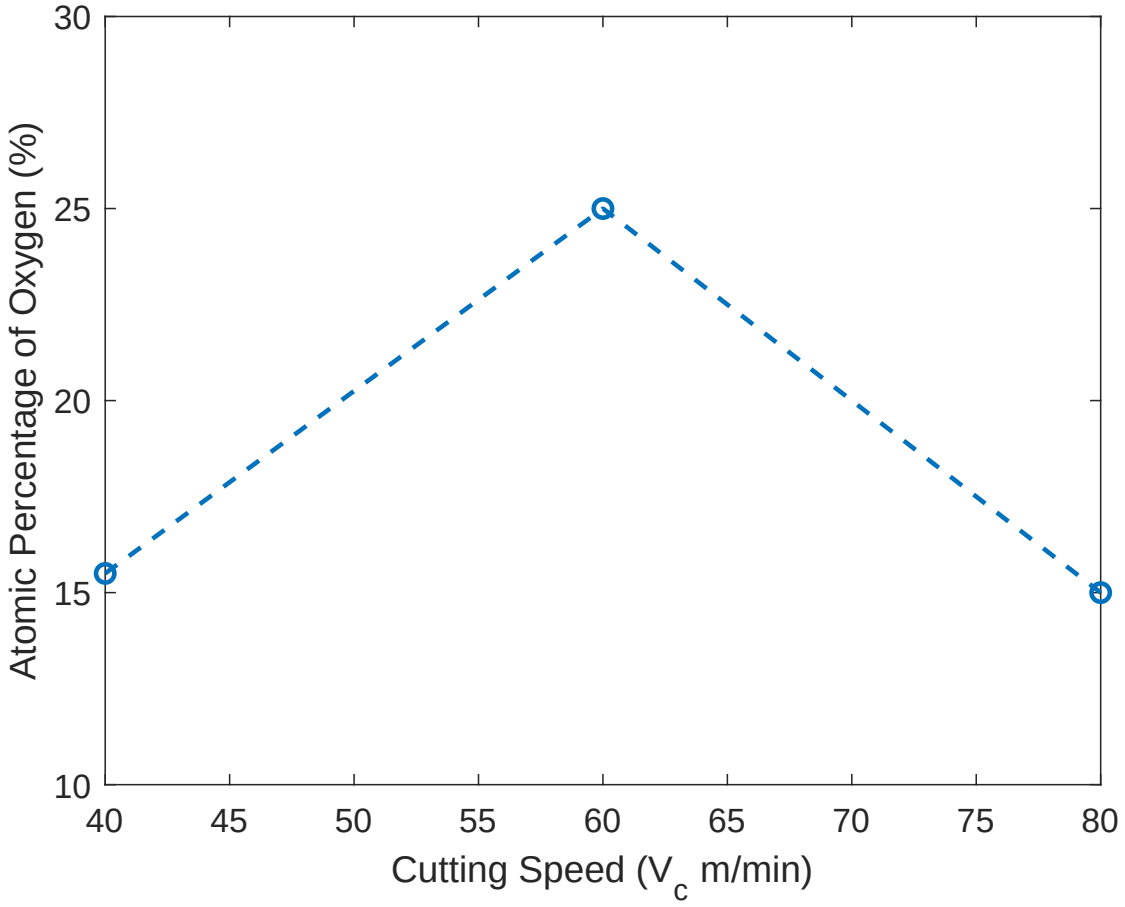

Figure 4.11: *Variation of oxygen concentration with cutting speed*

4.3.4 Diffusion

Unlike abrasion, adhesion, and oxidation, the analysis of diffusion wear was confined to the rake face. As depicted in Figure 4.13a, the results of the EDS analysis revealed no evidence of W elements on the surface of the chips at 40 or 60 m/min. Conversely, W elements were observed at 80 m/min. The absence of W elements at 40 or 60 m/min was due to the insufficient activation energy at low cutting temperature, given the case of larger atomic radius of W as compared to Co.

In contrast, the analysis showed an increasing trend of Co diffusion with the cutting speed. However, the low concentration of Co elements at 40 and 60 m/min was attributed to the low and medium cutting temperatures, which as well reduced the activation energy. The decline in the concentration of Co elements led to a decrease in the ductility of the tool, rendering it susceptible to various forms of mechanical wear mechanisms, such as cyclic ad-

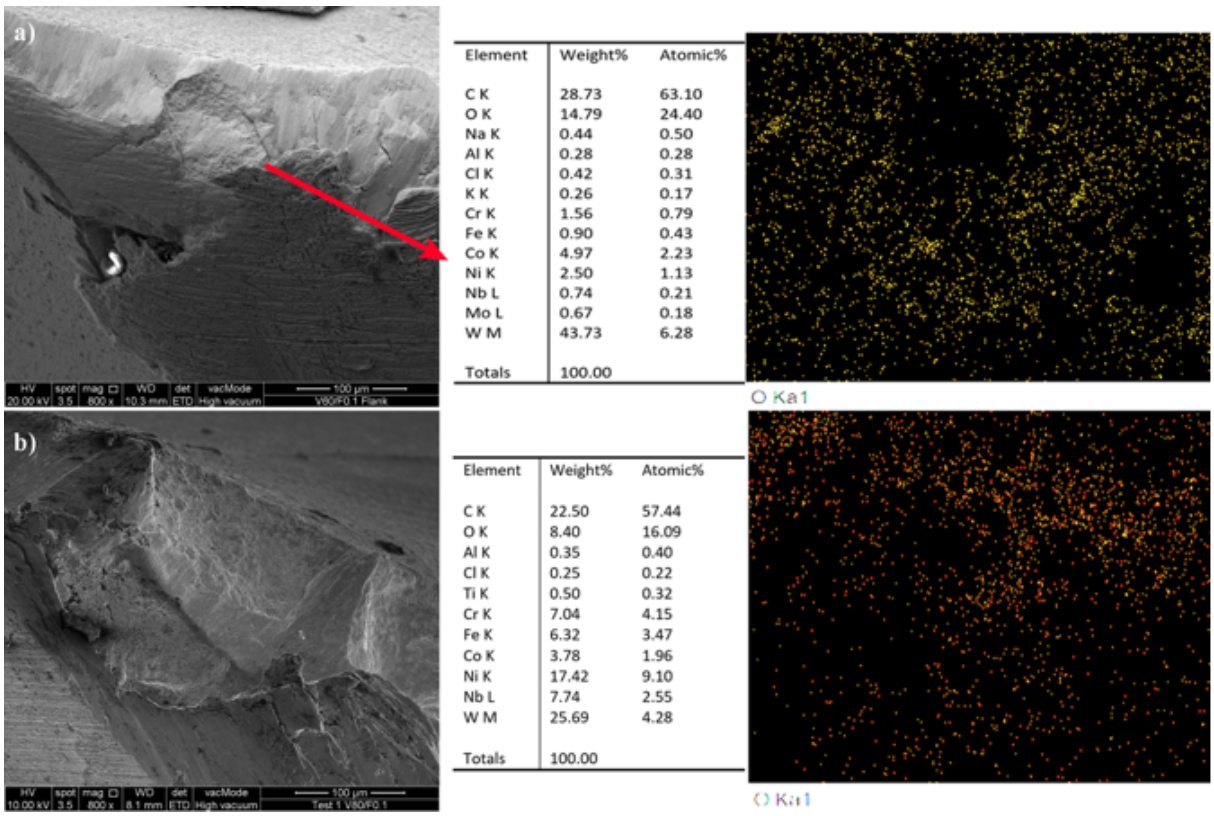

Figure 4.12: *EDX mapping of oxygen at (a) 60 and (b) 80 m/min*

hesion and severe abrasion that led to notching, chipping, flaking, and mechanical cracks. The presence of Inconel 718 elements displayed an upward trend with the cutting speed, with Ni exhibiting the highest diffusion rate, followed by Fe, Cr, and Mo, as indicated in Figure 4.13b. It was observed that the atomic radii of Ni and Mo significantly influenced the high diffusion rate, with Ni, having the smallest atomic radius, diffusing faster than Mo.

4.3.5 Thermal and Mechanical Cracks

It was reported that the thermal and mechanical cracks experienced by the PVD-coated carbide inserts were attributed to the synergistic impact of wear mechanisms during face milling of Inconel 718. [364]. Figure 4.15a illustrates thermal and mechanical cracks at 80 m/min, a consequence of the most exigent thermal strains and thermo-mechanical cycles. The former refers to the critical stresses generated in the tool material as a result of temperature fluctuations, whereas the latter refers to the periodic loading of the shear force during machining [364, 365].

It was observed that the rise in temperature caused thermal expansion on the surface of

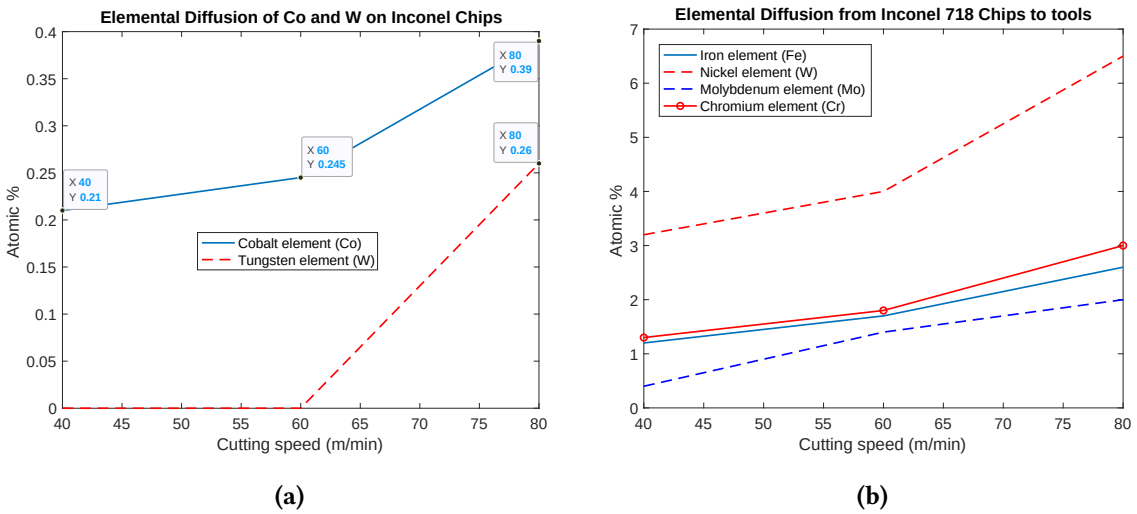

Figure 4.13: *Particle diffusion and adhesion: (a) from the tools to Inconel 718 chips and (b) from Inconel 718 chips to the tools*

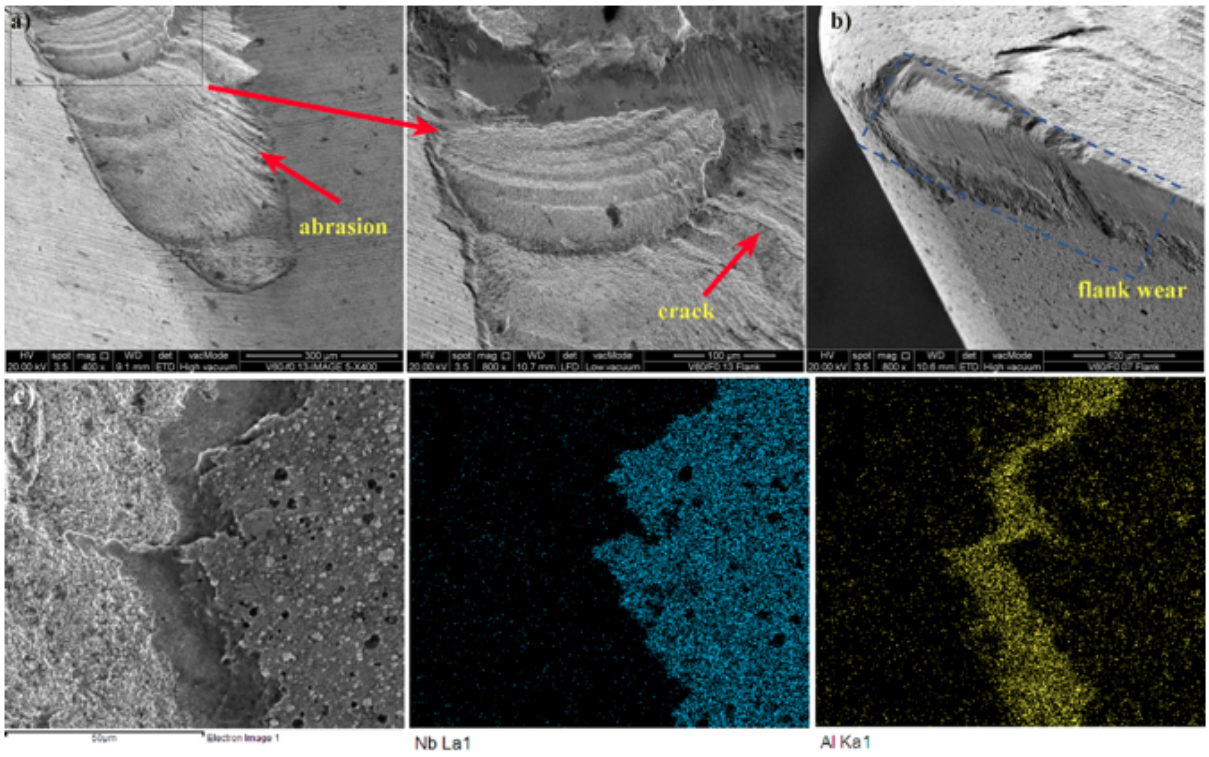

Figure 4.14: *Abrasive wear and cracks on the surface after flaking (b) EDX mapping showing delamination of coating layers (c) Abrasive wear led to widening of flank wear width*

the tool. Conversely, the subjacent layer experienced less thermal expansion as a result of low temperature, thereby incurring compressive stress, while the surface layer, with higher cutting temperature, incurred tensile stresses. Upon the tool's exit from the workpiece, the surface layer, which was immediately subjected to cutting fluid, cooled at a faster rate than the subjacent layer, resulting in an inversion of stresses. This recurring inversion caused by the

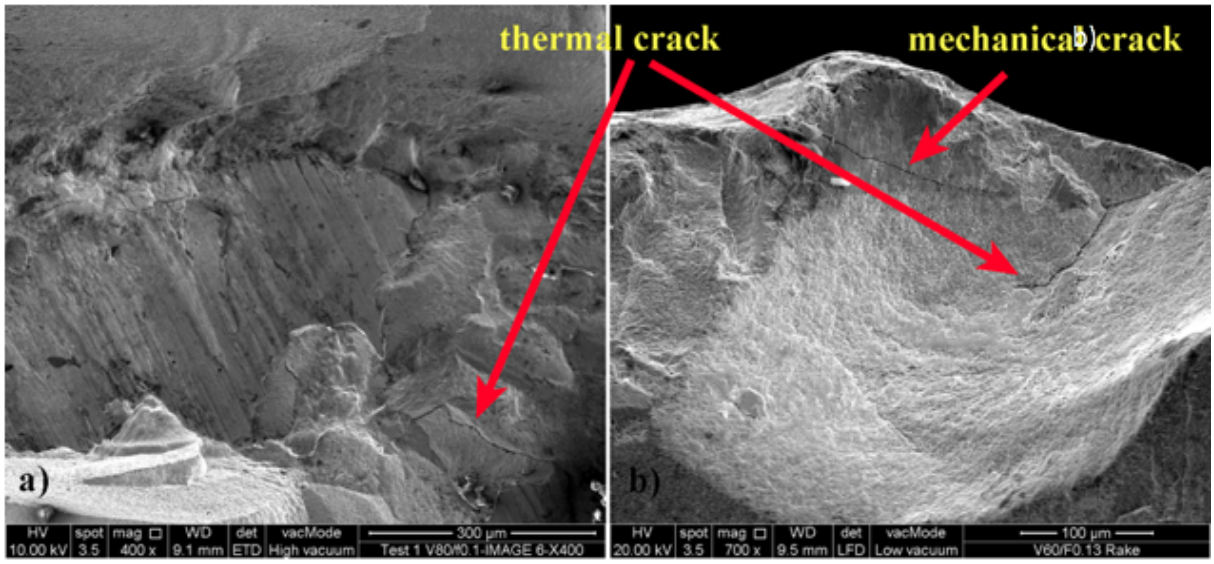

Figure 4.15: *Thermal crack (perpendicular to cutting edge) and mechanical cracks (parallel to cutting edge) at (a)V80 (b) F0.13 mm/tooth*

interrupted cutting produced thermal cracks at the cutting edge of the tool [64]. Besides the cutting speed that substantiate the thermal cracks, the feed rate also potentially exacerbated mechanical cracks due to increased chip load. Figure 4.15b demonstrates that the mechanical and thermal cracks were a result of high shear force required to deform a substantial chip load at the highest feed/tooth.

4.4 Chip Morphology

Studies have demonstrated that a substantial proportion, approximately 50%, of the tool's efficiency is wasted through energy loss due to chip deformation during the metal cutting process [366]. This affects the progression of failure modes and wear mechanisms during face milling of Inconel 718, which, in turn, impacts the tool's performance. To counteract this, an optimized face milling strategy should aim to produce fragmented chips to decrease the energy loss resulting from continuous chip deformation. The magnitude of chip deformation also influences the cutting force and the formation of built-up edges on the tool's cutting edge. Thus, tool efficiency can be improved by limiting the energy consumption required to plastically deform the chip load/tooth [366]. The energy consumption during plastic chip deformation is contingent on the fluctuating tool-workpiece contact temperature and deformations in proximity to the tool's cutting edge. The energy expenditure increases as a function of the fluctuating mechan-

ical properties of the workpiece material, with precipitation hardening of Inconel 718 being a primary contributor to high cutting force and energy consumption during machining [367]. In light of these considerations, the effect of feed rate on chip morphology was investigated at varying speeds with an entry angle of 102.6°, ADOC of 0.75 mm, and RDOC of 12.5 mm. The chip evolution is depicted in Figure 4.16.

The low thermal conductivity of Inconel 718 led to a reduced heat dissipation capacity in chips during machining operations [368]. Furthermore, elevated temperatures not only increased the material's ductility, but also accelerated the rate of precipitation hardening on the surface layers of the workpiece material. Additionally, the cooling aspect of the mineral oil-based cutting fluid reduced the rate of heat absorption into the chips. Hence, the complex chip deformation rate is dependent on the cooling rate, heat dissipation capacity, and the effect of precipitation hardening, rendering the evolution of chips during the cutting of Inconel 718 more convoluted compared to other ductile materials. At elevated cutting temperatures, one segment of the chip (the non-hardened layer) deforms at a faster rate than the precipitation hardened segment, resulting in a curved chip. Such chips pose a significant challenge during casting when analyzing the chip profile. Unlike most ductile materials, an increase in both speed and feed rate, as shown in Figure 4.16, leads to an increase in both chip thickness and segmentation angle [328].

It was observed that by reducing the speed to 40 m/min, there was decrease in the shearing force, leading to a less power consumption and a reduction in both deformation, total chip thickness, and segmentation angle (Figure 4.17a). This attributed to a low chip compression ratio (Figure 4.17d) and a high shearing plane angle. Consequently, the high chip compression ratio signified substantial strain rate in the shear plane [369]. Typically, the chip compression ratio was a direct indicator of plastic deformation, which decreased with both cutting speed and temperature. This was considered a desirable characteristic in ductile materials, as an increase in the chip compression ratio increased the cutting force, heat generation, and overall tool wear rate [370]. However, the synergistic effect of the plastic deformation and precipitation hardening in Inconel 718 negated this trend, such that at times, an increase in cutting speed led to an increase in both plastic deformation and the chip compression ratio.

Furthermore, it was reported that the flow stress in materials decreases as a result of

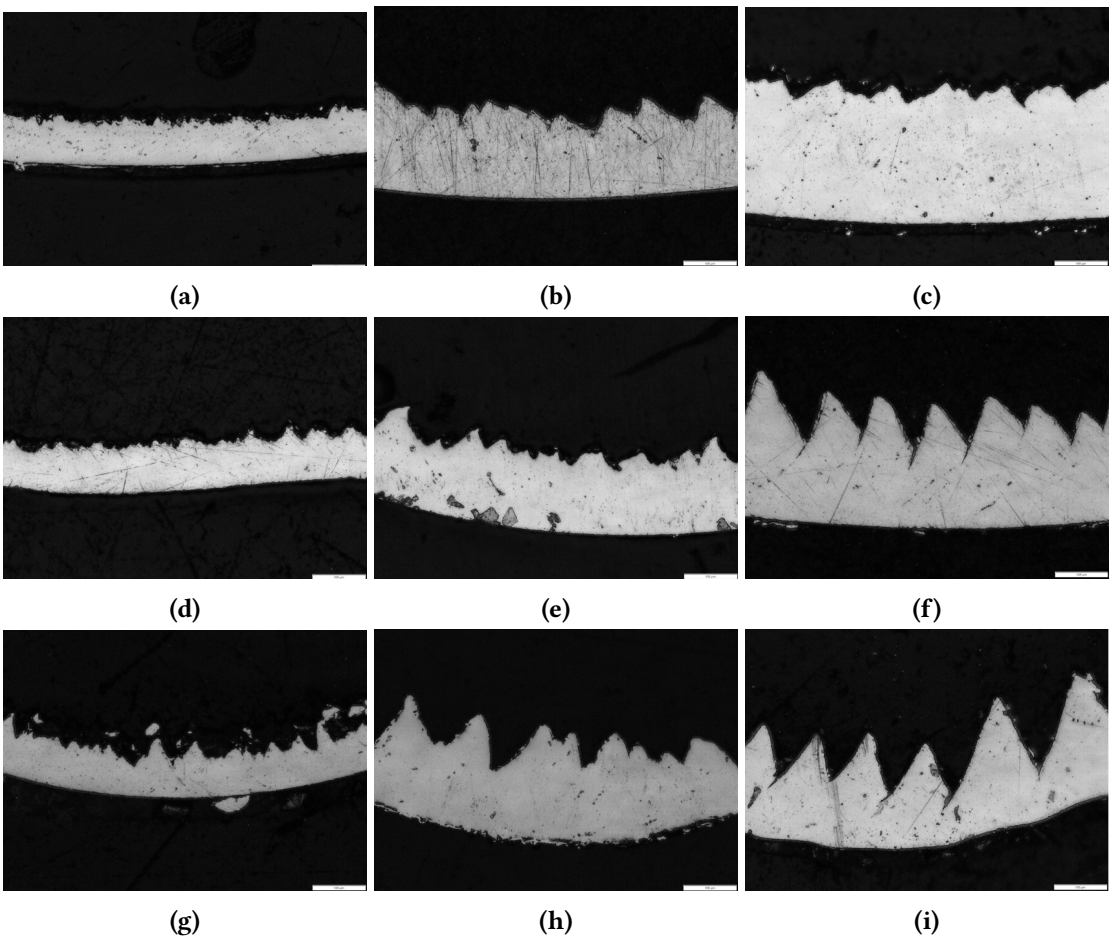

Figure 4.16: *Evolution of chip morphology at [V m/min, F mm/tooth]: (a) V40, F0.07; (b) 40, 0.1; (c) 40, 0.13; (d) 60, 0.07; (e) 60, 0.1; (f) 60, 0.13; (g) 80, 0.07; (h) 80, 0.1; and (i) 80 m/min, 0.13 mm/tooth*

adiabatic temperature fluctuations and shear band heating [371]. There is a direct correlation between the shear strain rate and cutting speed, and that the same held true for the precipitation hardening rate of Inconel 718, which led to the formation of narrow shear zones at elevated strain rates [372]. Furthermore, this study discovered that a shear plane angle was proportional to both the cutting speed and feed rate, as were the saw tooth height and pitch, as shown in Figures 4.17b and 4.17c. These chip profiles served as direct indicators of chip segmentation, and similar observation was made in [373]. The saw tooth height and pitch increased with both the cutting speed and feed/tooth, leading to a high degree of segmentation in Inconel 718 chips. As a result, it was noted that the minimum energy loss, and fine surface finish of Inconel 718 were favorable at a cutting speed of 80 m/min and feed of 0.13 mm/tooth, where the highest degree of chip segmentation was observed (Figure 4.16i). However, there was a trade-off between tool performance and surface finish or energy loss. At the lowest cutting speed and feed, tools experienced low rate of wear mechanisms, failure modes, and VB

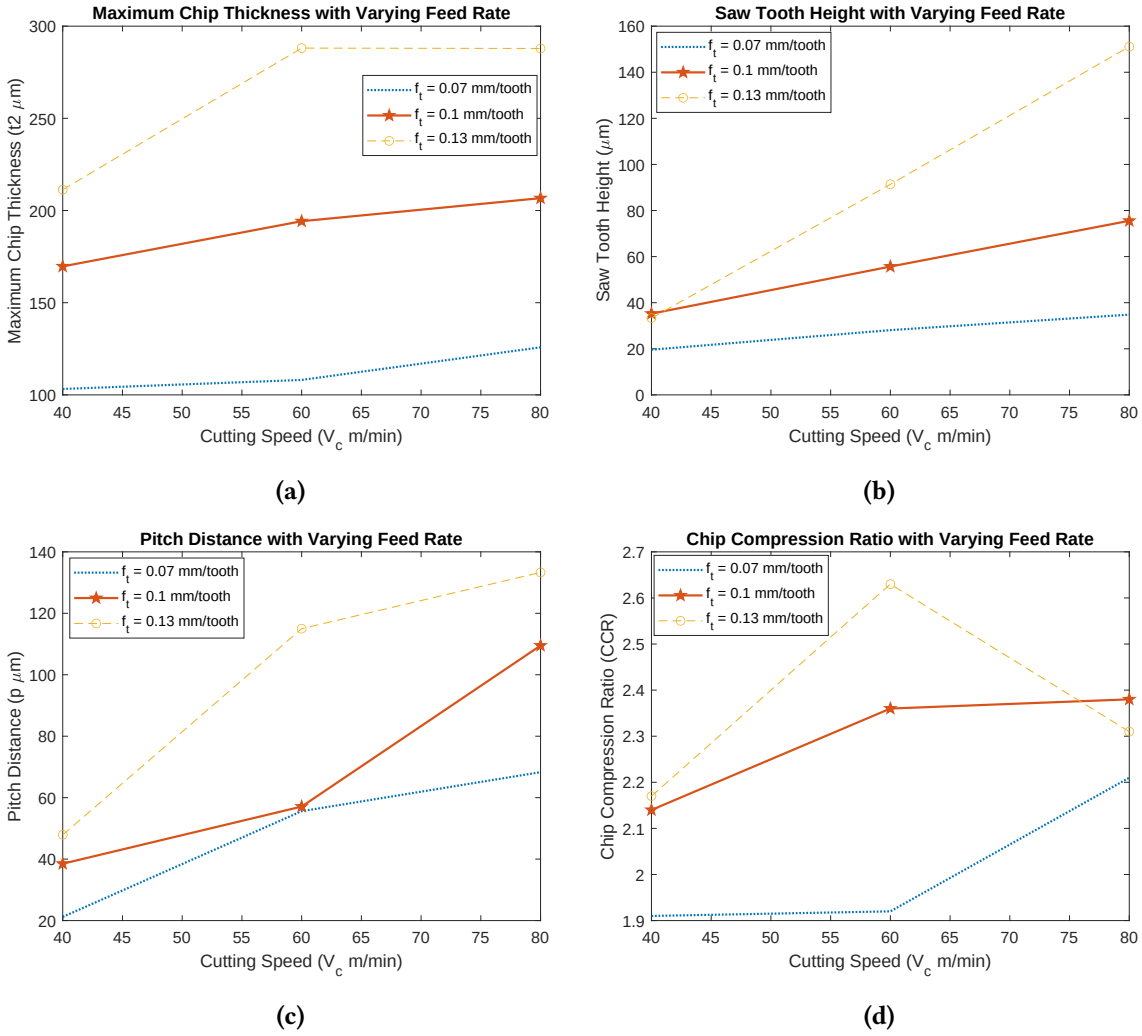

Figure 4.17: *Evolution of chip morphological properties: (a) total chip thickness; (b) saw tooth height; (c) pitch distance; and (d) chip compression ratio*

evolution, leading to a more stable and controlled cutting condition as compared to moderate and highest speed and feed/tooth. Despite the undesirable chip characteristics, the lowest cutting speed and feed still provided optimal tool performance and were selected as optimal conditions during face milling of Inconel 718.

4.5 Conclusion

The experimental findings underscored some remarkable relationships between the process parameters, wear mechanisms, failure modes, progressive VB, and chip morphology, which constitutes a substantial contribution to the qualitative and quantitative comprehension of the machinability of Inconel 718 using multi-layer PVD TiAlN/NbN cemented carbide inserts.

- At the lowest speed, tools failed due to localized chipping on the flank wear region due to severe adhesion and abrasion. At the highest feed, tools failed due to severe chipping, notching, and flaking by cyclic BUE formation, thermal cracks, and abrasion.
- At the lowest feed, tools failed by severe chipping due to long tool-workpiece contact time and accelerated Ti and Al oxidation, especially at the highest cutting speed.
- At the lowest depth of cut, the tools experienced localized chipping at the DOC line due to the precipitation-hardening of Inconel 718, which intensified the cutting force on the tool-workpiece contact zone. At the highest depth of cut, tools experienced a variety of failure modes, including BUE/BUL, notching, chipping, and catastrophic failure.

Therefore, according to ANOVA analysis, the lowest speed of 40 m/min, the lowest feed rate of 0.07 mm/tooth, and the highest ADOC of 1 mm were significant levels of process parameters that minimize VB rate during face milling of Inconel 718. On the other hand, the dominant failure modes during milling of Inconel 718 using TiAlN-NbN were uniform flank wear, BUE, chipping, flaking, and notching. At the highest speed, chips are highly segmented due to high cutting temperature, which facilitated plastic deformation.

Chapter 5

Tool Wear Prediction using the Developed ML Models

The feature engineering and ML models were trained and evaluated using a supervised learning process. The outcome of this chapter is a trained ML model that can be directly implemented in the MV-TCM system for in-process monitoring and control of tool wear evolution to enhance the performance of PVD-coated carbide inserts during face milling of Inconel 718. The salient features derived from the experimental findings above were harnessed to create a Diverse Feature Synthesis Strategy (DFSV) for training the ML models. In the filtered dataset, a total of 506 flank wear images were collected. The DFSV derived from the experimental data contained features, such as process parameters, the multi-sectional SVD feature (F_i) and nominal attributes (failure modes magnitudes), as shown in Table 5.1.

5.1 Training Performance of Feature Engineering and ML Models

In this section, the feature engineering techniques were trained to evaluate their effectiveness in detecting diverse features on the tools cutting edge, which best represent the complex wear morphology during face milling of Inconel 718. The objective was to achieve features that could enhance the robustness of ML models in predicting VB profile, as well as controlling the in-process evolution of wear mechanisms and failure modes during face milling of Inconel 718.

Table 5.1: The basic data matrix for training ML models

No.	V	f_t	a_p	L	F_i	UFW	CW	NW	FLW	BUE	VB(μm)	$Tmin$
1	40	0.07	0.5	400	F_i	1	0	0	0	0	109	4.7
	.	.	.	.	.	.	.	.	.	.	.	.
	.	.	.	.	.	.	.	.	.	.	.	.
	.	.	.	.	.	.	.	.	.	.	.	.
.	40	0.13	1	3600	F_q	0	1	0	0	1	564	28.9
	60	0.07	0.5	400	F_q	1	0	0	0	0	42	3.11
	.	.	.	.	.	.	.	.	.	.	.	.
.	.	.	.	.	.	.	.	.	.	.	.	.
	.	.	.	.	.	.	.	.	.	.	.	.
	60	0.13	1	1600	F_P	0	1	0	1	1	685	6.676
.	80	0.07	0.5	400	F_P	1	0	0	0	0	222	3.9
	.	.	.	.	.	.	.	.	.	.	.	.
	.	.	.	.	.	.	.	.	.	.	.	.
	.	.	.	.	.	.	.	.	.	.	.	.
506	80	0.13	1	800	F_N	0	1	0	1	1	566	2.5

Therefore, the diverse features had two principal functions: (1) prediction of VB progression to determine the actual time for tool replacement and (2) determining the underlying wear mechanisms to enhance the regulation of cutting parameters during in-process tool performance control. In the case of the former, the features were combined with the process parameters to formulate a Diverse Features Synthesis Vector (DFSV) that was used to predict VB progression during machining. Thus, the complete DFSV consisted of the process parameters, the magnitude of the wear region extracted by the multi-sectional SVD (F_i), and the failure modes extracted by the YOLOv3-TWDM. This was compared to the commonly used spatial binary features to ensure the system's robustness was contingent upon the features diversity and not the size of dataset. Whereas the later case focused on the predictive control of identifiable nominal features (wear mechanisms and failure modes) to prevent the rapid failure rate, as well as enhance tool life extension during machining.

5.1.1 Multi-sectional SVD Performance

The multi-sectional SVD proved to be efficient in mapping the progressive change in energy layers, thus predicting the evolution of the flank wear region on the tool's cutting edge. Figure 5.1a illustrates the truncated images at various SVD ranks. At rank 1, the image features were not distinct enough to accurately define the feature patterns and magnitude of the flank

wear region. However, at ranks 60 to 100, the clarity of the image features improved, thus distinguishing the key descriptors of the worn and unworn parts of the tool. At rank 60, the original images, randomly selected from various cutting inserts, were uniformly compressed by 93%, while preserving the pixel distribution and spatial resolution, as shown in Figure 5.1b. This yielded a structural similarity index (SSIM) of 96%. As a result, an optimal rank (q = 60) was selected for further analysis of features extraction.

Furthermore, the plots representing the average relative norm, root mean square error (RMSE), signal-to-noise ratio (SNR), and peak signal-to-noise ratio (PSNR) delineated a steady image transformation after rank 50, as depicted in Figures 5.1c, 5.1d, 5.1e, and 5.1f. This signifies the complete restoration of the prevalent flank wear features before extraction. Therefore, increasing the rank had no significant impact on the image quality and could reintroduce the noise component in the wear region. The magnitudes of F_i were used to track the gradual changes in the wear depth (similar the direction of the progressive VB) by computing the mathematical equivalence of the magnitude of energy layers across the tool's cutting edge. The F_i magnitude was further substantiated and validated as a descriptor of flank wear depth by correlating it with the cutting speed (V_c m/min), feed/tooth (f_t mm/tooth or f mm/min), and depth of cut (a_p mm), as well as actual VB obtained from the experiment (Figure 5.2).

Cutting Speed: The magnitudes of F_i were strongly correlated with the cutting speed, as shown in Figure 5.2a. At a cutting speed of 80 m/min, the high rate of friction and abrasion accelerated the progressive change in energy layers on the flank wear region, resulting in rapid evolution of the F_i magnitudes towards the critical and failure region. In this case, the F_i features failed to exhibit a steady wear phase. On the other hand, at cutting speeds of 40 and 60 m/min, the F_i magnitudes displayed a uniform wear region. At 40 m/min, this phenomenon was attributed to the low cutting temperature, which reduced friction and abrasion wear mechanisms, thereby maintaining the slow evolution of the energy layers in the uniform flank wear region. The trend of F_i progression at 40 m/min was consistent with the VB curve obtained in Chapter 4, indicating a high correlation between the F_i and VB progression for the lowest cutting condition. At 60 m/min, there was a rapid rate of F_i progression, which was attributed to intermittent evolution of energy layers in some sections of the flank wear region due to cyclic BUE and chipping formation. This eventually caused inconsistent and fluctuating

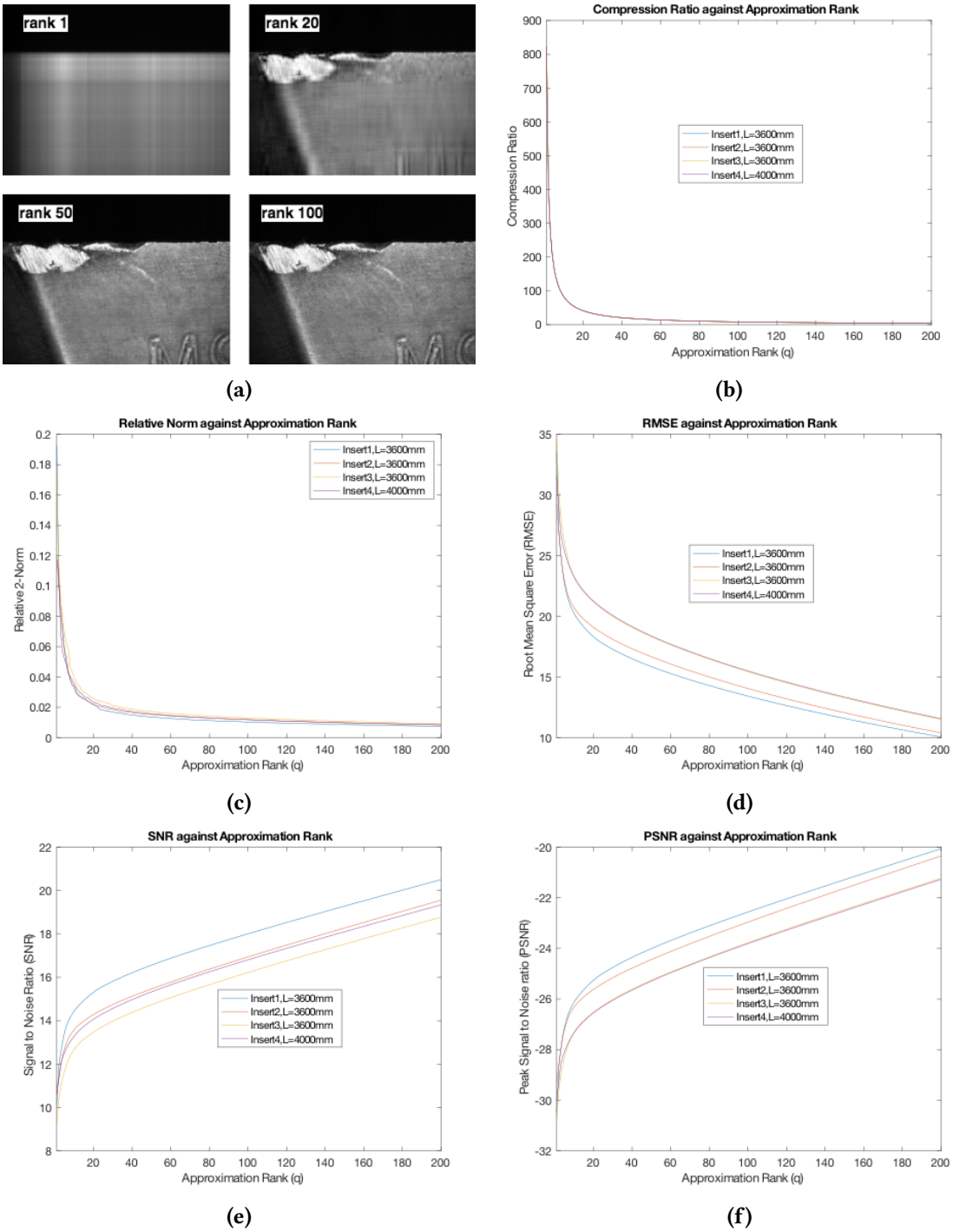

Figure 5.1: *Multi-sectional SVD performance for rank approximation: (a) variation of images at various ranks; (b) compression ratio; (c) Realtive-2 norm; (d) RMSE; (e) SNR; and (f) PSNR*

evolution of the F_i magnitudes, as compared to the lowest cutting speed of 40 m/min.

Feed/tooth: The magnitudes of F_i were correlated with the feed per tooth, as shown in Figure 5.2b. At 0.13 mm/tooth, the formation of Built-Up Edge (BUE) was attributed to the largest chip load, which led to progressive chipping under moderate abrasion at medium speed of 60 m/min. This caused the F_i magnitudes to fluctuate towards the critical and failure regions,

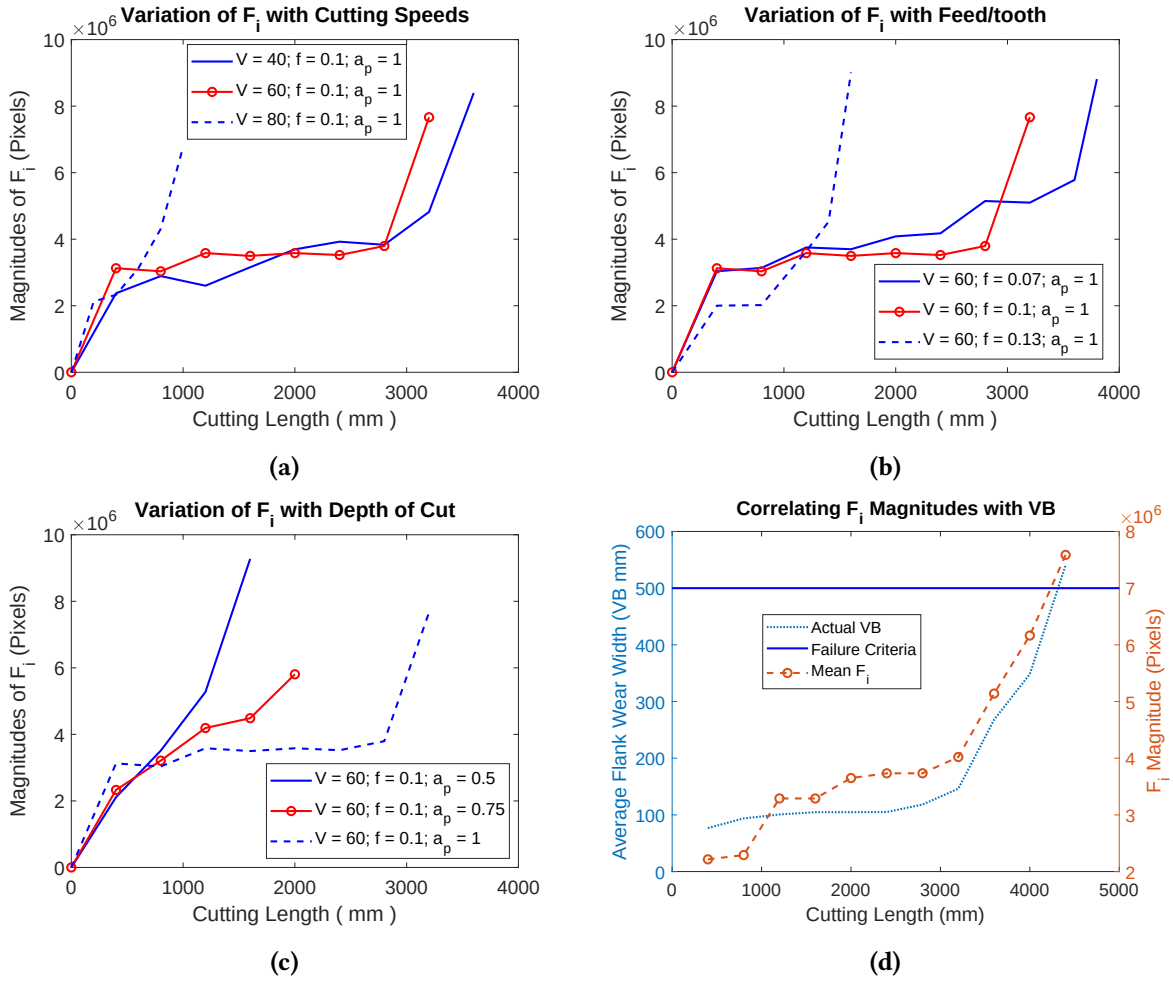

Figure 5.2: *The variation of F_i magnitudes with the: (a) cutting speed at $f_t = 0.1mm/tooth$ and $a_p = 0.75mm$; (b) feeds at $V_c = 60m/min$ and $a_p = 0.75mm$; (c) ADOC at $V_c = 60m/min$ and $f_t = 0.1mm/tooth$ and (d) optimum cutting condition ($V_c = 40m/min$, $f_t = 0.07mm/tooth$ and $a_p = 1mm$)*

resulting in an unpredictable trend that cannot accurately extrapolate the VB profile. At 0.1 mm/tooth, the F_i progressed uniformly, owing to the consistent evolution of the energy layers at the flank wear region due to less chipping and BUE formation at a medium speed. At the lowest feed rate of 0.07 mm/tooth, the reduced chip load resulted in a rubbing action between the tool and workpiece, generating more friction and abrasion wear mechanism, especially at a medium speed of 60 m/min. This led to higher energy layers as compared to 0.1 mm/tooth, which progressed consistently to generate the uniform evolution of F_i magnitude. Therefore, the progressive trend of F_i magnitudes at the lowest speed was in accordance with the VB curve obtained in Chapter 4, indicating high predictive efficiency for a uniform VB rate during face milling of Inconel 718.

Depth of cut: The magnitudes of F_i were correlated with the ADOC, as shown in Fig-

ure 5.2c. It was observed that at a 0.5 mm ADOC, F_i progressed exponentially due to severe chipping at the DOC line, as the effective cutting edge was used to remove the precipitation hardened layer of Inconel 718. At a 0.75 mm ADOC, the cutting edge still experienced progressive chipping at the DOC line, but at a slower rate as compared to 0.5 mm due to the reduced impact of the precipitation-hardening at slightly larger ADOC. At 1 mm, the magnitudes of F_i progressed uniformly due to lower chipping magnitudes as most of the cutting edge was used to cut the subjacent layers of the workpiece material, free from the precipitation hardening effect. Additionally, the synergistic effect of the largest ADOC, medium feed, and speed increased the chip load and friction, generating high-energy layers that stabilized the evolution of F_i magnitudes in the uniform wear stage. Therefore, the results of F_i evolution at the largest ADOC agreed with the VB profile found in Chapter 4.

Correlating F_i with VB: In summary, the evolution of the F_i magnitudes was a strong indicator of the cutting mechanism at the lowest speed of 40 m/min, lowest feed of 0.07 mm/tooth, and largest ADOC of 1 mm. Therefore, the mean values of F_i magnitudes were plotted together with the measured VB at this cutting condition, as shown in Figure 5.2d. The results showed that F_i values ranged between 2,000,000 and 7,000,000 for all flank wear levels, including early, uniform, critical, and failure stages, with 7,000,000 corresponding to the maximum failure criteria of $VB = 500\mu m$. This strong correlation was used to establish F_i thresholds at various flank wear levels. Although F_i magnitudes were strong predictors of the flank wear depth in the early and uniform wear region, where the wear mechanisms and failure modes were insignificant, the R^2 of 83% with the measured VB (*Appendix B.3*) demonstrated a 17% loss in the predictive efficiency. It was observed that due to the occurrence of uncontrolled failure modes, which exacerbated loss in energy layers for some sections of the flank wear region, especially in the critical and failure stages, F_i magnitudes could not fully capture the complex flank wear morphology. To address this issue, YOLOv3-TWDM was employed to detect the evolution of failure modes and identify the causative mechanisms of the loss in energy layers as nominal descriptors of the flank wear region. In this way, the features were diverse enough to represent the flank wear morphology during face milling of Inconel 718.

5.1.2 YOLOv3-TWDM for Failure Modes Detection

It was reported that the presence of different failure modes is a significant indicator of rapid VB rate and sub-optimal processing condition during face milling of Inconel 718. Therefore, apart from extracting the magnitude of the entire wear region (F_i) by the multi-sectional SVD, the YOLOv3-TWDM was utilized to detect the failure modes as nominal features that describe the complex wear morphology. Unlike the multi-sectional SVD, which was used directly to extract the features, the YOLOv3-TWDM, being a deep learning architecture, was first trained and tested. During training, the uniform flank wear was used to select the optimal hyper-parameters due to its extensive data, as it was the dominant failure mode at the early wear stages, as illustrated in Chapter 4. After several iterations, Figure 5.3 illustrates that the optimal values of the learning rate, number of epochs, warm-up period, penalty threshold, and mini-batch size were 0.0001, 80, 103, 0.5, and 16, respectively.

The warm-up period stabilized the gradients, while the penalty threshold ensured that the predicted bounding boxes that had less than 50% overlap with the ground truth were penalized. In this scenario, the mini-batch size of 16 provided better generalization during the learning process, as shown in Figure 5.3b, as compared to the commonly used value of 32 [374]. The small batch size signified the difficulty in distinguishing feature maps generated from different failure modes. Due to this complexity, a small number of flank wear images were needed at each iteration to effectively learn the feature maps during the training process. On the other hand, the overlap and confidence thresholds were set to 0.3, meaning that a confidence value less than 30% was rejected before applying non-maximum suppression to the predicted bounding boxes and classes. Additionally, any predicted bounding box whose area of intersection with the ground truth was less than 0.3 with a score less than 30% was also rejected. After manually labelling the test dataset to create the ground truths, the YOLOv3-TWDM model was further validated offline using test dataset. The performance of the model during testing is shown in the precision-recall (PR) curve (Figure 5.3d). The area under the curve (AUC) for flank wear, chipping, BUE, and flaking was 0.9102, 0.7253, 0.5154, and 0.3333, respectively. The highest AUC value of flank wear indicated the model's reliability in detecting uniform flank wear as the dominant failure mode of the PVD-TiAlN/NbN coated carbide inserts during down-milling of Inconel 718.

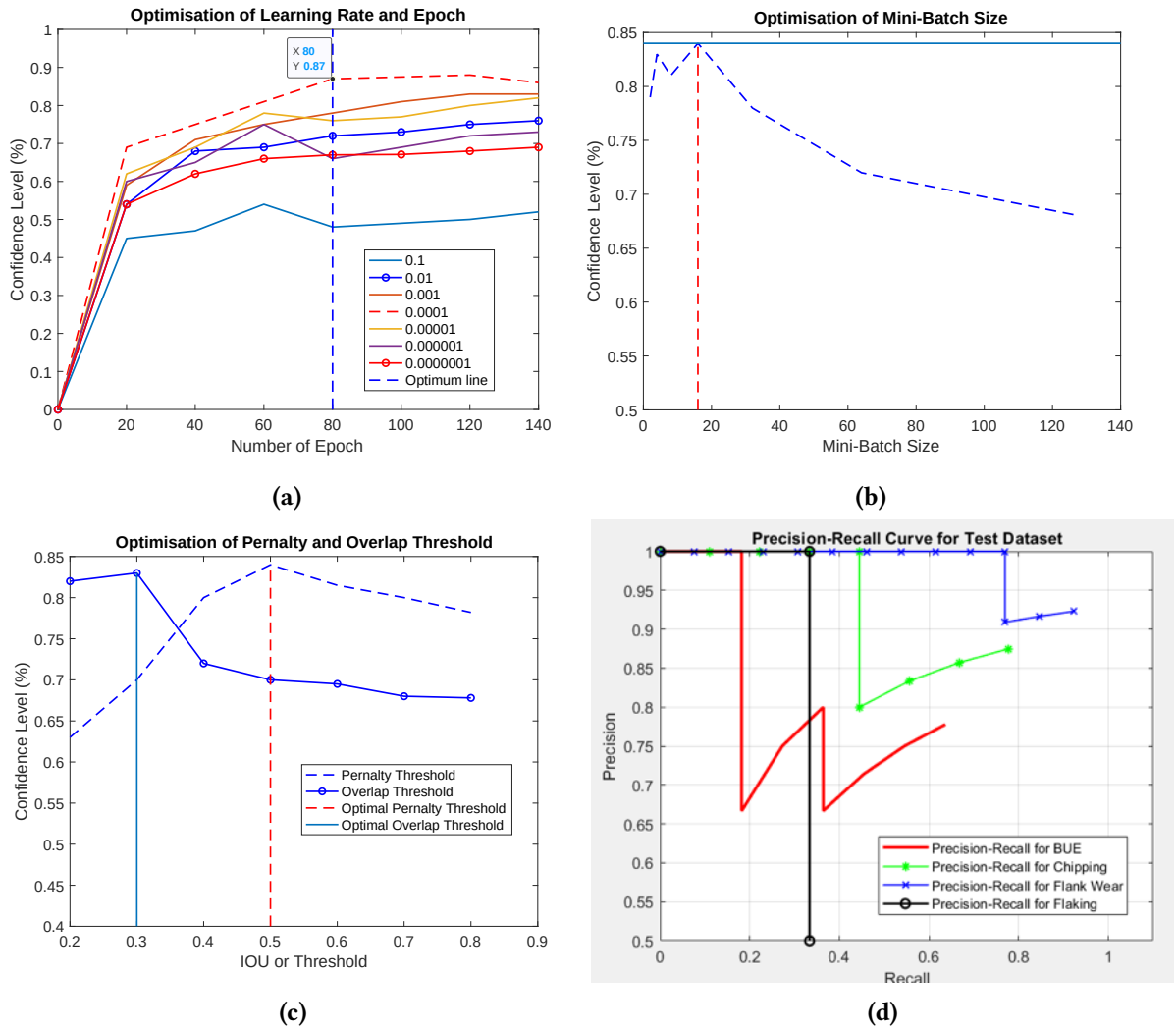

Figure 5.3: *Optimisation of YOLOv3 Hyper-parameters: (a) Learning rate; (b) batch-size; (c) Threshold; and (d) Precision-Recall curves of failure modes for test dataset*

This was attributed to the abrasion, as a prevalent wear mechanism in the early cutting stages at a speed of 40 m/min and a feed of 0.13 mm/tooth, thus, increasing the model's capability to learn more flank wear scenarios as compared to other failure modes during face milling of Inconel 718 [74]. It was also observed that approximately 40%, 35%, 13%, 8%, and 4% of the test data consisted of flank wear, chipping, BUE, flaking, and notching. Furthermore, the feature maps used to detect flank wear were consistent across all labels in the dataset, making it easier for YOLOv3-TWDM to learn and detect. The AUC value for uniform flank wear was followed by chipping, which was attributed to cyclic adhesion (due to intermittent BUE and BUL formation at a largest chip load of 0.13 mm/tooth) and severe abrasion (as the BUE and BUL gets plucked together with chip flow) in the critical and failure stages of the machining process. Therefore, chipping had relatively higher dataset as compared to BUE, notching

and flaking. However, research has shown that the feature maps for chipping and BUE were inconsistent in terms of their location, which reduced the detection rate and lowered their respective AUC values as compared to uniform flank wear.

Conversely, the low AUC for flaking and notching was attributed to a lack of sufficient labels in the dataset as these failure modes were mainly attributed to the synergistic effect of the diffusion, oxidation, attrition, and severe abrasion, which barely occurred at the lowest speed of 40 m/min due to the low cutting temperature on the tool-workpiece contact zone [2]. In addition, the surface texture of the flaking region was similar to that of the substrate and unworn part of the tools, making it difficult for YOLOv3-TWDM to detect it. Notching was mainly observed at medium, but not low speed and highest feed/tooth, due to high impact force, which attributed to a narrow gauge on the tool's entry into the precipitation-hardened Inconel 718 workpiece surface. In summary, YOLOv3-TWDM achieved the outstanding performance as a feature engineering technique, with a test overall accuracy and mAP of 87.86% and 0.4907, respectively, at an IoU threshold of 0.65. The model also demonstrated a rapid detection rate of 1.792 sec/image for the test dataset, indicating its reliability for in-process detection of failure modes during face milling of Inconel 718.

Therefore, YOLOv3-TWDM was found to be most effective in detecting flank wear, BUE, and chipping. As a result, the uniform flank wear depth (Bh_{FW}), chipping height ($Bh_{chipping}$) and chipping width ($Bw_{chipping}$) were detected and correlated with process parameters to show the evolution of failure modes during face milling of Inconel 718. Considering that the flank wear and chipping were dominant failure modes that significantly affected the performance of PVD-TiAlN/NbN coated carbide inserts, the Bh_{FW}, $Bh_{chipping}$, and $Bw_{chipping}$ were detected as dominant features that revealed sub-optimal tool performance. The features were correlated with process parameters to determine the optimal cutting condition. Additionally, by mapping the features with the actual VB values (serving as reference features) at the optimal condition, equivalent thresholds were established to determine the multi-stage failure criteria, where the speed and feed were regulated to control evolution of wear mechanisms and failure modes during face milling of Inconel 718.

Uniform Wear depth (Bh_{FW}): The correlation between the Bh_{FW} and the cutting speed is illustrated in Figure 5.4a. At 80 m/min, the rate of Bh_{FW} was high due to the synergistic

effect of both thermally and mechanically induced wear mechanisms at the highest cutting temperature (due to the high cutting speed) and largest chip load (due to medium feed/tooth and largest cutting depth). At this condition, the Bh_{FW} profile did not display any steady wear state until failure. The high cutting speed and temperature exacerbated abrasion, oxidation, and diffusion wear mechanisms, which attributed to thermal cracks and uncontrolled tool failure during machining. At moderate speed of 60 m/min, the wear rate was steady between 800 and 2800 mm cutting length due to the reduction in cutting temperature, which minimized the thermally induced wear mechanisms, such as cyclic adhesion, oxidation, thermal cracks, and severe abrasion. At the lowest speed of 40 m/min, a uniform Bh_{FW} rate occurred between 400 and 2400 mm cutting length, but with smaller magnitudes as compared to 60 m/min due to the lowest cutting temperature, which further reduced the chemical wear by oxidation, pitting corrosion, and adhesion, thus yielding the minimum flank wear rate and longest cutting length. Therefore, 40 m/min yielded the desirable performance by slowing down the rate of Bh_{FW} evolution in the early and uniform wear stages.

The influence of feed rate on the magnitudes of Bh_{FW} is shown in Figure 5.4b. The highest feed rate of 0.13 mm/tooth was observed to increase the rate of flank wear evolution due to the combined effect of high friction and shear force associated with the moderate temperature and largest chip load (at a depth of cut of 1 mm). This led to an increase in cyclic adhesion wear mechanism, which resulted in high BUE formation, thus exacerbating the evolution of Bh_{FW} magnitudes in the critical and failure regions. However, the evolution of Bh_{FW} magnitudes at 0.07 and 0.1 mm/tooth was comparable, even though the lowest feed rate showed the lowest Bh_{FW} rate in the break-in zone. The smallest chip load at 0.07 mm/tooth increased the friction and reduced the adhesion wear mechanism, which trivially minimized galling, severe abrasion, and cyclic adhesion in the critical and failure regions. The Bh_{FW} magnitudes also correlated with the depth of cut during face milling of Inconel 718. The highest depth of cut of 1 mm resulted in the lowest Bh_{FW} rate and the longest cutting length (Figure 5.4c). This was also attributed to the largest cutting depth of 1 mm, which allowed the largest part of the effective cutting edge to shear the subjacent layers of the workpiece material, free from precipitation hardening effect. This resulted in insignificant impact of localized chipping on the DOC line as compared to the lowest ADOC. Just like the feed rate of 0.07 mm/tooth, the ADOC of 1mm also

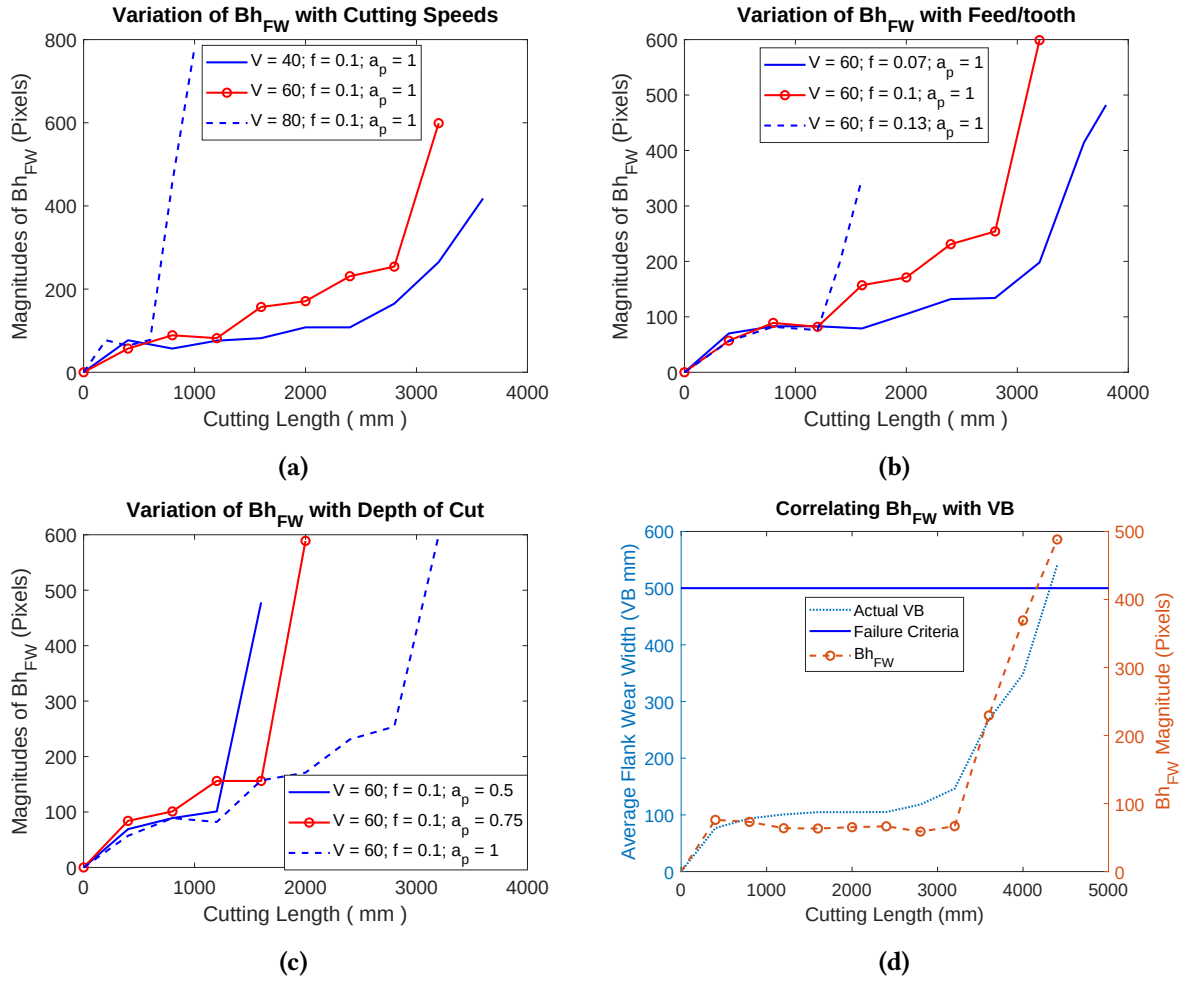

Figure 5.4: *The variation of Bh_{FW} magnitudes with the: (a) cutting speed at $f_t = 0.1mm/tooth$ and $a_p = 0.75mm$; (b) feeds at $V_c = 60m/min$ and $a_p = 0.75mm$; (c) ADOC at $V_c = 60m/min$ and $f_t = 0.1mm/tooth$ and (d) optimum cutting condition ($V_c = 40m/min$, $f_t = 0.07mm/tooth$ and $a_p = 1mm$)*

yielded the highest tool performance and the process parameters was found to be consistent with the findings in Chapter 4.

In summary, the evolution of Bh_{FW} was consistent with the magnitudes of F_i as both delineated the depth of the entire wear region. Optimal results were achieved at a speed of 40 m/min, feed of 0.07 mm/tooth, and ADOC of 1 mm. Figure 5.4d shows that the limiting threshold value of Bh_{FW} corresponding to the maximum failure criterion ($VB = 500\mu m$) was 430 pixels, which deviated only 14% from the ISO-8688-1 designated value. This small deviation suggests that the Bh_{FW} magnitude extracted by the YOLOv3-TWDM can be used to determine the failure criteria and actual time for tool replacement during face milling of Inconel 718. However, ISO-8688-1 specifies other failure modes, such as chipping width, which were analyzed as well to determine the limiting thresholds that corresponded to the maximum

VB criterion during face milling operation. Unlike previous studies that mainly focused on VB and chipping width ($Bw_{chipping}$) as the main indicators of tool life, this study also considered the chipping depth ($Bh_{chipping}$) to show the progressive change in chipping area, as one of the dominant features that can determine the extent of wear severity on the tool's cutting edge. This decision was arrived at by considering the chipping width ($Bw_{chipping}$) was always affected by the ADOC value. It was observed that if a small ADOC less than $280\mu m$ is applied, the maximum effective cutting length of the tool insert is $400\mu m$, which means $Bw_{chipping} = 400\mu m$ cannot used as a failure criterion. Contrary, the chipping depth ($Bh_{chipping}$) progressed with the flank wear depth (VB), without considering changes in the axial depth of cut during machining, making it more reliable as compared to the chipping width designated by the ISO-8688-1 face milling standard.

Chipping depth ($Bh_{chipping}$): Figure 5.5 illustrates the rate of $Bh_{chipping}$ under different cutting conditions. Contrary to the trend observed at a depth of cut in Figure 5.5c, the progressive change in $Bh_{chipping}$ was consistent for both cutting speed and feed rate, as demonstrated in Figures 5.5a, 5.5b, and 5.5c. A steady $Bh_{chipping}$ rate was observed at a speed of 40 m/min from 800 to 3000 mm cutting length due to the reduced impact of thermally induced wear mechanisms at the lowest cutting temperature. The rapid $Bh_{chipping}$ rate after 3000 mm was attributed to the synergistic effect of cyclic adhesion and abrasion in the critical and failure regions. At a speed of 80 m/min, the $Bh_{chipping}$ curve accelerated linearly due to the highest cutting temperature, which exacerbated the thermally induced wear mechanisms, such as oxidation, pitting corrosion, thermal cracks, and coating delamination. In addition, the high rate of precipitation hardening at the highest cutting temperature exacerbated high shear force, leading to severe abrasion and high chipping magnitudes on the tool's cutting edge [375].

The $Bh_{chipping}$ also correlated with the feed/tooth during face milling of Inconel 718 (Figure 5.5b). At a feed rate of 0.13 mm/tooth, the synergistic effect of the largest chip load, high friction, and shear stress exacerbated the cyclic adhesion and severe abrasion, which plastically deformed the tool's cutting edge, leading to a rapid $Bh_{chipping}$ rate, especially under the precipitation hardening effect of the workpiece's surface layer. At the lowest feed rate of 0.07 mm/tooth, the progressive evolution of $Bh_{chipping}$ magnitudes only occurred in the critical and failure region, above 3000 mm cutting length, due to the small chip load, which

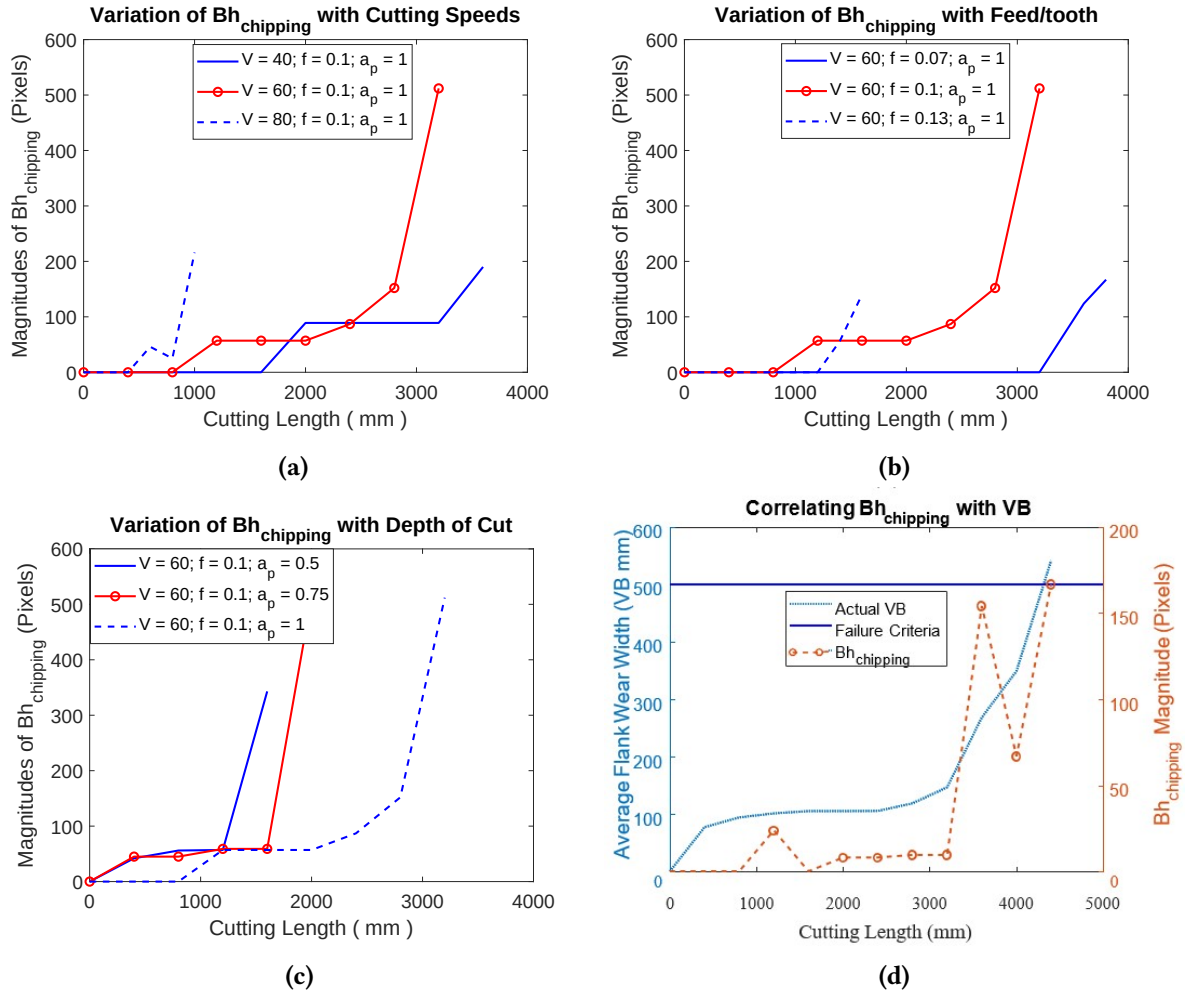

Figure 5.5: *The variation of $Bh_{chipping}$ with the: (a) cutting speed at $f_t = 0.1mm/tooth$ and $a_p = 0.75mm$; (b) feeds at $V_c = 60m/min$ and $a_p = 0.75mm$; (c) ADOC at $V_c = 60m/min$ and $f_t = 0.1mm/tooth$ and (d) optimum cutting condition ($V_c = 40m/min$, $f_t = 0.07mm/tooth$ and $a_p = 1mm$)*

trivially reduced the shearing stress and plastic deformation during the early and uniform cutting stages. Furthermore, the $Bh_{chipping}$ correlated with the axial depth of cut (Figure 5.5c). At the lowest depth of cut, there was rapid $Bh_{chipping}$ rate at the DOC region as the entire effective cutting edge was utilized to cut the precipitation-hardened layer of Inconel 718 workpiece surface. Whereas, at the largest ADOC, there was slow rate of $Bh_{chipping}$ progression due to the reduced impact of precipitation hardening as more that 50% of the effective cutting edge was utilized to cut the subjacent layers of the workpiece material, free from the precipitation-hardened effect. This was attributed to the moderate temperature, chip load, friction, shear stress, and plastic deformation at the medium speed and feed/tooth. Therefore, the evolution of the $Bh_{chipping}$ was optimally reduced at a speed of 40 m/min, feed of 0.07 mm/tooth, and 1 mm ADOC.

In summary, the progressive change in chipping magnitudes was utilized to select the thresholds by plotting the $Bh_{chipping}$ values against the measured VB profile, as shown in Figure 5.5d. The results showed that there was negligible impact of $Bh_{chipping}$ magnitudes in the early and uniform wear regions, which was attributed to minimum thermal and mechanical wear mechanisms at the lowest speed and feed/tooth due to low cutting temperature and reduced chip load [2]. However, as the cutting progressed towards the critical and failure regions, the $Bh_{chipping}$ magnitudes emerged due to synergistic impact of the cyclic adhesion and severe abrasion wear mechanisms. Therefore, the maximum threshold of $Bh_{chipping}$, corresponding to VB = 500 µm, was found to be 170 pixels. Being the proposed feature in this study, the percentage deviation of $Bh_{chipping}$ was not computed as there was no designated value in ISO-8688-1 face-milling standard for this measurement. However, the $Bh_{chipping}$ had a recommended value, and it was evaluated in the proceeding section, in addition to the $Bh_{chipping}$.

Chipping width ($Bw_{chipping}$): The magnitude of the chipping width ($Bw_{chipping}$) followed a similar trend to that of $Bw_{chipping}$ at the highest speed and feed/tooth as shown in Figure 5.6a and 5.6b. However, at the lowest speed and medium feed/tooth, the $Bw_{chipping}$ significantly decreased at the end of tool life due to the large chip load at the highest ADOC. Similarly, the $Bw_{chipping}$ magnitude significantly decreased at 0.5 mm ADOC due to BUE formation at medium the speed and feed rate. At a medium ADOC, the $Bw_{chipping}$ remained constant between 400 and 1200 mm cutting length due to the medium cutting temperature, chip load, friction and abrasion at the medium speed and feed/tooth. However, as cutting progressed, the magnitude of $Bw_{chipping}$ increased linearly due to progressive chipping attributed to the severe abrasion towards the failure region. At a medium ADOC, the $Bw_{chipping}$ remained constant between 400 and 1200 mm cutting length due to the medium cutting temperature, chip load, and plastic deformation (Figure 5.6c).

With subsequent passes, the magnitude of $Bw_{chipping}$ increased linearly due to progressive chipping attributed to the severe abrasion towards the critical and failure stages. At the highest ADOC, the magnitude of $Bw_{chipping}$ remained constant between 1000 and 2000 mm cutting length. However, the notching width kept on increasing and later transformed into localized chipping, thus exacerbating the magnitudes of $Bw_{chipping}$ during machining. Furthermore, the synergistic impact of the lowest speed, feed/tooth, and the largest ADOC re-

vealed that $Bw_{chipping}$ progression had a higher correlation with the measured VB during face milling of Inconel 718 (Figure 5.6d). It was observed that at this condition, tools failed by localized chipping, which progressively changed along the effective cutting edge, leading to an increase in $Bw_{chipping}$ magnitudes. Nevertheless, this condition also yielded the lowest failure rate, thus, attributing 40 m/min, 0.07 mm/tooth, and 1 mm as optimal process parameters that reduced the rate of $Bw_{chipping}$ evolution during machining. The maximum threshold of $Bw_{chipping}$ at this optimal condition, equivalent to VB of 500 µm, was 420 pixels, exhibiting a minimum deviation of 5% from the actual chipping width of 400 µm.

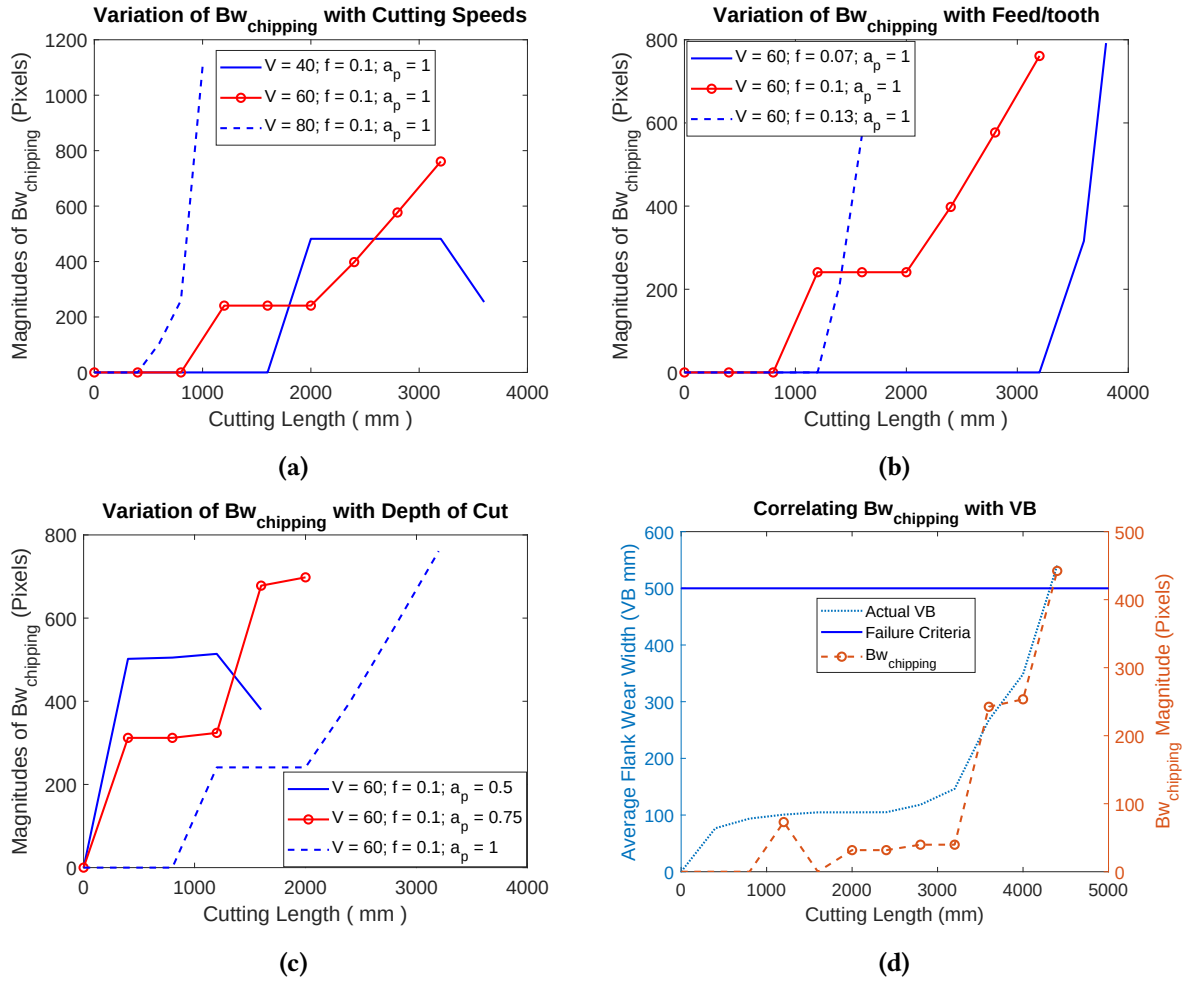

Figure 5.6: *The variation of $Bw_{chipping}$ with the: (a) cutting speed at $f_t = 0.1mm/tooth$ and $a_p = 0.75mm$; (b) feeds at $V_c = 60m/min$ and $a_p = 0.75mm$; (c) ADOC at $V_c = 60m/min$ and $f_t = 0.1mm/tooth$ and (d) optimum cutting condition ($V_c = 40m/min$, $f_t = 0.07mm/tooth$ and $a_p = 1mm$)*

From the above analysis, it was observed that the processing condition of the lowest speed of 40 m/min, feed of 0.07mm/tooth, and ADOC of 1 mm minimized the evolution of F_i, Bh_{FW}, $Bh_{chipping}$ and $Bw_{chipping}$ during face milling of Inconel 718. Consequently, these parameters

were considered as the optimum cutting conditions, which were also consistent with the experimental findings in Chapter 4. However, to assess their synergistic effect on the wear rate in the early, uniform, critical, and failure regions, another experiment was conducted wherein the optimal speed and feed/tooth, obtained from the contour plots established by the GKRR model in [6], were tweaked. It was during this experiment that the informed decisions of the inductive-reasoning algorithm were used to adjust the speed and feed at different levels of wear progression. However, at this point, the 400 mm incremental cutting length was not observed to eliminate the unnecessary delays and machine downtime during in-process MV-TCM application. Instead, the failure modes and wear mechanisms were observed at 4 wear stages, where solutions were implemented to reduce the rapid wear rate during machining. Therefore, Table 5.2 was derived from Figures 5.2d, 5.4d, 5.5d, and 5.6d to delineate the significant Limiting thresholds of these features for determining the multi-stage failure criteria during machining.

Table 5.2: Features threshold values for determining the failure criteria

Levels	VB (μm)	F_i (pixels)	Bh_{FW} (pixels)	Bh_{chip} (pixels)	$Bwchip$ (pixels)
LTV_{early}	100	2,000,000	90	30	80
$LTV_{Uniform}$	200	4,000,000	170	70	180
$LTV_{critical}$	300	5,000,000	250	100	270
$LTV_{Failure}$	500	7,000,000	430	170	420

5.1.3 Training Performance of the DFSV-ML Model

After training and evaluating the feature engineering techniques, the 4 process parameters were integrated with the F_i feature and the five failure modes to formulate a Diverse Feature Synthesis Vector ($DFSV = [V_c, f_t, a_p, L, F_i, FW, CW, NW, BUE, FLW)$]), which was used to train MLPNN for VB prediction. During training, the dataset was partitioned into 80% training and 20% testing. This means 405 out of 506 flank wear images were used to train the DFSV-ML model for VB prediction, whereas the remaining 101 images were used for offline validation of the trained DFSV-ML, ensuring high predictive efficiency outside the vicinity of the training data. Thus, the time-series test data was selected from a specific cutting condition ($V_c = 40m/min$, $f_t = 0.13mm/tooth$, and $a_p = 1mm$) to ensure the DFSV-ML was able to

predict the VB profile under complex flank wear morphology. The performance of the DFSV-ML architecture during training was investigated by varying the number of neurons in the hidden layer between 4 and 9 (i.e., the maximum number of neurons was the difference between number of inputs, 10, and outputs, 1). Results indicated that an increase in the number of neurons led to more divergence among the training performance curves. After several iterations, at a learning rate of 0.0001, the optimum weights were found at 7 neurons, as illustrated in Table 5.3.

The bias vector in the input layer was [2.17, 1.47, -1.54, 2.36, 2.49, -1.76, -2.21], corresponding to a bias factor of -0.002 in the output layer. Figure 5.7a exhibits the error histogram for DFSV-ML, which demonstrates a similar error distribution for all MLPNN architectures, indicating minimal deviation between the predicted and actual VB data. In addition, the high frequency instances occurred at a minimum error of 0.01579 μm. It is important to note that this analysis only compared error instances and not the overall mean absolute percentage error (MAPE), which was later evaluated to provide a reasonable performance metric when validating the DFSV-ML. Additionally, the correlation coefficient R^2 was evaluated to provide general information on how well the predicted fitted the measured VB values during the training process, as illustrated in Figure 5.7b. DFSV-ML exhibited an R^2 of 96.52%, indicating high efficiency in predicting VB progression during face milling of Inconel 718. However, the robustness of the DFSV-ML was further validated using the test dataset. In the mean time, another ML technique used spatial binary features (SBF-ML) to predict VB progression and again was evaluated by the MLPNN in MATLAB R2021a.

Table 5.3: Parameters for DFSV-ML [IW1– Weight for layer 1; OW– weight for output layer]

IW1	IW2	IW3	IW4	IW5	IW6	IW7	IW8	IW9	IW10	OW
0.12	0.69	-0.86	1.53	-1.67	-0.85	-0.72	1.89	0.46	0.71	0.42
-0.39	-2.09	-3.30	0.88	0.61	1.22	-0.80	-2.89	-0.48	0.678	0.17
-1.58	0.09	-0.66	0.82	-4.01	2.16	-0.77	-0.73	-0.96	0.75	-0.84
-5.71	-1.78	0.37	0.63	0.95	-1.11	-0.24	0.39	1.42	-1.87	0.04
-0.82	1.82	-1.13	1.41	-2.27	-1.82	-0.17	-0.56	-1.60	0.91	0.10
0.94	0.06	-2.80	-4.41	3.20	-1.19	0.65	1.27	-0.26	-1.42	-0.16
-1.17	2.00	3.29	-0.39	-1.89	2.06	1.01	-2.81	-0.02	0.786	0.55

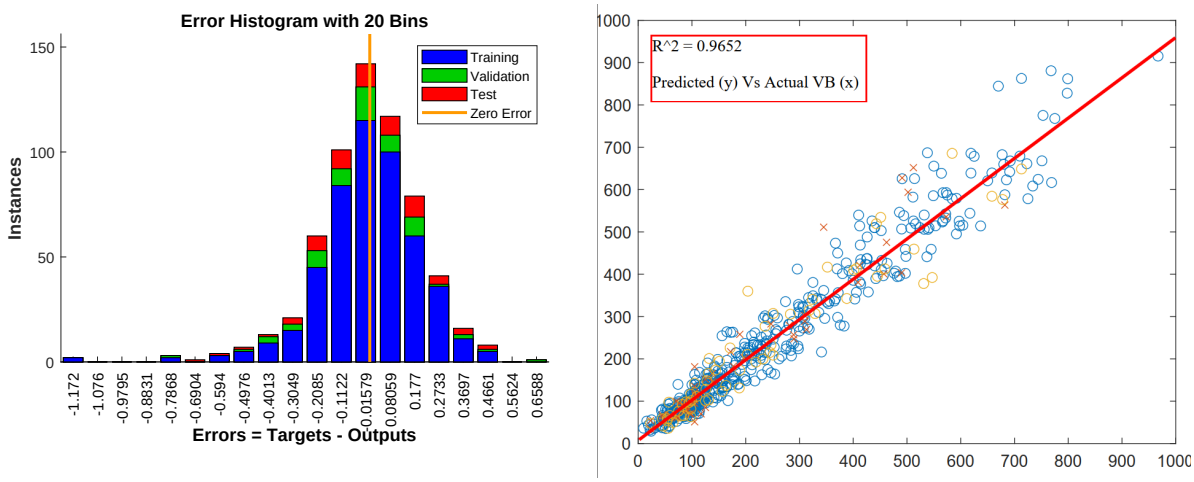

(a) (b)

Figure 5.7: *Training and validation of different MLPNN architectures with: (a) Error histogram and (b) parity plot*

5.1.4 Training Performance of the SBF-ML model

The robustness of spatial binary features (SBF) in predicting VB wear was first assessed by generating a Pearson correlation matrix in MATLAB R2019a, as shown in *Appendix A.1*. Among the all, the wear area (var1) exhibited the strongest R^2 of 95% (var4), thereby emerging as the most dominant feature, which also agreed with an observation made in [227]. Its strength was attributed to the uniform evolution of the wear region, owing to the paucity of uncontrolled failure modes on the depth of cut (DOC) line. Conversely, the perimeter (var2), on the other hand, displayed the lowest R^2 of 55% (Figure 5.8b).

It was noted that by utilizing the ECED to skeletonise the binary image, some pixel information was lost, leading to fluctuations in the thickness of the edge surrounding the wear region. In contrast, the fractal dimension exhibited a higher R^2 of 90% as compared to the perimeter, with substantial variations attributed to the progressive chipping and BUE formation on the Depth of Cut (DOC) line. In summary, both the wear area (Figure 5.8a) and the fractal dimension (Figure 5.8c) were strong binary features that can be used to predict VB progression during face milling of Inconel 718. The consistent evolution of the wear region on the side cutting edge was observed at the initial cutting stage, where the tools predominantly experienced uniform flank wear, as demonstrated in Figure 5.8c4. However, at the uniform and failure regions [66], other modes of failure, such as chipping and BUE, distort the morphology of the flank wear geometry on the DOC line. For instance, the localized chipping on the DOC

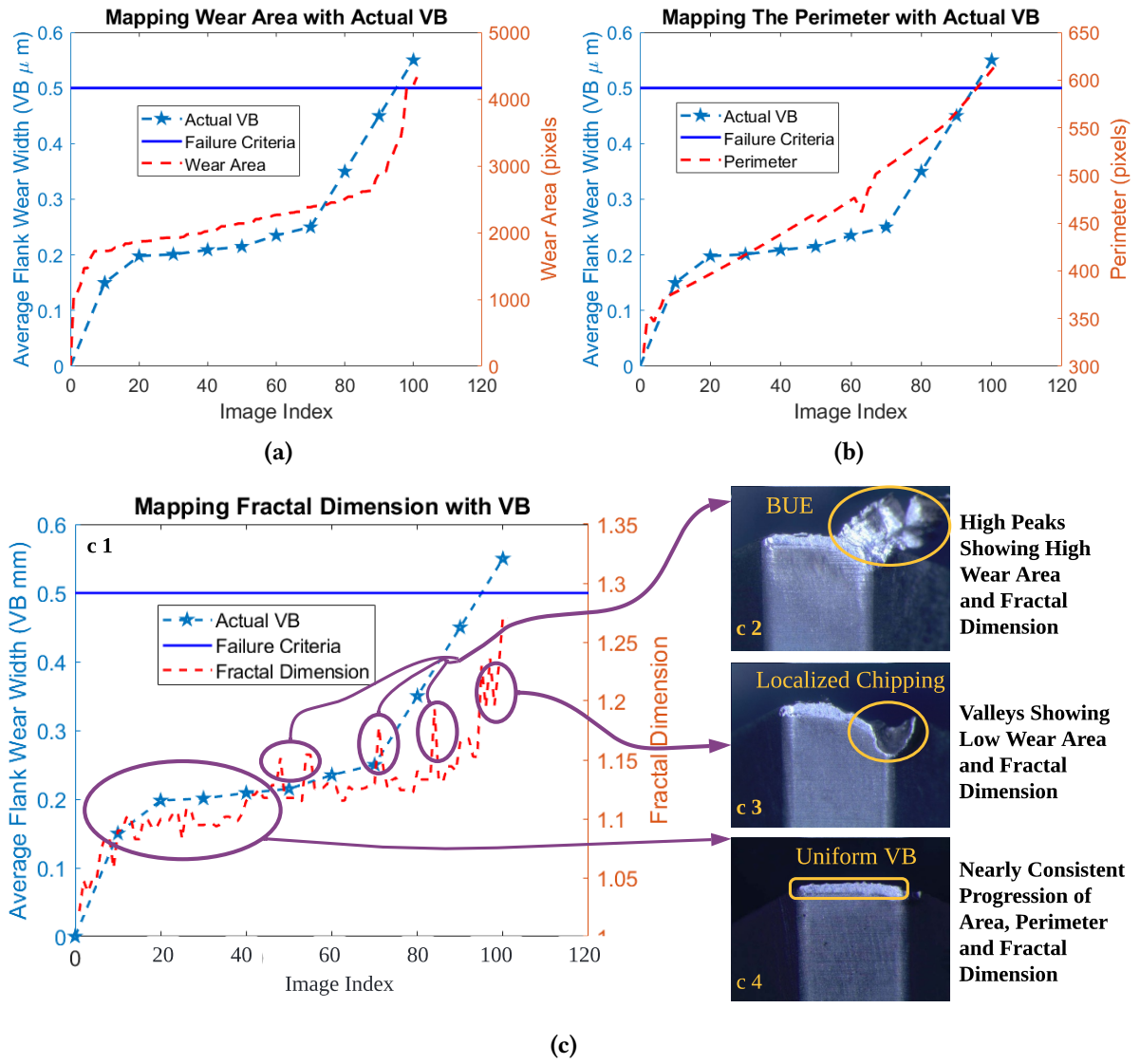

Figure 5.8: *The evolution of spatial binary features against VB: (a) Wear area; (b) Perimeter (c1) Fractal dimension*

line exposed the tool substrate after the TiAlN/NbN coating layer delaminated by the abrasive particles of Inconel 718 [10]. This led to a reduction in the wear area and fractal dimension, as depicted in Figure 5.8c3.

On the other hand, the adhesive particles of Inconel 718 protruded outside the cutting edge, and this occurred at the early cutting phase, where BUE formation was prevalent at the highest speed and lowest feed/tooth (Figure 5.8c2). Additionally, the BUE that filled the chipped region enhanced the consistent evolution of the wear region, thereby normalizing the spatial binary features during extraction. However, the Inconel 718's hard particles increased the localized chipping by removing the BUE with the chip flow in the subsequent passes during machining [2]. This caused a substantial reduction in the wear geometry, which eventually

decreased the area, perimeter, and fractal dimension.

After noticing that the area and perimeter could not fully encapsulate the complexity of the flank wear geometry, especially in the presence of chipping and BUE, they were augmented by another feature, fractal dimension, as shown in Figure 5.8c. The peaks on the fractal curve corresponded to the instances of BUE formation on the Depth of Cut line (Figure 5.8c2), leading to a substantial increase in the fractal features. Conversely, valleys signified localized chipping on the DOC line (Figure 5.8c3), resulting in a substantial reduction in the fractal dimension. Therefore, by augmenting the fractal dimension to known geometric features, the features revealed the presence of the uncontrolled failure modes and yielded the highest R^2 of 99.73%, as shown in (*Appendix A.2*), which previous studies struggled to achieve with geometric parameters alone [37, 331]. Just like the DFSV, the spatial binary feature technique was also substantiated by training an MLPNN in MATLAB to validate the effectiveness of the these features in predicting flank wear progression during machining. During SBF-ML training, the parameters that were used to achieve the optimum performance are summarized in Table 5.5.

The initial bias and the maximum number of epochs were set at 0 and 1000. The transfer function called hyperbolic function ('tansig') was applied to activate the neurons when computing the output from the first layer. In this case, the tansig varied from -1 to +1 because the weights, which are coefficients to inputs can either be positive or negative when computing the output. However, due to the standard flank wear curve [9], the output transfer function was purelin, that allows a non-negative and linear VB output during prediction. The number of neurons tested in the hidden layer was 20, as shown in Figure 5.9a. The architectures with 5 neurons performed better than all other MLPNN architectures during training. The validation MSE of MLPNN-5 after training was 0.0085. It was observed that the training progress converged at epoch 6 with a validation MSE of 0.00013118, as shown in Figure 5.9c. Figure 5.9b shows the actual and predicted VB with a minimum test error of 0.0128 mm. In addition, the average errors were distributed between -0.0189 and 0.0280, where the highest instances were found at 0.00026, dispersing around a zero-error line, as shown in Figure 5.9d.

Table 5.4: Parameters for SBF-ML [IW1– Weight for layer 1; OW– output weight; b–bias]

b1	b2	IW1	IW2	IW3	OW
2.36459		-1.5651	-2.6522	0.6588	-0.1005
-1.49572		1.8466	-1.4726	0.6123	-0.0792
-1.63674	[0.0296]	-7.0727	-0.9645	0.0954	-0.3322
0.41660		-1.7855	0.9697	-0.0003	-0.2592
-5.32979		-8.4452	-0.5294	0.0738	-0.4014

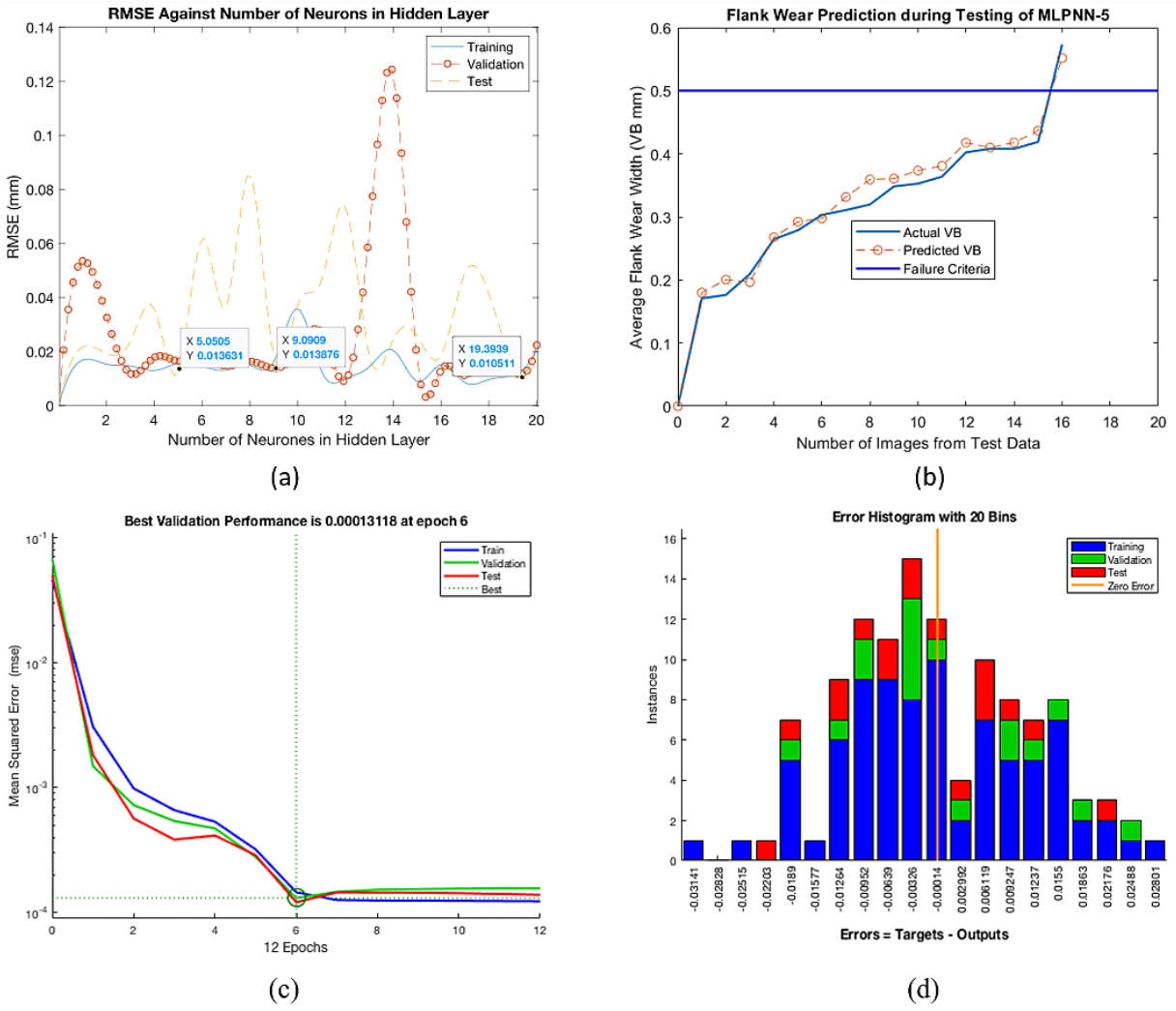

Figure 5.9: *The training performance of the SBF-ML: (a) optimization of neurons in the hidden layer; (b) the actual and predicted VB profile; (c) training progress; and (d) the error histogram*

5.2 Offline Validation of the DFSV-ML and SBF-ML

After assessing the effectiveness of feature engineering and the performance of both the DFSV-ML and SBF-ML models, they were validated using the test dataset to compare and select the viable ML model for in-process MV-TCM application. During this process, the actual VB measurements were compared with the predicted values generated by the models to evaluate

scoring metrics, such as Mean Average Percentage Error (MAPE) and R^2. This enabled offline validation of the trained feature engineering and ML models before deploying them for online MV-TCM application. Furthermore, a comparative study was conducted to determine the viable ML model for in-process tool wear prediction and control during face milling of Inconel 718. As previously stated, the goal was to predict and control VB rate, thus, the diversity of features was a more significant attribute for achieving this task. Figure 5.10b illustrates the VB profiles and box-plots for the actual, DFSV-ML and SBF-ML predicted VB values.

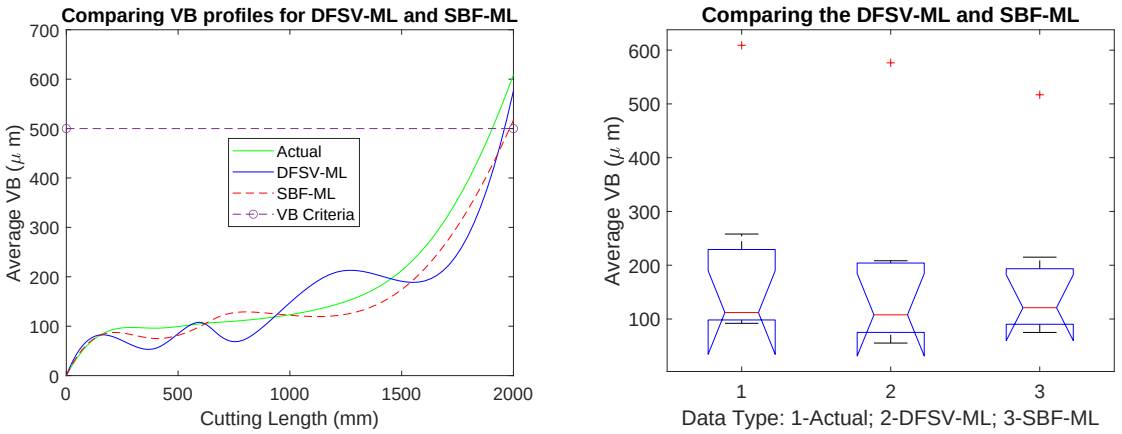

(a) **(b)**

Figure 5.10: *Comparative analysis of DFSV-ML and SBF-ML against the conventional method: (a) VB profiles; (b) Perimeter (c1) Fractal dimension*

5.2.1 Evaluating the Test Performance of DFSV-ML

The trained MLPNN was further validated using a test dataset, which was within the vicinity of the training data. Figure 5.10b displays the boxplot for the actual and predicted VB for a speed of 40 m/min, feed of 0.13 mm/tooth, and ADOC of 1 mm. The results indicated that the RMSE between the actual VB (data1) and the predicted VB (data2) was $45.5\mu m$, whereas the mean absolute percentage error (MAPE) was 3.7%. This score was lower than the scoring metrics obtained by Wu et al. (with MAPE of 4.76%) [46], where geometric features were utilized to predict the VB progression for the PVD and CVD coated carbide inserts during face milling of Inconel 718. It was also discovered that the DFSV-ML had relatively higher performance in terms of MAPE as compared to Kaya et al. (MAPE of 5.42%) [376], which applied features of force-torque to predict VB progression during CNC milling of Inconel 718 using PVD-coated

carbide inserts. This validates the effectiveness of applying the DFSV to enhance the predictive efficiency of the ML model during face milling of Inconel 718. Furthermore, the boxplot exhibited 1 outlier for the last VB measurement. However, this agreed with measured values, which also indicated that the last VB value is the outlier. This agreement proves the best fitting ability of the predicted data within the anticipated range of the measured VB values.

The median values for the actual and DFSV-ML box-plots were 112 and $107.8\mu m$, indicating the absolute deviation of $4.2\mu m$. In addition, the median values for both methods skewed towards values less than 200 μm, demonstrating a high prediction accuracy for small VB values. This was attributed to the insignificant evolution of failure modes during early cutting stages. In the absence of these failure modes, the strong predictor variables of VB progression were found to be F_i and cutting length. However, high magnitudes of $Bh_{chipping}$, $Bw_{chipping}$, and BUE emerged towards the critical and failure regions, mutilating the feature patterns and energy layers, which affected the consistent evolution of the F_i feature. This wear phenomenon resulted in a rapid VB rate, as shown in Figure 5.10a. Additionally, a significant reduction in VB progression during the uniform cutting stage was observed due to cyclic adhesion and BUE formation caused by a large chip load at the maximum feed of 0.13 mm/tooth, as shown in Figure 5.11(b). The large BUE induced another layer superjacent to the TiAlN/NbN coating, thus protecting the tool's substrate from further degradation during machining. However, subsequent passes eliminated the BUE through continuous chip flow, resulting in localized chipping on the tool's cutting edge, as demonstrated in Figures 5.11(c) and 5.11(d). This wear phenomenon exacerbated the magnitudes of $Bh_{chipping}$ and $Bw_{chipping}$ during face milling of Inconel 718.

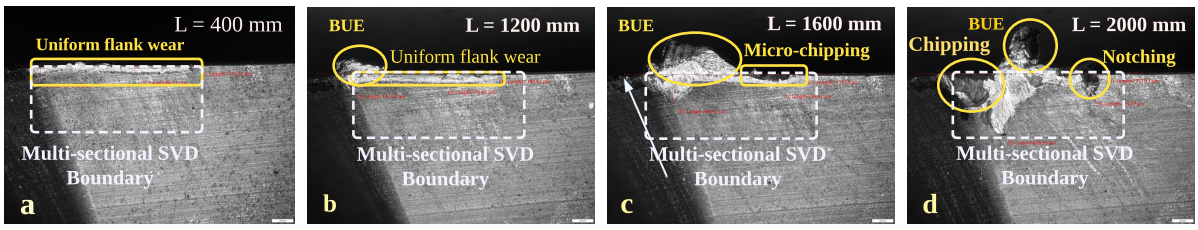

Figure 5.11: *Fig 9. Evolution of failure modes with cutting length (L) at V_c = 40 m/min, f = 0.13 mm/tooth, and ap = 1 mm*

It was observed that tool failure was not only determined by VB progression since catastrophic failure could still occur even before the tools reached the maximum VB criteria, as

long as they experienced high magnitudes of $Bh_{chipping}$ and $Bw_{chipping}$. Therefore, it was worth noting that, determining the maximum failure criteria at the end of tool life based on the VB criteria was not feasible during face milling of Inconel 718. As a result, this research proposed a new approach of the multi-stage failure criteria, which utilized threshold values of F_i, Bh_{FW}, $Bh_{chipping}$, and $Bw_{chipping}$ magnitudes to identify the significant levels of different VB stages. By focusing on the significant levels of VB progression, this approach did not regulate the process parameters at the intermediate intervals between thresholds to minimize the processing time during MV-TCM. Therefore, it was essential to apply the DFSV-ML to enhance the MV-TCM's ability to detect and control in-process failure modes and VB evolution, enhancing tool life extension during face milling of Inconel 718.

5.2.2 Evaluating the Test Performance of SBF-ML

The spatial binary feature technique was validated using the test data, which was different from the one utilized in the previous section because the features were extracted from the side cutting edge, where images presented a different flank wear profile. The system shows an RMSE of $45.118\mu m$. The high prediction accuracy at the early cutting stage was attributed to minimum failure modes experienced on the side cutting edge of the tools. As such, the wear region could easily be segmented to extract area, perimeter, and fractal dimension. In addition, the boxplot in Figure 5.10b shows that the average actual VB of all 4 inserts were larger than the predicted values. Moreover, the whiskers of the boxplot also showed that the distribution of measured VB was scattered across a wider range than predicted values. Nevertheless, the median values of mean actual and predicted VB are 112 and $121\mu m$, indicating an average deviation of $9\mu m$ between actual and predicted VB values.

On average, the box-plot shows the Mean Absolute Percentage Error (MAPE) of 2.099%, lower than the error found in [37], where geometric parameters were applied for VB measurement. In addition, the MAPE was even lower than the one found in [46], where features extracted by CNN auto-encoders were used to predict flank wear progression for PVD and CVD coated inserts CNC milling of Inconel 718. This indicates high efficiency of the spatial binary features, extracted from side cutting edge of the tools, in predicting VB progression even with limited dataset. However, it was observed that the low prediction accuracy in the failure

region, above $300\mu m$, as shown in Figure 5.10a, was attributed to the localized chipping and BUE. Besides, the model had already shown a more accurate prediction for lower VB values less than $300\mu m$, at the early cutting stage of flank wear progression, validating its practical use for most face milling operations as recommended by ISO 8688-1 standard.

5.2.3 Comparing the DFSV-ML and SBF-ML for MV-TCM Application

Taking into account the presence of two viable feature engineering techniques developed in this research, the evaluation matrix played a crucial role in determining the optimal method that met all the necessary criteria for the intended MV-TCM application. Table 5.4 shows the evaluation matrix, which was used to select the best technique based on the design specifications required to accomplish the research objectives and the intended MV-TCM application. The criterion is that for each aspect, if a method surpasses a reference (Ref), it receives a score of $+1$; otherwise, it gets -1. A fair comparison of the matrix involved treating each method as a reference at least once during evaluation.

Table 5.5: Evaluation the ML models: [Opt1– DFSV-ML; Opt2– SBF-ML; Opt3: Conventional Measurement]

Evaluation Matrix for feature engineering techniques									
Criteria	Opt1	Opt2	Ref	Opt1	Ref	Opt3	Ref	Opt2	Opt3
R^2	-1	-1	x	-1	x	1	x	1	1
Accuracy	-1	-1	x	-1	x	1	x	1	1
Adaptability	1	1	x	1	x	-1	x	-1	-1
Sensitivity	-1	-1	x	1	x	1	x	-1	1
Extraction Complexity	1	1	x	1	x	-1	x	-1	-1
Features diversity	1	1	x	1	x	-1	x	-1	-1
Integrability with ML	1	1	x	0	x	-1	x	0	-1
Feasibility	-1	-1	x	1	x	1	x	-1	1
TPO Enhancement	1	-1	x	1	x	1	x	-1	-1
Processing Speed	1	1	x	-1	x	-1	x	1	-1
Industrial Applicability	1	-1	x	1	x	1	x	-1	-1
Cost-effectiveness	1	1	x	0	x	-1	x	0	-1
Overall $\sum$+ve Scores	8	6	x	7	x	6	x	3	4
Overall $\sum$ 0 scores	0	0	x	2	x	0	x	2	0
Overall $\sum$-ve Scores	4	6	x	3	x	6	x	7	8

Predictive Efficiency during MV-TCM Utilization: Based on the evaluation matrix, options 1, 2, and 3 had positive scores of 15, 9, and 10, respectively. Overall, this means

the DFSV-ML exhibited superior characteristics as compared to the conventional and spatial binary features. Although option 2 had higher accuracy, with a RMSE, R^2 and MAPE of $45.118\mu m$, 99.73% and 2.099% as compared to the DFSV-ML, it was limited in terms of features diversity and sensitivity to enhance in-process tool wear control. Moreover, it could not detect the failure modes to reveal the extent of wear severity and sub-optimal tool performance. Option 3 was the most effective in capturing high-resolution tool wear images, but its low processing speed and high cost of tool wear inspection made it less practical for in-process application. However, the DFSV effectively captured similar diverse features, but with relatively high simplicity, speed, and cost-effectiveness, making it more efficient for online MV-TCM application than the conventional method.

Extraction Complexity from time-series tool wear data: Spatial binary features are relatively easy to extract from tool wear images, whereas DFSV is relatively more complex because the models need to differentiate failure patterns by combining features of color, shape, or edges. This requires more computationally intensive deep learning techniques that can convolve the pixel information to extract latent features from the tool wear images. However, setting up the hardware system for image capturing was relatively easy for DFSV because it utilized the main cutting edge, which was oriented at a 45°angle to capture the flank wear surface. On the other hand, setting up a camera to capture the side cutting edge of the tool inserts required a complex hardware system. The camera had to be oriented parallel to the spindle axis to view the bottom side of the cutter, which posed challenges such as lighting inconsistency, staining the camera lens with residual coolant droplets, and, in the long run, poor image resolution.

Features Diversity for in-process tool performance control: To ensure optimal performance of DFSV-ML and SBF-ML models during MV-TCM applications, it is essential to consider features diversity during training. Increasing the diversity of features during ML training can improve accuracy and effectiveness in predicting and controlling tool wear evolution during MV-TCM application. Unlike SBF-ML, DFSV-ML was trained on diverse features that can be utilized for both predicting and controlling tool wear during face milling of Inconel 718. Such diversity makes the model more reliable in its performance during online application, as it relies on the robustness and strength of various features for its prediction. Thus,

the inconsistency of one feature due to uncertain factors could not significantly affect the predictive efficiency of entire DFSV-ML.

Features Sensitivity to various cutting parameters: Cutting parameters significantly affect the evolution of tool wear features during machining. If models are trained on data collected from specific parameters, they may not be used to extrapolate VB progression when new cutting parameters are applied during the machining process. Therefore, the ML model's robustness should depend on features that are sensitive to tool wear evolution and not process parameters. Both SBF and DFSV were sensitive to cutting parameters, with SBF being more sensitive to speed and depth of cut, as the side cutting edge experienced the highest friction, exacerbating the abrasion and localized chipping, which affected the progressive change in the area, perimeter, and fractal dimension. On the other hand, changes in failure modes location, especially notching, BUE, and localized chipping, of DFSV were sensitive to the feed rate, radial and axial depth of cut, although they can still be detected by shape, edges, and colour. Additionally, the F_i magnitude in DFSV was not sensitive to all process parameters, as it increased with wear depth regardless of changes in speed, feed, and ADOC. The different sensitivity of features to cutting parameters makes DFSV more stable in predicting and controlling tool wear evolution during face milling of Inconel 718. To further validate this point, an experiment conducted in Chapter 6 applied a new cutting condition.

5.3 Conclusion

The ML models, including the multi-sectional SVD, and YOLOv3-TWDM, were successfully trained and tested to extract a variety of features that accurately predicted the VB profile during machining. The multi-sectional SVD successfully extracted the (F_i) magnitudes, which displayed a strong correlation with the progressive VB for the test dataset, with an R^2 value of 83%. Due to the presence of chipping, notching, and flaking on the flank wear region, it was recommended that the F_i feature should always be augmented by nominal features (failure modes) to improve the predictive efficiency of VB progression under complex flank wear morphology. On the other hand, the YOLOv3-TWDM successfully detected the 5 dominant failure modes as nominal features of the flank wear region with an accuracy and mAP of 87.86%

and 0.4907, respectively, at an IoU threshold of 0.65 and a detection rate of 1.792 seconds per image. It exhibited the highest AUC when detecting uniform flank wear and chipping, which was attributed to its prevalence in the dataset. Therefore, the multi-sectional SVD and YOLOv3-TWDM were found powerful in extracting diverse features from tool wear images, thus augmenting the process parameters to formulate a DFSV, which was used to train MLPNN to predict and control VB progression.

The DFSV-ML was validated using test dataset and compared with SBF-ML. Despite SBF-ML having lower MAPE and R^2, the DFSV-ML was found more efficient and reliable as it utilized diverse features for predicting and controlling VB progression during face milling of Inconel 718. Furthermore, YOLOv3-TWDM was also utilized to extract the magnitudes of Bh_{FW}, $Bh_{chipping}$ and $Bw_{chipping}$ to reveal the impact of specific failure modes on the flank wear evolution during face milling of Inconel 718. It was also believed that the correlation of these magnitudes with process parameters could be used to design the optimum cutting condition by identifying the parameters, which minimized the magnitudes of these features. As such, the evolution of F_i, Bh_{FW}, $Bh_{chipping}$ and $Bw_{chipping}$ magnitudes was correlated with process parameters, and the speed of 40 m/min, feed of 0.07 mm/tooth, and ADOC of 1 mm were found optimum in the process. By establishing threshold values for F_i, Bh_{FW}, $Bh_{chipping}$, and $Bw_{chipping}$ based on their correlation with VB at the optimal condition during face milling of Inconel 718, it becomes possible to determine significant stages of flank wear and adjust process parameters for in-process tool wear control. This is particularly crucial during machine vision TCM, as it helps reduce machining interruptions by focusing on significant wear stages instead of randomly regulating process parameters.

Chapter 6

Predicting Tool Wear Evolution by ML-based MV-TCM

Having meticulously conducted training and testing on feature engineering and machine learning (ML) models, the next step involved their integration into the MV-TCM setup, resulting in the development of an ML-based MV-TCM system. To validate and affirm the versatility of this system, it was rigorously tested through down-milling experiments carried out under both known and unknown cutting conditions. Each experiment was repeated three times, evaluating the system's performance across various dimensions, including structural stability, data acquisition and pre-processing, feature extraction, VB prediction, and in-process control of tool performance. This comprehensive evaluation served as a proof to the reliability, applicability, and proficiency of the developed system. In addition, the research also implemented a multi-stage control of speed and feed, strategically designed to minimize the rapid evolution of failure modes and enhance tool life extension during CNC milling of Inconel 718. In assessing tool longevity, the maximum cutting length emerged as a pivotal metric, serving as a reliable indicator of tool performance during the cutting operation. Comparative analyses across all conditions were conducted, and the condition that yielded the highest cutting length was identified as the optimal choice in the process. This same criterion was applied to comparatively analyze ML-based MV-TCM system against both conventional methods and the GKRR soft-computing approach.

6.1 MV-TCM Structural Analysis and Data Acquisition

The performance of the system was assessed in terms of its ability to acquire, transfer, and classify images for wear inserts within a reasonable processing time.

6.1.1 Structural Analysis

To ensure high integrity of the image acquisition process, the stability of the camera and lighting assembly was analysed through the evaluation of the MV-TCM structural design using ANSYS 2021 R2 software. The obtained results of equivalent stress, total deformation and fatigue life at a scale factor of 3σ are presented in Figures 6.1 and 6.2. The highest stress and lowest fatigue life were observed at the stand base, as depicted in Figures 6.1a and 6.1b, which were attributed to the elevated vibration intensity at the point of contact between the base and the worktable. Additionally, the vibration transmitted from the stand-base joint to the entire structure created an initial stress concentration zone due to the relatively small cross-section area. The results showed that by modifying the damping factor from 0 to 1, the maximum stress at the base decreased, enabling the structure to withstand both fatigue and yield stress.

A minimum damping factor of 0.9 reduced the stress distribution throughout the entire structure by 81%, providing a safety factor of 2.258 for yield and 1.05 for fatigue, as presented in Figure 6.2a. It was noted that the fatigue life of the arms remained consistently above 1,000,000 seconds for all damping factors due to the minimal damage caused by low stress concentration and elastic deformation on the nodes of the friction contacts. However, the arms exhibited the highest deformation for all damping factors, as presented in Figure 6.2a, indicating their substantial impact on the camera and light stability during image acquisition. Furthermore, the loads exerted at the arms due to the resonant force generated at the excitation point (the PDS displacement at the base of the MV-TCM structure) increased the maximum vertical displacement. The analysis further revealed that the maximum deformation at both the camera and light arm was around 1.7 mm, as shown in Figure 6.2a, at a damping ratio of 0.9, thus, maintaining the minimum Field of View of the Baumer camera. It should be noted that all deformations remained within the +/- 11.385 mm FoV range, fulfilling the minimum viewing requirements of the camera and lens during image capturing. In addition, Figure 6.2b

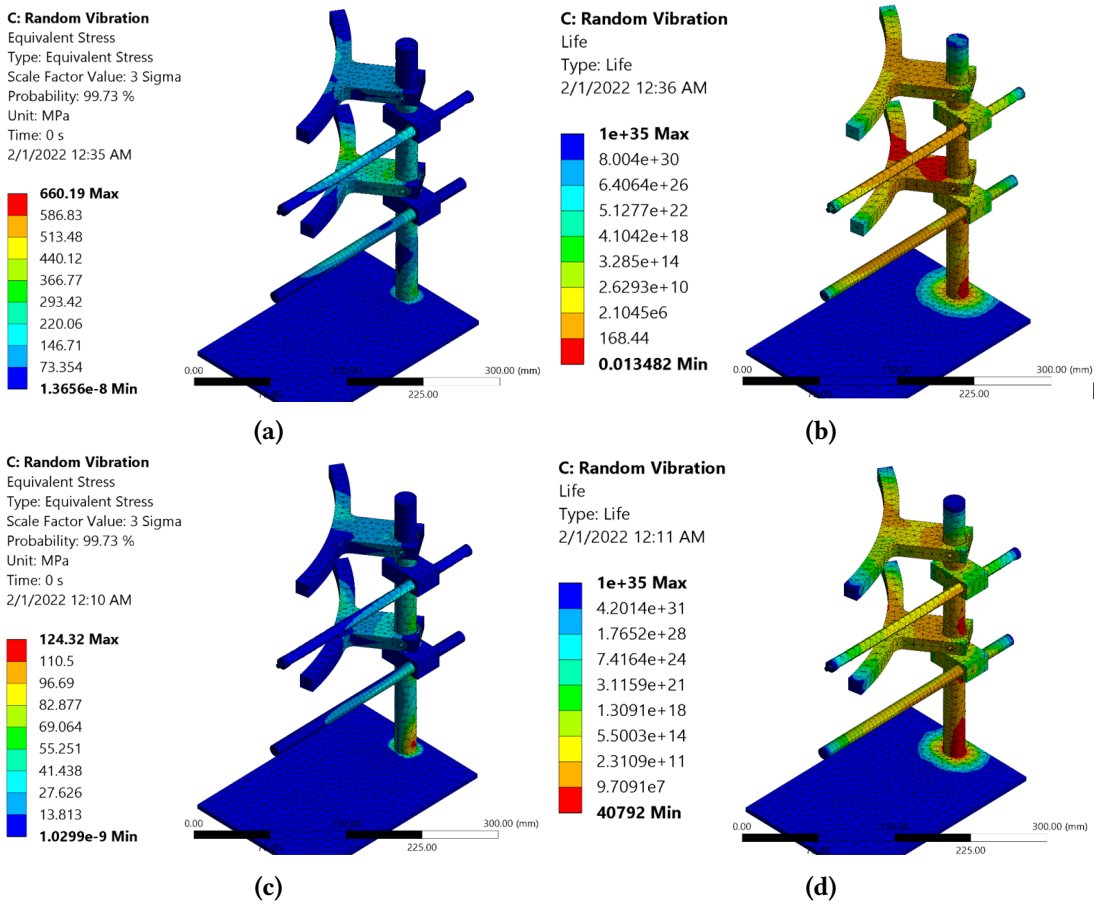

Figure 6.1: *The simulated results from ANSYS 2021 R2: (a) equivalent stress without a damping factor; (b) fatigue life without a damping factor; (c) equivalent stress with a damping factor of 0.9; and (d) fatigue life at a damping factor of 0.9*

shows the uniform stress for the camera and light arms (65 MPa and 47 MPa), thus rendering a damping factor of more than 0.9 safe for use in this research.

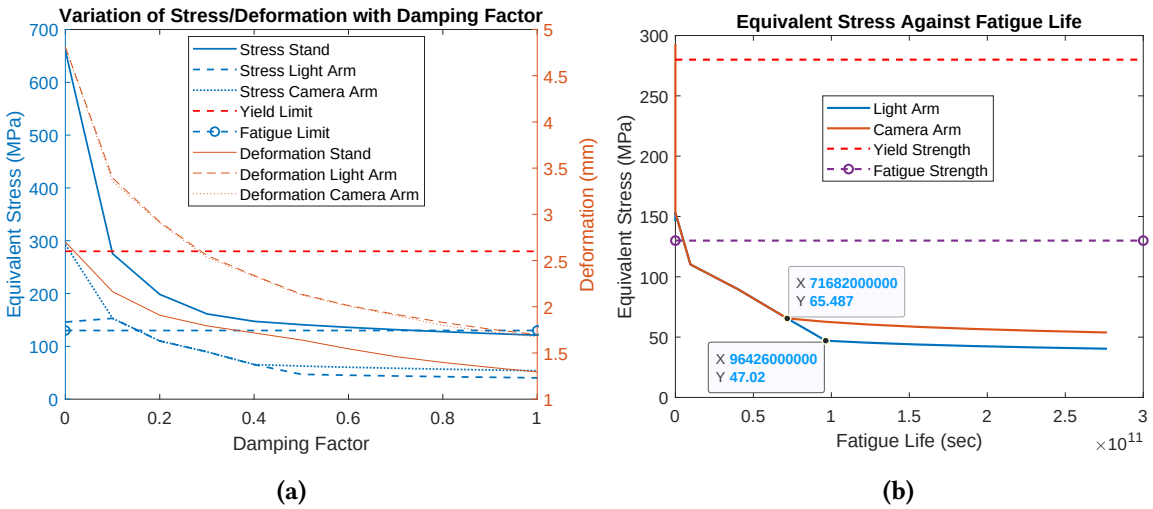

Figure 6.2: *The Results of structural damping and various factors: (a) stress/deformation against damping factor; (b) Equivalent stress against fatigue life*

Therefore, the camera was securely affixed to the MV-TCM stand, supported by four magnet discs (HD-MAG-2003, Strong N52, with a diameter × thickness of 20 mm × 3mm), along with vibration pads to absorb shocks caused by any extraneous vibrations at the CNC worktable during the cutting of Inconel 718. Furthermore, due to its low yield and fatigue strength, Aluminium alloy was not recommended for constructing the camera and light arms, especially for continuous CNC milling operations, where high-frequency vibrations can cause high stress and elastic deformation on the nodes, destabilizing the camera, lens, light, and photo-electric proximity sensor. Thus, stainless steel would be a superior choice due to its higher fatigue and yield strength, which is typically 3 - 10 times greater than that of Aluminium. Additionally, stainless steel exhibits comparable corrosion resistance under the flood cooling conditions of mineral oil-based cutting fluids.

6.1.2 Data Acquisition and Processing

After analysing the structural design, it was implemented for data acquisition. The findings in this research show that a photoelectric proximity sensor was capable of detecting the cutter as it approached the MV-TCM set-up. In addition, the Arduino Uno micro-controller harmoniously synchronized with the MATLAB computer vision software to enhance in-process data acquisition, controlling the camera's shutter to auto-capture the wear images during MV-TCM. This also overcame the challenge of data transfer, as the file was directly saved to the disk (by date and time) and transferred to the MATLAB programs for further processing. To prevent the impact of random vibrations on the photoelectric proximity sensor's sensitivity, the entire circuit was affixed in the MV-TCM setup. Once the cutter was detected, the camera was triggered to auto-capture time-series flank wear images.

After data acquisition, the binary classifier was employed to separate the wear inserts from the residues. The binary classifier was first trained and tested to ensure the efficient classification of these wear inserts. To further improve its robustness, additional experiments were conducted online to acquire enough training data for the binary classifier. Thus, the total dataset for training and testing the binary classifier was 1830 wear inserts and 2992 residues. This data was divided into 80% training and 20% validation. The hyper-parameters were attuned to optimal settings using SGD, including a learning rate of 0.0001, batch-size of 32,

momentum of 0.9. Due to the distinct edges, boundaries, orientation, and shapes between the wear inserts and residues, very few residues were misclassified as wear inserts, attributing to a precision loss of approximately 0.3%, as shown in Figure 6.3b. Therefore, it was adept at separating the wear inserts at a recall of 100%, with an AUC of 1, as shown in Figures 6.3a and 6.3b. Its overall accuracy, recall, and precision are 97.49, 94.76 and 47.71%, attributing to a 97.55% residues detection rate (where 216 out of 8976 residues were detected as worn inserts for the entire in-process experiment of 3 replicates ×17 runs). The efficacy of the binary classifier at these three replicates is compared in Table 6.1. The goal was to ensure that the TP and TN Rates (TPR and TNR), which were accurate detections of both wear inserts and residues, were greater than the FP and FN Rates (FPR and FNR), which signified misclassified wear inserts and residues.

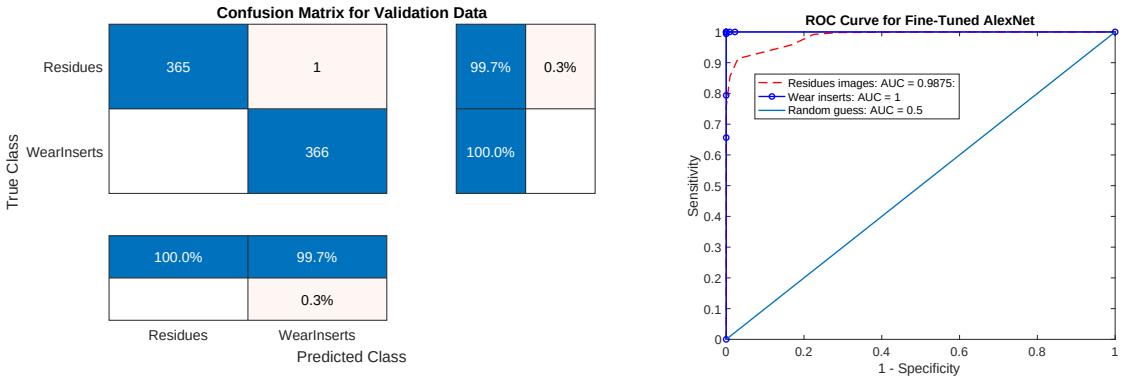

(a) **(b)**

Figure 6.3: *Performance of Fine-tuned AlexNet at optimum hyper-parameters (a) confusion matrix during training (b) The ROC curve for test dataset*

Table 6.1: The performance of a binary classifier

Replicates	TP	TN	FP	FN	TPR	PPV	TNR	FPR	Accuracy
1	64.00	2912.00	80.00	4.00	94.12	44.44	97.33	2.67	97.25
2	56.00	2404.00	59.00	3.00	94.92	48.70	97.60	2.40	97.54
3	60.00	2578.00	60.00	3.00	95.24	50.00	97.73	2.27	97.67
Mean	60.00	2631.33	66.33	3.33	94.76	47.71	97.55	2.45	97.49
Variance	16.00	66649.33	140.33	0.33	0.33	8.44	0.04	0.04	0.04
STDV	4.00	258.17	11.85	0.58	0.58	2.91	0.20	0.20	0.21

The overall standard deviation of all 3 replicates was 0.21, with 0.58 for wear inserts and 0.20 for residues, indicating high repeatability and reliability of the binary classifier in separating the wear inserts from the residues. Therefore, more than 4 wear inserts were transferred

to YOLOv3-TWDM for failure modes analysis. Owing to significant discrepancies between the wear inserts and residues, the model demonstrated a greater aptitude for classifying wear inserts as opposed to residues. Because of this, an AUC loss of 1.25% was observed in Figure 6.3b as a few residues were misclassified as wear inserts. The precision rate reported in Figure 6.3a resulted in more than 4 wear inserts transferred to the YOLOv3-TWDM for failure modes analysis. While this generated a slightly higher computational cost and processing time, it ensured no insert was missed during the analysis. After wear inserts were separated, the useful images were transformed by CLAHE and 180°-rotation to standardize their resolution and orientation for failure modes detection. The processed images were almost similar to the training samples, as illustrated in Figures 6.4a, 6.4b, and 6.4c.

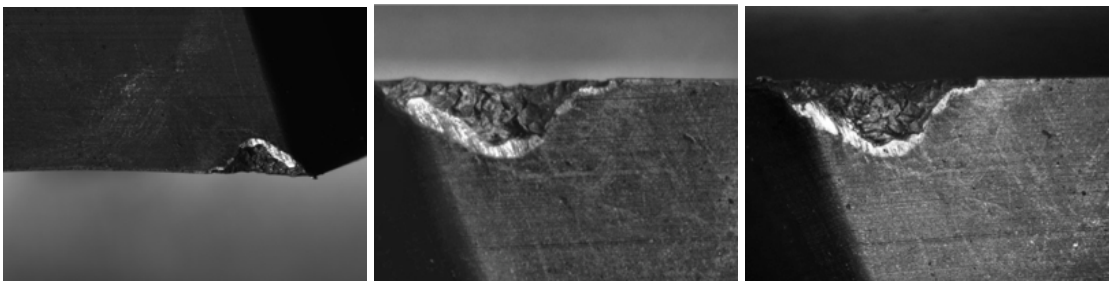

(a) **(b)** **(c)**

Figure 6.4: *Difference between various images: (a) online; (b) online processed and (c) offline*

6.2 Validating ML-MV-TCM for Tool Wear Prediction

After assessing the ML-based MV-TCM system for data acquisition, it was validated for failure modes detection and flank wear prediction by comparing with the actual results measured through the optical microscope. In this case, three conditions were used to validate the system and each condition was repeated 3 times to ensure the data obtained is reliable to generate plausible conclusions. The validation procedure was executed in accordance with the hypothetical outline of this research, which encompassed the prognostic analysis of wear mechanisms and failure modes evolution, along with the predominant features' magnitudes (VB, F_i, Bh_{FW}, $Bh_{chipping}$, and $Bw_{chipping}$) as key indicators of the failure criteria and tool life during machining. During this process, online images were captured by both optical microscope (for actual measurement) and Baumer camera (for in-process wear detection and prediction) at an

incremental length of 400 mm. The optical microscope was used to identify the actual failure modes through the utilization of SECO tools catalogue and ISO-8688-1 standard. In addition, it was also used to measure actual flank wear depth (VB), and other features, such as chipping width and depth ($Bh_{chipping}$, and $Bw_{chipping}$). It should also be noted that the tool life was measured in terms of the maximum cutting length. As such, it was assumed that the optimum cutting condition should yield the longest cutting length. Therefore, this research compared the maximum tool life obtained while using the conventional, GKRR soft-computing, and ML-based MV-TCM methods.

Appendices F.1, F.2, and F.3 show the summary of the actual and detected features for the three cutting conditions. It is also worth mentioning that, in order to guarantee the system's reliability, the performance metrics were computed by considering the mean values of all 4 wear inserts across all replicates and conditions. This means that the actual validation data was $4\times$ the data displayed in the *Appendix F*, which is equivalent to 368 flank wear images. This attributed to a data matrix of 368×11 for VB prediction in the proceeding section, where the first 10 columns were input features and the last column was the VB response. As can be seen in *Appendices F.1, F.2, and F.3*, the adoption of the new cutting conditions (speed = 40 m/min, feed = 0.08 mm/tooth, ADOC = 0.9 mm; speed = 60 m/min, feed = 0.08 mm/tooth, ADOC = 0.9 mm; and speed = 100 m/min, feed = 0.15 mm/tooth, ADOC = 0.9 mm) resulted in a significant wear phenomenon that revealed the synergistic impact of various speed and feed levels. Among these, it can be observed that the first condition (*Appendix F.1*), designed by the GKRR model, yielded the highest cutting length and tool performance as compared to the other two conditions, with an approximate tool life extension of 39.4%, relative to the previously determined optimal condition (speed = 40 m/min, feed = 0.07 mm/tooth, ADOC = 1 mm) during the offline experiment in Chapter 4.

6.2.1 Failure Modes Detection

During validation, the ML-MV-TCM detections were compared with actual failure modes identified through conventional method and ISO-8688-1 standard. The online processed images were then loaded into the YOLOv3-TWDM for failure modes detection. Figure 6.6 shows 2 sets of the first replicate data obtained at a cutting length of 2400 mm. The results show that

failure modes were repeatedly detected on the flank wear images, despite changes in the position, orientation, and height of the images during data acquisition. The YOLOv3-TWDM was efficient in detecting all 5 failure modes during in-process MV-TCM application, as shown in Figure 6.6. However, the performance of the YOLOv3-TWDM had a slight drop due to inconsistent lighting conditions and changes in the locations for most failure modes. Therefore, to enhance the model's performance, some online images were used to augment the training dataset. Thus, the model was retrained through the same supervised transfer learning approach after increasing the dataset to 1226 (with 506 offline and 720 online images).

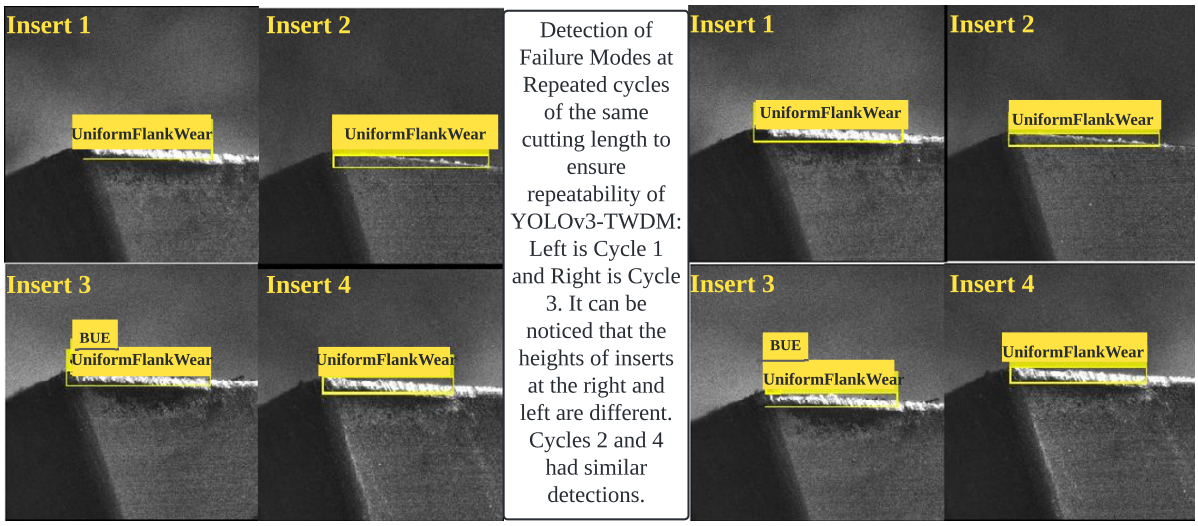

Figure 6.5: *Detection of failure modes for repeated cycles by YOLOv3-TWDM at* $V_c = 40m/min$, $f_t = 0.08mm/tooth$, $a_p = 0.9mm$, *and* $L = 800$

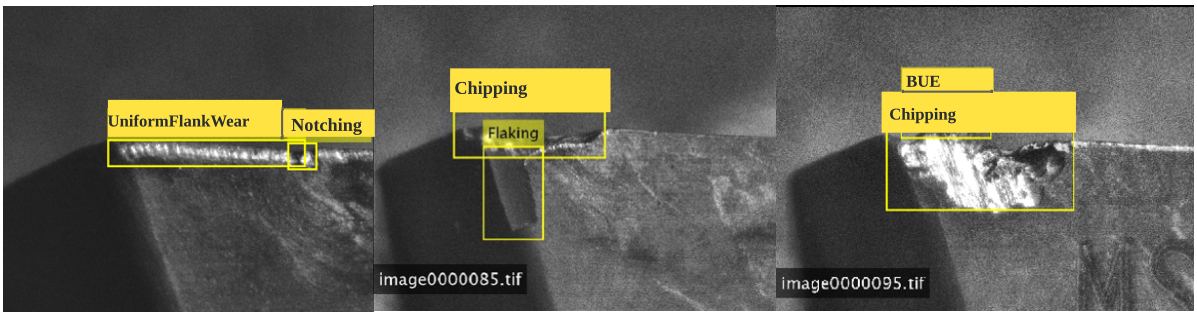

Figure 6.6: *Failure modes detections by YOLOv3-TWDM at* $V_c = 40m/min$, $f_t = 0.08mm/tooth$, $a_p = 0.9mm$, *and* $L = 6000$

The general observation made in this research revealed that the early cutting stages exhibited steady wear rate with some minor notching, micro-chipping, BUE and BUL. However, the variation in the VB values between $100\mu m$ and $200\mu m$ was minimal across all the replicates

and conditions, indicating minimum evolution of the wear mechanisms and failure modes at the break-in zone. The reduced wear mechanisms were evidenced by the decrease in the magnitudes of localized chipping during the early and uniform wear stages. For instance, in *Appendix F.1*, it was observed that the micro-chipping emerged at $L = 2800$, which later disappeared due to larger BUE formation, especially at the transitioning point between uniform and critical failure regions ($L > 4400mm$). The BUE in the steady wear stage enhanced the formation of the protective layer superjacent to the TiAlN/NbN coating, which prevented the tool from severe degradation under abrasion wear, thus extending the economic life of the carbide inserts during face milling of Inconel 718. However, it was also observed that the same BUE exacerbated the magnitude of chipping in the critical and failure stages ($VB > 200\mu m$) due to cyclic adhesion and severe abrasion, leading to a rapid failure rate of the tools across all replicates and conditions. Nevertheless, the chipping magnitudes intensified towards the end of tool life, except for condition 3, where it emerged in the early wear stage due to the highest cutting speed and temperature, which exacerbated the thermally induced wear mechanisms and failure modes.

However, by comparing the actual and detected values, the study also revealed that certain failure modes went undetected at specific cutting lengths during the experiment. For instance, in replicate 1 of condition 1, the system failed to detect BUE at cutting lengths of 4800, 5200, 6000, and 6400 mm due to their small magnitudes in the uniform wear stages as the LED light and the Baumer camera were unable to accurately illuminate and capture the feature patterns around these failure regions. In replicate 2 of the same condition, the system failed to detect chipping between 3600 – 4000 mm cutting length due to their small magnitudes as well, which could not produce the actual substrate colour under inconsistent lighting conditions during online data acquisition. In addition, it confused notching wear with unknown wear debris on the tool's cutting edge, while BUE's shape was somewhat opaque and did not contrast well with the background under inconsistent LED illumination. It is worth noting that these reasons apply to all undetected failure modes for the three cutting conditions. The detailed analysis of the validation process is presented in the proceeding sections. To validate its reliability for industrial use, it was further evaluated by computing the precision and recall values for each failure mode to analyze their respective AUC performances during in-

process MV-TCM application. The detected and actual features were used to plot a PR-curve, which was used to compute the AUC values of specific failure modes under different cutting conditions.

Condition 1 *[$V_c = 40m/min$, $f_t = 0.08mm/tooth$, $a_p = 0.9mm$]*: The findings in Figure 6.7 show that the uniform flank wear (UFW) had the highest AUC of 0.7790, which was attributed to the largest detections due to its prevalence in the early cutting stages. It was observed that the PVD-TiAlN/NbN coated carbide inserts experienced the uniform flank wear due to the moderate abrasion wear mechanism at the lowest speed of 40 m/min and feed of 0.08 mm/tooth. In addition, the early cutting stage had the longest life-span, which influenced the largest size of UFW dataset during in-process MV-TCM application, as shown in *Appendices F.1, F.2, and F.3*. The AUC of chipping was 0.6924, slightly lower than uniform flank wear and higher than notching, BUE, and flaking. This was attributed to the substantial chipping dataset due to the cyclic adhesion and abrasion, especially in the critical and failure stages. Progressive chipping was dominant in the critical and failure regions due to the synergistic impact of moderate chip load at 0.08 mm/tooth and speed of 40 m/min, which plastically deformed the cutting edge towards permanent degradation at the end of tool life [2]. In addition, the detection of localized chipping was somehow confused with notching, especially when both occurred at the 'tool's entry point' into the workpiece. As a result, some notching wear was detected as localized chipping, thus, increasing the AUC of chipping as compared to notching. However, since the occurrence of the chipping and notching were attributed to high impact force and severe abrasion wear mechanisms as the cutting edge tries to shear the precipitation-hardened layers of Inconel 718 [74], both features were deciphered as the mechanical failure modes on the tool's cutting edge.

Considering the fact that this experiment was conducted at the lowest speed of 40 m/min, and feed of 0.08 mm/tooth, the system recorded the minimum adhesion wear due to the small chip load and low cutting temperature, which reduced the BUE formation on the tool's cutting edge [64]. In addition, the small chip load could not successfully weld onto the tool's cutting edge at a low-temperature condition. Furthermore, it reduced the friction force on the tool-workpiece contact zone, minimizing the rubbing action that led to attrition and flaking of TiAlN/NbN layer fragments. Besides, the low cutting temperature reduced the dissolution

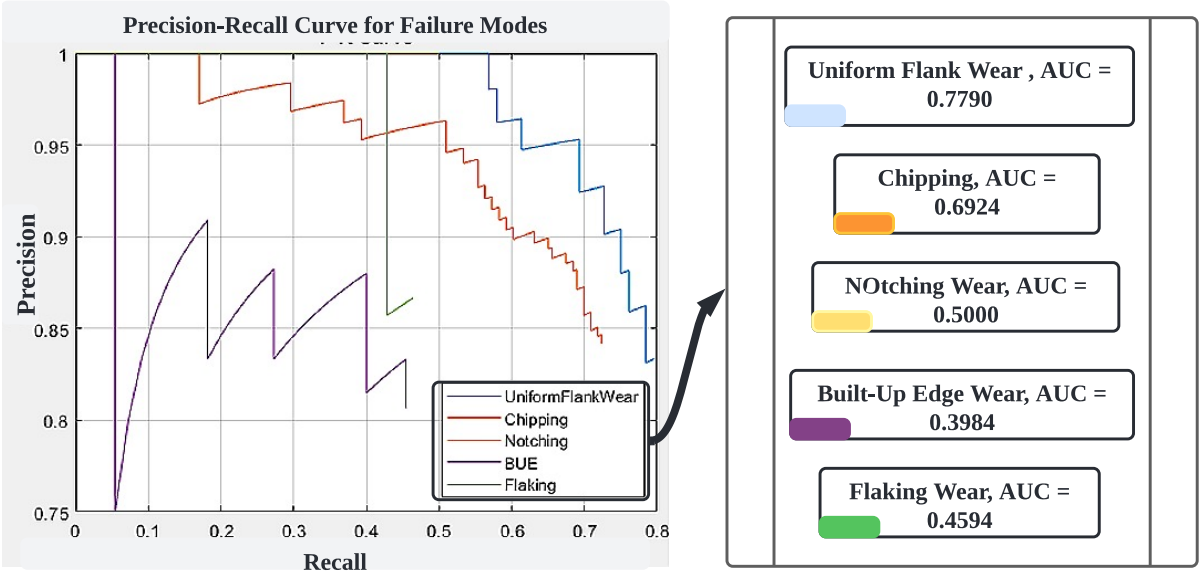

Figure 6.7: *Precision-recall curve for YOLOv3-TWDM during online failure modes detection for the first condition of* $V_c = 40m/min$, $f_t = 0.08mm/tooth$, *and* $a_p = 0.9mm$

of the Cobalt binder between the TiAlN layer and the substrate of the tools, thus maintaining the bonding strength of coating layers to prevent flaking in the early cutting stages. Therefore, flaking was the lowest detected failure mode by YOLOv3-TWDM. However, as the tool wear progressed towards the critical and failure stages, the synergistic impact of the wear mechanisms exacerbated the progressive chipping, flaking, and BUE, whose magnitudes negatively influenced the tool performance during face milling of Inconel 718.

In summary, the average mAP of YOLOv3-TWDM for all replicates was 0.6572 at an IoU threshold of 0.65. This was still considered an above-average score as compared to other applications, which reported a mAP of 0.691, relative to a small IoU value of 0.5 [377]. In addition, the YOLOv3-TWDM had an average accuracy of 95.24% for uniform Flank Wear, 88.24% for Chipping, 71.43% for Notching, 83.33% for BUE, and 57.14% for Flaking, thus yielding an overall relative accuracy of 79.08% for the entire detection efficiency. This shows that a YOLOv3-TWDM had a high detection rate for uniform flank wear, chipping, and BUE for the lowest speed and feed of 0.08 mm/tooth, which was obtained within the vicinity of the training conditions. It was noted that regardless of slight variation in the position, orientation and resolution of the tool wear images during online data acquisition, the failure modes were precisely detected throughout the entire experiment, indicating the robustness of YOLOv3-TWDM despite the changes in the tool's failure patterns.

However, there was low detection rate for notching, flaking, and some instances of BUE. It was observed that YOLOv3-TWDM still possess some challenges in accurately detecting objects that are small or have low resolution in the image. For stance, if the notching size is smaller than the network's receptive field, it could not be well represented in the feature maps during detection. On the other hand, BUE, flaking and notching with low contrast or visibility due to poor LED lighting conditions, occlusions, or cluttered backgrounds could not be detected. Furthermore, it was noted that in the detection of multiple failure modes, notching and chipping had more overlapping instances, and flaking had complex structures which definitely confused the model's detection rate. Finally, the training data for BUE, notching and flaking were relatively low, and could not adequately represent the variety of scenarios. This caused poor generalization for the unseen failure modes scenarios. Moreover, the dataset was imbalanced, with few dataset for BUE, notching and flaking, causing the YOLOv3-TWDM under-perform for these under-represented classes.

Apart from identifying various failure modes in the flank wear region, the YOLOv3-TWDM model was also utilized to determine the magnitudes of flank wear depth (Bh_FW), as well as chipping width and depth ($Bh_{chipping}$ and $Bw_{chipping}$), as complementary indicators of tool life during machining. The detected Bh_FW was found to be correlated with the actual VB values, with an average R^2, RMSE, MAE, and MAPE of 83.2%, $18.3\mu m$, $26.3\mu m$, and $10.8\mu m$, respectively (Table 6.2). These values indicate high predictive efficiency and above-average correlation of actual and predicted VB. However, the mean average deviation of $4.5\mu m$ was caused by the inconsistent B-box coordinates due to complex wear morphology attributed to the progressive chipping, flaking, and BUE formation in the critical and failure stages ($VB > 200mm$). Therefore, Bh_FW was found to be reliable in predicting VB progression in the early and uniform wear regions, where the synergistic impact of wear mechanisms, such as cyclic adhesion and abrasion were insignificant and could not induce severe chipping, BUE, or flaking on the tool's cutting edge. Whereas in the critical and failure stages, the progressive change in $Bh_{chipping}$ had a strong correlation, with an average R^2, RMSE, MAE, and MAPE of 87.1%, $23.8\mu m$, $6.3\mu m$, and $4.6\mu m$. This was attributed to the permanent tool degradation in the critical and failure stages due to cyclic adhesion and abrasion wear mechanisms [64]. The cyclic adhesion induced the BUE formation, which was plastically deformed

and plucked together with aggressive chip flow and abrasive forces, resulting in chipping and flaking on the tool's cutting edge.

Table 6.2: The statistics of Failure Modes magnitudes at $V_c = 40m/min$, $f_t = 0.08mm/tooth$ and $a_p = 0.9mm$: For $Bh_{FW}^{(1)}$, (1) represents first replicate, whereas for $Mean_{a,p}$, a and p represent the actual and detected values

Metric	μ_a	μ_p	μ_{Res}	σ_a	σ_p	σ_{Res}	RMSE	MAE	MAPE	R^2
$Bh_{FW}^{(1)}$	131	127	4	87	76	-11	17.2	10.1	6.5	85.8
$Bh_{chipping}^{(1)}$	42.5	43.6	1.1	94.3	96.5	2.2	4.4	1.3	1.6	91.7
$Bw_{chipping}^{(1)}$	87.6	85.5	-2.1	186.7	181.8	-4.9	8.5	2.2	1.12	93.9
$Bh_{FW}^{(2)}$	171.5	170	1.1	153.1	136.4	-16.7	5.9	41.3	6.2	81.6
$Bh_{chipping}^{(2)}$	74.3	88.6	14.3	133.7	159.8	26.1	55.2	14.25	10	79.8
$Bw_{chipping}^{(2)}$	182.3	165.3	-17	326.6	296	-30.6	66.1	17.1	5.3	76.2
$Bh_{FW(Avg)}$	154	149.4	4.5	119.2	119.3	0.1	18.3	26.3	10.8	83.2
$Bh_{chip(Avg)}$	54.4	60.5	6.2	106.7	119.1	12.4	23.8	6.3	4.6	87.1
$Bw_{chip(Avg)}$	132.5	121.3	11.2	238.2	218.9	-19.4	42.9	11.3	4.1	86.14

Furthermore, the $Bw_{chipping}$ feature was exacerbated by the notching wear, which gradually propagated across the cutting edge by cyclic adhesion and abrasion to form localized chipping on the tool's cutting edge. Nevertheless, the $Bw_{chipping}$ had an average R^2, RMSE, MAE, and MAPE of 86.14%, $42.9\mu m$, $11.3\mu m$, and $4.1\mu m$. The mean average deviation of 11.2μ showed that the $Bw_{chipping}$ was somehow affected by the BUE formation along the tool's cutting edge. Unlike the $Bh_{chipping}$, when one part of the cutting edge experienced BUE, the $Bw_{chipping}$ reduced, thus, its propagation fluctuated with the cyclic adhesion wear mechanism during face milling of Inconel 718. Generally, all the scoring metrics were reproducible with the Bh_{FW} having the smallest average residual deviation (σ_{Res}) of $0.1\mu m$, indicating the highest reproducibility of the predicted against the actual values across all replicates. Therefore, the YOLOv3-TWDM was considered a powerful tool to decipher and explore the underlying micro-structures of various failure patterns on the tool's cutting edge. Thus, it was efficient to detect the presence of multiple failure modes, with flank wear and chipping being the dominant features that affect the performance of PVD-TiAlN/NbN coated carbide inserts during face milling of Inconel 718 [378]. Furthermore, the system successfully detected the size of flank wear and chipping with an average deviation of $7.3\mu m$, relative to the conventional method, indicating its reliability for industrial use in the smart machining systems.

Condition 2 [$V_c = 60m/min$, $f_t = 0.08mm/tooth$, $a_p = 0.9mm$]: Figure 6.8 shows the

highest AUC value for uniform flank wear (AUC = 0.782), agreeing to the results obtained at the lowest speed of 40 m/min as both conditions were obtained within the vicinity of the training parameters. Just like the previous condition, the tools at this condition experienced the uniform flank wear due to the moderate abrasion wear mechanism at early cutting stages. In addition, the early cutting stage had the longest tool life-span that attributed to the largest dataset of UFW as compared to other failure modes (*Appendix F.2*). Again, the UFW was followed by chipping, which had an AUC value of 0.587. Progressive chipping was predominant in the critical and failure stages due to the synergistic impact of moderate chip load at 0.08 mm/tooth and medium speed of 60 m/min, which increased the temperature and the rate of precipitation hardening, thus plastically deforming the tool's cutting edge towards permanent degradation [2]. In addition, some notching wear was detected as localized chipping, hence, decreasing the AUC of notching to 0.275 during detection, despite both being mechanical failure modes during machining of Inconel 718 [74].

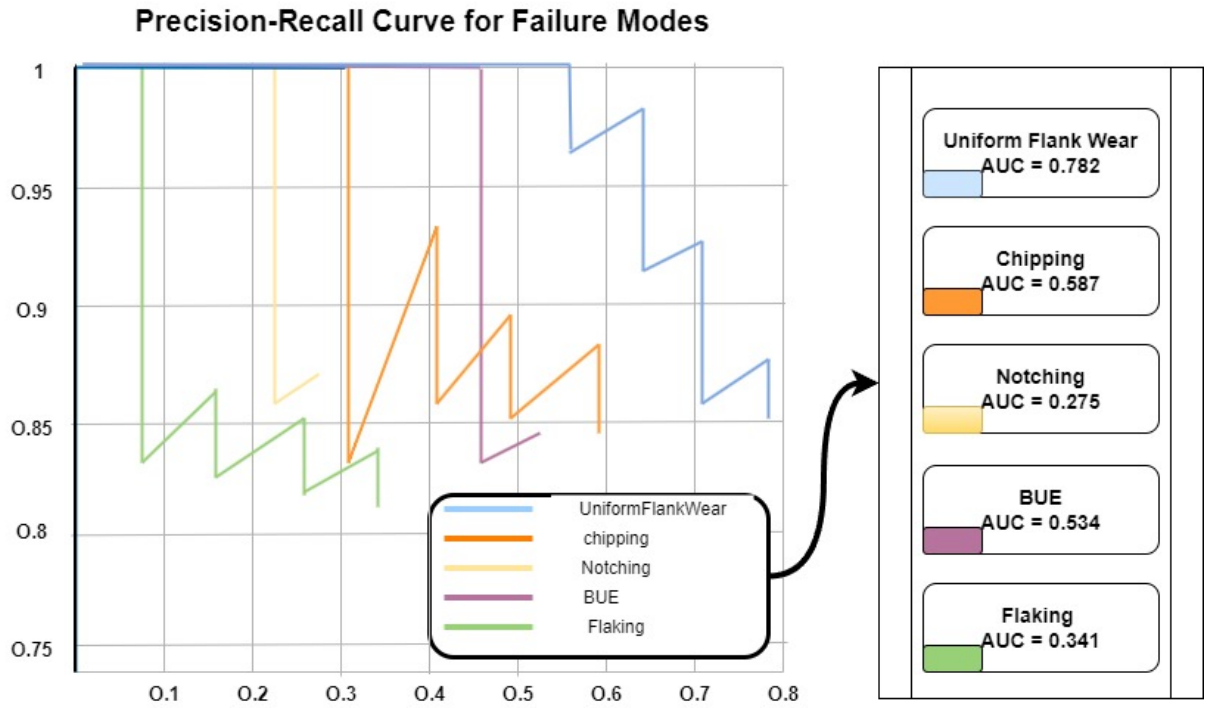

Figure 6.8: *Precision-recall curve for YOLOv3-TWDM during online failure modes detection for the second condition of* $V_c = 60m/min$, $f_t = 0.08mm/tooth$, *and* $a_p = 0.9mm$

In view of the fact that this experiment was conducted at the medium speed of 60 m/min, there was medium temperature that increased the rate of adhesion wear mechanism, thus increasing the rate of BUE formation on the tool's cutting edge [64]. Thus, BUE had an AUC

of 0.534 as the miniature chip fragments could still weld against the tool's cutting edge at the medium cutting temperature. On the other hand, such wear phenomena increased the friction force on the tool-workpiece contact zone, exacerbating the rubbing action that led to attrition and flaking of TiAlN/NbN layer fragments, especially in the critical and failure wear stages. With passage of time, the medium cutting temperature gradually caused the dissolution of the Cobalt binder between the TiAlN layer and the substrate of the tools, thus weakening the bonding strength of coating layers to exacerbate the rate of flaking. Hence, flaking followed BUE with an AUC of 0.341. In general, the average mAP of YOLOv3-TWDM for all replicates was 0.7254 at an IoU threshold of 0.65. This was higher than the previous threshold and was considered the best score in this research as compared to other applications, which applied an IoU of 0.5 [377]. In addition, the YOLOv3-TWDM had an average accuracy of 92% for uniform Flank Wear, 79.3% for Chipping, 52% for Notching, 64% for BUE, and 57% for Flaking, thus yielding an overall relative accuracy of 70%, indicating high detection rate at the medium speed of 60 m/min and feed of 0.08 mm/tooth. Therefore, the YOLOv3-TWDM was adept at detecting the failure modes at high precision and speed for data within the vicinity of the training conditions.

Again, after detecting different types of failure modes, the YOLOv3-TWDM model was employed to quantify the extent of flank wear depth (Bh_{FW}), as well as chipping magnitudes ($Bh_{chipping}$ and $Bw_{chipping}$). These features served as supplementary metrics for assessing tool life during the face milling process of Inconel 718. Again, the second condition demonstrated a strong correlation between the detected and actual features across the replicates (Table 6.3). The parameter Bh_{FW} exhibited a significant correlation, with an average R^2 value of 90%, along with an RMSE of $18.3\mu m$, an MAE of $13.45\mu m$, and a MAPE of $7.5\mu m$. The mean average deviation of 8.9 µm was attributed to the edge loss due to chipping in the critical and failure stages. Therefore, similar to the lowest speed of 40 m/min, Bh_{FW} was also found to be a reliable predictor of VB in the early cutting stages at medium speed of 60 m/min. Such a wear phenomenon was characterized by the consistent evolution of pixel distribution and energy layers on the cutting edge of the tool. However, the critical and failure stages still exhibited an irregular evolution of the energy layers, attributing features, such as $Bh_{chipping}$ and $Bw_{chipping}$, as prevalent indicators of tool life under these wear stages. $Bh_{chipping}$ evolution

displayed an average R^2 value of 83.7%, an RMSE of $19.2\mu m$, an MAE of $9.9\mu m$, and an MAPE of $10\mu m$, with an average deviation of 6.4μ attributed to cyclic adhesion and abrasion wear mechanisms, which exacerbated edge loss as the tools slide against the precipitation-hardened layer of Inconel 718 at the medium speed and cutting temperature during face milling of Inconel 718.

Table 6.3: The statistics of Failure Modes magnitudes at $V_c = 60m/min$, $f_t = 0.08mm/tooth$ and $a_p = 0.9mm$: For $Bh_{FW}^{(1)}$, (1) represents first replicate, whereas for $Mean_{a,p}$, a and p represent the actual and detected values

Metric	μ_a	μ_p	μ_{Res}	σ_a	σ_p	σ_{Res}	RMSE	MAE	MAPE	R^2
$Bh_{FW}^{(1)}$	154.8	140.1	14.7	139.5	113.8	25.7	43.9	4.6	8.1	93
$Bh_{FW}^{(2)}$	125.5	122.4	3.1	80.6	81.2	0.6	9.25	22.3	6.2	87
$Bh_{chipping}^{(1)}$	95.8	94.9	0.87	130	121.7	8.3	2.7	7.9	7.6	75.8
$Bh_{chipping}^{(2)}$	69.9	81.8	11.9	67	78.9	11.9	35.7	11.9	12.4	91.6
$Bw_{chipping}^{(1)}$	340.8	307	33.8	361.6	324.4	37.2	101.4	33.8	7.8	81.7
$Bw_{chipping}^{(2)}$	278.9	268	10.9	281.8	270	11.8	32.75	14.75	5.5	89.3
$Bh_{FW(Avg)}$	140.1	131.2	8.9	110	97.5	13.15	26.23	13.45	7.15	90
$Bh_{chip(Avg)}$	82.65	178.7	6.4	98.5	100.3	10.1	19.2	9.9	10	83.7
$Bw_{chip(Avg)}$	309.9	135.9	22.3	321.5	297.2	24.5	67	24.3	6.65	85.5

Furthermore, the $Bw_{chipping}$ was particularly affected by the rapid propagation of notching wear at a medium speed of 60 m/min, gradually leading to localized chipping on the tool's cutting edge. This was further exacerbated by an increased rate of precipitation hardening at medium speed and temperature. Despite this, $Bw_{chipping}$ still exhibited a strong performance, with an average R^2 value of 85.5%, an RMSE of $67\mu m$, an MAE of $24.3\mu m$, and an MAPE of $6.65\mu m$. The highest average deviation of 22.35 µm indicated that $Bw_{chipping}$ was more influenced by the wide-spreading of notching and localized chipping. This resulted in an irregular evolution of $Bw_{chipping}$, especially when one part of the cutting edge experienced BUE, which could potentially be dislodged along with the chip flow during machining [64]. In general, $Bh_{chipping}$ exhibited a minimum residual deviation (σ_{Res}) of $10.1\mu m$, indicating highest reproducibility of its results as compared to $Bw_{chipping}$ and Bh_FW. The ML still showed a higher reproducibility of results at the lowest condition of 40 m/min as compared to the medium speed of 60 m/min. This discrepancy was attributed to the prevalence of uniform flank wear as the dominant failure mode at the minimum speed, accounting for nearly 67% of the validation dataset. Nonetheless, the system remained robust in predicting VB progression within

the vicinity of the training conditions, despite slight variations in the scoring metrics.

Condition 3 [$V_c = 100m/min$, $f_t = 0.15mm/tooth$, $a_p = 0.9mm$]: After increasing the speed and feed to 100 m/min and 0.15 mm/tooth, a maximum condition outside the vicinity of the training parameters, chipping had the highest AUC of 0.778 (Figure 6.9), which was attributed to the largest detections due to its prevalence throughout the entire experiment. It was observed that at this condition the tools experienced the progressive chipping both in the early and failure wear stages as shown in *Appendix F.3*. This was attributed to high rate of precipitation hardening due to the highest cutting speed and temperature, as well as largest chip load due to the highest feed rate of 0.15 mm/tooth. This exacerbated the cyclic adhesion and severe abrasion, causing high cutting forces, which increased the rate of chipping in the critical and failure stages during face milling of Inconel 718. Chipping was followed by the uniform flank wear (UFW) with an AUC of 0.68. As observed in *Appendix F.3*, the uniform flank wear was experienced in the early cutting stages, which had the short life-span as compared to chipping due to rapid wear progression towards failure. Like the previous condition of 60 m/min, the BUE had an AUC of 0.519, following the uniform flank wear. This was attributed to some few welds, which occurred due to the highest cutting speed and temperature. However, the high cutting temperature also exacerbated the flaking wear as facilitated the dissolution of cobalt binder between the tool and workpiece material, resulting in some TiAlN/NbN layer plucked off together with chip flow on the flank face. Hence the flaking followed the BUE with an AUC of 0.4. Finally, the notching wear had the lowest AUC of 0.367 as most notching was identified as localized chipping during the detection process.

In summary, the average mAP of YOLOv3-TWDM for all replicates was 0.5488, which is still considered a good score at an IoU threshold of 0.65. Additionally, the average accuracy was 68.3%, lower than the previous two conditions. However, this still demonstrates that the model achieved a relatively high prediction accuracy even under the intense condition of the highest speed and feed rate, beyond the scope of the training parameters. The deviation in accuracy can be attributed to the low detection rate of uniform flank wear, which constituted the largest dataset during training of the ML network. Conversely, the highest condition exhibited a high detection rate of chipping, which negated the desired trend of failure mode detection used to train the YOLOv3-TWDM. In addition to detecting different failure modes in the flank

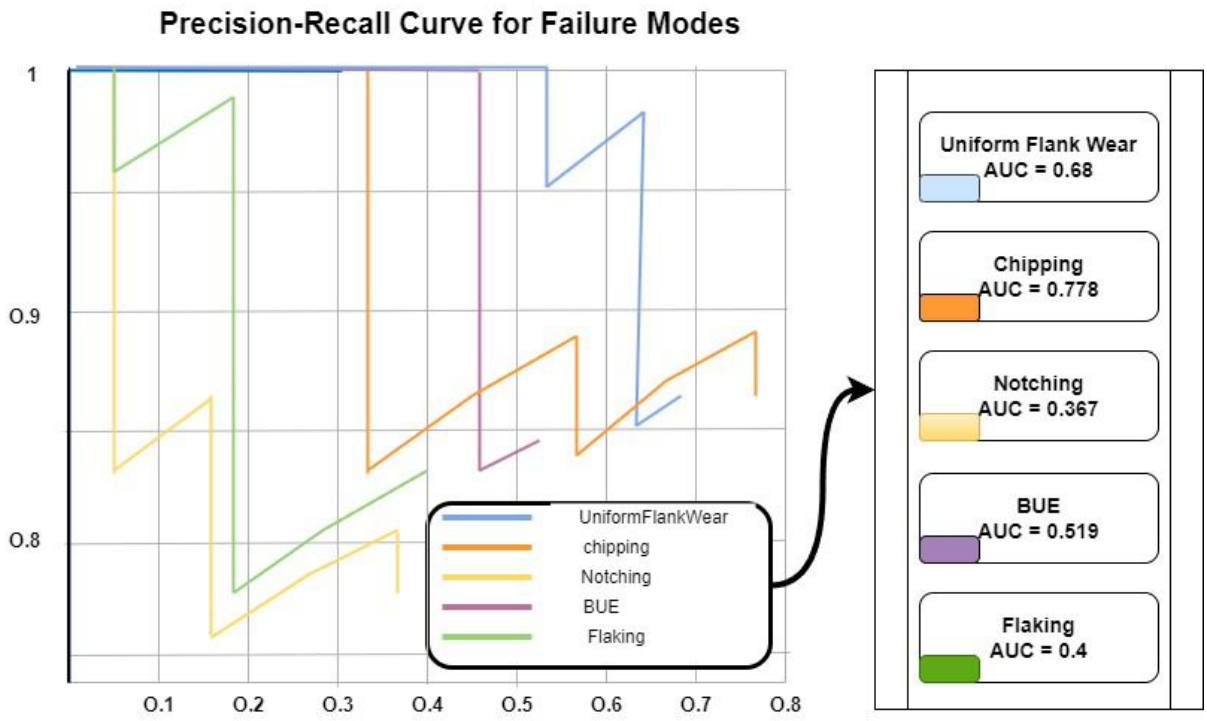

Figure 6.9: *Precision-recall curve for YOLOv3-TWDM during online failure modes detection for the first condition of* $V_c = 100m/min$, $f_t = 0.15mm/tooth$, *and* $a_p = 0.9mm$

wear area, the YOLOv3-TWDM model was employed to assess the extent of flank wear depth (Bh_FW), as well as chipping width and depth ($Bh_{chipping}$ and $Bw_{chipping}$). These measurements served as supplementary indicators of tool life during machining. It was observed that the detected values showed a fair correlation with the actual features for all the replicates.

The detected Bh_{FW} (flank wear width) had an average R^2 of 75%, with RMSE, MAE, and MAPE of $62.25\mu m$, $9.9\mu m$, and $11.75\mu m$, respectively (Table 6.4). Although the performance was above average (with $R^2 > 50\%$), it was not as good as the previous two conditions, which were obtained within the vicinity of the training conditions. The average deviation (μ_{Res} and σ_{Res}) values were $35\mu m$ and $38.5\mu m$, respectively, which were higher than the values obtained in the previous conditions. At this condition, there was a rapid progression of tool flank wear, characterized by continuous edge loss, built-up edge (BUE) formation, and progressive chipping. The continuous edge loss and progressive chipping were attributed to the high cutting forces and intense precipitation hardening effects at the highest cutting speed and temperature. The formation of BUE further exacerbated the situation, as it continuously got plucked together with the chip flow during machining. Thus, the synergistic effect of cyclic adhesion and severe abrasion caused rapid evolution of failure modes, leading to a reduction

in the uniform progression of the wear region and Bh_{FW} during face milling of Inconel 718.

Table 6.4: The statistics of Failure Modes magnitudes at $V_c = 100m/min$, $f_t = 0.15mm/tooth$ and $a_p = 0.9mm$: For $Bh_{FW}^{(1)}$, (1) represents first replicate, whereas for $Mean_{a,p}$, a and p represent the actual and detected values

Metric	μ_a	μ_p	μ_{Res}	σ_a	σ_p	σ_{Res}	RMSE	MAE	MAPE	R^2
$Bh_{FW}^{(1)}$	260	251	9	211	235	24	16.5	1.05	1.5	78
$Bh_{FW}^{(2)}$	281	220	61	249	196	53	108	18.75	22	71.8
$Bh_{chipping}^{(1)}$	158	156	2	178	138	40	3.9	23.85	62.5	93.3
$Bh_{chipping}^{(2)}$	222	184	38	268	224	44	69	30.85	8.5	82.8
$Bw_{chipping}^{(1)}$	568	467	101	425	247	178	181	100.75	13.2	86.5
$Bw_{chipping}^{(2)}$	569	461	108	502	412	90.5	194.4	86.95	12.2	68.7
$Bh_{FW(Avg)}$	21	235	35	230	215	38.5	62.25	9.9	11.75	75
$Bh_{chip(Avg)}$	190	170	20	223	181	42	36.45	27.35	35.5	88.05
$Bw_{chip(Avg)}$	569	464	104.7	463.7	329.5	134.2	187.7	93.85	12.7	77.6

The evolution of the detected $Bh_{chipping}$ (chipping depth) exhibited a similar rapid trend, but showed a slightly better correlation with the actual values compared to the Bh_{FW} feature. The R^2 value was 88.05%, with RMSE, MAE, and MAPE values of $36.45\mu m$, $27.35\mu m$, and 35.5μ, respectively. The average deviation values were $\mu_{Res} = 20$ and $\sigma_{Res} = 42$, with the average mean lower and the standard deviation higher than that of Bh_{FW}. Overall, the prediction of $Bh_{chipping}$ was better than that of Bh_{FW} because progressive chipping emerged at the early cutting stage for the highest cutting condition. On the other hand, the evolution of the detected $Bw_{chipping}$ (chipping width) resulted in an R^2 value of 77.6%, with RMSE, MAE, and MAPE values of 187.7, 93.85, and 12.7, respectively. These values were slightly lower than those of $Bh_{chipping}$ but higher than those of Bh_{FW}. The average deviation values were $\mu_{Res} = 104.75$ and $\sigma_{Res} = 134.25$, indicating a large deviation between the actual and predicted values. However, this condition was attributed to the large values of $Bw_{chipping}$ throughout the entire experiment. As previously mentioned, the synergistic impact of high cutting forces due to intense precipitation hardening at high cutting speeds and temperatures, combined with cyclic abrasion caused by continuous BUE formation at the largest feed/tooth and chip load, exacerbated the formation of chipping even in the early cutting stages, leading to rapid tool failure during machining.

6.2.2 Flank Wear Prediction

Just like failure modes detection and features detection above, the ML-based MV-TCM was also substantiated by predicting VB progression online. This was achieved by conducting experiments at various processing conditions to ensure that the ML-based MV-TCM was robust enough to predict VB progression within the vicinity of the training conditions (all the process parameters are within the range used during the training process) and outside the vicinity of the training conditions (at least one of the significant process parameters is outside the range used during the training process). The experiments were repeated to show the reproducibility of the predicted against the actual data, as well as the reliability of the system for industrial use. It is also worth noting that the data used in these tables, as well as *Appendices F.1, F.2, and F.3* contain the mean values of all 4 cutting inserts.

Condition 1 *[$V_c = 40m/min$, $f_t = 0.08mm/tooth$, $a_p = 0.9mm$]*: After validating the performance of YOLOv3-TWDM for features extraction, the detected failure modes augmented with Fi feature, speed, feed, depth of cut, and cutting length to predict the VB progression through the utilization of the DFSV-ML. Considering that the process parameters were fixed ($V_c = 40m/min$, $f_t = 0.08mm/tooth$, $a_p = 0.9mm$, and $a_e = 12.5mm$), the VB progression was susceptible to changes in the cutting length and wear morphology, whose features consists of the F_i magnitude and failure modes. It was noted that the predicted agreed with the measured VB values as shown in *Appendix B.1*. The performance of the DFSV-ML is presented in Table 6.5. It shows that an average R^2 across the replicates was 97%, indicating a strong correlation between the predicted and actual VB values. The parity plots for estimated R^2 are shown in *Appendix B.2*. The minor deviations were attributed to the absence of chipping, notching, and flaking in the early cutting stages, which made it difficult for the ML model to generate accurate predictions. The lack of significant changes in the failure modes led to over-generalization of the ML model as it assumed that the uniform flank wear (UFW) was the dominant failure mode across all VB stages. However, after several training iterations, the model adapted to the changes in failure modes, with more emphasis on the failure modes, such as chipping, notching and flaking, as significant predictor variables of VB progression in the critical and failure stages.

Even though the DFSV-ML adapted to VB prediction, the deviations between actual and

Table 6.5: The statistics of VB $V_c = 40m/min$, $f_t = 0.08mm/tooth$, and $a_p = 0.9mm$: For $VB^{(1)}$, (1) represents first replicate, whereas for $Mean_{a,p}$, a and p represent the actual and predicted values

Metric	μ_a	μ_p	μ_{Res}	σ_a	σ_p	σ_{Res}	RMSE	MAE	MAPE	R^2
$VB^{(1)}$	131.1	138.6	7.5	87.4	85.7	1.99	31.1	10	7.6	97.97
$VB^{(2)}$	171.5	157.4	14.1	153	112.5	40.5	54.4	27.7	1.59	95.25
VB_μ	151.3	148	10.8	120.2	99.1	21.2	42.75	18.85	4.6	97

predicted values were still persistent across the cutting process. These persistent errors were as well caused by the fluctuation in F_i magnitudes due to inconsistent energy layers in the critical and failure regions, which were attributed to failure modes, such as notching, flaking and chipping. However, the fluctuation of the F_i magnitude was compensated by the consistent evolution of the failure modes as nominal descriptors of the flank wear region, and this demonstrated the robustness of the DFSV in representing the complex flank wear morphology during face milling of Inconel 718. It was observed that the average MAPE and RMSE of 4.6% and $42.75\mu m$, indicating high predictive efficiency of VB for all replicates during in-process MV-TCM application. In addition, the average deviations were $\mu_{Res} = 10.8$ and $\sigma_{Res} = 21.2$, indicating high repeatability of the results across the replicates. Finally, the R^2_{VB} value was 97%, indicating high correlation of the predicted and actual VB.

Condition 2 [$V_c = 60m/min$, $f_t = 0.08mm/tooth$, $a_p = 0.9mm$]: To further validate the reliability of the system in predicting VB progression within the vicinity of the training conditions, the ML model was tested at a medium speed of 60 m/min, a feed of 0.08 mm/tooth, and an ADOC of 0.9 mm. Again, under these fixed conditions, the VB progression was susceptible to changes in the cutting length and wear morphology. Similar to the 40 m/min test, the predicted values agreed with the measured VB values at this condition, with an R^2 value, RMSE, and MAPE of 93%, $27.97\mu m$, and 11.9%, respectively (Table 6.6). The results showed a strong correlation between the predicted and measured values. The minor deviations of $\mu_{Res} = 9.3$ and $\sigma_{Res} = 6.4\mu m$ were attributed to the inconsistent evolution of the flank wear region due to micro-chipping and notching, which distorted the energy layers, affecting the rate of F_i and Bh_FW evolution in the critical and failure stages. This exacerbated the magnitudes of $Bh_{chipping}$ and $Bw_{chipping}$, highlighting the significance of using the magnitudes of chipping wear as indicators of tool life. This means that even if the VB was not accurately predicted at this point, the failure criteria and tool life could still be predicted by utilizing the magnitudes

of $Bh_{chipping}$ and $Bw_{chipping}$ in the critical and failure wear stages. Nevertheless, the small deviations between the actual and predicted values indicated high repeatability of the results during in-process MV-TCM application. Furthermore, the high correlation and minor deviations between the predicted and measured VB validated the robustness and repeatability of the DFSV-ML in predicting VB progression during in-process MV-TCM application.

Table 6.6: The statistics of VB at $V_c = 60m/min$, $f_t = 0.08mm/tooth$, and $a_p = 0.9mm$: For $VB^{(1)}$, (1) represents first replicate, whereas for $Mean_{a,p}$, a and p represent the actual and predicted values

Metric	μ_a	μ_p	μ_{Res}	σ_a	σ_p	σ_{Res}	RMSE	MAE	MAPE	R^2
$VB^{(2)}$	154.7	148	6.7	135.9	127.7	8.2	20.1	14	12.8	94
$VB^{(1)}$	125.5	113.6	11.9	80.55	75.9	4.65	35.83	11.94	10.38	92.65
VB_{μ}	140.1	130.8	9.3	108.225	101.8	6.42	27.97	12.97	11.59	93

Condition 3 [$V_c = 100m/min$, $f_t = 0.15mm/tooth$, $a_p = 0.9mm$]: After considering the variations in the working conditions of the CNC milling machine, another test was conducted to further validate the system. This time, the parameters were selected outside the vicinity of the training range. To ensure the process parameters were outside the vicinity of the training range, they were selected above the maximum speed and feed/tooth (which is $V_c = 80m/min$ and $f_t = 0.13mm/tooth$). This condition include $V_c = 100mm/tooth$, $f_t = 0.15mm/tooth$, and $a_p = 0.9mm$. By predicting the VB progression under this condition, it was believed that the model could perform outside the vicinity of the dataset used to train the ML model in this research, hence robust enough to extrapolate VB under unknown cutting conditions. The predicted still agreed with the measured VB values with an average R^2, RMSE, and MAPE of 81%, $55.2\mu m$, and 6.7%, which was still an above average score, especially considering that the condition applied was outside the range of the training parameters (Table 6.7). The average deviations were $\mu_{Res} = 31.9$ and $\sigma_{Res} = 42.1$, which were higher than the previous conditions. However, in view of the fact that Bh_{FW} was also used to detect the progressive change in the VB, the DFSV-ML showed a higher performance as compared to the YOLOv3-TWDM. This means the diverse features synergistically contributed to the accurate VB prediction during face milling of Inconel 718. Thus, this research demonstrates the robustness of the DFSV in representing the evolution of the complex wear morphology during face milling of Inconel 718.

However, the deviations of the actual from predicted values were attributed to several

Table 6.7: The statistics of VB at $V_c = 100m/min$, $f_t = 0.15mm/tooth$, and $a_p = 0.9mm$: For $VB^{(1)}$, (1) represents first replicate, whereas for $Mean_{a,p}$, a and p represent the actual and predicted values

Metric	μ_a	μ_p	μ_{Res}	σ_a	σ_p	σ_{Res}	RMSE	MAE	MAPE	R^2
$VB^{(1)}$	260.3	253.7	6.6	211.4	221.8	10.4	10.4	26	8.57	83.7
$VB^{(2)}$	281.6	224.4	57.2	249.3	175.5	73.8	100	86.95	4.9	78.5
VB_μ	271	239	31.9	230.4	198.7	42.1	55.2	56.5	6.7	81

factors. The tools experienced high cutting force due to high rate of precipitation hardening effect at high cutting speed and temperature. This exacerbated failure modes, such as chipping and BUE, which caused rapid evolution of the flank wear progression during machining. However, such failure modes also induced heterogeneous pixel distribution and unstructured energy layers, which fluctuated the rate of F_i and Bh_{FW} evolution in the early cutting stages. Furthermore, it was observed that some failure modes, such as BUE, notching, and flaking, were not detected during the machining process due to rather changes in the location and shape as such samples were not common in the training dataset (*Appendix B.2*). This was attributed to less scenarios of BUE, notching, and flaking in the training dataset as such failure modes were not common in the early and uniform wear stages. Due to low detection rate of these failure modes, the DFSV-ML's performance was somehow affected, leading to either under- or over-generalization of the output. This could be avoided with an increased number of notching, flaking, and BUE samples in the training dataset. In the meantime, it is believed that the model still has high detection rate for uniform flank wear and chipping, which were reported as dominant failure modes during face milling of Inconel 718 [74], as well as throughout the entire experiment in this study. Therefore, the model is robust enough in detecting dominant failure modes and predicting the average flank wear depth (VB) as key indicators of tool performance.

6.2.3 Evaluating the Processing Time

The time complexity is another aspect to be validated in this research to consider minimum processing speed and maximum acquired information during ML-based MV-TCM application. However, the ML-based MV-TCM was compared to the conventional method, which took an average time (Conv. T_c) of 900 s for every experimental run. By considering that time is a

determinant of tool productivity rate, justifying the fraction of time the ML-MV-TCM process took over the total conventional time was very crucial as it ensured the minimum delay during in-process tool performance control and optimization. The detailed analysis of the processing time is presented in Table 6.8. The cutting time and processing time by binary classifier were almost constant in each iteration, whereas the multi-sectional SVD and YOLOv3-TWDM were time-variant due to inconsistent number of wear inserts. However, due to a linear trend in the time response, the models had a slightly higher computational cost but could not crash under an unexpected increase in the number of flank wear images.

Table 6.8: Time Analysis for in-process ML-MV-TCM application

Images	Conv. T_c	YOLOv3	BC	T_c	T. Reg.	ML Time	Total	% Reduction
4	900	20.9	4.9	248.7	60	25.8	334.5	63
8	1800	27.1	7.4	248.7	60	34.5	343.2	81
12	2700	32.6	10.7	248.7	60	43.3	352.0	87
16	3600	38.7	14.4	248.7	60	53.0	361.8	90
20	4500	45.8	17.9	248.7	60	63.7	372.5	92
24	5400	52.3	21.4	248.7	60	73.7	382.4	93

Therefore, the total processing time, including the time to cut Inconel 718, register at the camera's location, binary classification, and ML models (especially in a case where 5-9 images were classified and detected) varied between 334.545 and 382.442 seconds (Where 25.803 - 73.700 sec was a range for the ML models, 248.742 sec was the total cutting time (T) of an incremental length of 400 mm, and 60 sec is the time for tools registration (Tool Reg.) at the focal coordinate), with an allowable tolerance of $+/-2\,sec$. Therefore, the ML-based MV-TCM takes approximately 25.64% to 35% of the total time, with 7.7 - 19.27% for ML models and 17.9 - 15.69% for tool registration to the MV-TCM set-up. Therefore, considering that the conventional method took 3150 sec on average to process 14 images, the ML-based MV-TCM system reduced the processing time by 84.3%. It was also worth noting that the processing time could be minimized further by improving the system's robustness with more control mechanisms, such as the implementation of automatic pattern matching algorithm, which can precisely select the actual wear inserts, thus reducing the number of images to be transmitted to and processed by the ML models.

6.3 In-process Control of Tool Wear Evolution

After validating the ML-based MV-TCM system with the conventional method, the in-process experiment was further extended to control the flank wear and chipping magnitudes at different wear levels by manually regulating the cutting speed and feed rate. At this point, only the CMOS industrial camera was used to acquire online data and no actual measurement was conducted. During this process, the YOLOv3-TWDM was used to detect the failure modes, which were inductively used to predict the wear mechanisms by an inductive-reasoning algorithm. These failure modes and wear mechanisms were used as predictor variables of the sub-optimal process conditions, including inappropriate level of the cutting speed and feed rate. Thus, upon detecting these features, the Limiting Threshold Values (LTV) of different flank wear features established in Table 5.2 were used to determine the wear levels for in-process adjustment of the cutting speed and feed rate. This means the incremental cutting length of 400 mm was no longer observed at this point to reduce the processing time because modulating these parameters empirically is time-consuming as it involved adjusting the G-code of the CNC machine [379].

According to the observations made in Chapter 4, the uniform flank wear, whose depth was detected as F_i and Bh_{FW} in this research, was the most preferred failure mode in face-milling Inconel 718. For this reason, the abrasion wear, which is the main causative mechanism for the uniform flank wear progression [294], was supposed to be minimized to reduce and control the evolution of $Bh_{chipping}$ and $Bw_{chipping}$ magnitudes, especially in the uniform wear stages, thereby enhancing tool life extension during face milling of Inconel 718. Therefore, the lowest speed below 40 m/min was selected due to its influence in reducing the cutting temperature and friction, thus, minimizing the severe abrasion wear mechanism, as well as the evolution of the $Bh_{chipping}$ and $Bw_{chipping}$ magnitudes, especially in the early and uniform wear stages. On the other hand, the feed rate below 0.08 mm/tooth reduced cyclic adhesion and Built-Up Edge (BUE) formation due to moderate chip load, especially in the critical and failure regions. The result of such wear phenomenon is the low rate of $Bh_{chipping}$ and $Bw_{chipping}$ evolution, especially in the critical and failure region as no significant adhesive and BUE particles got removed by severe abrasion and aggressive chip flow during machining [64].

In addition, the ADOC greater than 0.9 mm reduced the localized chipping in the DOC region, making the tools survive more impact forces at the lowest speed and feed/tooth. Nevertheless, the findings in Chapter 4 revealed that the ADOC had minimum influence on the evolution of wear mechanisms, hence, it was fixed at 0.9 mm as this value promised the highest tool life according to the contour plots designed by GKRR model in *Appendix C.5*. Therefore, the cutting speed of 35 and 40 m/min, and the feed rate of 0.06, 0.07, and 0.08 mm/tooth were selected in this research as significant levels of speed and feed, whose synergy would extend the tool life, according to the GKRR contour plots. Figure 6.10 shows the progressive change in the failure modes magnitudes after regulating the speed and feed at various wear levels until the failure criteria. Therefore, the speed and feed were regulated using two strategies: (1) one-time adjustment ([speed, feed] was adjusted once throughout the entire experiment to simulate the typical approach in conventional, evolutionary, and soft-computing strategies) and (2) multi-stage adjustment ([speed, feed] was adjusted several times at different wear stages – early, uniform, critical, failure), a strategy proposed in this research.

6.3.1 One-time adjustment of speed and feed

The one-time speed and feed adjustment was first performed at a condition of 40 m/min and feed of 0.08 mm/tooth, which was the initial optimal condition designed by the GKRR model, and slightly higher than optimal values obtained in Chapters 4 and 5. It was perceived that the tools sustained a moderate temperature, friction, and chip load, which were attributed to the moderate BUE and BUL formation on the tool's cutting edge. The moderate chip load and speed resulted in high friction and plastic deformation, which exacerbated the asperities deformation and galling in the early and uniform wear stages, producing a protective layer superjacent to the TiAlN/NbN coating. This layer prevented the tool's coating or substrate from further degradation or chipping wear by reducing the impact of severe abrasion wear mechanism in the subsequent passes of the machining process. As a result, tools at this condition experienced the lowest F_i and F_{FW} magnitudes in the uniform wear region, as shown in Figures 6.10a and 6.10b. However, the moderate chip load at 0.08 mm/tooth feed rate exacerbated the cyclic adhesion and abrasion, which resulted in the high evolution of the chipping magnitudes ($Bh_{chipping}$ and $Bh_{chipping}$) in the critical and failure regions (Figures 6.10c and

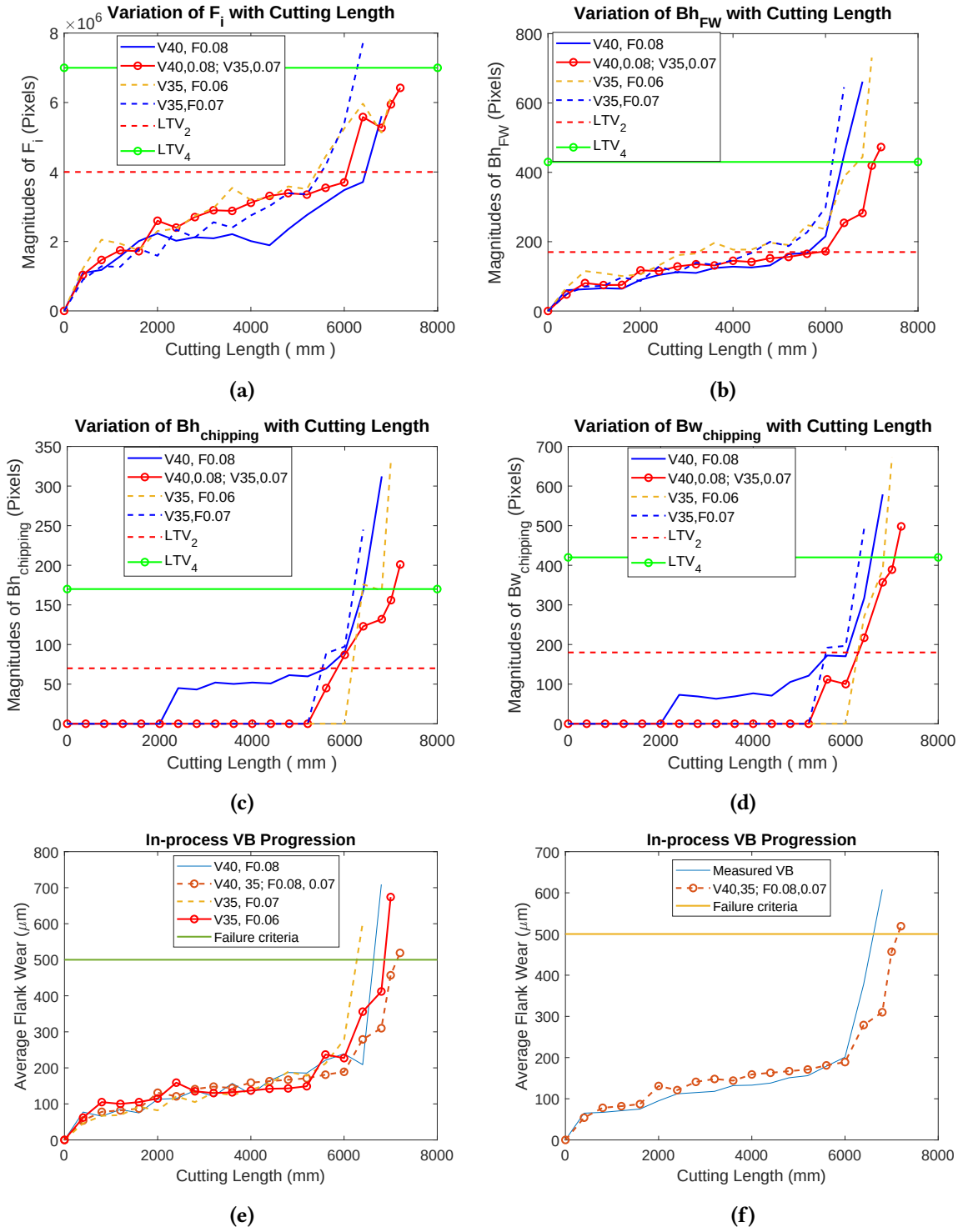

Figure 6.10: *The predictive control of flank wear evolution at various speeds (V_c or V m/min) and feeds (f_t or F mm/tooth): (a) evolution of F_i; (b) evolution of Bh_{FW}; (c) evolution of $Bh_{chipping}$; (d) evolution of $Bw_{chipping}$; (e) the predicted VB, and (f) the predicted and measured VB at a multi-stage optimal cutting condition*

6.10d), thus, reducing the overall cutting length during machining.

After randomly reducing the speed from 40 to 35 m/min and feed from 0.08 to 0.07 mm/tooth, the tools experienced low friction, galling, plastic and asperities deformation due

to low temperature and reduced chip load on the tool's cutting edge. This reduced the BUE, thereby preventing the formation of the protective layer superjacent to the TiAlN/NbN coating, making the rate of tool degradation faster as compared to the 40 m/min and 0.08 mm/tooth. Although this wear phenomenon minimized the evolution of the chipping magnitudes in the critical and failure wear stages (Figures 6.10c and 6.10d), the absence of the protective layer hastened the rate of F_i and Bh_{FW} progression due to abrasion wear mechanism, especially in the early cutting stages.

By further decreasing the feed rate to 0.06 mm/tooth, the deleterious effects of intense friction and rubbing action further reduced the rate of $Bh_{chipping}$ and $Bw_{chipping}$ evolution in the early cutting stages. Contrary, such wear phenomenon also increased the energy layers on the wear region, leading to high F_i and Bh_{FW} evolution (Figures 6.10a and 6.10b). Nevertheless, it reduced the impact of the cyclic adhesion and severe abrasion wear mechanisms, which, in the long run, minimized the progressive chipping in the critical wear stage as no BUE was plucked together with chip flow. This yielded a longer cutting length in the critical and failure regions as compared to 40 m/min and 0.08 mm/tooth. Therefore, it can be seen that the 40 m/min and 0.08 mm/tooth yielded a better performance in the early cutting stages, whereas 35 m/min and 0.07 mm/tooth yielded a better performance in the critical and failure stages. As a result, one more round of experiment was conducted to apply this multi-stage adjustment of speed and feed.

6.3.2 Multi-stage adjustment of speed and feed

During this phase, the moderate VB rate in the critical and failure wear regions at 35 m/min and 0.07 mm/tooth was harmoniously blended with the success of 40 m/min and 0.08 mm/tooth in reducing the tool degradation, especially in the early cutting stages. As previously observed, the former minimized the cyclic adhesion, thus, mitigating the impact of the chipping magnitudes in the critical and failure regions. On the other hand, the latter was employed in the initial and steady wear stages due to the moderate chip load, which induced intense rubbing, asperities deformation, and galling to produce an additional protective layer superjacent to the TiAlN/NbN coating. This prevents the uncontrolled failure of the multi-layer PVD-TiAlN/NbN coated carbide inserts during face milling of Inconel 718. As a result, a multi-

stage adjustment of speed and feed was found to be more effective in consistently yielding the longer cutting length and low VB rate throughout the wear stages as compared to one-time adjustment. Therefore, by utilizing the detections of the YOLOv3-TWDM to predict the wear mechanisms and devise process conditions through the utilization of the inductive-reasoning algorithm, this research necessitated the speed and feed to be regulated at least twice to consistently minimize the VB rate and enhance tool life extension during machining.

In summary, after plotting the graph of predicted Bh_{FW} (designated as predicted VB) and measured VB at this optimal condition Figure 6.10f, the estimated MAPE, R^2, and RMSE for the predicted VB was 5.678%, 87.89%, and $32.61\mu m$, indicating a reasonable agreement between the predicted and measured VB values at the optimal processing condition. Considering that the conventional method achieved the maximum cutting length of 4400 mm, at the optimal cutting condition of $V_c = 40m/min$, $ft = 0.07mm/tooth$, and $a_p = 1mm$, the GKRR optimal condition achieved a length of 4600 mm, signifying a tool life extension of 4.5%, making it more efficient in predicting and optimizing VB rate under limited dataset. On the other hand, the YOLOv3-based MV-TCM achieved an average cutting length of 6133 mm at the same optimal condition of $V_c = 40m/min$, $f_t = 0.08mm/tooth$, and ADOC = 0.9 mm, thereby extending the tool life by 39.39% (relative to the conventional method) and 33.33% (relative to the GKRR soft-computing method). Furthermore, the method applied in this research was informed by the real-time changes in the microstructures (in-process evolution of wear mechanisms and failure modes) in selecting or designing the promising cutting condition. This makes the proposed system more significant in enhancing the in-process tool performance control and optimization, as the detected failure modes can be used to decipher the sub-optimal processing parameters, which have shown that upon adjustment, can improve the performance of the carbide inserts during face milling of Inconel 718. After further conducting the multi-stage parameters adjustment to minimize the evolution of flank wear and chipping magnitudes, the tool life was further extended by 17% (6133 to 7200 mm).

6.4 Comparing the ML-based MV-TCM with GKRR

GKRR Cross Plots Analysis: Considering the competitive nature of the GKRR model with the proposed ML-MV-TCM, a comparison was made to authenticate the system's robustness against known conventional and soft computing techniques. The GKRR model was developed by the same experimental data obtained in Chapter 4. Table 6.9 shows the statistics of features used to train GKRR model.

Table 6.9: The statistics of each feature used to establish the optimum cutting parameters

Feature	Maximum	Minimum	Average	Standard deviation	Unit
Flank wear (VB)	674	0	41.4	114.5	µm
Cutting speed (V)	100	0	41.0	27.5	m/min
Feed rate (f_t)	0.15	0	0.07	0.05	mm/tooth
Axial depth of cut (a_p)	1.5	0	0.6	0.4	mm
Cutting length (L)	5400	0	1179	1199	mm

The GKRR model's evaluation from full-fit (RMSE = $30.9\mu m$ and $R^2 = 0.93$) and 5-fold CV test (RMSE = $49.7\mu m$ and $R^2 = 0.81$) suggested that the model had some predictive ability (see *Appendix C.1*). The model's fitting quality was evaluated by cross-plot analysis, which visualized the relationship between multi-variables. *Appendix C.2, C3, and C4* show the cutting length cross plots at cutting speed of 40, 60, and 80 m/min, respectively. Values in parenthesis, i.e., (X,Y,Z), shown in the each plot represents cutting speed, feed rate, ADOC, respectively, which were held constant during evaluation. The scattered point and the solid line in the plot represent the measured and ML predicted VB data, respectively. In general, all the predicted data agreed well with the measured VB in Chapter 4. At the lowest cutting speed of 40 m/min and the lowest feed rate of 0.07 mm/tooth, the VB profile exhibited four stages – (1) rapid VB formation due to break-in of the tools when cutting initializes, (2) a slow increase in VB in the middle of the cutting length due to minimum plastic deformation and wear mechanisms, (3) increasing VB acceleration due to the synergistic wear mechanisms, and (4) rapid VB rate due to severe chipping and permanent material loss as the tools approach the failure criteria.

The observed profiles were consistent with the literature finding that flank wear evolves as early rapid wear, uniform wear, critical and failure region. While increasing the feed rate from 0.07 to 0.13 mm/tooth, the above-mentioned stage 2 gradually vanished. In this case,

VB accelerated into the rapid failure region after the initial break-in, indicating a high tool deterioration rate caused by severe wear mechanisms and failure modes. When the cutting speed was increased to 80 m/min, all the VB profiles exhibited the type in which only stage 1 and stage 3 existed even at the lowest feed rate. These profiles suggest that face milling of Inconel 718 at such a high speed would cause severe wear mechanisms and failure modes on the tool's cutting edge, which was not feasible for real applications. This viewpoint is consistent with literature findings, but this was the first time that a quantitative VB profile of PVD-TiAlN/NbN coated tools was possible in terms of the multiple cutting parameters. More detailed mechanistic study of these VB profiles was presented in Chapter 4.

GKRR Optimization Design by Contour Plots: As previously discussed that the ADOC less than 0.75 mm exacerbated $Bh_{chipping}$ and $Bw_{chipping}$ due to severe abrasion on the precipitation-hardened layer, an ADOC of 0.9 mm was thus selected to plot the VB contour diagram at various cutting speeds, feeds, and cutting lengths. Figures a to f in *Appendix C.5* show the VB contour plots at various cutting speeds. The red hollow circle represents $VB < 500\mu m$ at the given cutting condition. The convenience of the VB contour diagram was to visualize the promising cutting condition space where the minimum VB, minimum cutting time and maximum material removal rate could be achieved. For instance, at ADOC of 0.9 mm, cutting speed of 30 m/min, and feed rate of 0.1 mm/tooth, removed depth of 50 mm with cutting time of $ca.$ 60 min was required and VB was less than the $500\mu m$ criteria. On contrary, at ADOC of 0.9 mm, cutting speed of 80 m/min, and feed rate of 0.05 mm/tooth, removed depth of $< 15mm$ and VB exceeded the $500\mu m$ criteria. Based on the contour property plot shown in *Appendix C.6*, a promising condition at the cutting speed of 40 m/min, feed rate of 0.08 mm/tooth, and ADOC of 0.9 mm was designed. These parameters were relatively consistent with the findings presented in Chapters 4 and 5, where the cutting speed of 40 m/min, the feed of 0.07 mm/tooth, and ADOC of 1 mm mitigated the severity of failure modes magnitudes during face milling of Inconel 718.

The ML model predicted that cutting at this condition can extend tool life, achieving the cutting depth of 43 mm within 50 minutes before VB reached $500\mu m$. The GKRR statistics along with the cross-plot analyses suggested that the model captured the correct VB profile, which was consistent with the findings in Chapter 4. The GKRR was further applied to design

the desirable processing conditions, where a speed of 40 m/min, feed rate of 0.08 mm/tooth, and ADOC of 0.9 mm minimized the rapid evolution of wear mechanisms and failure modes in the early and uniform wear regions (as presented in *Appendix C.7*). To further confirm this condition, a parallel experiment was performed to validate the designed cutting condition. Figure 6 shows the VB progression with respect to the cutting length diagram. The scatted points are the measured VB while the solid line is the ML predicted VB. There were some discrepancies between the measured and the predicted data. Before the cutting length of 3000 mm, the prediction was underestimated, while after that, the prediction was overestimated. It was until cutting length of 4400 mm that the prediction agreed well with the measured one. Although there was an error of ca. $100\mu m$ at cutting length of 4000 mm, overall, these errors were considered minor.

After the experimental validation, it was confirmed that the newly designed cutting condition yielded a removed depth of 42 mm in 47 minutes with a maximum VB of $551\mu m$. *Appendix C.7* shows the microstructure of the tool's cutting edge after facing-milling up to 4600-mm cutting length. *Appendix C.7a* shows the optical micrograph of the tool exhibiting the uniform flank wear at cutting length of 1200 mm. When the cutting length reached 4000 mm, a progressive chipping occurred in the failure region as shown in *Appendix C.7b*. It was attributed to synergistic effect of abrasion and cyclic adhesion on the tool's cutting edge [375]. BUE or built-up layer (BUL) formation accelerated progressive chipping as BUE got plucked by the subsequent cut [64], as shown in *Appendix C.7c* and *d*, when the cutting length reached 4400 and 4600 mm, respectively. The small chip load also reduced the cutting force and cyclic adhesion by BUE or BUL formation. *Appendix C.7e* and *e* show SEM image of the dotted-line region in *Appendix C.7c* and *d*, respectively. The microstructure revealed that the localized chipping in the failure region was caused by abrasion and cyclic adhesion.

Therefore, considering that the conventional method achieved the maximum cutting length of 4400 mm, at the optimal cutting condition of V_c =40 m/min, f_t =0.07 mm/tooth and ADOC of 1 mm, the GKRR optimal condition extended the tool life by 4.5%. Hence, it was more efficient in optimizing the tool performance as compared to the conventional method. The complexity of the GKRR primarily includes predicting flank wear evolution in a high dimensional space where the practical processing parameters were used. Even though it was only informed by

the cutting conditions with a small amount of data, it still predicted the correct VB profile, and deciphered its complex physics. Thus, it was competitive to the proposed ML-based MV-TCM system, as both could predict VB profile and select the desirable cutting condition under limited datasets. However, the ML-based MV-TCM achieved an average cutting length of 6133 mm at the same optimal condition of V_c =40 m/min, f_t =0.08 mm/tooth and ADOC = 0.9 mm, thus extending the tool life by 39.39% for conventional methods, and 33.33% for GKRR. After further conducting the multi-stage parameters adjustment to minimize the evolution of the failure modes magnitudes, the tool life was further extended by 17.39% (6133.333 to 7200 mm), exceeding the performance of the conventional and GKRR methods by 63.63% and 56.52%, respectively.

As it can be noted, the ML-based MV-TCM yielded better tool performance as compared to both the conventional and GKRR method despite both being conducted at relatively the same cutting conditions. Though this was not thoroughly investigated in this research, it was believed that the combined effect of fully interrupted cutting operation, manual handling of tools, and chemical treatment during conventional method induced further degradation on the unused sides of the tool inserts, thus lowering the tool's strength, exacerbating the wear mechanisms and failure modes during machining. Just like the conventional method, the GKRR data was also collected using the interrupted cutting operation. In addition, the feature engineering technique applied when training GKRR model was not informed by the microstructural evolution of wear mechanisms and failure modes. This limited its ability to capture the actual behaviour of the flank wear evolution during face milling of Inconel 718. In this regard, the ML-based MV-TCM and the conventional approach were still more imperative for the predictive control of flank wear evolution as compared to the soft computing method of GKRR model. They were able to predict the causative mechanisms of sub-optimal tool performance through the in-process detection of wear mechanisms and failure modes. To summarize this, an evaluation matrix was designed in Table 6.10 to compare the general characteristics of these methods. The detailed analysis of the scoring metrics applied to distinguish the performance of the models is presented below Table 6.10.

Predictive Efficiency–Accuracy and Processing Speed: Predictive efficiency refers to a model or system's ability to make accurate predictions based on historical data. This metric

Table 6.10: Comparing the predictive performance: [Opt1– ML-based MV-TCM; Opt2– Gaussian Kernel Ridge Regression; Opt3: Conventional Measurement]

Evaluation Matrix for the predictive models									
Criteria	Opt1	Opt2	Ref	Opt1	Ref	Opt3	Ref	Opt2	Opt3
Accuracy	-1	-1	x	-1	x	1	x	1	1
Features diversity	-1	-1	x	1	x	1	x	-1	1
Feasibility	1	1	x	0	x	-1	x	0	-1
Predictive Efficiency	1	1	x	0	x	-1	x	0	-1
Processing Speed	1	1	x	1	x	-1	x	-1	-1
Repeatability	-1	-1	x	1	x	1	x	-1	1
Cost-effectiveness	1	1	x	0	x	-1	x	0	-1
Reliability	1	1	x	1	x	-1	x	-1	-1
Simplicity	1	1	x	1	x	-1	x	-1	-1
Inductive-Reasoning	1	-1	x	1	x	1	x	-1	-1
Adaptability	1	1	x	1	x	-1	x	-1	-1
Overall $\sum$+ve Scores	7	6	x	7	x	5	x	1	4
Overall $\sum$ 0 scores	0	0	x	3	x	0	x	3	0
Overall $\sum$-ve Scores	4	5	x	1	x	6	x	7	7

gauges the accuracy of the model, and it is evaluated by comparing the predicted with measured values. While a system/model might perform well in predicting flank wear evolution in the vicinity of the training dataset, unprecedented circumstances or new data might render the model useless. Based on the outcome of this research, the GKRR had a comparable performance [training (RMSE = $30.9\mu m$ and $R^2 = 0.93$) and 5-fold CV offline validation (RMSE = $49.7\mu m$ and $R^2 = 0.81$)], to the ML-based MV-TCM system [offline validation ($R^2 = 96.52\%$, $RMSE = 45.5\mu m$, MAPE = 2.36%) and in-process validation (MAPE, R^2, and RMSE was 3.52%, 97%, and $29.09\mu m$)]. Except for the optical microscopes, which was a datum at this point, the two techniques were adept at providing similar predictive efficiency offline, except that the ML-based MV-TCM could be used for in-process tool wear prediction and control during face milling of Inconel 718.

Features Diversity: Feature diversity refers to the multiplicity of the features that capture various aspects of the flank wear phenomenon under different cutting conditions. This was critical since it enhanced the performance and resilience of ML models applied in MVTCM. If all the features utilized in a model are interconnected or superfluous, the model may become exclusively specific to a particular data subset, thus making it difficult to generalize to new data from the new cutting conditions. Conversely, if the features are diverse and encapsulate vari-

ous information of the flank wear morphology, the model was likely to identify the underlying patterns and make accurate predictions on new data. Based on this description, the conventional method had the most diverse features. That is why its data was used to train, as well as validate both GKRR and ML-based MV-TCM system. This was followed by the ML-based MV-TCM system, as it could detect the magnitudes of failure modes as additional features to the known process parameters, thereby enhancing the features diversity to improve the predictive efficiency during in-process application. The GKRR soft-computing, on the other hand, applied the features of the cutting speed, feed rate, ADOC, and cutting length, which could only predict the quantitative measure of VB progression without being informed by the microstructural evolution of the failure modes during face milling of Inconel 718.

Feasibility during In-process Utilization: System or model feasibility assessment involves determining whether a proposed system or model can be successfully developed and implemented within the limitations of the existing dataset and cutting conditions, while considering the possible advantages and drawbacks of its execution. In addition, it also considered the availability of essential hardware and software integration and the technical impact on non-expert users. Based on the understanding established in this research, both the ML-based MV-TCM and GKRR methods were found to be more feasible for in-process application. However, the conventional digital microscopes cannot be installed in the CNC milling environment, as such, it was infeasible for in-process MV-TCM application.

Cost-effectiveness: Cost-effectiveness was a critical factor that had a significant impact on the success of this research, especially during in-process flank wear prediction and control. Just like the conventional method, the robustness of the GKRR was dependent on the numerical data obtained from various processing conditions, including cooling conditions, tool grades, workpiece properties, and cutting operations, which could deplete the limited resources and time allocated for the experiment. In contrast, the ML-based MV-TCM was automated using an inductive-reasoning script that prioritized the predicted information from flank wear images irrespective of the cutting conditions applied. Furthermore, by applying the multi-stage parameters adjustment to control tool wear evolution, the ML-based MV-TCM saved time and resources as only few experiments were required to optimize the cutting mechanism. Moreover, the early diagnosis of failure modes ensured that corrective measures were

taken before the cutting mechanism became uncontrollable, thus enhancing the predictive control of rapid tool failure during face milling of Inconel 718.

Reliability for In-process Application: System or model reliability refers to the capacity of a system or model to predict tool wear evolution under specific cutting conditions with minimum losses for a particular period of time. The fatigue and stress analysis of the MV-TCM structure illustrated that, under intensive utilization, it had relatively high Mean-Time-Between-Failure (MTBF), Mean-Time-To-Repair (MTTR), Failure-Rate (FR), and availability for the entire cutting operation, making it more effective for in-process application. This ensured more safety, efficiency, and effectiveness for industrial use as compared to the conventional method, which could not even be used for in-process tool wear analysis due to its sophisticated hardware system, which has relatively low MTBF, MTTR, and FR if intensively utilized for online.

Simplicity in Operation: Simplicity in system operation pertains to the art of being user-friendly, even for non-expert machinists. With an introduction of a GUI, an ML-based MV-TCM system had a well-defined and easy-to-use interface and logical workflow, which simplified tool wear monitoring and control without requiring extensive technical know-how. This reduced the time and effort of the non-expert machinists to understand the fundamentals of the cutting mechanism before using the system. In addition, users can quickly learn how to use the ML-MV-TCM system without requiring extensive training to mount the set-up and execute the software. Finally, by automating it to minimize human intervention, the system reduced more effort required for tool wear monitoring by the conventional methods.

Inductive-Reasoning Capability: The MV-TCM system possessed the ability to engage in inductive reasoning, which involved the utilization of the specific failure modes to derive generalizations about underlying wear mechanisms. It analysed the patterns in the historical tool wear data and utilized them to construct a wear mechanisms hypothesis, which was scrutinized against additional data to predict the plausible processing conditions during face milling of Inconel 718. While inductive reasoning was a powerful tool for making and forming hypotheses, it was crucial to keep in mind that these predictions were based solely on the empirical observations made in the existing dataset, which may not always be reliable or accurate for the unknown conditions. However, unlike the conventional and GKRR, the ML-

based MV-TCM inductive-reasoning capability still gave hope for in-process tool performance control and optimization during face milling of Inconel 718.

Adaptability with Varying Cutting Conditions: Adaptability to various cutting conditions is a vital attribute for the models utilized in machining operations. It pertains to the system's proficiency under different machining parameters, including cutting speed, feed rate, and depth of cut. This research shows that an ML-based MV-TCM is more adaptable to different cutting conditions due to its diverse features as compared to GKRR and conventional methods. Additionally, it can be used to adjust the machining parameters, such as cutting speed and feed rate, to optimize the cutting tool's performance online, which results in tool life extension, better surface finish, and higher productivity.

6.5 Conclusion

This chapter presents an experiment that aimed to test the effectiveness of an ML-based MV-TCM model for predictive control of tool performance during face milling of Inconel 718. The study found that the MV-TCM successfully detected the cutter and controlled the camera's shutter to auto-capture the flank wear images during machining. This technique overcame the challenge of data transfer by directly transferring the file to MATLAB programs for further processing. The binary classifier was efficient in separating the images for the wear inserts. These inserts were then loaded into the multi-sectional SVD for feature extraction. The results showed that the extracted feature, F_i, was a strong predictor of flank wear evolution in the early and uniform wear regions, where severe wear mechanisms and failure modes were less prevalent. However, the study also found that F_i was insufficient in representing the complexity of the VB profile. As a result, YOLOv3-TWDM was employed to delineate the complexity of the flank wear morphology by detecting multiple failure modes in the critical and failure stages.

After evaluation, it was found that the YOLOv3-TWDM achieved a mAP of 0.5659 at an IoU threshold of 0.65, which was higher than the score obtained during training. This score was still considered above average when compared to other known applications. Additionally, the YOLOv3-TWDM demonstrated an overall accuracy of 90.86% and a relative accuracy

of 79.08%, making it an ideal choice for detecting failure modes during MV-TCM. YOLOv3-TWDM also detected the magnitudes of flank wear height/depth (Bh_{FW}), chipping height ($Bh_{chipping}$), and chipping width ($Bw_{chipping}$), though the utilization of the bounding box coordinates. Finally, the F_i, Bh_{FW}, $Bh_{chipping}$, and $Bw_{chipping}$ were correlated with the process parameters, where a cutting speed of 40 m/min, a feed of 0.07 mm/tooth, and an ADOC of 1 mm were found optimum in the process. An inductive-reasoning algorithm was utilized to predict the underlying wear mechanisms associated with the detected failure modes. During this process, limiting thresholds of F_i, Bh_{FW}, $Bh_{chipping}$, and $Bw_{chipping}$ were used to estimate the stopping criteria for adjusting the optimum speed and feed/tooth.

As a result, the research concluded that a multi-stage adjustment of speed and feed was more effective than a one-time approach in achieving low VB rates across all flank wear levels. Therefore, the optimal condition for face milling Inconel 718 required the speed and feed to be adjusted at least twice during the machining process to maximize cutting efficiency. Specifically, a speed of 40 m/min and feed of 0.08 mm/tooth were recommended for the early and uniform wear stages, while a speed of 35 m/min and feed of 0.07 mm/tooth were suggested for the critical and failure regions. By employing this strategy, the VB rate was minimized, and cutting length was maximized. The estimated MAPE, R^2, and RMSE for the predicted VB profile were 5.678%, 87.89%, and $32.61\mu m$, respectively, indicating a strong agreement between the predicted and measured VB values at the optimal processing condition. Furthermore, the ML-based MV-TCM system was validated with a soft-computing technique (GKRR) and found to be capable of predicting VB and optimizing the process parameters using limited datasets. However, unlike conventional and soft-computing techniques, the ML-based MV-TCM system used a multi-stage optimization strategy that recognized the need to adjust process parameters more than once at various flank wear levels to achieve optimal cutting efficiency.

Chapter 7

Conclusion

The research conclusion was divided into principal accomplishments (research findings and contributions) and shortcomings (limitations and proposed future work) of this study. Given that this topic is constantly evolving, there are several enhancements that must be made to the MV-TCM system's design as a sequel to the significant strides presented in this thesis.

7.1 Research Findings

In this study, an experiment was conducted to investigate the wear complexity in terms of wear mechanisms, failure modes, and progressive VB for the multi-layer PVD-coated carbide inserts during face milling of Inconel 718. The experimental findings showed an inherent correlation among the wear mechanisms, failure modes, progressive VB, and processing parameters, which prompted the creation of coherent tool wear dataset for training the ML models. The outcome of this experiment successfully responded to the first question by achieving the first objective of this research. The key findings on the first methodology are highlighted as follows:

- The cutting speed, feed rate and axial depth of cut had a significant impact on the evolution of failure modes and VB rate, with the synergistic effect of the speed and feed rate predominantly affecting wear mechanisms, such as adhesion, abrasion, oxidation, and diffusion.
- The increase in speed and feed led to the rapid tool deterioration rate and uncontrolled

failure modes, such as chipping, flaking, notching, built-up edge (BUE), flank wear, thermal cracks, mechanical cracks, and coating delamination. However, flank wear, chipping, BUE, flaking, and notching were dominant failure modes, which affected tool performance at the lowest/medium speed and feed.

- Therefore, it was discovered that predicting and controlling these failure modes in the early cutting stage can improve the performance of carbide inserts during CNC milling of Inconel 718.

However, due to the complex flank wear morphology on the time-series imagery signals, achieving online detection of failure modes and VB rate necessitated the enhancement of MV-TCM system's design through the utilization of the advanced feature engineering and machine learning techniques. The robustness of these models were contingent upon a Diverse Feature Synthesis Vector (DFSV) even under complex wear morphology and varying processing conditions, thus responding the second question by achieving the second objective of this research. The key findings on the second methodology are highlighted as follows:

- The multi-sectional SVD was able to extract the magnitudes of energy layers to quantify the progressive change in the flank wear depth.
- The YOLOv3-TWDM detected and quantified the magnitudes of dominant failure modes, including uniform flank wear, chipping, notching, flaking, and BUE.
- The key descriptor variables of VB progression, which formulated the DFSV under complex wear morphology consisted of the cutting parameters (input features), failure modes (categorical features), and magnitude of the wear region (numerical feature).
- The sensitivity to VB progression of the DFSV-ML was attributed to the inclusion of the failure modes as nominal features that attributed to the rate of VB evolution during machining. Conversely, the SBF-ML features were affected by the multi-modal nature of the time-series flank wear images under complex evolution of the uncontrolled failure modes.

After evaluating the stability of the MV-TCM structure, it was successfully integrated with the feature engineering and ML models to form an ML-based MV-TCM. Despite some

challenging machining domains, which caused a slight drop in its performance, the developed ML-based MV-TCM system demonstrated the simplified way of auto-detecting, capturing, and analysing tool wear signals with high processing time as compared to the conventional, evolutionary, and soft-computing techniques. The outcome provide a response to the third question by achieving the third objective of this research. The following are key findings of the third method applied in this research:

- Although there was image noise due to smearing and inconsistent illumination of the LED light, the system managed to detect failure modes with an overall accuracy, relative accuracy, and mAP of 90.86%, 79.08%, and 0.5659, respectively. It also predicted VB progression at an average MAPE, R2, and RMSE of 3.52%, 97%, and 29.09 μm, respectively.
- By leveraging the feature thresholds at different wear levels, the ML-MV-TCM was able to provide necessary information for speed and feed regulation.
- The ML-based MV-TCM proved to be more efficient, reliable, and practical for real-life applications as it detected online evolution of the wear mechanisms and failure modes, thereby furnishing significant information that facilitated the in-process selection of the optimal speed and feed rate during machining.
- Unlike one-time optimization employed in the conventional and GKRR methods, the ML-based MV-TCM system utilized a "multi-stage parameters control" approach by recognizing that the process parameters should be adjusted more than once at various VB levels to determine the critical stage of tool's diagnosis, which can improve the real-time cutting mechanism during CNC milling of Inconel 718.

By employing this strategy, the tool life was extended by 63.63% (relative to the conventional method) and 56.52% (relative to the GKRR soft computing technique) with a MAPE, R2, and RMSE of 5.678%, 87.89%, and 32.61 μm, respectively. This justifies the significance and novelty of utilizing the ML-based MV-TCM system's design for in-process predictive control of tool wear evolution during face milling of Inconel 718, thus achieving the overall hypothesis of this study.

7.2 Research Contributions

The research contributions were divided into: (1) knowledge enhancement; (2) database enhancement and (3) impact to society.

7.2.1 Knowledge Enhancement

The contributions under knowledge enhancement were divided into 3, aligning with the research questions, objectives, and methods applied in this research: (a) Enhancing versatile data synthesis; (b) demonstrates the need for ML for in-process tool wear prediction; and (c) demonstrates the need for ML-based MV-TCM in streamlining tool performance prediction and control under challenging CNN machining domains. The description of these points are given below:

a –In response to the first objective and research question, the experimental findings demonstrated a strong correlation between wear mechanisms, failure modes, and process parameters, elucidating the understanding of wear complexities that necessitated the synthesis of versatile features, which fostered the creation of a coherent dataset in the field of machine vision-based TCM. The dataset was leveraged to train the feature engineering and ML models for the predictive control of tool wear evolution during face milling of Inconel 718. Thus, unlike the previous MV-TCM approach, the ML models in this research were enhanced to extract more versatile features that were exclusively leveraged to predict and control VB rate under limited dataset.

b –In response to the second objective and research question, the findings in chapters 5 and 6 highlight the imperative need for data-mining analytics (multi-sectional SVD) and Deep Learning (YOLOv3-TWDM, MLPNN, and pre-trained CNNs) to effectively streamline feature engineering and wear prediction, especially when dealing with limited and complex data within the MV-TCM framework. This approach has been demonstrated to be reliable, particularly in challenging CNC milling domains, where traditional methods and classical image processing techniques may fall short in enhancing the efficiency and accuracy of wear diagnosis. Therefore, a comprehensive contribution to the field of MV-TCM is the integration of advanced ML models, which streamlined feature engineering,

wear prediction, and facilitated multi-stage tool performance control and optimization. By utilizing these elements, the research successfully achieved a more efficient and adaptive MV-TCM framework for addressing the complexities of tool wear evolution during CNC milling of Inconel 718. Furthermore, the induction reasoning algorithm employed in this research played a pivotal role of enhancing adaptive decision-making strategies during TCM. This contributed significantly to the overall improvement in efficiency and resource utilization.

c –In response to the third objective and research question, the robustness and versatility of the ML-MV-TCM system's design significantly diminished human-machine interaction, giving rise to innovative tool wear monitoring and control under varying cutting conditions. By minimizing human-machine interaction, the ML-MV-TCM system contributes to enhanced health and safety of machine operators, reducing potential risks associated with manual wear inspection. The reduction in downtime, coupled with the in-process optimization of tool performance, results in a substantial decrease in the cost associated with tool wear monitoring. The ML-MV-TCM system introduces a user-friendly interface, allowing non-expert machinists to engage in simplified in-process wear characterization and control. By providing timely and accurate information on tool wear, it allows for more precise planning and execution of tool-change routines, minimizing unexpected tool failures, and leading to increased overall productivity and reduced unnecessary disruptions in the machining process. Therefore, the ML-MV-TCM system's design stands as a transformative approach that addresses the complexities of wear diagnosis but also elevates safety standards, reduces downtime, and lowers costs, making it a substantial contribution to the body of knowledge in the field of TCM.

7.2.2 Impact to Society

The societal impact of this work was achieved in terms of the safety of the ML-MV-TCM system, which reduced the need for human-machine interaction and streamlined innovation for wear detection, prediction, and control during face milling of Inconel 718. The reduction in human-machine interaction was made possible by eliminating the time-intensive practices,

such as manually removing tools from the CNC environment and cleaning them with dangerous chemicals to inspect wear mechanisms, failure modes, and measure the progressive VB using optical microscopes. On the scientific aspect, it was further observed that such practices can alleviate the significant failure modes on the tools cutting edge, such as notching and BUE, which reveal dominant wear mechanisms and sub-optimal cutting conditions during face milling of Inconel 718. Furthermore, the successful implementation of the multi-sectional SVD, YOLOv3-TWDM, and inductive-reasoning algorithm in the MV-TCM system's design simplified the in-process wear characterization and optimization, allowing non-expert machinists to effectively monitor and control process parameters to improve the overall cutting efficiency during face milling of Inconel 718.

7.3 Research Limitations

The first limitation encountered in this study was the difficulty to generate a large and well-balanced dataset with diverse wear mechanisms and failure modes, which would have further enhanced the robustness of features used to train the feature engineering and ML models. This was attributed to the limited time, resources, as well as variations in the processing conditions, such as cutting fluids, tool grades, workpiece material properties and compositions, which could have again enhanced the diversity of features in the DFSV. The third constraint arose from the fact that the DFSV was formulated by prioritizing the perceived dominant failure modes affecting the flank wear progression, while disregarding the influence of alternative forms of wear, such as crater wear, which could have influenced the evolution of wear mechanisms and failure modes for other milling operations, tools, and workpiece materials. Therefore, it was believed that the DFSV may not have fully captured the broader spectrum of the wear mechanisms and failure modes, which may limit the system's application in other milling operations. Finally, the system was designed using a laboratory setup, where aspects like system's feasibility, reliability, and integrability with multiple CNC controllers for in-line production were not physically validated in a real manufacturing setup.

7.4 Proposed Future Work

To further advance this research, five topics were proposed based on the limitations encountered in this research.

7.4.1 Proposed Topic 1

The first topic pertains to the development of a control system that enhances the data acquisition of the MV-TCM set-up. The data acquisition process can be automated to control the camera capturing and ML processing of the time-series tool wear data during machining. The auto-capturing system can improve the efficiency of the manufacturing processes by providing real-time tool wear information, which can indicate the state of tool wear conditions and provide a solution to prevent rapid tool failure. This reduces the risk of damage to the workpiece's material and enhance tool life extension. To enhance this feed-forward process, a closed-loop control system can be used to provide the adaptive response to the CNC controller to optimize the decision-making process of the ML-based MV-TCM system. The performance of the system can be evaluated and validated through both simulation and experiment conducted at various processing conditions.

7.4.2 Proposed Topic 2

In addition to Inconel 718, the microstructural evolution of wear mechanisms and failure modes for various aerospace metals, such as Waspaloy, Rene 41, Haynes 282, $\gamma - TiAlN$-based alloy, CMSX-4, and TMS-82, can also be affected by changes in input conditions of the CNC milling process. Changes in the microstructures of tool coatings and tribological properties of different cutting fluids can influence the evolution of dominant wear mechanisms and failure modes when cutting these superalloys. This will diversify the training dataset when developing robust machine learning models. Therefore, this research proposes a further study to monitor the evolution of wear mechanisms and failure modes by utilizing the ML-based MV-TCM during CNC milling of these superalloys using different tool coatings and cutting fluids.

7.4.3 Proposed Topic 3

Given that the CNC machine utilizes motion controllers, logic controllers, and programmable logic controllers (PLCs), it is evident that improving the inductive reasoning algorithm of the ML-based MV-TCM system could enable it to communicate with these controllers and implement plausible solutions for predictive control of tool wear progression during machining. This improvement could enhance the functionality of CNC controllers, especially the PLC, by utilizing the information predicted by the ML-MV-TCM to adaptively control the input parameters and improve the cutting mechanism, scrap rate, and manufacturing productivity. Therefore, the third area of research investigates the viability of advanced deep learning techniques, such as graphical neural networks and deep reinforcement learning, in regulating process parameters and communicating feedback to the CNC PLC controller to optimize overall cutting efficiency during the machining of superalloys.

7.4.4 Proposed Topic 4

To optimize the cutting mechanism, it is essential to improve the predictive control of the machining errors for various CNC milling operations. This is critical to minimize machine downtime, increase energy efficiency, reduce scrap rate, and improve manufacturing productivity. One effective approach is to develop a deep learning algorithm that utilizes the MV-TCM system to detect and predict patterns of the machining errors during real-time operation. The model can be trained on historical data to predict the patterns of poor machining indicators arising from the uncontrolled wear mechanisms and failure modes in the early cutting stages. By doing so, the dimensional tolerance of the machined components, energy efficiency, and overall cutting mechanism can be improved in early cutting stages before the tools experience the unprecedented failure during machining. This approach has a significant impact in the aerospace industry, where prediction of machining errors is critical to maintain the precision standards of high and low-pressure compressor blades and discs.

7.4.5 Proposed Topic 5

Despite their exceptional properties for high-temperature applications in high-pressure compressor blades, discs, and casings, the machinability rating of Inconel 718 and Waspaloy is below par, leading to rapid edge loss of most carbide inserts due to the high cutting forces and intense heat generated in the primary and secondary shear zones. The interrupted milling process, coupled with flood cooling conditions, exacerbates this issue by facilitating fluctuating loads, impact forces, and cyclic mechanical and thermal stresses. This, in turn, results in sub-surface thermal or mechanical cracks, chipping, and even catastrophic failure of the tool's cutting edge. Furthermore, the tendency of Inconel 718 to weld onto the tool's edge causes adhesion wear and build-up edge (BUE). The subsequent removal of BUE with aggressive chip flow accelerates edge degradation, particularly when dealing with uncoated or insufficient tool coatings, inadequate cooling or lubrication, improper tool geometry, vibration, and chatter. Hence, monitoring instantaneous changes in edge loss during such cutting conditions becomes crucial.

Considering carbide inserts with multiple edges, tool wear signals or data streams can be acquired at different edge profiles using digital cameras and computer vision software. By analysing this information using a machine vision-based tool condition monitoring (MV-TCM) system, it is possible to determine the real-time deviation of the cutter's edge from its initial position. Compensating such deviations can significantly improve the machining tolerance and precision standards of aerospace structural components. Therefore, Cutting Edge-Wear Compensation pertains to the real-time process of offsetting the gradual degradation and deterioration of a tool's cutting edge, aiming at improving the surface finish, dimensional tolerance of the components, and the performance of carbide tools during CNC milling of superalloys. Therefore, this research proposed a further study on monitoring of cutting Edge-Wear Compensation using multiplexing vision system in CNC milling of Inconel 718 or Waspaloy.

Bibliography

[1] M. I. Faraz and J. Petru, "Evaluation of Machining Variables on Machinability of Nickel Alloy Inconel 718 Using Coated Carbide Tools," 2024.

[2] R. Polvorosa, A. Suárez, L. de Lacalle, I. C. J. o. M. …, and undefined 2017, "Tool wear on nickel alloys with different coolant pressures: Comparison of Alloy 718 and Waspaloy," *Elsevier*. [Online]. Available: https://www.sciencedirect.com/science/article/pii/S1526612517300129

[3] Y. S. Liao, H. M. Lin, and J. H. Wang, "Behaviors of end milling Inconel 718 superalloy by cemented carbide tools," *Journal of Materials Processing Technology*, vol. 201, no. 1-3, pp. 460–465, 2008.

[4] D. Dudzinski, A. Devillez, A. Moufki, D. Larrouquère, V. Zerrouki, and J. Vigneau, "A review of developments towards dry and high speed machining of Inconel 718 alloy," *International Journal of Machine Tools and Manufacture*, vol. 44, no. 4, pp. 439–456, 2004.

[5] F. J. G. Silva, N. P. V. Sebbe, R. D. F. S. Costa, A. F. V. Pedroso, R. C. M. Sales-contini, M. L. S. Barbosa, and R. P. Martinho, "Investigations on the Surface Integrity and Wear Mechanisms of TiAlYN-Coated Tools in Inconel 718 Milling Operations," 2024.

[6] R. K. Palakudtewar and S. V. Gaikwad, "Dry Machining of Superalloys : Difficulties and Remedies," *International Journal of Science and Research (IJSR)*, vol. 3, no. 7, pp. 277–282, 2014.

[7] C. H. Chan, M. S. Kasim, R. Izamshah, H. A. Bakar, S. A. Sundi, K. A. Zakaria, C. H. Haron, J. A. Ghani, and M. S. Hafiz, "Analysis of face milling performance on Inconel 718 using FEM and historical data of RSM," *IOP Conference Series: Materials Science and Engineering*, vol. 270, no. 1, 2017.

[8] P. Maj, B. Adamczyk-Cieslak, M. Slesik, J. Mizera, T. Pieja, J. Sieniawski, T. Gancarczyk, and S. Dudek, "The precipitation processes and mechanical properties of aged inconel 718 alloy after annealing," *Archives of Metallurgy and Materials*, vol. 62, no. 3, pp. 1695–1702, 2017.

[9] W. Huang, S. Cao, H. N. Li, Q. Zhou, C. Wu, D. Zhu, and K. Zhuang, "Tool wear in ultrasonic vibration–assisted drilling of CFRP: a comparison with conventional drilling," *International Journal of Advanced Manufacturing Technology*, pp. 1809–1820, 2021.

[10] K. Kamdani, S. Hasan, A. Farid, I. A. Ashaary, A. Lajis, and E. A. Rahim, "Study on tool wear and wear mechanisms of end milling Nickel-based alloy," Tech. Rep., 2019. [Online]. Available: https://jurnaltribologi.mytribos.org/v21/JT-21-82-92.pdf

[11] M. Rakesh and S. Datta, "Machining of Inconel 718 Using Coated WC Tool: Effects of Cutting Speed on Chip Morphology and Mechanisms of Tool Wear," *Arabian Journal for Science and Engineering*, vol. 45, no. 2, pp. 797–816, 2020. [Online]. Available: https://doi.org/10.1007/s13369-019-04171-4

[12] I. Standard, "INTERNATIONAL," vol. 1989, 1989.

[13] Y. Liu, S. Yu, Q. Shi, X. Ge, and W. Wang, "Multilayer Coatings for Tribology : A Mini Review," 2022.

[14] E. Kaya and B. Akyüz, "Effects of cutting parameters on machinability characteristics of Ni-based superalloys: a review," *Open Engineering*, vol. 7, no. 1, pp. 330–342, 2017.

[15] R. N. Ibrahim, M. A. Rahmat, R. H. Oskouei, and R. K. Singh Raman, "Monolayer TiAlN and multilayer TiAlN/CrN PVD coatings as surface modifiers to mitigate fretting fatigue of AISI P20 steel," *Engineering Fracture Mechanics*, vol. 137, pp. 64–78, 2015. [Online]. Available: http://dx.doi.org/10.1016/j.engfracmech.2015.01.009

[16] Y. Liu, L. Guo, H. Gao, Z. You, Y. Ye, and B. Zhang, "Machine vision based condition monitoring and fault diagnosis of machine tools using information from machined surface texture: A review," *Mechanical Systems and Signal Processing*, vol. 164, no. July 2021, p. 108068, 2022. [Online]. Available: https://doi.org/10.1016/j.ymssp.2021.108068

[17] V. F. Sousa, F. J. G. Da Silva, G. F. Pinto, A. Baptista, and R. Alexandre, "Characteristics and wear mechanisms of tialn-based coatings for machining applications: A comprehensive review," *Metals*, vol. 11, no. 2, pp. 1–49, 2021.

[18] M. A. Xavior, M. Manohar, P. Jeyapandiarajan, and P. M. Madhukar, "Tool Wear Assessment during Machining of Inconel 718," in *Procedia Engineering*, vol. 174. Elsevier Ltd, 2017, pp. 1000–1008. [Online]. Available: www.sciencedirect.com

[19] M. Jahanbakhsh, A. Akhavan Farid, and M. Lotfi, "Optimal flank wear in turning of Inconel 625 super-alloy using ceramic tool," *Proceedings of the Institution of Mechanical Engineers, Part B: Journal of Engineering Manufacture*, vol. 232, no. 2, pp. 208–216, 2018.

[20] C. Nath, Z. Brooks, and T. R. Kurfess, "Machinability study and process optimization in face milling of some super alloys with indexable copy face mill inserts," *Journal of Manufacturing Processes*, vol. 20, pp. 88–97, 2015. [Online]. Available: http://dx.doi.org/10.1016/j.jmapro.2015.09.006

[21] R. Gao, L. Wang, R. Teti, D. Dornfeld, S. Kumara, M. Mori, and M. Helu, "Cloud-enabled prognosis for manufacturing," *CIRP Annals - Manufacturing Technology*, vol. 64, no. 2, pp. 749–772, 2015. [Online]. Available: http://dx.doi.org/10.1016/j.cirp.2015.05.011

[22] K. Zhu, "Smart Machining Systems," 2022. [Online]. Available: https://link.springer.com/10.1007/978-3-030-87878-8

[23] M. S. Babu and T. B. Rao, "Real-time cutting tool condition assessment and stochastic tool life predictive models for tool reliability estimation by in-process cutting tool vibration monitoring," *International Journal on Interactive Design and Manufacturing (IJIDeM)*, vol. 17, no. 3, pp. 1237–1253, 2023. [Online]. Available: https://doi.org/10.1007/s12008-022-01109-3

[24] C. Yuan, G. Li, S. Kamarthi, X. Jin, and M. Moghaddam, "Trends in intelligent manufacturing research: a keyword co-occurrence network based review," *Journal of Intelligent Manufacturing*, vol. 33, no. 2, pp. 425–439, 2022. [Online]. Available: https://doi.org/10.1007/s10845-021-01885-x

[25] Z. You, H. Gao, L. Guo, Y. Liu, and J. Li, "On-line milling cutter wear monitoring in a wide field-of-view camera," *Wear*, vol. 460-461, no. June, p. 203479, 2020. [Online]. Available: https://doi.org/10.1016/j.wear.2020.203479

[26] Y. Li, Z. Zhao, Y. Fu, and Q. Chen, "A novel approach for tool condition monitoring based on transfer learning of deep neural networks using time–frequency images," *Journal of Intelligent Manufacturing*, no. Dl, 2023. [Online]. Available: https://doi.org/10.1007/s10845-023-02099-z

[27] P. M. Sieberg and S. Hanke, "Challenges and potentials in the classification of wear mechanisms by artificial intelligence," *Wear*, vol. 522, no. December 2022, p. 204725, 2023. [Online]. Available: https://doi.org/10.1016/j.wear.2023.204725

[28] D. Liu, Z. Liu, J. Zhao, Q. Song, X. Ren, and H. Ma, "Tool wear monitoring through online measured cutting force and cutting temperature during face milling Inconel 718," *The International Journal of Advanced Manufacturing Technology*, vol. 122, no. 2, pp. 729–740, 2022. [Online]. Available: https://doi.org/10.1007/s00170-022-09950-2

[29] G. Serin, B. Sener, A. M. Ozbayoglu, and H. O. Unver, "Review of tool condition monitoring in machining and opportunities for deep learning," *International Journal of Advanced Manufacturing Technology*, vol. 109, no. 3-4, pp. 953–974, 2020.

[30] T. Mohanraj, S. Shankar, R. Rajasekar, N. R. Sakthivel, and A. Pramanik, "Tool condition monitoring techniques in milling process-a review," pp. 1032–1042, jan 2020. [Online]. Available: www.sciencedirect.com

[31] B. Ye, J. Liu, R. Peng, L. Xu, and X. Zhao, "Study on fuzzy data fusion for real-time intelligent recognition of tool wear state," *Key Engineering Materials*, vol. 375-376, pp. 626–630, 2008.

[32] G. Jadick, E. Abadi, and T. A. Trainor, "Deep Learning Algorithms for Tool Condition Monitoring in Milling : A Review Deep Learning Algorithms for Tool Condition Monitoring in Milling : A Review," 2021.

[33] S. Wen, Z. Chen, and C. Li, "Vision-based surface inspection system for bearing rollers using convolutional neural networks," *Applied Sciences (Switzerland)*, vol. 8, no. 12, 2018.

[34] N. H. A. Halim, C. H. C. Haron, J. A. Ghani, and M. F. Azhar, "Prediction of cutting force for milling of Inconel 718 under cryogenic condition by response surface methodology," *Journal of Mechanical Engineering*, vol. 16, no. 1, pp. 1–16, 2019.

[35] N. G. Patil, A. Asem, R. S. Pawade, D. G. Thakur, and P. K. Brahmankar, "New production technologies in aerospace industry - 5th machining innovations conference (MIC 2014) comparative study of high speed machining of inconel 718 in dry condition and by using compressed cold carbon dioxide gas as coolant," *Procedia CIRP*, vol. 24, no. C, pp. 86–91, 2014. [Online]. Available: http://dx.doi.org/10.1016/j.procir.2014.08.009

[36] K. Zhu, "Machine Vision Based Smart Machining System Monitoring," pp. 267–295, 2022. [Online]. Available: https://link.springer.com/chapter/10.1007/978-3-030-87878-8_8

[37] A. A. Thakre, A. V. Lad, and K. Mala, "Measurements of Tool Wear Parameters Using Machine Vision System," 2019. [Online]. Available: https://doi.org/10.1155/2019/1876489

[38] M. B. Ponce, I. D. S. Illana, S. R. Fernandez-Vidal, and J. S. Gomez, "Experimental parametric model for adhesion wear measurements in the dry turning of an AA2024 alloy," *Materials*, vol. 11, no. 9, 2018.

[39] Ruitao Peng, H. Pang, H. Jiang, and Y. Hu, "Study of Tool Wear Monitoring Using Machine Vision," *Automatic Control and Computer Sciences*, vol. 54, no. 3, pp. 259–270, 2020.

[40] R. Peng, J. Liu, X. Fu, C. Liu, and L. Zhao, "Application of machine vision method in tool wear monitoring," *International Journal of Advanced Manufacturing Technology*, vol. 116, no. 3-4, pp. 1357–1372, 2021.

[41] M. Arav, F. Hall, Z. Li, S. Belkasim, M. Stewart, F. Hall, M. Bakonyi, G. Davis, L. Ding, Y. Hsu, G. Qin, N. Patterson, J. Walker, and Y. Zhao, "SVD and PCA in Image Processing," 2015.

[42] W. Yang, J.-Y. Hong, J.-Y. Kim, S.-h. Paik, S. H. Lee, J.-S. Park, G. Lee, B. M. Kim, and Y.-J. Jung, "A Novel Singular Value Decomposition-Based Denoising Method in 4-Dimensional Computed Tomography of the Brain in Stroke Patients with Statistical Evaluation," *Sensors*, vol. 20, no. 11, p. 3063, may 2020. [Online]. Available: https://www.mdpi.com/1424-8220/20/11/3063

[43] D. Brandoni and V. Simoncini, "Tensor-Train decomposition for image recognition," *Calcolo*, vol. 57, no. 1, pp. 1–24, 2020. [Online]. Available: https://doi.org/10.1007/s10092-020-0358-8

[44] I. Goodfellow, "Generative Neural Network.pdf," 2020.

[45] J. Liu, X. Niu, and W. Kong, "Image watermarking based on singular value decomposition," *Proceedings - 2006 International Conference on Intelligent Information Hiding and Multimedia Signal Processing, IIH-MSP 2006*, pp. 457–460, 2006.

[46] X. Wu, Y. Liu, X. Zhou, and A. Mou, "Automatic identification of tool wear based on convolutional neural network in face milling process," *Sensors (Switzerland)*, vol. 19, no. 18, sep 2019.

[47] R. Girshick, "Fast R-CNN," *Proceedings of the IEEE International Conference on Computer Vision*, vol. 2015 Inter, pp. 1440–1448, 2015.

[48] Z. Zhao, P. Hui, F. Liu, Y. Xu, L. Zhong, and M. Zhao, "Fabrication of niobium carbide coating on niobium by interstitial carburization," *International Journal of Refractory Metals and Hard Materials*, vol. 88, no. January, p. 105187, 2020. [Online]. Available: https://doi.org/10.1016/j.ijrmhm.2020.105187

[49] A. Shakarami, M. B. Menhaj, A. Mahdavi-Hormat, and H. Tarrah, "A fast and yet efficient YOLOv3 for blood cell detection," *Biomedical Signal Processing and Control*, vol. 66, no. September 2020, p. 102495, 2021. [Online]. Available: https://doi.org/10.1016/j.bspc.2021.102495

[50] P. Ong, W. K. Lee, and R. J. H. Lau, "Tool condition monitoring in CNC end milling using wavelet neural network based on machine vision," *International Journal of Advanced Manufacturing Technology*, vol. 104, no. 1-4, pp. 1369–1379, 2019.

[51] C. Ratnam, K. Adarsha Kumar, B. S. Murthy, and K. Venkata Rao, "An experimental study on boring of Inconel 718 and multi response optimization of machining parameters using Response Surface Methodology," *Materials Today: Proceedings*, vol. 5, no. 13, pp. 27 123–27 129, 2018. [Online]. Available: https://doi.org/10.1016/j.matpr.2018.09.020

[52] G. Asala, J. Andersson, and O. A. Ojo, "A study of the dynamic impact behaviour of IN 718 and ATI 718Plus® superalloys," *Philosophical Magazine*, vol. 99, no. 4, pp. 419–437, 2019. [Online]. Available: https://doi.org/10.1080/14786435.2018.1540891

[53] G. Kartheek, K. Srinivas, and C. Devaraj, "Optimization of Residual Stresses in Hard Turning of Super Alloy Inconel 718," *Materials Today: Proceedings*, vol. 5, no. 2, pp. 4592–4600, 2018. [Online]. Available: https://doi.org/10.1016/j.matpr.2017.12.029

[54] N. H. Abdul Halim, C. H. Che Haron, and J. Abdul Ghani, "Sustainable Machining of Hardened Inconel 718: A Comparative Study," *International Journal of Precision Engineering and Manufacturing*, vol. 21, no. 7, pp. 1375–1387, 2020. [Online]. Available: https://doi.org/10.1007/s12541-020-00332-w

[55] Y. H. Fan, Z. P. Hao, M. L. Zheng, F. L. Sun, and S. C. Yang, "Study of surface quality in machining nickel-based alloy Inconel 718," *International Journal of Advanced Manufacturing Technology*, vol. 69, no. 9-12, pp. 2659–2667, 2013.

[56] F. Pusavec, D. Kramar, P. Krajnik, and J. Kopac, "Transitioning to sustainable production - Part II: Evaluation of sustainable machining technologies," *Journal of Cleaner Production*, vol. 18, no. 12, pp. 1211–1221, 2010. [Online]. Available: http://dx.doi.org/10.1016/j.jclepro.2010.01.015

[57] N. Beer, E. Özkaya, and D. Biermann, "New production technologies in aerospace industry - 5th machining innovations conference (MIC 2014) drilling of inconel 718 with geometry-modified twist drills," *Procedia CIRP*, vol. 24, no. C, pp. 49–55, 2014. [Online]. Available: http://dx.doi.org/10.1016/j.procir.2014.07.124

[58] A. Devillez, F. Schneider, S. Dominiak, D. Dudzinski, and D. Larrouquere, "Cutting forces and wear in dry machining of Inconel 718 with coated carbide tools," *Wear*, vol. 262, no. 7-8, pp. 931–942, mar 2007. [Online]. Available: https://linkinghub.elsevier.com/retrieve/pii/S0043164806003553

[59] F. Klocke, G. Eisenblätter, and T. Krieg, "Machining: wear of tools," 2001.

[60] J. G. Corrêa, R. B. Schroeter, and Á. R. Machado, "Tool life and wear mechanism analysis of carbide tools used in the machining of martensitic and supermartensitic stainless steels," *Tribology International*, vol. 105, no. July 2016, pp. 102–117, 2017. [Online]. Available: http://dx.doi.org/10.1016/j.triboint.2016.09.035

[61] V. Varghese, D. Chakradhar, and M. R. Ramesh, "Micro-mechanical characterization and wear performance of TiAlN/NbN PVD coated carbide inserts during End milling of AISI 304 Austenitic Stainless Steel," *Materials Today: Proceedings*, vol. 5, no. 5, pp. 12 855–12 862, 2018. [Online]. Available: https://doi.org/10.1016/j.matpr.2018.02.270

[62] D. Jianxin, L. Lili, L. Jianhua, Z. Jinlong, and Y. Xuefeng, "Failure mechanisms of TiB2 particle and SiC whisker reinforced Al2O3 ceramic cutting tools when machining nickel-based alloys," *International Journal of Machine Tools and Manufacture*, vol. 45, no. 12-13, pp. 1393–1401, 2005.

[63] P. Hoier, K. B. Surreddi, and U. Klement, "Tool wear by dissolution during machining of alloy 718 and Waspaloy: a comparative study using diffusion couples," *International Journal of Advanced Manufacturing Technology*, vol. 106, no. 3-4, pp. 1431–1440, 2020.

[64] A. C. De Melo, J. C. G. Milan, M. B. Da Silva, and Á. R. Machado, "Some observations on wear and damages in cemented carbide tools," *Journal of the Brazilian Society of Mechanical Sciences and Engineering*, vol. 28, no. 3, pp. 269–277, 2006.

[65] W. Akhtar, J. Sun, P. Sun, W. Chen, and Z. Saleem, "Tool wear mechanisms in the machining of Nickel based super-alloys: A review," *Frontiers of Mechanical Engineering*, vol. 9, no. 2, pp. 106–119, 2014.

[66] Z. Hao, D. Gao, Y. Fan, and R. Han, "New observations on tool wear mechanism in dry machining Inconel718," *International Journal of Machine Tools and Manufacture*, vol. 51, no. 12, pp. 973–979, 2011. [Online]. Available: http://dx.doi.org/10.1016/j.ijmachtools.2011.08.018

[67] C. Liu and X. Ai, "Study on cutting temperature and wear mechanism of tool in high speed turning superalloy GH2132," *2010 International Conference on Computing, Control and Industrial Engineering, CCIE 2010*, vol. 2, pp. 327–330, 2010.

[68] J. Thrinadh, A. Mohapatra, S. Datta, and M. Masanta, "Machining behavior of Inconel 718 superalloy: Effects of cutting speed and depth of cut," *Materials Today: Proceedings*, vol. 26, pp. 200–208, 2019. [Online]. Available: https://doi.org/10.1016/j.matpr.2019.10.128

[69] M. S. Kasim, C. H. Che Haron, J. A. Ghani, M. A. Sulaiman, and M. Z. Yazid, "Wear mechanism and notch wear location prediction model in ball nose end milling of Inconel 718," *Wear*, vol. 302, no. 1-2, pp. 1171–1179, 2013. [Online]. Available: http://dx.doi.org/10.1016/j.wear.2012.12.040

[70] D. Kakaš, B. Škorić, S. Mitrović, M. Babić, P. Terek, A. Miletić, and M. Vilotić, "Influence of load and sliding speed on friction coefficient of IBAD deposited TiN," *Tribology in Industry*, vol. 31, no. 3-4, pp. 3–10, 2009.

[71] G. A. Ibrahim, C. H. Che Haron, and J. A. Ghani, "Tool wear mechanism in continuous cutting of difficult-to-cut material under dry machining," *Advanced Materials Research*, vol. 126-128, no. December 2016, pp. 195–201, 2010.

[72] A. Gåård, P. V. Krakhmalev, J. Bergström, and N. Hallbäck, "Galling resistance and wear mechanisms - Cold work tool materials sliding against carbon steel sheets," *Tribology Letters*, vol. 26, no. 1, pp. 67–72, 2007.

[73] A. Riza Motorcu, Y. Isik, A. Kus, and M. C. Cakir, "ANALYSIS OF THE CUTTING TEMPERATURE AND SURFACE ROUGHNESS DURING THE ORTHOGONAL MACHINING OF AISI 4140 ALLOY STEEL VIA THE TAGUCHI METHOD ANALIZA TEMPERATURE REZANJA IN HRAPAVOSTI POVR[INE S TAGUCHI METODO PRI ORTOGONALNI STROJNI OBDELAVI LEGIRANEGA JEKLA."

[74] E. O. Ezugwu, Z. M. Wang, and C. I. Okeke, "Tool life and surface integrity when machining inconel 718 with pvd- and cvd-coated tools," *Tribology Transactions*, vol. 42, no. 2, pp. 353–360, 1999.

[75] E. O. Ezugwu, D. A. Fadare, J. Bonney, R. B. D. Silva, and W. F. Sales, "Modelling the correlation between cutting and process parameters in high-speed machining of Inconel 718 alloy using an artificial neural network," vol. 45, pp. 1375–1385, 2005.

[76] L. A. Dobrzański and D. Pakuła, "Comparison of the structure and properties of the PVD and CVD coatings deposited on nitride tool ceramics," *Journal of Materials Processing Technology*, vol. 164-165, pp. 832–842, 2005.

[77] N. C. Chen and F. H. Sun, "Cutting performance of multilayer diamond coated silicon nitride inserts in machining aluminum-silicon alloy," *Transactions of Nonferrous Metals Society of China (English Edition)*, vol. 23, no. 7, pp. 1985–1992, 2013. [Online]. Available: http://dx.doi.org/10.1016/S1003-6326(13)62687-4

[78] W. Grzesik and J. Małecka, "Documentation of tool wear progress in the machining of nodular ductile iron with silicon nitride-based ceramic tools," *CIRP Annals - Manufacturing Technology*, vol. 60, no. 1, pp. 121–124, 2011.

[79] R. F. Ávila, R. D. Mancosu, A. R. Machado, S. D. Vecchio, R. B. da Silva, and J. M. Vieira, "Comparative analysis of wear on PVD TiN and (Ti1-x Alx)N coatings in machining process," *Wear*, vol. 302, no. 1-2, pp. 1192–1200, 2013.

[80] H. Du, H. Zhao, J. Xiong, and G. Xian, "Effect of interlayers on the structure and properties of TiAlN based coatings on WC-Co cemented carbide substrate," *International Journal of Refractory Metals and Hard Materials*, vol. 37, pp. 60–66, 2013. [Online]. Available: http://dx.doi.org/10.1016/j.ijrmhm.2012.10.017

[81] K. D. Bouzakis, N. Michailidis, S. Gerardis, G. Katirtzoglou, E. Lili, M. Pappa, M. Brizuela, A. Garcia-Luis, and R. Cremer, "Correlation of the impact resistance of variously doped CrAlN PVD coatings with their cutting performance in milling aerospace alloys," *Surface and Coatings Technology*, vol. 203, no. 5-7, pp. 781–785, 2008. [Online]. Available: http://dx.doi.org/10.1016/j.surfcoat.2008.08.009

[82] C. Nouveau, C. Labidi, R. Collet, Y. Benlatreche, and M. A. Djouadi, "Effect of surface finishing such as sand-blasting and CrAlN hard coatings on the cutting edge's peeling tools' wear resistance," *Wear*, vol. 267, no. 5-8, pp. 1062–1067, 2009.

[83] A. Liu, J. Deng, H. Cui, Y. Chen, and J. Zhao, "Friction and wear properties of TiN, TiAlN, AlTiN and CrAlN PVD nitride coatings," *International Journal of Refractory Metals and Hard Materials*, vol. 31, pp. 82–88, 2012. [Online]. Available: http://dx.doi.org/10.1016/j.ijrmhm.2011.09.010

[84] S. Khamseh, M. Nose, T. Kawabata, T. Nagae, K. Matsuda, and S. Ikeno, "A comparative study of CrAlN films synthesized by dc and pulsed dc reactive magnetron facing target sputtering system with different pulse frequencies," *Journal of Alloys and Compounds*, vol. 508, no. 1, pp. 191–195, 2010. [Online]. Available: http://dx.doi.org/10.1016/j.jallcom.2010.08.042

[85] Y. Long, J. Zeng, D. Yu, and S. Wu, "Microstructure of TiAlN and CrAlN coatings and cutting performance of coated silicon nitride inserts in cast iron turning," *Ceramics International*, vol. 40, no. 7 PART A, pp. 9889–9894, 2014. [Online]. Available: http://dx.doi.org/10.1016/j.ceramint.2014.02.083

[86] J. H. Yang, M. F. Cheng, X. D. Luo, and T. H. Zhang, "Surface properties and microstructure of implanted TiN films using MEVVA ion source," *Materials Science and Engineering A*, vol. 445-446, pp. 558–562, feb 2007.

[87] Z. Tonghe, W. Yuguang, Z. Zhiyong, and D. Zhiwei, "The ternary Ti(Zr, N) phases formation and modification of TiN coatings by Zr+ MEVVA ion implantation," *Surface and Coatings Technology*, vol. 131, no. 1-3, pp. 326–329, sep 2000.

[88] H. Rafezi, J. Akbari, M. B. . t. International, and undefined 2012, "Tool condition monitoring based on sound and vibration analysis and wavelet packet decomposition," *ieeexplore.ieee.org*. [Online]. Available: https://ieeexplore.ieee.org/abstract/document/6215170/

[89] K. P. Purushotham, L. P. Ward, N. Brack, P. J. Pigram, P. Evans, H. Noorman, and R. R. Manory, "Wear behaviour of CrN coatings MEVVA ion implanted with Zr," *Wear*, vol. 257, no. 9-10, pp. 901–908, nov 2004.

[90] D. McIntyre, J. E. Greene, G. Håkansson, J. E. Sundgren, and W. D. Münz, "Oxidation of metastable single-phase polycrystalline Ti 0.5Al0.5N films: Kinetics and mechanisms," *Journal of Applied Physics*, vol. 67, no. 3, pp. 1542–1553, 1990.

[91] H. Ichimura and A. Kawana, "High temperature oxidation of ion plated TiN and CrN films," *First International Conference on Processing Materials for Properties*, no. December 1992, pp. 1189–1192, 1993.

[92] Y. Tanaka, T. M. Gür, M. Kelly, S. B. Hagstrom, T. Ikeda, K. Wakihira, and H. Satoh, " Properties of (Ti 1 x Al x)N coatings for cutting tools prepared by the cathodic arc ion plating method ," *Journal of Vacuum Science Technology A: Vacuum, Surfaces, and Films*, vol. 10, no. 4, pp. 1749–1756, 1992.

[93] H. C. Barshilia, N. Selvakumar, B. Deepthi, and K. S. Rajam, "A comparative study of reactive direct current magnetron sputtered CrAlN and CrN coatings," *Surface and Coatings Technology*, vol. 201, no. 6, pp. 2193–2201, 2006. [Online]. Available: http://dx.doi.org/10.1016/j.surfcoat.2006.03.037

[94] Y. C. Zhu, K. Fujita, N. Iwamoto, H. Nagasaka, and T. Kataoka, "Influence of boron ion implantation on the wear resistance of TiAlN coatings," *Surface and Coatings Technology*, vol. 158-159, pp. 664–668, sep 2002.

[95] B. Deng, Y. Tao, H. Liu, and P. Liu, "Influence of niobium ion implantation on the microstructure and tribological properties of TiAlN coatings," *Surface and Coatings Technology*, vol. 228, no. SUPPL.1, pp. 554–557, 2013.

[96] J. F. Ziegler and J. P. Biersack, "The Stopping and Range of Ions in Matter," in *Treatise on Heavy-Ion Science*. Springer US, 1985, pp. 93–129. [Online]. Available: https://link.springer.com/chapter/10.1007/978-1-4615-8103-1_3

[97] B. Deng, J. F. Pei, and Y. Tao, "Microstructure, mechanical and tribological properties of the TiAlN coatings after Nb and C dual ion implantation," *Materials Science Forum*, vol. 789, pp. 455–460, 2014.

[98] Americanmachinists, "Coatings for Problem-Material Turning — American Machinist." [Online]. Available: https://www.americanmachinist.com/cutting-tools/article/21893181/coatings-for-problemmaterial-turning

[99] J. W. Ma, Z. Y. Jia, G. Z. He, Z. Liu, X. X. Zhao, and F. Z. Qin, "Influence of cutting tool geometrical parameters on tool wear in high-speed milling of Inconel 718 curved surface," *Proceedings of the Institution of Mechanical Engineers, Part B: Journal of Engineering Manufacture*, vol. 233, no. 1, pp. 18–30, 2019.

[100] M. Kuntoğlu and H. Sağlam, "Investigation of signal behaviors for sensor fusion with tool condition monitoring system in turning," *Measurement: Journal of the International Measurement Confederation*, vol. 173, no. October 2020, 2021.

[101] F. Klocke, D. Lung, S. E. Cordes, and K. Gerschwiler, "Performance of PVD-Coatings on Cutting Tools for Machining Inconel 718, Austenitic Steel and Quenched and Tempered Steel," *Proceedings of the 7th International Conference THE Coatings in Manufacturing*, no. October, 2008. [Online]. Available: http://www.researchgate.net/profile/Susanne_Cordes/publication/240626748_PERFORMANCE_OF_PVD-COATINGS_ON_CUTTING_TOOLS_FOR_MACHINING_INCONEL_718_AUSTENITIC_STEEL_AND_QUENCHEND_AND_TEMPERED_STEEL/links/00b7d528a091fbd223000000.pdf

[102] B. Zhang, M. J. Njora, and Y. Sato, "High-speed turning of Inconel 718 by using TiAlN- and (Al, Ti) N-coated carbide tools," *International Journal of Advanced Manufacturing Technology*, vol. 96, no. 5-8, pp. 2141–2147, 2018.

[103] A. H. Musfirah, J. A. Ghani, and C. H. Haron, "Tool wear and surface integrity of inconel 718 in dry and cryogenic coolant at high cutting speed," *Wear*, vol. 376-377, pp. 125–133, 2017.

[104] O. Pereira, G. Urbikain, A. Rodríguez, A. Fernández-Valdivielso, A. Calleja, I. Ayesta, and L. N. de Lacalle, "Internal cryolubrication approach for Inconel 718 milling," *Procedia Manufacturing*, vol. 13, pp. 89–93, 2017. [Online]. Available: https://doi.org/10.1016/j.promfg.2017.09.013

[105] K. Aslantas and A. Çiçek, "The effects of cooling/lubrication techniques on cutting performance in micro-milling of Inconel 718 superalloy," *Procedia CIRP*, vol. 77, no. Hpc, pp. 70–73, 2018. [Online]. Available: https://doi.org/10.1016/j.procir.2018.08.219

[106] L. Sterle, D. Mallipeddi, P. Krajnik, and F. Pušavec, "The influence of single-channel liquid CO2 and MQL delivery on surface integrity in machining of Inconel 718," *Procedia CIRP*, vol. 87, pp. 164–169, 2020. [Online]. Available: https://doi.org/10.1016/j.procir.2020.02.032

[107] K. Khanafer, A. Eltaggaz, I. Deiab, H. Agarwal, and A. Abdul-latif, "Toward sustainable micro-drilling of Inconel 718 superalloy using MQL-Nanofluid," *International Journal of Advanced Manufacturing Technology*, vol. 107, no. 7-8, pp. 3459–3469, 2020.

[108] V. Sivalingam, Z. Zhuoliang, S. Jie, S. Baskaran, N. Yuvaraj, M. K. Gupta, and M. K. Aqib, "Use of Atomized Spray Cutting Fluid Technique for the Turning of a Nickel Base Superalloy," *Materials and Manufacturing Processes*, vol. 00, no. 00, pp. 1–8, 2020. [Online]. Available: https://doi.org/10.1080/10426914.2020.1832687

[109] S. Zhang, J. F. Li, and Y. W. Wang, "Tool life and cutting forces in end milling Inconel 718 under dry and minimum quantity cooling lubrication cutting conditions," *Journal of Cleaner Production*, vol. 32, pp. 81–87, 2012.

[110] A. Marques, M. Paipa Suarez, W. Falco Sales, and Á. Rocha Machado, "Turning of Inconel 718 with whisker-reinforced ceramic tools applying vegetable-based cutting fluid mixed with solid lubricants by MQL," *Journal of Materials Processing Technology*, vol. 266, no. August 2018, pp. 530–543, 2019. [Online]. Available: https://doi.org/10.1016/j.jmatprotec.2018.11.032

[111] R. Bertolini, L. Gong, A. Ghiotti, and S. Bruschi, "Graphene Nanoplatelets-Assisted Minimum Quantity Lubrication in Turning to Enhance Inconel 718 Surface Integrity," *Procedia CIRP*, vol. 87, pp. 71–76, 2020. [Online]. Available: https://doi.org/10.1016/j.procir.2020.02.021

[112] S. Sarkar and S. Datta, "Machining Performance of Inconel 718 Under Dry, MQL, and Nanofluid MQL Conditions: Application of Coconut Oil (Base Fluid) and Multi-walled Carbon Nanotubes as Additives," *Arabian Journal for Science and Engineering*, vol. 718, 2020. [Online]. Available: https://doi.org/10.1007/s13369-020-05058-5

[113] A. D. Bartolomeis, S. T. Newman, and A. Shokrani, "Initial investigation on Surface Integrity when Machining Inconel 718 with Conventional and Electrostatic Lubrication," *Procedia CIRP*, vol. 87, pp. 65–70, 2020. [Online]. Available: https://doi.org/10.1016/j.procir.2020.02.019

[114] G. de Paula Oliveira, M. Cindra Fonseca, and A. C. Araujo, "Analysis of residual stress and cutting force in end milling of Inconel 718 using conventional flood cooling and minimum quantity lubrication," *International Journal of Advanced Manufacturing Technology*, vol. 92, no. 9-12, pp. 3265–3272, 2017.

[115] M. A. Makhesana, K. M. Patel, and B. K. Mawandiya, "Environmentally conscious machining of Inconel 718 with solid lubricant assisted minimum quantity lubrication," *Metal Powder Report*, vol. xxx, no. xx, pp. 1–6, 2020. [Online]. Available: https://doi.org/10.1016/j.mprp.2020.08.008

[116] O. Pereira, J. E. Martín-Alfonso, A. Rodríguez, A. Calleja, A. Fernández-Valdivielso, and L. N. López de Lacalle, "Sustainability analysis of lubricant oils for minimum quantity lubrication based on their tribo-rheological performance," *Journal of Cleaner Production*, vol. 164, pp. 1419–1429, 2017.

[117] S. Chaabani, P. J. Arrazola, Y. Ayed, A. Madariaga, A. Tidu, and G. Germain, "Surface integrity when machining Inconel 718 using conventional lubrication and carbon dioxide coolant," *Procedia Manufacturing*, vol. 47, no. 2019, pp. 530–534, 2020. [Online]. Available: https://doi.org/10.1016/j.promfg.2020.04.150

[118] S. B. Adejuyigbe and S. P. Ayodeji, "21445-Article Text-15025-1-10-20040622.pdf," pp. 18–24, 2000.

[119] S. Kunle and K. Corresponding, "Performance Evaluation of Vegetable Oil-Based Cutting Fluids in Mild Steel Machining," vol. 3, no. 9, pp. 35–46, 2013.

[120] H. S. Abdalla and S. Patel, "The performance and oxidation stability of sustainable metal-working fluid derived from vegetable extracts," *Proceedings of the Institution of Mechanical Engineers, Part B: Journal of Engineering Manufacture*, vol. 220, no. 12, pp. 2027–2040, 2006.

[121] Y. C. Liu, T. Y. Liu, T. H. Huang, K. C. Chiu, and S. K. Lin, "Exploring dielectric constant and dissipation factor of ltcc using machine learning," *Materials*, vol. 14, no. 19, pp. 1–14, 2021.

[122] R. F. Recht, "Catastrophic thermoplastic shear," *Journal of Applied Mechanics, Transactions ASME*, vol. 31, no. 2, pp. 189–193, 1964.

[123] M. Rakesh and S. Datta, "Effects of Cutting Speed on Chip Characteristics and Tool Wear Mechanisms During Dry Machining of Inconel 718 Using Uncoated WC Tool," *Arabian Journal for Science and Engineering*, vol. 44, no. 9, pp. 7423–7440, 2019. [Online]. Available: https://doi.org/10.1007/s13369-019-03785-y

[124] P. Li and W. Zhao, "Image fire detection algorithms based on convolutional neural networks," *Case Studies in Thermal Engineering*, vol. 19, no. February, 2020.

[125] W. Bing and L. Zhanqiang, "Serrated chip formation mechanism based on mixed mode of ductile fracture and adiabatic shear," *Proceedings of the Institution of Mechanical Engineers, Part B: Journal of Engineering Manufacture*, vol. 228, no. 2, pp. 181–190, 2014.

[126] J. Fei, G. Liu, K. Patel, and T. Özel, "Effects of machining parameters on finishing additively manufactured nickel-based alloy inconel 625," *Journal of Manufacturing and Materials Processing*, vol. 4, no. 2, 2020.

[127] D. G. Thakur, B. Ramamoorthy, and L. Vijayaraghavan, "A study on the parameters in high-speed turning of superalloy inconel 718," *Materials and Manufacturing Processes*, vol. 24, no. 4, pp. 497–503, 2009.

[128] Y. A. Youssef, Y. Beauchamp, and M. Thomas, "Comparison of a full factorial experiment to fractional and taguchi designs in a lathe dry turning operation," *Computers and Industrial Engineering*, vol. 27, no. 1-4, pp. 59–62, 1994.

[129] T. R. Lin, "Optimisation technique for face milling stainless steel with multiple performance characteristics," *International Journal of Advanced Manufacturing Technology*, vol. 19, no. 5, pp. 330–335, 2002.

[130] S. Shaji and V. Radhakrishnan, "Analysis of process parameters in surface grinding with graphite as lubricant based on the Taguchi method," *Journal of Materials Processing Technology*, vol. 141, no. 1, pp. 51–59, 2003.

[131] I. Mukherjee and P. K. Ray, "A review of optimization techniques in metal cutting processes," *Computers and Industrial Engineering*, vol. 50, no. 1-2, pp. 15–34, 2006.

[132] D. C. Montgomery, "Using fractional factorial designs for robust process development," *Quality Engineering*, vol. 3, no. 2, pp. 193–205, 1990.

[133] U. Natarajan, P. R. Periyanan, and S. H. Yang, "Multiple-response optimization for micro-endmilling process using response surface methodology," *International Journal of Advanced Manufacturing Technology*, vol. 56, no. 1-4, pp. 177–185, 2011.

[134] A. A. Farid, S. Sharif, S. A. Ashrafi, and M. H. Idris, "Statistical analysis, modeling, and optimization of thrust force and surface roughness in high-speed drilling of Al-Si alloy," *Proceedings of the Institution of Mechanical Engineers, Part B: Journal of Engineering Manufacture*, vol. 227, no. 6, pp. 808–820, 2013.

[135] S. Sharif, A. Akhavan Farid, and M. H. Idris, "Tool life prediction model of uncoated carbide tool in high speed drilling of Al-Si alloy using response surface methodology," *International Journal of Surface Science and Engineering*, vol. 6, no. 1-2, pp. 112–121, 2012.

[136] B. Davoodi and B. Eskandari, "Tool wear mechanisms and multi-response optimization of tool life and volume of material removed in turning of N-155 iron-nickel-base superalloy using RSM," *Measurement: Journal of the International Measurement Confederation*, vol. 68, pp. 286–294, 2015. [Online]. Available: http://dx.doi.org/10.1016/j.measurement.2015.03.006

[137] R. Gupta, J. L. Batra, and G. K. Lal, "Determination of optimal subdivision of depth of cut in multipass turning with constraints," *International Journal of Production Research*, vol. 33, no. 9, pp. 2555–2565, 1995.

[138] G. S. Sekhon, "Application of dynamic programming to multi-stage batch machining," *Computer-Aided Design*, vol. 14, no. 3, pp. 157–159, 1982.

[139] D. Goldberg, "Genetic algorithms in search, optimization, and machine learning," *Choice Reviews Online*, vol. 27, no. 02, pp. 27–0936–27–0936, oct 1989.

[140] C. F. Prasad, S. Jayabal, and U. Natarajan, "Optimization of tool wear in turning using genetic algorithm," *Indian Journal of Engineering and Materials Sciences*, vol. 14, no. 6, pp. 403–407, 2007.

[141] D. Q. Gao, Z. Y. Li, and Z. Y. Mao, "Study of high-speed machining parameters on nickel-based alloy GH2132," *Advanced Materials Research*, vol. 189-193, pp. 3142–3147, 2011.

[142] B. Sen, M. Mia, U. K. Mandal, and S. P. Mondal, "GEP- and ANN-based tool wear monitoring: a virtually sensing predictive platform for MQL-assisted milling of Inconel 690," *International Journal of Advanced Manufacturing Technology*, vol. 105, no. 1-4, pp. 395–410, 2019.

[143] S. Jamshidi, A. Yadollahi, M. M. Arab, M. Soltani, M. Eftekhari, H. Sabzalipoor, A. Sheikhi, and J. Shiri, "Combining gene expression programming and genetic algorithm as a powerful hybrid modeling approach for pear rootstocks tissue culture media formulation," *Plant Methods*, vol. 15, no. 1, pp. 1–18, 2019. [Online]. Available: https://doi.org/10.1186/s13007-019-0520-y

[144] R. Mahdavinejad, "Optimizing of turning parameters using multi-objective genetic algorithm," *Advanced Materials Research*, vol. 118-120, pp. 359–363, 2010.

[145] N. Srinivas and K. Deb, "Muiltiobjective Optimization Using Nondominated Sorting in Genetic Algorithms," *Evolutionary Computation*, vol. 2, no. 3, pp. 221–248, 1994.

[146] J. Knowles and D. Corne, "The Pareto archived evolution strategy: A new baseline algorithm for Pareto multiobjective optimisation," *Proceedings of the 1999 Congress on Evolutionary Computation, CEC 1999*, vol. 1, pp. 98–105, 1999.

[147] E. Zitzler and L. Thiele, "Multiobjective optimization using evolutionary algorithms - A comparative case study," *Lecture Notes in Computer Science (including subseries Lecture Notes in Artificial Intelligence and Lecture Notes in Bioinformatics)*, vol. 1498 LNCS, no. September, pp. 292–301, 1998.

[148] Y. Yusoff, A. M. Zain, H. Haron, and J. Bahru, "Akademia Baru Experimental Study of Genetic Algorithm Optimization on WC / Co Material Machining Akademia Baru," vol. 21, no. 1, pp. 14–26, 2016.

[149] K. Deb, A. Pratap, S. Agarwal, and T. Meyarivan, "A fast and elitist multiobjective genetic algorithm: NSGA-II," *IEEE Transactions on Evolutionary Computation*, vol. 6, no. 2, pp. 182–197, 2002.

[150] R. N. Yadav and V. Yadava, "Multiobjective optimization of slotted electrical discharge abrasive grinding of metal matrix composite using artificial neural network and non-dominated sorting genetic algorithm," *Proceedings of the Institution of Mechanical Engineers, Part B: Journal of Engineering Manufacture*, vol. 227, no. 10, pp. 1442–1452, 2013.

[151] K. Bouacha and A. Terrab, "Hard turning behavior improvement using NSGA-II and PSO-NN hybrid model," *International Journal of Advanced Manufacturing Technology*, vol. 86, no. 9-12, pp. 3527–3546, 2016. [Online]. Available: http://dx.doi.org/10.1007/s00170-016-8479-6

[152] Y. Jin, "A comprehensive survey of fitness approximation in evolutionary computation," *Soft Computing*, vol. 9, no. 1, pp. 3–12, 2005.

[153] Y. Jin and B. Sendhoff, "Fitness Approximation In Evolutionary Computation - a Survey." *Gecco*, pp. 1105–1112, 2002.

[154] U. Župerl, F. Čuš, and V. Gecevska, "Optimization of the characteristic parameters in milling using the PSO evolution technique," *Strojniski Vestnik/Journal of Mechanical Engineering*, vol. 53, no. 6, pp. 354–368, 2007.

[155] N. Yusup, A. M. Zain, and S. Z. M. Hashim, "Evolutionary techniques in optimizing machining parameters: Review and recent applications (2007-2011)," *Expert Systems with Applications*, vol. 39, no. 10, pp. 9909–9927, 2012. [Online]. Available: http://dx.doi.org/10.1016/j.eswa.2012.02.109

[156] R. V. Rao, P. J. Pawar, and R. Shankar, "Multi-objective optimization of electrochemical machining process parameters using a particle swarm optimization algorithm," *Proceedings of the Institution of Mechanical Engineers, Part B: Journal of Engineering Manufacture*, vol. 222, no. 8, pp. 949–958, 2008.

[157] X. Li, G. Ouyang, and Z. Liang, "Complexity measure of motor current signals for tool flute breakage detection in end milling," *International Journal of Machine Tools and Manufacture*, vol. 48, no. 3-4, pp. 371–379, 2008.

[158] H. Huang, A. Li, and X. Lin, "Application of PSO-based wavelet neural network in tool wear monitoring," *Proceedings of the IEEE International Conference on Automation and Logistics, ICAL 2007*, vol. 2, no. 3, pp. 2813–2817, 2007.

[159] B. Akay and D. Karaboga, "Artificial bee colony algorithm for large-scale problems and engineering design optimization," *Journal of Intelligent Manufacturing*, vol. 23, no. 4, pp. 1001–1014, 2012.

[160] S. Samanta and S. Chakraborty, "Parametric optimization of some non-traditional machining processes using artificial bee colony algorithm," *Engineering Applications of Artificial Intelligence*, vol. 24, no. 6, pp. 946–957, 2011. [Online]. Available: http://dx.doi.org/10.1016/j.engappai.2011.03.009

[161] J. T. Lin, D. Bhattacharyya, and V. Kecman, "Multiple regression and neural networks analyses in composites machining," *Composites Science and Technology*, vol. 63, no. 3-4, pp. 539–548, 2003.

[162] P. Thangavel, V. Selladurai, and R. Shanmugam, "Application of response surface methodology for predicting flank wear in turning operation," *Proceedings of the Institution of Mechanical Engineers, Part B: Journal of Engineering Manufacture*, vol. 220, no. 6, pp. 997–1003, 2006.

[163] A. K. Gupta, "Predictive modelling of turning operations using response surface methodology, artificial neural networks and support vector regression," *International Journal of Production Research*, vol. 48, no. 3, pp. 763–778, 2010.

[164] S. Berkani, L. Bouzid, H. Bensouilah, M. A. Yallese, F. Girardin, and T. Mabrouki, "Modeling and optimization of tool wear and surface roughness in turning of austenitic stainless steel using response surface methodology Abstract :," pp. 1–16, 2015.

[165] K. L. Petri, R. E. Billo, and B. Bidanda, "A Neural Network Process Model for Abrasive Flow Machining Operations," *Journal of Manufacturing Systems*, vol. 17, no. 1, pp. 52–64, 1998.

[166] D. E. Rumelhart and G. E. Hintont, "Learning Representations by Back-Propagating Errors," *Cognitive Modeling*, no. 2, pp. 3–6, 2019.

[167] G. Sathyanarayanan, I. Joseph Lin, and M. K. Chen, "Neural network modelling and multiobjective optimization of creep feed grinding of superalloys," *International Journal of Production Research*, vol. 30, no. 10, pp. 2421–2438, 1992.

[168] R. K. Jain, V. K. Jain, and P. K. Kalra, "Modelling of abrasive flow machining process: A neural network approach," *Wear*, vol. 231, no. 2, pp. 242–248, 1999.

[169] W. M. Geerdes, M. Á. T. Alvarado, M. Cabrera-Ríos, and A. Cavazos, "An application of physics-based and artificial neural networks-based hybrid temperature prediction schemes in a hot strip mill," *Journal of Manufacturing Science and Engineering, Transactions of the ASME*, vol. 130, no. 1, pp. 0 145 011–0 145 015, 2008.

[170] R. Arun Ramnath, P. R. Thyla, N. Mahendra Kumar, and S. Aravind, "Optimization of machining parameters of composites using multi-attribute decision-making techniques: A review," pp. 77–89, 2018.

[171] K. K. Thyagharajan and T. Vignesh, "Soft Computing Techniques for Land Use and Land Cover Monitoring with Multispectral Remote Sensing Images: A Review," pp. 275–301, 2019.

[172] L. A. Zadeh, "Outline of a New Approach to the Analysis of Complex Systems and Decision Processes," *IEEE Transactions on Systems, Man and Cybernetics*, vol. SMC-3, no. 1, pp. 28–44, 1973.

[173] W. L. Ip, "A fuzzy basis material removal optimization strategy for sculptured surface machining using ball-nosed cutters," *International Journal of Production Research*, vol. 36, no. 9, pp. 2553–2571, 1998.

[174] S. Shankar, T. Mohanraj, and A. Pramanik, "Tool Condition Monitoring while Using Vegetable Based Cutting Fluids during Milling of Inconel 625," *Journal of Advanced Manufacturing Systems*, vol. 18, no. 4, pp. 563–581, 2019.

[175] D. A. Ragab, M. Sharkas, S. Marshall, and J. Ren, "Breast cancer detection using deep convolutional neural networks and support vector machines," *PeerJ*, vol. 2019, no. 1, p. e6201, jan 2019.

[176] J. Sun, M. Rahman, Y. S. Wong, and G. S. Hong, "Multiclassification of tool wear with support vector machine by manufacturing loss consideration," *International Journal of Machine Tools and Manufacture*, vol. 44, no. 11, pp. 1179–1187, sep 2004.

[177] D. Kong, Y. Chen, and N. Li, "Hidden semi-Markov model-based method for tool wear estimation in milling process," *International Journal of Advanced Manufacturing Technology*, vol. 92, no. 9-12, pp. 3647–3657, oct 2017.

[178] Statinfer, "204.6.8 SVM : Advantages Disadvantages and Applications – Statinfer." [Online]. Available: https://statinfer.com/204-6-8-svm-advantages-disadvantages-applications/

[179] F. Gong, J. Zhao, and J. Pang, "Evolution of cutting forces and tool failure mechanisms in intermittent turning of hardened steel with ceramic tool," *International Journal of Advanced Manufacturing Technology*, vol. 89, no. 5-8, pp. 1603–1613, 2017.

[180] F. Ahmadzadeh and J. Lundberg, "Remaining useful life estimation: review," *International Journal of Systems Assurance Engineering and Management*, vol. 5, no. 4, pp. 461–474, 2014.

[181] X. Lu, F. Wang, Z. Jia, S. Y. Liang, X. Lu, F. Wang, and S. Y. Liang, "The fl ank wear prediction in micro-milling Inconel 718," 2018.

[182] N. Pugno, M. Ciavarella, P. Cornetti, and A. Carpinteri, "A generalized Paris' law for fatigue crack growth," *Journal of the Mechanics and Physics of Solids*, vol. 54, no. 7, pp. 1333–1349, 2006.

[183] G. Terrazas, G. Martínez-Arellano, P. Benardos, and S. Ratchev, "Online Tool Wear Classification during Dry Machining Using Real Time Cutting Force Measurements and a CNN Approach," *Journal of Manufacturing and Materials Processing*, vol. 2, no. 4, p. 72, oct 2018. [Online]. Available: http://www.mdpi.com/2504-4494/2/4/72

[184] F. Bleicher, P. Schörghofer, Christoph, and H. 1, "IN-PROCESS CONTROL WITH A SENSORY TOOL HOLDER TO AVOID CHATTER," *Journal of Machine Engineering*, vol. 18, no. 3, pp. 16–27, 2018. [Online]. Available: https://doi.org/10.5604/01.3001.0012.4604

[185] D. E. Dimla, "The Correlation of Vibration Signal Features to Cutting Tool Wear in a Metal Turning Operation," Tech. Rep., 2002. [Online]. Available: https://link.springer.com/content/pdf/10.1007/s001700200080.pdf

[186] A. J. Torabi, M. J. Er, X. Li, B. S. Lim, L. Zhai, L. San, O. P. Gan, and C. T. Ching, "Application of classical clustering methods for online tool condition monitoring in high speed milling processes," in *Proceedings of the 2012 7th IEEE Conference on Industrial Electronics and Applications, ICIEA 2012*, 2012, pp. 1249–1254. [Online]. Available: https://ieeexplore.ieee.org/abstract/document/6360914/

[187] G. Ghule, N. Ambhore, and S. Chinchanikar, "Tool Condition Monitoring Using Vibration Signals During Hard Turning: A Review," *SSRN Electronic Journal*, feb 2017. [Online]. Available: https://www.ssrn.com/abstract=3101977

[188] R. Corne, C. Nath, M. E. Mansori, and T. Kurfess, "Enhancing Spindle Power Data Application with Neural Network for Real-time Tool Wear/Breakage Prediction During Inconel Drilling," *Procedia Manufacturing*, vol. 5, pp. 1–14, 2016. [Online]. Available: http://dx.doi.org/10.1016/j.promfg.2016.08.004

[189] X. Li and Z. Yuan, "Tool wear monitoring with wavelet packet transform-fuzzy clustering method," *Wear*, vol. 219, no. 2, pp. 145–154, sep 1998.

[190] R. V. Rao and V. D. Kalyankar, "Multi-pass turning process parameter optimization using teaching-learning-based optimization algorithm," *Scientia Iranica*, vol. 20, no. 3, pp. 967–974, 2013. [Online]. Available: http://dx.doi.org/10.1016/j.scient.2013.01.002

[191] W. Weingaertner, R. Schroeter, M. P. J. o. M. . . . , and undefined 2006, "Evaluation of high-speed end-milling dynamic stability through audio signal measurements," *Elsevier*. [Online]. Available: https://www.sciencedirect.com/science/article/pii/S0924013606002196

[192] J. V. Abellan-Nebot and F. Romero Subirón, "A review of machining monitoring systems based on artificial intelligence process models," pp. 237–257, mar 2010.

[193] X. Shi, X. Wang, L. Jiao, Z. Wang, P. Yan, and S. Gao, "A real-time tool failure monitoring system based on cutting force analysis," *International Journal of Advanced Manufacturing Technology*, vol. 95, no. 5-8, pp. 2567–2583, mar 2018.

[194] H. Ohzeki, A. Mashine, H. Aoyama, and I. Inasaki, "Development of a magnetostrictive torque sensor for milling process monitoring," *Journal of Manufacturing Science and Engineering, Transactions of the ASME*, vol. 121, no. 4, pp. 615–622, nov 1999.

[195] M. B. Jun, O. Burak Ozdoganlar, R. E. DeVor, S. G. Kapoor, A. Kirchheim, and G. Schaffner, "Evaluation of a spindle-based force sensor for monitoring and fault diagnosis of machining operations," *International Journal of Machine Tools and Manufacture*, vol. 42, no. 6, pp. 741–751, may 2002.

[196] Y. Altintas, "Prediction of cutting forces and tool breakage in milling from feed drive current measurements," *Journal of Manufacturing Science and Engineering, Transactions of the ASME*, vol. 114, no. 4, pp. 386–392, nov 1992.

[197] P. Twardowski and M. Wiciak-Pikula, "Prediction of tool wear using artificial neural networks during turning of hardened steel," *Materials*, vol. 12, no. 19, oct 2019.

[198] R. Corne, C. Nath, M. E. Mansori, T. K. J. of Manufacturing, and undefined 2017, "Study of spindle power data with neural network for predicting real-time tool wear/breakage during inconel drilling," *Elsevier*. [Online]. Available: https://www.sciencedirect.com/science/article/pii/S0278612517300043

[199] R. Silva, R. Reuben, K. Baker, S. W. M. S. And, and undefined 1998, "Tool wear monitoring of turning operations by neural network and expert system classification of a feature set generated from multiple sensors," *Elsevier*. [Online]. Available: https://www.sciencedirect.com/science/article/pii/S0888327097901230

[200] C. Drouillet, J. Karandikar, C. Nath, A. J. J. o. M. …, and undefined 2016, "Tool life predictions in milling using spindle power with the neural network technique," *Elsevier*. [Online]. Available: https://www.sciencedirect.com/science/article/pii/S1526612516300123

[201] A. Siddhpura and R. Paurobally, "A review of flank wear prediction methods for tool condition monitoring in a turning process," *Springer*. [Online]. Available: https://link.springer.com/content/pdf/10.1007/s00170-012-4177-1.pdf

[202] J. Kaye, D. Yan, N. P. I. J. of …, and undefined 1995, "Predicting tool flank wear using spindle speed change," *Elsevier*. [Online]. Available: https://www.sciencedirect.com/science/article/pii/0890695594E0031D

[203] P. J.C. Lynn, W.R. Warke, "SECOND ISRAEL MATERIALS ENGINEERING CONFERENCE CONFERENCE PROCEEDINGS," Tech. Rep., 1974.

[204] M. Ritou, S. Garnier, B. Furet, , J. H. M. S. Signal, and undefined 2014, "Angular approach combined to mechanical model for tool breakage detection by eddy current sensors," *Elsevier*. [Online]. Available: https://www.sciencedirect.com/science/article/pii/S0888327013000836

[205] I. Marinescu, D. A. I. J. o. M. T. And, and undefined 2008, "A critical analysis of effectiveness of acoustic emission signals to detect tool and workpiece malfunctions in milling operations," *Elsevier*. [Online]. Available: https://www.sciencedirect.com/science/article/pii/S0890695508000266

[206] Q. Ren, M. Balazinski, L. Baron, K. Jemielniak, R. Botez, and S. Achiche, "Type-2 fuzzy tool condition monitoring system based on acoustic emission in micromilling," *Information Sciences*, vol. 255, pp. 121–134, jan 2014. [Online]. Available: https://linkinghub.elsevier.com/retrieve/pii/S0020025513004362

[207] G. Student Elijah Kannatey-Asibu and J. Professor, "Ming-Chyuan Lu Analysis of Sound Signal Generation Due to Flank Wear in Turning," *asmedigitalcollection.asme.org*, 2002. [Online]. Available: https://asmedigitalcollection.asme.org/manufacturingscience/article-abstract/124/4/799/477989

[208] Z. Tekıner, S. Y. M. . Design, and undefined 2004, "Investigation of the cutting parameters depending on process sound during turning of AISI 304 austenitic stainless steel," *Elsevier*. [Online]. Available: https://www.sciencedirect.com/science/article/pii/S0261306903002632

[209] M.-C. Lu and B.-S. Wan, "Study of high-frequency sound signals for tool wear monitoring in micromilling," *Springer*. [Online]. Available: https://link.springer.com/content/pdf/10.1007/s00170-012-4458-8.pdf

[210] K. Prakash and A. Samraj, "Tool flank wears estimation by simplified SVD on emitted sound signals," in *2017 Conference on Emerging Devices and Smart Systems, ICEDSS 2017*. Institute of Electrical and Electronics Engineers Inc., oct 2017, pp. 1–5.

[211] Sandvik Coromant, "Heat resistant super alloys – HRSA," pp. 9–42, 2010. [Online]. Available: http://www.sandvik.coromant.com/SiteCollectionDocuments/downloads/global/technicalguides/en-us/C-2920-034.pdf

[212] Seccotools, "SEEX09T3AFN-M05 MS2050 — Secotools.com." [Online]. Available: https://www.secotools.com/article/p_02899501

[213] S. Chinchanikar and S. K. Choudhury, "Wear behaviors of single-layer and multi-layer coated carbide inserts in high speed machining of hardened AISI 4340 steel," *Journal of Mechanical Science and Technology*, vol. 27, no. 5, pp. 1451–1459, 2013.

[214] Q. Niu, Q. An, M. Chen, and W. Ming, "Wear mechanisms and performance of coated inserts during face milling of TC11 and TC17 alloys," *Machining Science and Technology*, vol. 17, no. 3, pp. 483–495, 2013.

[215] X. Ma, J. Xu, W. Ding, D. Lv, and Y. Fu, "Wear behavior of Ti(N, C)-Al2O3 coated cemented carbide tools during milling Ti2AlNb-based alloy," *Key Engineering Materials*, vol. 589-590, pp. 361–365, 2014.

[216] S. Sahu and B. B. Choudhury, "Optimization of Surface Roughness Using Taguchi Methodology Prediction of Tool Wear in Hard Turning Tools," *Materials Today: Proceedings*, vol. 2, no. 4-5, pp. 2615–2623, 2015.

[217] A. Mohanty, S. Gangopadhyay, and A. Thakur, "On Applicability of Multilayer Coated Tool in Dry Machining of Aerospace Grade Stainless Steel," *Materials and Manufacturing Processes*, vol. 31, no. 7, pp. 869–879, 2016.

[218] S. Sun, M. Brandt, and M. S. Dargusch, "Effect of tool wear on chip formation during dry machining of Ti-6Al-4V alloy, part 2: Effect of tool failure modes," *Proceedings of the Institution of Mechanical Engineers, Part B: Journal of Engineering Manufacture*, vol. 231, no. 9, pp. 1575–1586, 2017.

[219] S. Qin, Z. Li, G. Guo, Q. An, M. Chen, and W. Ming, "Analysis of minimum quantity lubrication (MQL) for different coating tools during turning of TC11 titanium alloy," *Materials*, vol. 9, no. 10, 2016.

[220] E. Kuram, "Nose radius and cutting speed effects during milling of AISI 304 material," *Materials and Manufacturing Processes*, vol. 32, no. 2, pp. 185–192, 2017. [Online]. Available: http://dx.doi.org/10.1080/10426914.2016.1198019

[221] Z. Li, G. Wang, and G. He, "Milling tool wear state recognition based on partitioning around medoids (PAM) clustering," *International Journal of Advanced Manufacturing Technology*, vol. 88, no. 5-8, pp. 1203–1213, feb 2017.

[222] A. S. Abdul Sani, E. A. Rahim, S. Sharif, and H. Sasahara, "The influence of modified vegetable oils on tool failure mode and wear mechanisms when turning AISI 1045," *Tribology International*, vol. 129, no. August 2018, pp. 347–362, 2019.

[223] X. Liang, Z. Liu, and B. Wang, "Multi-pattern failure modes and wear mechanisms of WC-Co tools in dry turning Ti–6Al–4V," *Ceramics International*, vol. 46, no. 15, pp. 24 512–24 525, 2020. [Online]. Available: https://doi.org/10.1016/j.ceramint.2020.06.238

[224] W. Ming, X. Huang, M. Ji, J. Xu, F. Zou, and M. Chen, "Analysis of cutting responses of Sialon ceramic tools in high-speed milling of FGH96 superalloys," *Ceramics International*, vol. 47, no. 1, pp. 149–156, 2021. [Online]. Available: https://doi.org/10.1016/j.ceramint.2020.08.118

[225] N. Verma, S. C. Vettivel, P. S. Rao, and S. Zafar, "Processing, tool wear measurement using machine vision system and optimization of machining parameters of boron carbide and rice husk ash reinforced AA 7075 hybrid composite," *Materials Research Express*, vol. 6, no. 8, 2019.

[226] A. Datta, S. Dutta, S. K. Pal, and R. Sen, "Progressive cutting tool wear detection from machined surface images using Voronoi tessellation method," *Journal of Materials Processing Technology*, vol. 213, no. 12, pp. 2339–2349, 2013. [Online]. Available: http://dx.doi.org/10.1016/j.jmatprotec.2013.07.008

[227] J. Loizou, W. Tian, J. Robertson, and J. Camelio, "Automated wear characterization for broaching tools based on machine vision systems," *Journal of Manufacturing Systems*, vol. 37, pp. 558–563, 2015. [Online]. Available: http://dx.doi.org/10.1016/j.jmsy.2015.04.005

[228] M. Murua, A. Suárez, L. N. L. D. Lacalle, R. Santana, and A. Wretland, "Feature extraction-based prediction of tool wear of Inconel 718 in face turning," pp. 1–8, 2017.

[229] S. Dutta, A. Datta, N. D. Chakladar, S. K. Pal, S. Mukhopadhyay, and R. Sen, "Detection of tool condition from the turned surface images using an accurate grey level co-occurrence technique," *Precision Engineering*, vol. 36, no. 3, pp. 458–466, 2012. [Online]. Available: http://dx.doi.org/10.1016/j.precisioneng.2012.02.004

[230] S. Dutta, S. K. Pal, S. Mukhopadhyay, and R. Sen, "Application of digital image processing in tool condition monitoring: A review," pp. 212–232, jan 2013.

[231] R. G. Lins, B. Guerreiro, P. R. Marques De Araujo, and R. Schmitt, "In-process tool wear measurement system based on image analysis for CNC drilling machines," *IEEE Transactions on Instrumentation and Measurement*, vol. 69, no. 8, pp. 5579–5588, 2020.

[232] N. Ambhore, D. Kamble, S. Chinchanikar, and V. Wayal, "Tool condition monitoring system: A review," *Materials Today: Proceedings*, vol. 2, no. 4-5, pp. 3419–3428, 2015. [Online]. Available: http://dx.doi.org/10.1016/j.matpr.2015.07.317

[233] R. M. J, R. C. G, T. R. Srinivas, and P. M. Pai, "A Study on Different Tool Condition Monitoring System Available To Monitor Tool Flank Wear," *National Conference on Advances in Mechanical Engineering Science*, p. 2016, 2016. [Online]. Available: http://www.ijettjournal.org

[234] D. Rajeev, D. Dinakaran, S. Sathishkumar, and A. W. Lenin, "A review on signal acquisition methods for tool wear monitoring in turning process," *Advanced Materials Research*, vol. 984-985, pp. 83–93, 2014.

[235] Q. Hou, J. Sun, and P. Huang, "A novel algorithm for tool wear online inspection based on machine vision," *International Journal of Advanced Manufacturing Technology*, vol. 101, no. 9-12, pp. 2415–2423, apr 2019.

[236] Y. D. Chethan, H. V. Ravindra, and Y. T. Krishnegowda, "Optimization of machining parameters in turning Nimonic-75 using machine vision and acoustic emission signals by Taguchi technique," *Measurement: Journal of the International Measurement Confederation*, vol. 144, pp. 144–154, 2019. [Online]. Available: https://doi.org/10.1016/j.measurement.2019.05.035

[237] M. T. García-Ordás, E. Alegre-Gutiérrez, R. Alaiz-Rodríguez, and V. González-Castro, "Tool wear monitoring using an online, automatic and low cost system based on local texture," *Mechanical Systems and Signal Processing*, vol. 112, pp. 98–112, 2018.

[238] Y. Dai and K. Zhu, "A machine vision system for micro-milling tool condition monitoring," *Precision Engineering*, vol. 52, pp. 183–191, apr 2018.

[239] S. Dutta, S. K. Pal, and R. Sen, "Progressive tool flank wear monitoring by applying discrete wavelet transform on turned surface images," *Measurement: Journal of the International Measurement Confederation*, vol. 77, pp. 388–401, 2016. [Online]. Available: http://dx.doi.org/10.1016/j.measurement.2015.09.028

[240] ——, "Tool condition monitoring in turning by applying machine vision," *Journal of Manufacturing Science and Engineering, Transactions of the ASME*, vol. 138, no. 5, pp. 1–17, 2016.

[241] L. Li and Q. An, "An in-depth study of tool wear monitoring technique based on image segmentation and texture analysis," *Measurement: Journal of the International Measurement Confederation*, vol. 79, pp. 44–52, 2016. [Online]. Available: http://dx.doi.org/10.1016/j.measurement.2015.10.029

[242] C. Zhang and J. Zhang, "On-line tool wear measurement for ball-end milling cutter based on machine vision," *Computers in Industry*, vol. 64, no. 6, pp. 708–719, 2013. [Online]. Available: http://dx.doi.org/10.1016/j.compind.2013.03.010

[243] H. H. Shahabi and M. M. Ratnam, "Assessment of flank wear and nose radius wear from workpiece roughness profile in turning operation using machine vision," *International Journal of Advanced Manufacturing Technology*, vol. 43, no. 1-2, pp. 11–21, jul 2009.

[244] Y. T. Liang and Y. C. Chiou, "An effective drilling wear measurement based on visual inspection technique," in *Proceedings of the 9th Joint Conference on Information Sciences, JCIS 2006*, vol. 2006, 2006.

[245] K. N. Prasad and B. Ramamoorthy, "Tool wear evaluation by stereo vision and prediction by artificial neural network," *Journal of Materials Processing Technology*, vol. 112, no. 1, pp. 43–52, 2001. [Online]. Available: https://www.sciencedirect.com/science/article/pii/S0924013600008967?casa_token=WN8Lm7Hpg1gAAAAA:GezKfmaLXfFdiqz3eRfftcPMvI_13RFYxDMmxxiDdvdrNVtKk3DmwSp_NQwWBOvC0Iup9K5DfA

[246] T. Pfeifer and L. Wiegers, "Reliable tool wear monitoring by optimized image and illumination control in machine vision," *Measurement: Journal of the International Measurement Confederation*, vol. 28, no. 3, pp. 209–218, oct 2000.

[247] M. Lanzetta, "A new flexible high-resolution vision sensor for tool condition monitoring," *Journal of Materials Processing Technology*, vol. 119, no. 1-3, pp. 73–82, dec 2001. [Online]. Available: https://linkinghub.elsevier.com/retrieve/pii/S0924013601008780

[248] M. Sortino, "Application of statistical filtering for optical detection of tool wear," *International Journal of Machine Tools and Manufacture*, vol. 43, no. 5, pp. 493–497, 2003. [Online]. Available: https://www.sciencedirect.com/science/article/pii/S0890695502002663?casa_token=P7n5hqr1-T4AAAAA:ryFWM1EFabFeVqLGV6iGBVZXC2uEMZKDKH5o1Xb99zV5MAxxZ4kwxBiXOe-J15KFNXGezAf2TQ

[249] A. Devillez, S. Lesko, and W. Mozer, "Cutting tool crater wear measurement with white light interferometry," *Wear*, vol. 256, no. 1-2, pp. 56–65, jan 2004.

[250] J. Jurkovic, M. Korosec, and J. Kopac, "New approach in tool wear measuring technique using CCD vision system," *International Journal of Machine Tools and Manufacture*, vol. 45, no. 9, pp. 1023–1030, 2005. [Online]. Available: https://www.sciencedirect.com/science/article/pii/S0890695504003128?casa_token=V8N5QR2kGxQAAAAA:Z4WBRNA7DlASsAYzQ_qsWdUrJgrVmdWv2mqU4U0MoMf9iR2IwWUOBF03WcWSVStig_yV2x5xTw

[251] D. Kerr, J. Pengilley, and R. Garwood, "Assessment and visualisation of machine tool wear using computer vision," *International Journal of Advanced Manufacturing Technology*, vol. 28, no. 7-8, pp. 781–791, apr 2006.

[252] J. C. Su, C. K. Huang, and Y. S. Tarng, "An automated flank wear measurement of microdrills using machine vision," *Journal of Materials Processing Technology*, vol. 180, no. 1-3, pp. 328–335, dec 2006.

[253] M. Castejón, E. Alegre, J. Barreiro, and L. K. Hernández, "On-line tool wear monitoring using geometric descriptors from digital images," *International Journal of Machine Tools and Manufacture*, vol. 47, no. 12-13, pp. 1847–1853, oct 2007.

[254] E. Alegre, R. Alaiz-Rodríguez, J. Barreiro, and J. Ruiz, "Use of contour signatures and classification methods to optimize the tool life in metal machining," *Estonian Journal of Engineering*, vol. 15, pp. 3–12, 2009.

[255] G. Duan, Y.-W. Chen, and T. Sukegawa, "Automatic optical flank wear measurement of microdrills using level set for cutting plane segmentation," *Machine Vision and Applications*, vol. 21, no. 5, pp. 667–676, aug 2010. [Online]. Available: https://idp.springer.com/authorize/casa?redirect_uri=https://link.springer.com/article/10.1007/s00138-010-0259-y&casa_token=na1Wi8rwIgUAAAAA:7e9OTNWqlyh8SnPEU3aB75ujLcZ7jHy-l9JNpoAsJITF_22FInynufkKKXMYffqXPVtYUyIV1582D07Ykw

[256] G. Xiong, J. Liu, and A. Avila, "Cutting tool wear measurement by using active contour model based image processing," in *2011 IEEE International Conference on Mechatronics and Automation, ICMA 2011*, 2011, pp. 670–675.

[257] R. Schmitt, Y. Cai, and A. Pavim, "Machine Vision System for Inspecting Flank Wear on Cutting Tools," *ACEEE International Journal on Control System and Instrumentation*, vol. 03, no. 01, pp. 27–31, 2012.

[258] O. G. Moldovan, S. Dzitac, I. Moga, T. Vesselenyi, and I. Dzitac, "Tool-wear analysis using image processing of the tool flank," *Symmetry*, vol. 9, no. 12, pp. 1–18, 2017.

[259] T. Mikołajczyk, K. Nowicki, A. Kłodowski, and D. Y. Pimenov, "Neural network approach for automatic image analysis of cutting edge wear," *Mechanical Systems and Signal Processing*, vol. 88, no. July 2016, pp. 100–110, 2017.

[260] A. Karthik, S. Chandra, B. Ramamoorthy, and S. Das, "3D tool wear measurement and visualisation using stereo imaging," *International Journal of Machine Tools and Manufacture*, vol. 37, no. 11, pp. 1573–1581, nov 1997.

[261] G. Landini, D. A. Randell, S. Fouad, and A. Galton, "Automatic thresholding from the gradients of region boundaries," *Journal of Microscopy*, vol. 265, no. 2, pp. 185–195, 2017.

[262] X. Y. Song and J. Zhao, "Failure mechanisms of carbide tool in high speed milling of Inconel 718," *Advanced Materials Research*, vol. 97-101, pp. 1920–1924, 2010.

[263] G. Zheng, J. Zhao, A. Li, X. Cui, and Y. Zhou, "Failure mechanisms of graded ceramic tool in ultra high speed dry milling of Inconel 718," *International Journal of Precision Engineering and Manufacturing*, vol. 14, no. 6, pp. 943–949, 2013.

[264] Y. Chethan, H. Ravindra, Y. K. Gowda, and G. M. Kumar, "Parametric Optimization in Drilling EN-8 Tool Steel and Drill Wear Monitoring Using Machine Vision Applied with Taguchi Method," *Procedia Materials Science*, vol. 5, pp. 1442–1449, 2014.

[265] J. Meng and Y. Yang, "Symmetrical two-dimensional pca with image measures in face recognition," *International Journal of Advanced Robotic Systems*, vol. 9, pp. 1–10, 2012.

[266] S. Karamizadeh, S. M. Abdullah, A. A. Manaf, M. Zamani, and A. Hooman, "An Overview of Principal Component Analysis," *Journal of Signal and Information Processing*, vol. 04, no. 03, pp. 173–175, 2013.

[267] S. Asadi, C. Rao, and V. Saikrishna, "A Comparative study of Face Recognition with Principal Component Analysis and Cross-Correlation Technique," *International Journal of Computer Applications*, vol. 10, no. 8, pp. 17–21, 2010.

[268] P. J. Phillips, P. J. Flynn, T. Scruggs, K. W. Bowyer, J. Chang, K. Hoffman, J. Marques, J. Min, and W. Worek, "Overview of the face recognition grand challenge," *Proceedings - 2005 IEEE Computer Society Conference on Computer Vision and Pattern Recognition, CVPR 2005*, vol. I, pp. 947–954, 2005.

[269] K. Konstantinides, B. Natarajan, and G. S. Yovanof, "Noise estimation and filtering using block-based singular value decomposition," *IEEE Transactions on Image Processing*, vol. 6, no. 3, pp. 479–483, 1997.

[270] R. A. Sadek, "SVD Based Image Processing Applications: State of The Art, Contributions and Research Challenges," Tech. Rep. 7, 2012. [Online]. Available: www.ijacsa.thesai.org

[271] H. C. Andrews and C. L. Patterson, "Singular Value Decompositions And Digital Image Processing," *IEEE Transactions on Acoustics, Speech, and Signal Processing*, vol. 24, no. 1, pp. 26–53, 1976.

[272] Y. Lecun, Y. Bengio, and G. Hinton, "Deep learning," *Nature*, vol. 521, no. 7553, pp. 436–444, 2015.

[273] C. Ledig, L. Theis, F. Huszár, J. Caballero, A. Cunningham, A. Acosta, A. Aitken, A. Tejani, J. Totz, Z. Wang, and W. Shi, "Photo-realistic single image super-resolution using a generative adversarial network," *Proceedings - 30th IEEE Conference on Computer Vision and Pattern Recognition, CVPR 2017*, vol. 2017-Janua, pp. 105–114, 2017.

[274] W. S. Lai, J. B. Huang, N. Ahuja, and M. H. Yang, "Deep laplacian pyramid networks for fast and accurate super-resolution," *Proceedings - 30th IEEE Conference on Computer Vision and Pattern Recognition, CVPR 2017*, vol. 2017-Janua, pp. 5835–5843, 2017.

[275] E. Shelhamer, J. Long, and T. Darrell, "Fully Convolutional Networks for Semantic Segmentation," *IEEE Transactions on Pattern Analysis and Machine Intelligence*, vol. 39, no. 4, pp. 640–651, 2017.

[276] X. Chen, K. Kundu, Y. Zhu, A. Berneshawi, H. Ma, S. Fidler, and R. Urtasun, "3D object proposals for accurate object class detection," *Advances in Neural Information Processing Systems*, vol. 2015-Janua, pp. 424–432, 2015.

[277] R. Girshick, J. Donahue, T. Darrell, and J. Malik, "Region-Based Convolutional Networks for Accurate Object Detection and Segmentation," *IEEE Transactions on Pattern Analysis and Machine Intelligence*, vol. 38, no. 1, pp. 142–158, 2016.

[278] K. He, X. Zhang, S. Ren, and J. Sun, "Deep residual learning for image recognition," *Proceedings of the IEEE Computer Society Conference on Computer Vision and Pattern Recognition*, vol. 2016-Decem, pp. 770–778, 2016.

[279] M. Mahdianpari, B. Salehi, M. Rezaee, F. Mohammadimanesh, and Y. Zhang, "Very deep convolutional neural networks for complex land cover mapping using multispectral remote sensing imagery," *Remote Sensing*, vol. 10, no. 7, 2018.

[280] C. Szegedy, W. Liu, Y. Jia, P. Sermanet, S. Reed, D. Anguelov, D. Erhan, V. Vanhoucke, and A. Rabinovich, "Going deeper with convolutions," *Proceedings of the IEEE Computer Society Conference on Computer Vision and Pattern Recognition*, vol. 07-12-June, pp. 1–9, 2015.

[281] B. Hariharan, P. Arbeláez, R. Girshick, and J. Malik, "Hypercolumns for object segmentation and fine-grained localization," *Proceedings of the IEEE Computer Society Conference on Computer Vision and Pattern Recognition*, vol. 07-12-June, pp. 447–456, 2015.

[282] J. Redmon, S. Divvala, R. Girshick, and A. Farhadi, "You only look once: Unified, real-time object detection," *Proceedings of the IEEE Computer Society Conference on Computer Vision and Pattern Recognition*, vol. 2016-Decem, pp. 779–788, 2016.

[283] S. Ren, K. He, R. Girshick, and J. Sun, "Faster R-CNN: Towards Real-Time Object Detection with Region Proposal Networks," *IEEE Transactions on Pattern Analysis and Machine Intelligence*, vol. 39, no. 6, pp. 1137–1149, 2017.

[284] P. Sermanet, D. Eigen, X. Zhang, M. Mathieu, R. Fergus, and Y. LeCun, "Overfeat: Integrated recognition, localization and detection using convolutional networks," *2nd International Conference on Learning Representations, ICLR 2014 - Conference Track Proceedings*, 2014.

[285] J. R. Uijlings, K. E. Van De Sande, T. Gevers, and A. W. Smeulders, "Selective search for object recognition," *International Journal of Computer Vision*, vol. 104, no. 2, pp. 154–171, 2013.

[286] C. Barnes, E. Shechtman, A. Finkelstein, and D. B. Goldman, "PatchMatch: A randomized correspondence algorithm for structural image editing," *ACM Transactions on Graphics*, vol. 28, no. 3, 2009.

[287] A. Van Den Oord, N. Kalchbrenner, and K. Kavukcuoglu, "Pixel recurrent neural networks," *33rd International Conference on Machine Learning, ICML 2016*, vol. 4, pp. 2611–2620, 2016.

[288] J. Y. Cheng, F. Chen, M. T. Alley, J. M. Pauly, and S. S. Vasanawala, "Highly Scalable Image Reconstruction using Deep Neural Networks with Bandpass Filtering," pp. 1–9, 2018. [Online]. Available: http://arxiv.org/abs/1805.03300

[289] Y. Liu, W. Shao, C. Wang, and C. Zhou, "Microstructure and oxidation behavior of Mo-Si-Al coating on Nb-based alloy," *Journal of Alloys and Compounds*, vol. 735, pp. 2247–2255, 2018. [Online]. Available: https://doi.org/10.1016/j.jallcom.2017.11.339

[290] A. Radford, L. Metz, and S. Chintala, "Unsupervised representation learning with deep convolutional generative adversarial networks," *4th International Conference on Learning Representations, ICLR 2016 - Conference Track Proceedings*, pp. 1–16, 2016.

[291] C. Qiu, K. Li, B. Li, X. Mao, S. He, C. Hao, and L. Yin, "Semi-supervised graph convolutional network to predict position- and speed-dependent tool tip dynamics with limited labeled data," *Mechanical Systems and Signal Processing*, vol. 164, no. July 2021, p. 108225, 2022. [Online]. Available: https://doi.org/10.1016/j.ymssp.2021.108225

[292] F. Baldassarre, K. Smith, J. Sullivan, and H. Azizpour, "Explanation-Based Weakly-Supervised Learning of Visual Relations with Graph Networks," *Lecture Notes in Computer Science (including subseries Lecture Notes in Artificial Intelligence and Lecture Notes in Bioinformatics)*, vol. 12373 LNCS, no. June, pp. 612–630, 2020.

[293] Y. Wang, W. Dai, and J. Xiao, "Detection for Cutting Tool Wear Based on Convolution Neural Networks," in *Proceedings - 12th International Conference on Reliability, Maintainability, and Safety, ICRMS 2018.* Institute of Electrical and Electronics Engineers Inc., jul 2018, pp. 297–300.

[294] M. Anderson, R. Patwa, and Y. C. Shin, "Laser-assisted machining of Inconel 718 with an economic analysis," *International Journal of Machine Tools and Manufacture*, vol. 46, no. 14, pp. 1879–1891, 2006.

[295] Y. Jia, E. Shelhamer, J. Donahue, S. Karayev, J. Long, R. Girshick, S. Guadarrama, and T. Darrell, "Caffe," pp. 675–678, 2014.

[296] Z. Cao, G. Hidalgo, T. Simon, S. E. Wei, and Y. Sheikh, "OpenPose: Realtime Multi-Person 2D Pose Estimation Using Part Affinity Fields," *IEEE Transactions on Pattern Analysis and Machine Intelligence*, vol. 43, no. 1, pp. 172–186, 2021.

[297] A. Mateus, D. Ribeiro, P. Miraldo, and J. C. Nascimento, "Efficient and robust Pedestrian Detection using Deep Learning for Human-Aware Navigation," *Robotics and Autonomous Systems*, vol. 113, pp. 23–37, 2019. [Online]. Available: https://doi.org/10.1016/j.robot.2018.12.007

[298] M. Zhao, X. Ji, and S. Y. Liang, "Micro-grinding temperature prediction considering the effects of crystallographic orientation," *Manufacturing Review*, vol. 6, p. 22, 2019.

[299] R. S. Sutton and A. G. Barto, "Reinforcement learning: An Introduction Second edition," *Learning*, vol. 3, no. 9, p. 322, 2012. [Online]. Available: https://books.google.com/books?id=CAFR6IBF4xYC&pgis=1%5Cnhttp://incompleteideas.net/sutton/book/the-book.html%5Cnhttps://www.dropbox.com/s/f4tnuhipchpkgoj/book2012.pdf

[300] Z. Fang and T. Obikawa, "Influence of cutting fluid flow on tool wear in high-pressure coolant turning using a novel internally cooled insert," *Journal of Manufacturing Processes*, vol. 56, no. June, pp. 1114–1125, 2020. [Online]. Available: https://doi.org/10.1016/j.jmapro.2020.05.028

[301] J. C. Caicedo and S. Lazebnik, "Active object localization with deep reinforcement learning," *Proceedings of the IEEE International Conference on Computer Vision*, vol. 2015 Inter, pp. 2488–2496, 2015.

[302] F. Abtahi, Z. Zhu, and A. M. Burry, "A deep reinforcement learning approach to character segmentation of license plate images," *Proceedings of the 14th IAPR International Conference on Machine Vision Applications, MVA 2015*, pp. 539–542, 2015.

[303] J. Zhou, G. Cui, S. Hu, Z. Zhang, C. Yang, Z. Liu, L. Wang, C. Li, and M. Sun, "Graph neural networks: A review of methods and applications," *AI Open*, vol. 1, no. September 2020, pp. 57–81, 2020. [Online]. Available: https://doi.org/10.1016/j.aiopen.2021.01.001

[304] C. W. Lee, W. Fang, C. K. Yeh, and Y. C. F. Wang, "Multi-label Zero-Shot Learning with Structured Knowledge Graphs," *Proceedings of the IEEE Computer Society Conference on Computer Vision and Pattern Recognition*, pp. 1576–1585, 2018.

[305] A. Krizhevsky, I. Sutskever, and G. E. Hinton, "ImageNet Classification with Deep Convolutional Neural Networks," Tech. Rep. [Online]. Available: http://code.google.com/p/cuda-convnet/

[306] H. Mamledesai, M. A., Soriano, and R. Ahmad, "A qualitative tool condition monitoring framework using convolution neural network and transfer learning," *Applied Sciences (Switzerland)*, vol. 10, no. 20, pp. 1–11, 2020.

[307] J. Li, "Scale-Aware Fast R-CNN for Pedestrian Detection," vol. 20, no. 4, pp. 985–996, 2018.

[308] L. Fu, Y. Majeed, X. Zhang, M. Karkee, and Q. Zhang, "Faster R–CNN–based apple detection in dense-foliage fruiting-wall trees using RGB and depth features for robotic harvesting," *Biosystems Engineering*, vol. 197, pp. 245–256, 2020. [Online]. Available: https://doi.org/10.1016/j.biosystemseng.2020.07.007

[309] W. Liu, D. Anguelov, D. Erhan, C. Szegedy, S. Reed, C. Y. Fu, and A. C. Berg, "SSD: Single shot multibox detector," *Lecture Notes in Computer Science (including subseries Lecture Notes in Artificial Intelligence and Lecture Notes in Bioinformatics)*, vol. 9905 LNCS, pp. 21–37, 2016. [Online]. Available: https://link.springer.com/chapter/10.1007/978-3-319-46448-0_2

[310] K. G. Shreyas Dixit, M. G. Chadaga, S. S. Savalgimath, G. Ragavendra Rakshith, and M. R. Naveen Kumar, "Evaluation and evolution of object detection techniques YOLO and R-CNN," *International Journal of Recent Technology and Engineering*, vol. 8, no. 2 Special issue 3, pp. 824–829, 2019.

[311] J. Redmon and A. Farhadi, "Yolo V2.0," *Cvpr2017*, no. April, pp. 187–213, 2017. [Online]. Available: http://www.worldscientific.com/doi/abs/10.1142/9789812771728_0012

[312] A. Bochkovskiy, C.-Y. Wang, and H.-Y. M. Liao, "YOLOv4: Optimal Speed and Accuracy of Object Detection," 2020. [Online]. Available: http://arxiv.org/abs/2004.10934

[313] S. Singha and B. Aydin, "Automated drone detection using YOLOv4," *Drones*, vol. 5, no. 3, 2021.

[314] T. Jintasuttisak, E. Edirisinghe, and A. Elbattay, "Deep neural network based date palm tree detection in drone imagery," *Computers and Electronics in Agriculture*, vol. 192, no. April 2021, p. 106560, 2022. [Online]. Available: https://doi.org/10.1016/j.compag.2021.106560

[315] D. G. Thakur, B. Ramamoorthy, and L. Vijayaraghavan, "Some investigations on high speed dry machining of aerospace material inconel 718 using multicoated carbide inserts," *Materials and Manufacturing Processes*, vol. 27, no. 10, pp. 1066–1072, 2012.

[316] L. Li, N. He, M. Wang, and Z. G. Wang, "High speed cutting of Inconel 718 with coated carbide and ceramic inserts," *Journal of Materials Processing Technology*, vol. 129, no. 1-3, pp. 127–130, 2002.

[317] B. Zhang, M. J. Njora, and Y. Sato, "High-speed turning of Inconel 718 by using TiAlN- and (Al, Ti) N-coated carbide tools," *International Journal of Advanced Manufacturing Technology*, vol. 96, no. 5-8, pp. 2141–2147, 2018.

[318] M. J. Er, H. Ge, P. Gan, S. Huang, L. Y. Zhai, S. Linn, and A. J. Torabi, "Adaptive Network Fuzzy Inference System and Support Vector Machine Learning for Tool Wear Estimation in High Speed Milling Processes," pp. 2821–2826, 2012.

[319] D. A. Stephenson and J. S. Agapiou, "Metal Cutting Theory and Practice," *Metal Cutting Theory and Practice*, sep 2018. [Online]. Available: https://www.taylorfrancis.com/books/mono/10.1201/9781315373119/metal-cutting-theory-practice-david-stephenson-john-agapiou

[320] I. S. Rout and P. P. Pandian, "Selection of cutting parameters for the machinability of Inconel 718 using Grey Relational Analysis." [Online]. Available: https://doi.org/10.1051/matecconf/201817204004

[321] V. Sivalingam, J. Sun, B. Yang, K. Liu, and R. Raju, "Machining performance and tool wear analysis on cryogenic treated insert during end milling of Ti-6Al-4V alloy," *Journal of Manufacturing Processes*, vol. 36, no. October, pp. 188–196, 2018. [Online]. Available: https://doi.org/10.1016/j.jmapro.2018.10.010

[322] A. Jawaid, S. Koksal, and S. Sharif, "Cutting performance and wear characteristics of PVD coated and uncoated carbide tools in face milling Inconel 718 aerospace alloy," *Journal of Materials Processing Technology*, vol. 116, no. 1, pp. 2–9, 2001.

[323] M. Abdul Hadi, J. A. Ghani, C. H. Che Haron, and M. S. Kasim, "Effect of cutting speed on the carbide cutting tool in milling Inconel 718 alloy," *Journal of Materials Research*, vol. 31, no. 13, pp. 1885–1892, 2016.

[324] M. A. Xavior, M. Patil, A. Maiti, M. Raj, and N. Lohia, "Machinability studies on INCONEL 718," *IOP Conference Series: Materials Science and Engineering*, vol. 149, no. 1, 2016.

[325] P. Adegbuyi, "Analysing the effect of cutting fluids on the mechanical properties of mild steel in a turning operation," *American Journal of Scientific and Industrial Research*, vol. 2, no. 1, pp. 1–10, 2011.

[326] S. A. Lawal, I. A. Choudhury, and Y. Nukman, "Application of vegetable oil-based metalworking fluids in machining ferrous metals - A review," *International Journal of Machine Tools and Manufacture*, vol. 52, no. 1, pp. 1–12, 2012. [Online]. Available: http://dx.doi.org/10.1016/j.ijmachtools.2011.09.003

[327] M. Moreno, J. M. Andersson, R. Boyd, M. P. Johansson-Jöesaar, L. J. Johnson, M. Odén, and L. Rogström, "Crater wear mechanism of TiAlN coatings during high-speed metal turning," *Wear*, vol. 484-485, no. June, 2021.

[328] A. Simoneau and J. Meehan, "The Impact of Machining Parameters on Peak Power and Energy Consumption in CNC Endmilling," vol. 3, no. 5, pp. 85–90, 2013.

[329] M. Witty, T. Bergs, A. Schäfer, and G. Cabral, "Cutting tool geometry for plunge milling-Process optimization for a stainless steel," *Procedia CIRP*, vol. 1, no. 1, pp. 506–511, 2012.

[330] Sandkiv, "Milling formulas and definition," pp. 1–10, 2019. [Online]. Available: https://www.sandvik.coromant.com/en-gb/knowledge/machining-formulas-definitions/pages/milling.aspx

[331] T. Mikołajczyk, K. Nowicki, A. Bustillo, and D. Y. Pimenov, "Predicting tool life in turning operations using neural networks and image processing," *Mechanical Systems and Signal Processing*, vol. 104, pp. 503–513, 2018.

[332] J. Redmon and A. Farhadi, "YOLOv3: An Incremental Improvement," 2018. [Online]. Available: http://arxiv.org/abs/1804.02767

[333] F. N. Iandola, S. Han, M. W. Moskewicz, K. Ashraf, W. J. Dally, and K. Keutzer, "SqueezeNet: AlexNet-level accuracy with 50x fewer parameters and ¡0.5MB model size," pp. 1–13, 2016. [Online]. Available: http://arxiv.org/abs/1602.07360

[334] V. Kolev, K. Tsvetkova, and M. Tsvetkov, "Singular value decomposition of images from scanned photographic plates," *VII Serbian-Bulgarian Astronomical Conference, SBAC 2010*, no. 11, pp. 187–200, 2010.

[335] V. Faghih Dinevari, G. Karimian Khosroshahi, and M. Zolfy Lighvan, "Singular Value Decomposition Based Features for Automatic Tumor Detection in Wireless Capsule Endoscopy Images," *Applied Bionics and Biomechanics*, vol. 2016, 2016.

[336] B. Qiang, Y. Zhai, M. Zhou, X. Yang, B. Peng, Y. Wang, and Y. Pang, "SqueezeNet and Fusion Network-Based Accurate Fast Fully Convolutional Network for Hand Detection and Gesture Recognition," *IEEE Access*, vol. 9, pp. 77 661–77 674, 2021.

[337] S. Han, H. Mao, and W. J. Dally, "Deep compression: Compressing deep neural networks with pruning, trained quantization and Huffman coding," *4th International Conference on Learning Representations, ICLR 2016 - Conference Track Proceedings*, pp. 1–14, 2016.

[338] M. Taheri, N. Lim, and J. Lederer, "Balancing Statistical and Computational Precision and Applications to Penalized Linear Regression with Group Sparsity," pp. 233–240, 2016. [Online]. Available: http://arxiv.org/abs/1609.07195

[339] B. Iyer, A. M. Rajurkar, and V. Gudivada, Eds., *Applied Computer Vision and Image Processing*, ser. Advances in Intelligent Systems and Computing. Singapore: Springer Singapore, 2020, vol. 1155. [Online]. Available: http://link.springer.com/10.1007/978-981-15-4029-5

[340] G. F. C. Campos, S. M. Mastelini, G. J. Aguiar, R. G. Mantovani, L. F. de Melo, and S. Barbon, "Machine learning hyperparameter selection for Contrast Limited Adaptive Histogram Equalization," *Eurasip Journal on Image and Video Processing*, vol. 2019, no. 1, 2019.

[341] A. M. Reza, "Realization of the contrast limited adaptive histogram equalization (CLAHE) for real-time image enhancement," *Journal of VLSI Signal Processing Systems for Signal, Image, and Video Technology*, vol. 38, no. 1, pp. 35–44, 2004.

[342] K. Sreedhar, "Enhancement of Images Using Morphological Transformations," *International Journal of Computer Science and Information Technology*, vol. 4, no. 1, pp. 33–50, 2012.

[343] X. Ma, B. Li, Y. Zhang, and M. Yan, "The Canny edge detection and its improvement," in *Lecture Notes in Computer Science (including subseries Lecture Notes in Artificial Intelligence and Lecture Notes in Bioinformatics)*, vol. 7530 LNAI. Springer, Berlin, Heidelberg, oct 2012, pp. 50–58. [Online]. Available: https://link.springer.com/chapter/10.1007/978-3-642-33478-8_7

[344] P. Shanmugavadivu and V. Sivakumar, "Fractal dimension based texture analysis of digital images," in *Procedia Engineering*, vol. 38. Elsevier Ltd, jan 2012, pp. 2981–2986.

[345] J. Arif, N. R. Chaudhuri, S. Ray, and B. Chaudhuri, "Online Levenberg-Marquardt algorithm for neural network based estimation and control of power systems," *Proceedings of the International Joint Conference on Neural Networks*, pp. 199–206, 2009.

[346] Techbriefs, "CCD and CMOS Sensors - Tech Briefs." [Online]. Available: https://www.techbriefs.com/component/content/article/tb/supplements/ptb/features/articles/20063

[347] J. Chouinard, "The Fundamentals of Camera and Image Sensor Technology," Tech. Rep.

[348] I. H. Sarker, "AI-Based Modeling: Techniques, Applications and Research Issues Towards Automation, Intelligent and Smart Systems," *SN Computer Science*, vol. 3, no. 2, pp. 1–20, 2022. [Online]. Available: https://doi.org/10.1007/s42979-022-01043-x

[349] Öztürk and B. Akdemir, "Application of Feature Extraction and Classification Methods for Histopathological Image using GLCM, LBP, LBGLCM, GLRLM and SFTA," in *Procedia Computer Science*, vol. 132. Elsevier B.V., jan 2018, pp. 40–46.

[350] D. Han, Q. Liu, and W. Fan, "A new image classification method using CNN transfer learning and web data augmentation," *Expert Systems with Applications*, vol. 95, pp. 43–56, 2018. [Online]. Available: https://doi.org/10.1016/j.eswa.2017.11.028

[351] A. A. Almisreb, N. Jamil, and N. M. Din, "Utilizing AlexNet Deep Transfer Learning for Ear Recognition," *Proceedings - 2018 4th International Conference on Information Retrieval and Knowledge Management: Diving into Data Sciences, CAMP 2018*, pp. 8–12, 2018.

[352] J. Wolfe, X. Jin, T. Bahr, and N. Holzer, "Application of softmax regression and its validation for spectral-based land cover mapping," *International Archives of the Photogrammetry, Remote Sensing and Spatial Information Sciences - ISPRS Archives*, vol. 42, no. 1W1, pp. 455–459, 2017.

[353] R. Jacobs, T. Mayeshiba, B. Afflerbach, L. Miles, M. Williams, M. Turner, R. Finkel, and D. Morgan, "The Materials Simulation Toolkit for Machine learning (MAST-ML): An automated open source toolkit to accelerate data-driven materials research," *Computational Materials Science*, vol. 176, no. October 2019, 2020.

[354] F. Pedregosa, G. Varoquaux, A. Gramfort, V. Michel, B. Thirion, O. Grisel, M. Blondel, P. Prettenhofer, R. Weiss, V. Dubourg, J. Vanderplas, A. Passos, D. Cournapeau, M. Brucher, M. Perrot, and É. Duchesnay, "Scikit-learn: Machine learning in Python," *Journal of Machine Learning Research*, vol. 12, no. May 2014, pp. 2825–2830, 2011.

[355] J. Caldeirani Filho and A. E. Diniz, "Influence of Cutting Conditions on Tool Life, Tool Wear and Surface Finish in the Face Milling Process," *Journal of the Brazilian Society of Mechanical Sciences*, vol. 24, no. 1, pp. 10–14, mar 2002. [Online]. Available: http://www.scielo.br/scielo.php?script=sci_arttext&pid=S0100-73862002000100002&lng=en&tlng=en

[356] X. Dai, K. Zhuang, D. Pu, W. Zhang, and H. Ding, "An investigation of the work hardening behavior in interrupted cutting inconel 718 under cryogenic conditions," *Materials*, vol. 13, no. 9, 2020.

[357] T. Ueda, A. Hosokawa, K. Oda, and K. Yamada, "Temperature on flank face of cutting tool in high speed milling," *CIRP Annals - Manufacturing Technology*, vol. 50, no. 1, pp. 37–40, 2001.

[358] G. A. Oosthuizen, G. Akdogan, and N. Treurnicht, "The performance of PCD tools in high-speed milling of Ti6Al4V," *International Journal of Advanced Manufacturing Technology*, vol. 52, no. 9-12, pp. 929–935, 2011.

[359] M. B. Bilgin, "Investigating the effects of cutting parameters on the built-up-layer and built-up-edge formation during the machining of AISI 310 austenitic stainless Steels," *Materiali in Tehnologije*, vol. 49, no. 5, pp. 779–784, 2015.

[360] M. Anthony Xavior, M. Manohar, P. M. Madhukar, and P. Jeyapandiarajan, "Experimental investigation of work hardening, residual stress and microstructure during machining Inconel 718," *Journal of Mechanical Science and Technology*, vol. 31, no. 10, pp. 4789–4794, 2017.

[361] A. Andersson, "Built-up edge formation in stainless steel milling," pp. 1–90, 2017. [Online]. Available: http://kth.diva-portal.org/smash/get/diva2:1139609/FULLTEXT01.pdf

[362] G. Kiswanto, M. Azmi, A. Mandala, and T. J. Ko, "The Effect of Machining Parameters to the Surface Roughness in Low Speed Machining Micro-milling Inconel 718," *IOP Conference Series: Materials Science and Engineering*, vol. 654, no. 1, 2019.

[363] H. S. Shan and P. C. Pandey, "Oxidation and wear behaviour of carbide cutting tools," *Wear*, vol. 37, no. 1, pp. 69–75, 1976.

[364] S. M. Bhatia and P. C. Pandey, "Wear of Cemented Carbide Tools in Intermittent Cutting." *Electric Power Research Institute (Report) EPRI EL*, pp. 492–500, 1979.

[365] L. R. da Silva, F. C. Souza, W. L. Guesser, M. J. Jackson, and A. R. Machado, "Critical assessment of compacted graphite cast iron machinability in the milling process," *Journal of Manufacturing Processes*, vol. 56, no. March, pp. 63–74, 2020. [Online]. Available: https://doi.org/10.1016/j.jmapro.2020.04.061

[366] V. P. ASTAKHOV, *METAL CUTTING MECHANICS*. CRC PRESS, 2019.

[367] C. K. Ng, S. N. Melkote, M. Rahman, and A. Senthil Kumar, "Experimental study of micro- and nano-scale cutting of aluminum 7075-T6," *International Journal of Machine Tools and Manufacture*, vol. 46, no. 9, pp. 929–936, 2006.

[368] A. Beranoagirre, D. Olvera, and L. N. López De Lacalle, "Milling of gamma titanium-aluminum alloys," *International Journal of Advanced Manufacturing Technology*, vol. 62, no. 1-4, pp. 83–88, 2012.

[369] L. R. Silva, A. M. Abrão, P. Faria, and J. P. Davim, "Machinability study of steels in precision orthogonal cutting," *Materials Research*, vol. 15, no. 4, pp. 589–595, 2012.

[370] R. Yousefi and Y. Ichida, "Study on ultra-high-speed cutting of aluminum alloy: Formation of welded metal on the secondary cutting edge of the tool and its effects on the quality of finished surface," *Precision Engineering*, vol. 24, no. 4, pp. 371–376, 2000.

[371] C. E. Becze, M. J. Worswick, and M. A. Elbestawi, "High strain rate shear evaluation and characterization of AISI D2 tool steel in its hardened state," *Machining Science and Technology*, vol. 5, no. 1, pp. 131–149, 2001.

[372] S. Lee, J. Hwang, M. Ravi Shankar, S. Chandrasekar, and W. D. Compton, "Large strain deformation field in machining," *Metallurgical and Materials Transactions A: Physical Metallurgy and Materials Science*, vol. 37, no. 5, pp. 1633–1643, 2006.

[373] S. Thamizhmanii and S. Hasan, "Machinability study using chip thickness ratio on difficult to cut metals by cbn cutting tool," *Key Engineering Materials*, vol. 504-506, pp. 1317–1322, 2012.

[374] M. Thoma, "Analysis and Optimization of Convolutional Neural Network Architectures," *arXiv*, no. May, 2017.

[375] E. O. Ezugwu, Z. M. Wang, and A. R. Machado, "Wear of coated carbide tools when machining nickel (Inconel 718) and titanium base (Ti-6A1-4V) alloys," *Tribology Transactions*, vol. 43, no. 2, pp. 263–268, 2000.

[376] B. Kaya, C. Oysu, and H. M. Ertunc, "Advances in Engineering Software Force-torque based on-line tool wear estimation system for CNC milling of Inconel 718 using neural networks," *Advances in Engineering Software*, vol. 42, no. 3, pp. 76–84, 2011. [Online]. Available: http://dx.doi.org/10.1016/j.advengsoft.2010.12.002

[377] X. Chen, J. Lv, Y. Fang, and S. Du, "Online Detection of Surface Defects Based on Improved YOLOV3," *Sensors 2022, Vol. 22, Page 817*, vol. 22, no. 3, p. 817, jan 2022. [Online]. Available: https://www.mdpi.com/1424-8220/22/3/817/htmhttps://www.mdpi.com/1424-8220/22/3/817

[378] E. O. Ezugwu, Z. M. Wang, and A. R. Machado, "The machinability of nickel-based alloys: A review," *Journal of Materials Processing Technology*, vol. 86, no. 1-3, pp. 1–16, 1998.

[379] S. Kosaraju, M. Kumar, N. S. M. T. Proceedings, and undefined 2018, "Optimization of machining parameter in turning Inconel 625," *Elsevier*. [Online]. Available: https://www.sciencedirect.com/science/article/pii/S2214785317330985

Appendix A

Performance of the Spatial Binary Features

A.1 Pearson Square Matrix for Spatial Binary Features: Var1= Area; Var= perimeter; Var3= Fractal Dimension; and Var4= VB

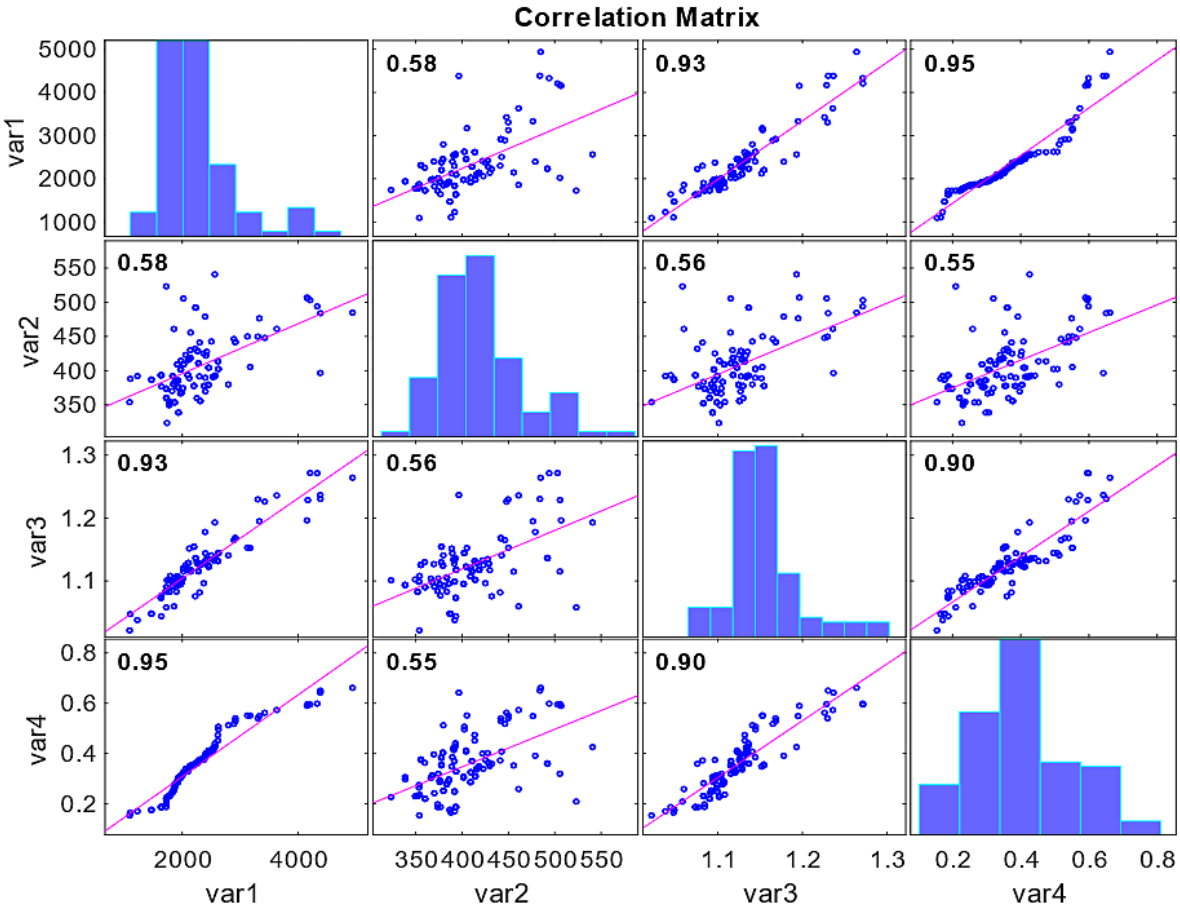

A.2 Regression Analysis of Spatial Binary Features

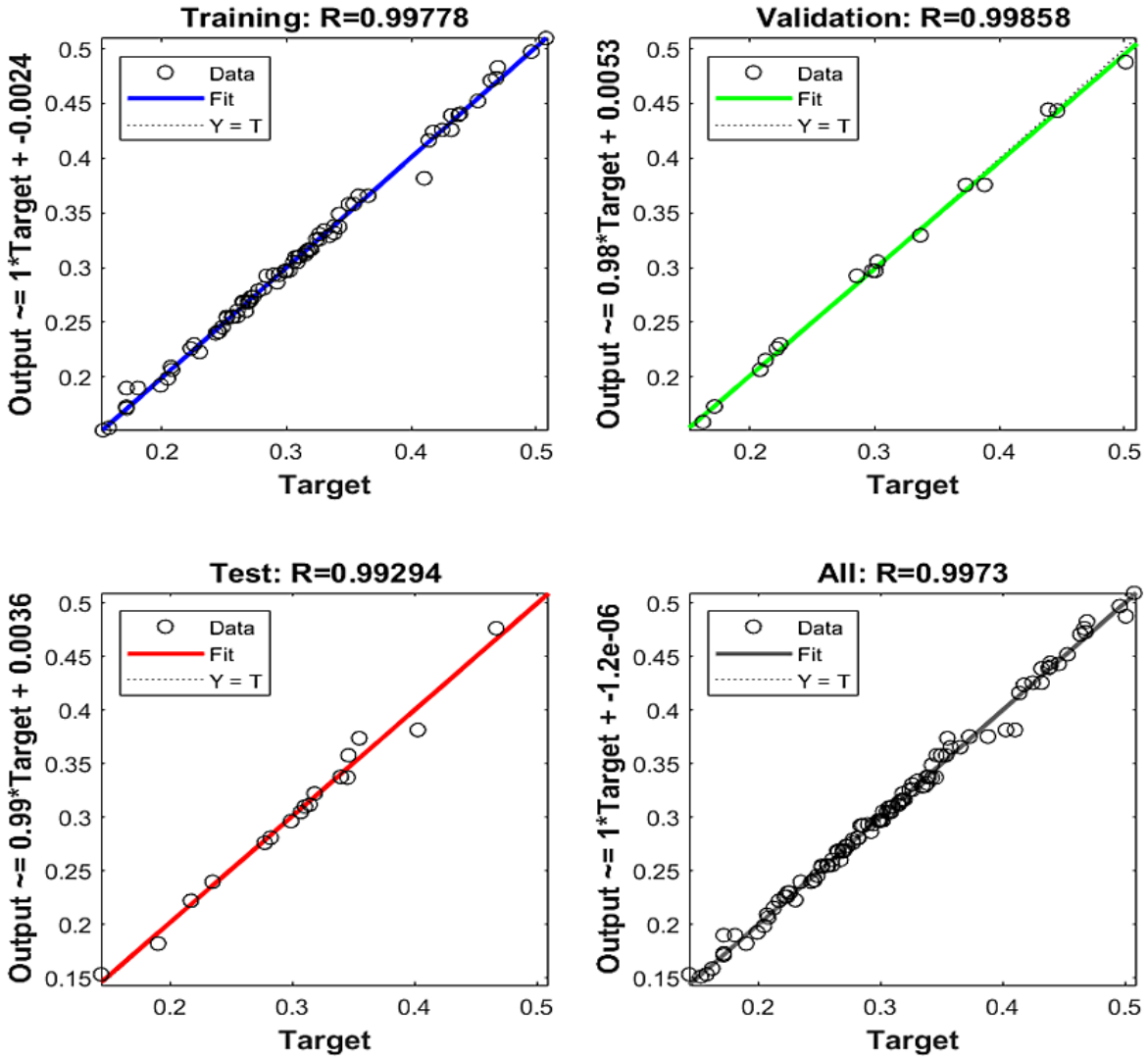

Appendix B

Prediction and parity plots of ML-based MV-TCM system

B.1 MLPNN VB profiles for the the first 2 replicates at $V_c = 40mm/min$, $f_t = 0.08mm/tooth$, $a_p = 0.9mm$, and $a_e = 12.5mm$

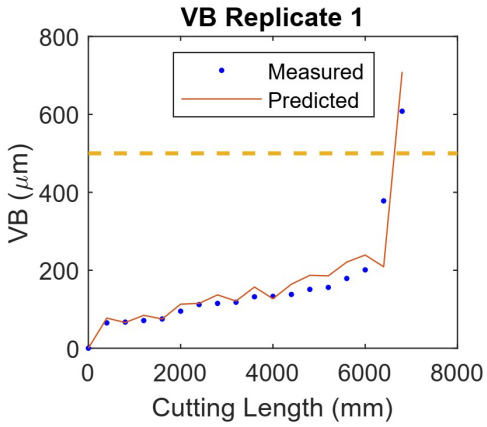

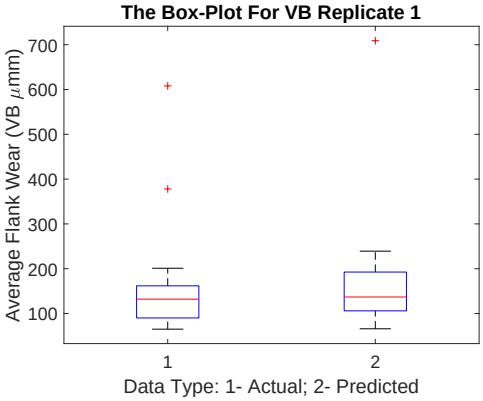

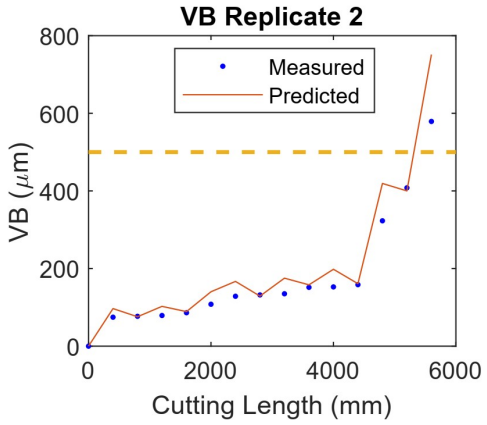

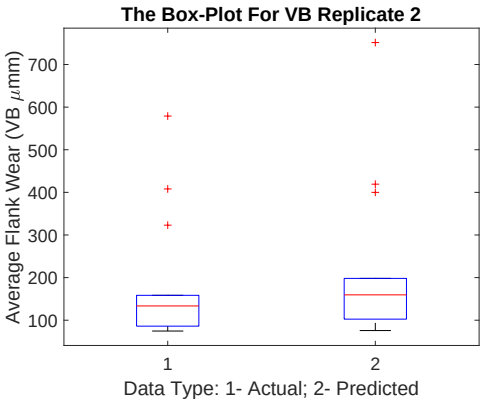

B.2 Parity plots at $V_c = 40mm/min$, $f_t = 0.08mm/tooth$, $a_p = 0.9mm$, and $a_e = 12.5mm$

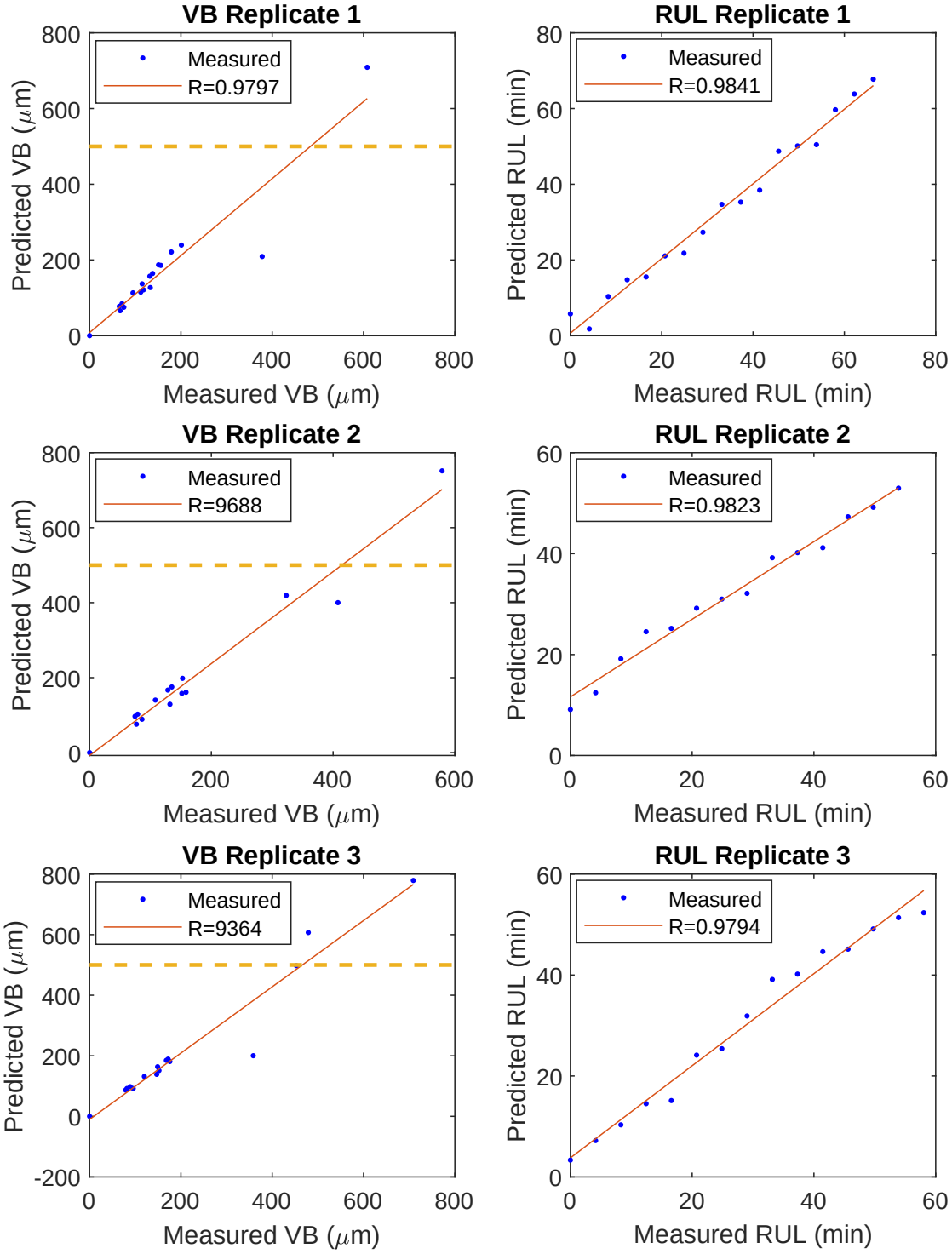

B.3 Pearson Matrix for Evaluating R2 of the SV magnitudes in DFSV

Var1=M1; Var2=M2; Var3=M3; Var4=M4; Var5=M5; Var6=F_i; Var7=VB; and Var8=RUL

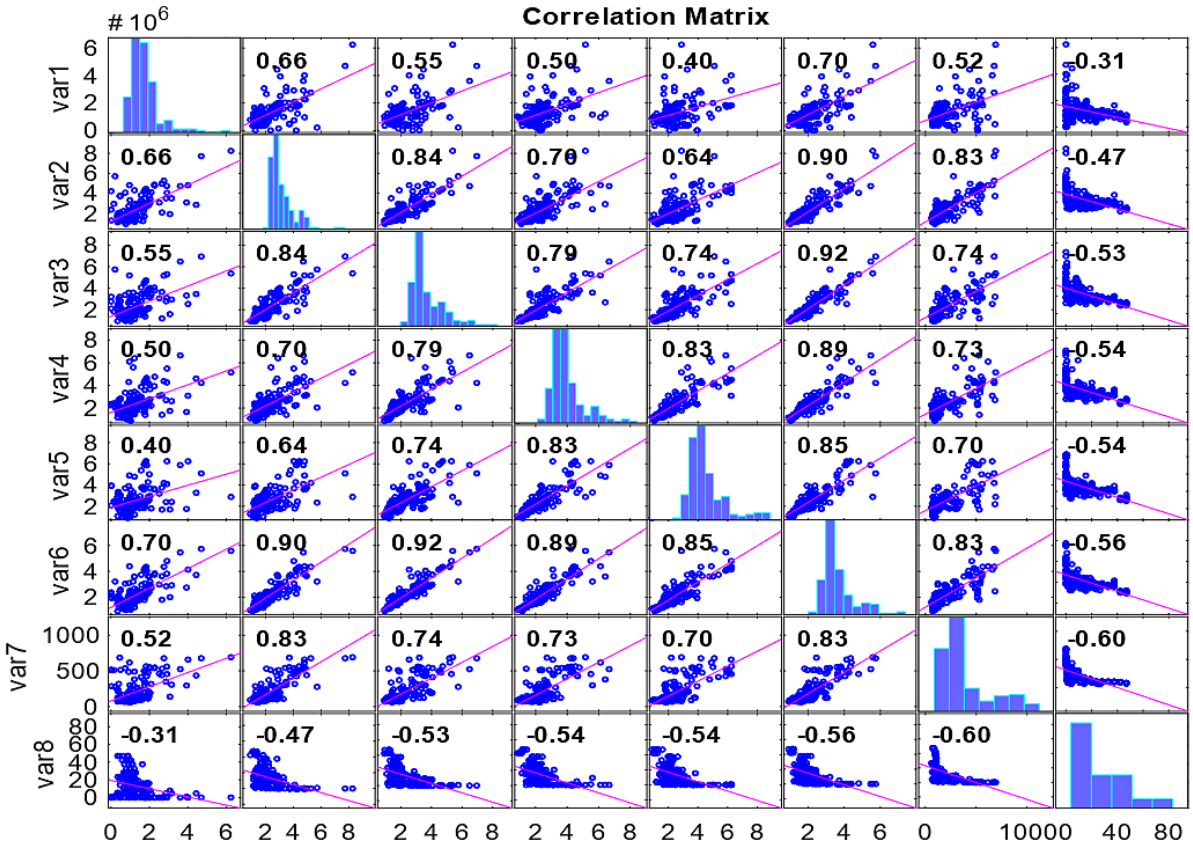

B.4 ML-based MV-TCM performance

(a) Bw_BUE magnitudes at various speeds during training and testing of the ML models; (b) Bw_BUE magnitudes at various feeds; (c) Bw_BUE magnitudes at optimal cutting condition; and (d) processing time analysis

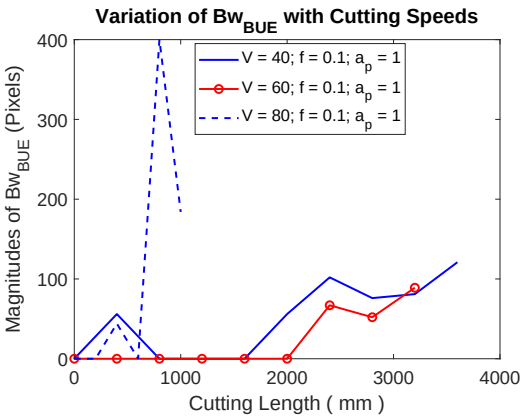

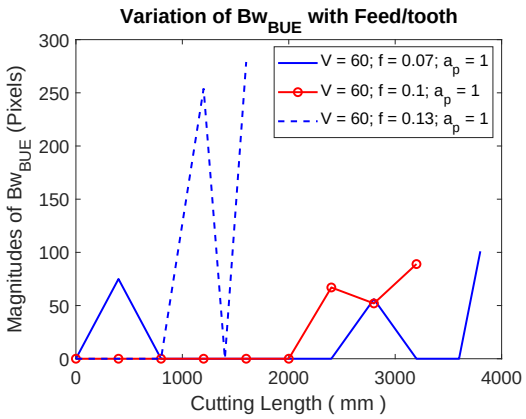

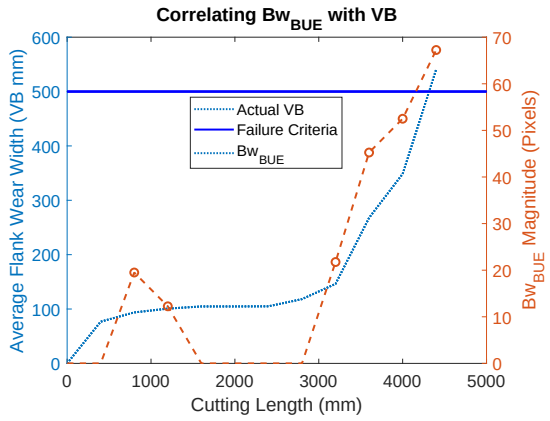

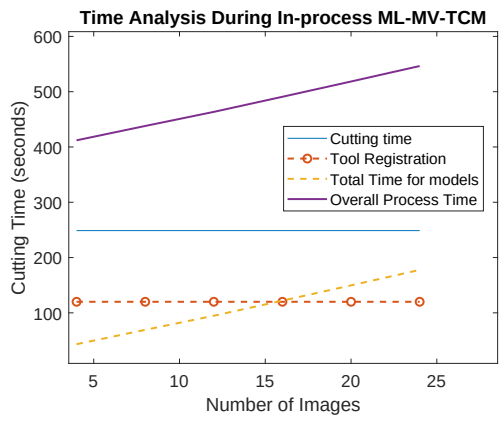

B.5 Proof of Concept for a cyber-physical ML-based MV-TCM system

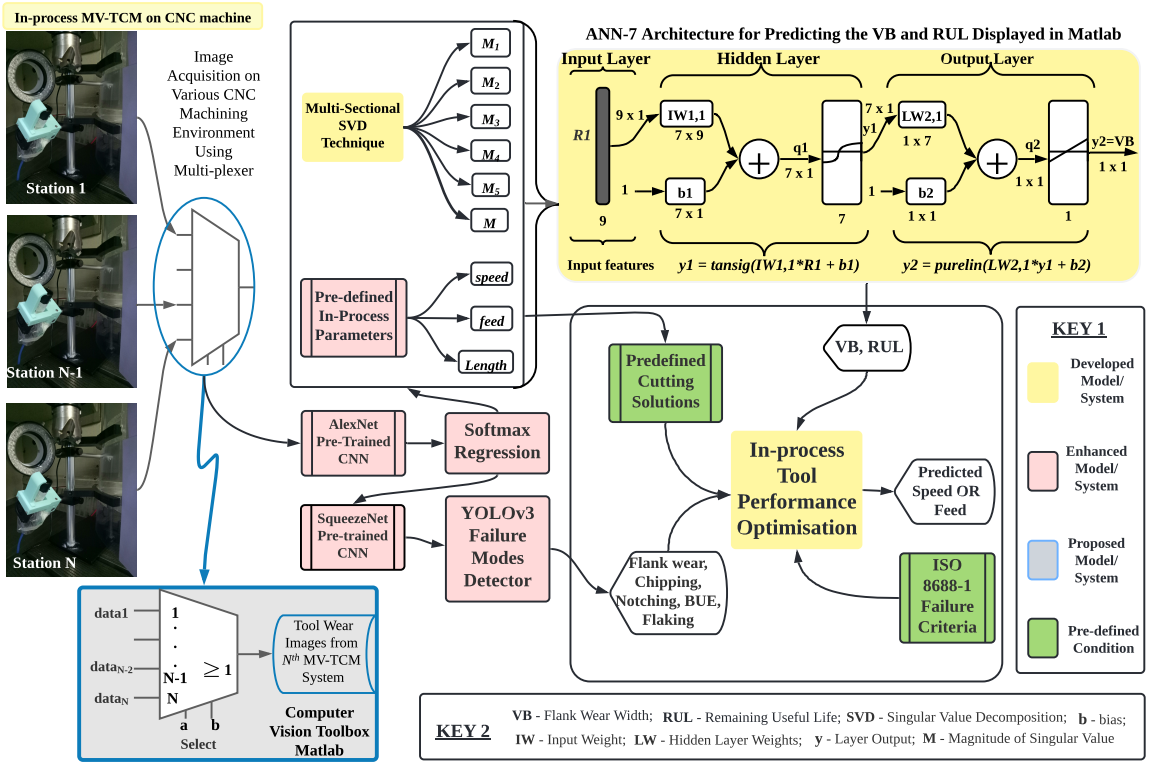

Appendix C

Performance of GKRR: Cross plots, parity plots, and Contour plots

C.1 Gaussian kernel ridge regression Model's Validation Plots

Figure illustrates the Parity plot of (a) full fit and (b) 5-fold cross validation. The error bar shown in the plots was the standard deviation of VB of the four inserts. In full fit, the root-mean-square error (RMSE), RMSE over standard deviation ratio ($RMSE/\sigma$), and R^2 value were 30.9, 0.27 and 0.93, respectively. In 5-fold CV test, the RMSE, $RMSE/\sigma$, and R^2 value were 49.7, 0.43 and 0.81, respectively. All the $RMSE/\sigma$ ratios were less than unity, which suggested some predictive ability of the present model.

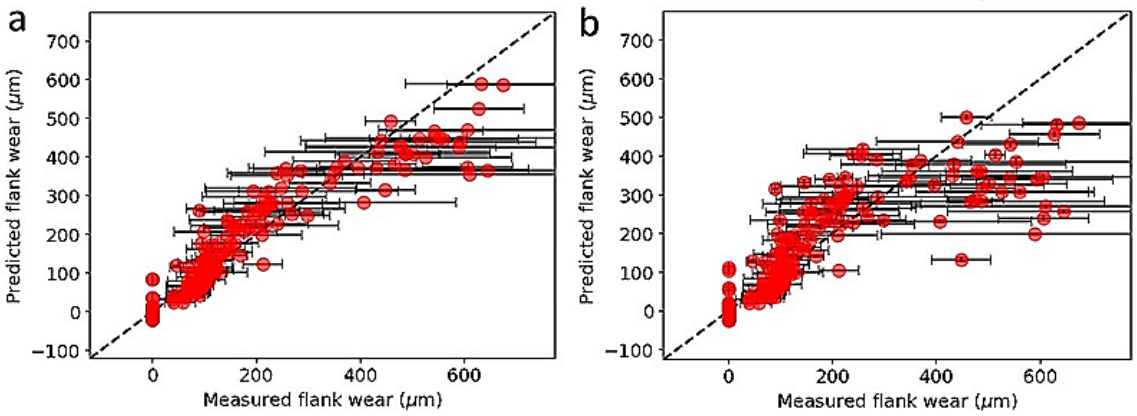

C.2 Gaussian kernel ridge regression Model's cross plot at 40 m/min

Cutting length cross plot at cutting speed = 40 m/min. The error bar shown in the plots was the standard deviation of VB from the four inserts. The dotted line represents VB criteria of $500\mu m$ based on ISO 8688-1 standard.

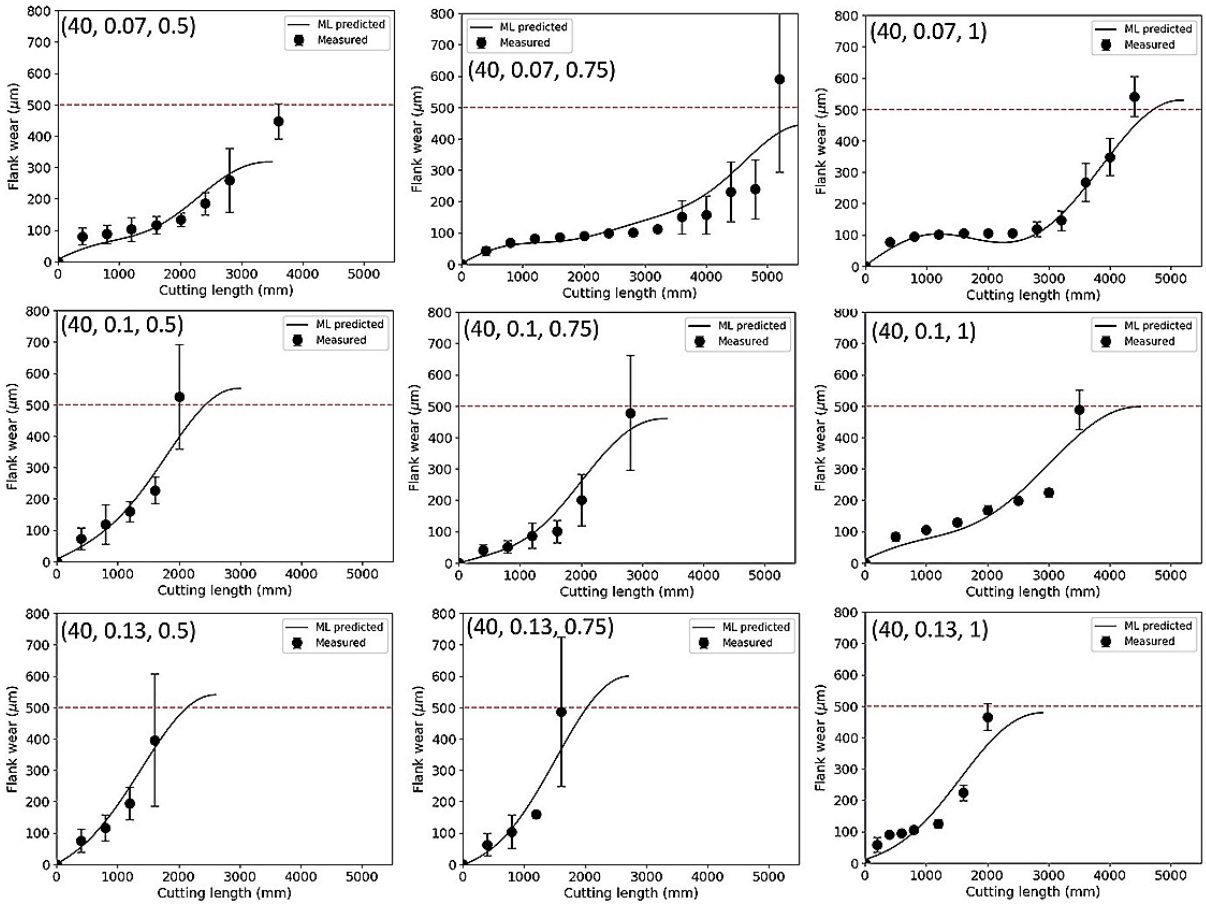

C.3 Gaussian kernel ridge regression Model's cross plots at 60 m/min

Cutting length cross plot at cutting speed = 60 m/min. The error bar shown in the plots was the standard deviation of VB from the four inserts. The dotted line represents VB criteria of $500\mu m$ based on ISO 8688-1 standard.

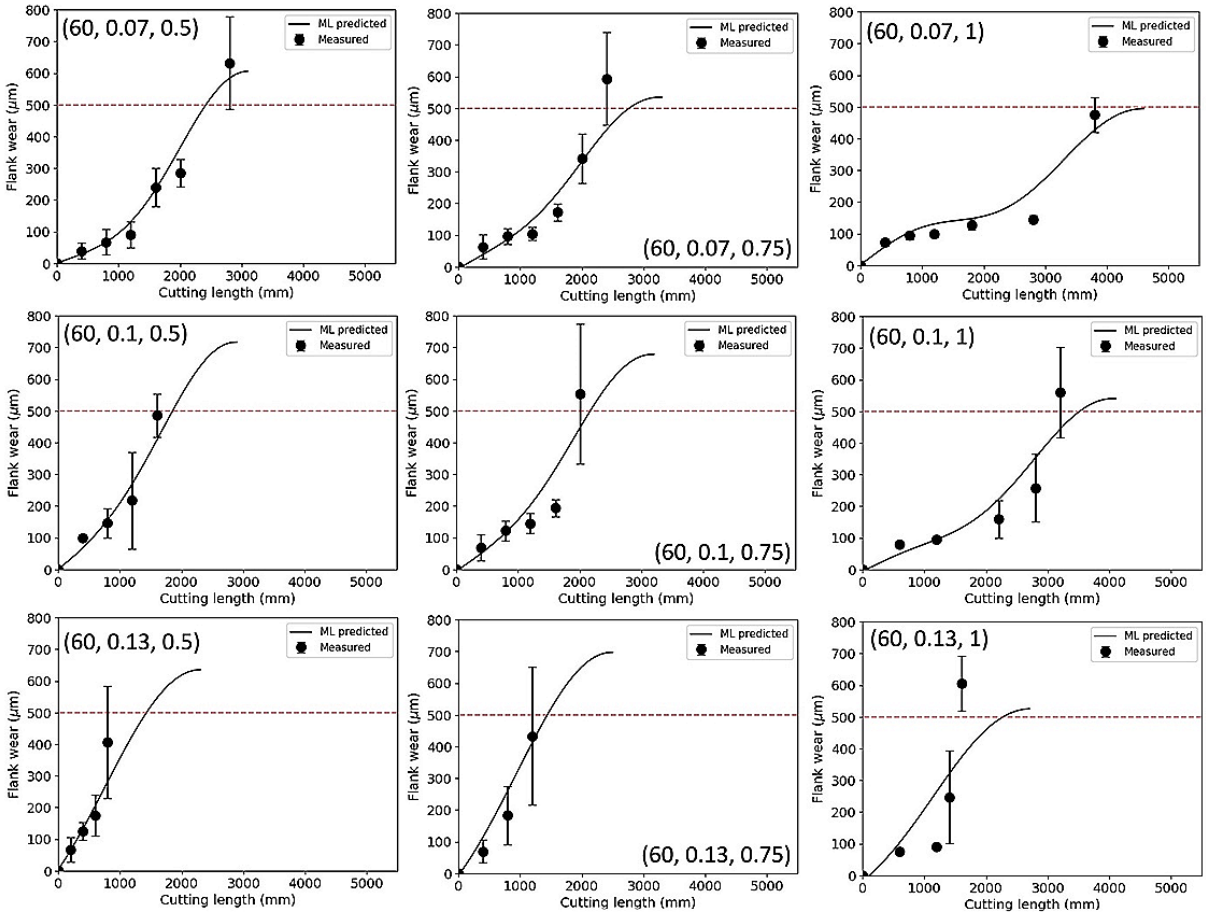

C.4 Gaussian kernel ridge regression Model's cross plots at 80 m/min

Cutting length cross plot at cutting speed = 80 m/min. The error bar shown in the plots was the standard deviation of VB from the four inserts. The dotted line represents VB criteria of $500\mu m$ based on ISO 8688-1 standard.

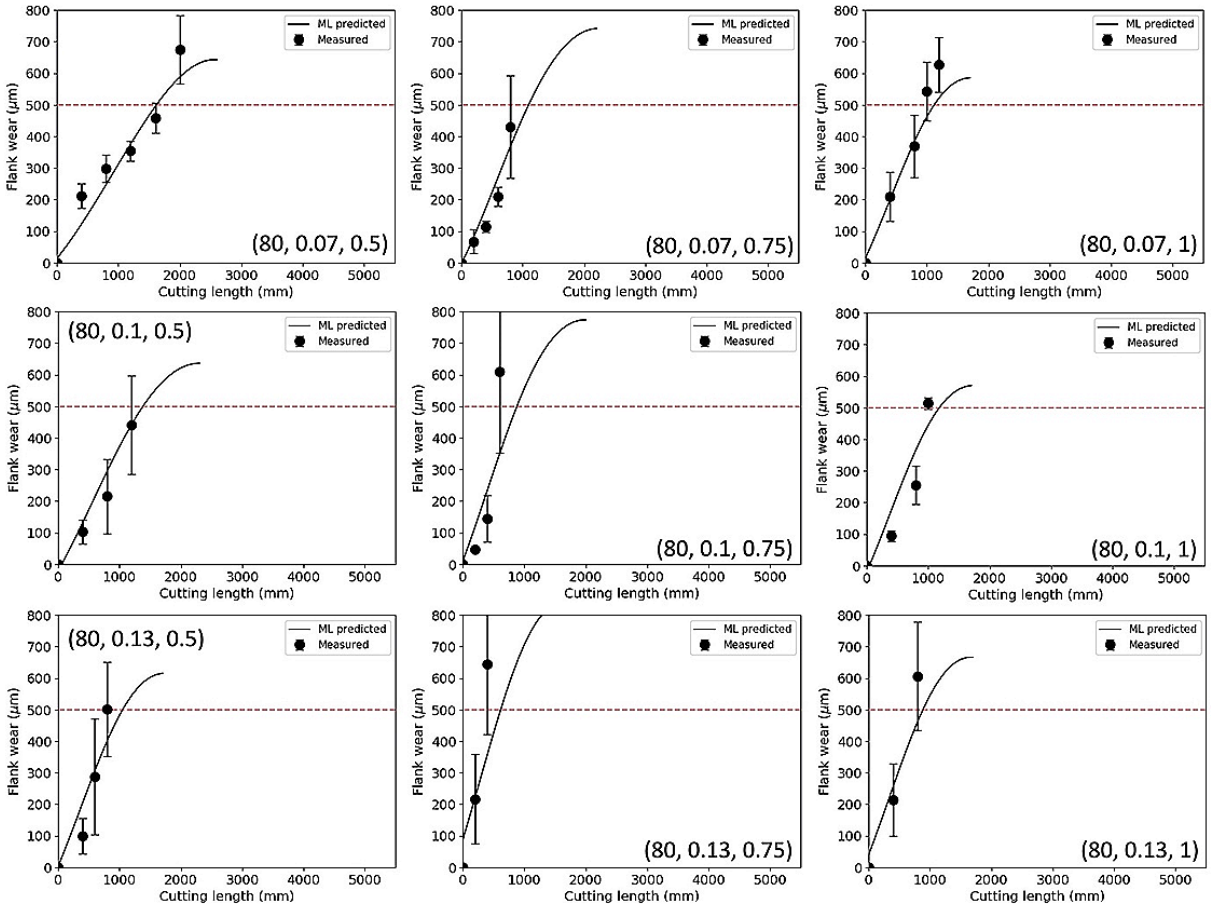

C.5 Gaussian kernel ridge regression Model's property plots

Cutting length vs. feed rate plot at ADOC of 0.9 mm and cutting speed of (a) 30, (b) 40, (c) 50, (d) 60, (e) 70, and (f) 80 m/min. The red hollow circle represents $VB < 500\mu m$ at the given cutting condition. The black solid line represents the cutting time in the unit of minutes. The blue solid line represents the removed depth from the cutting process in the unit of millimeter.

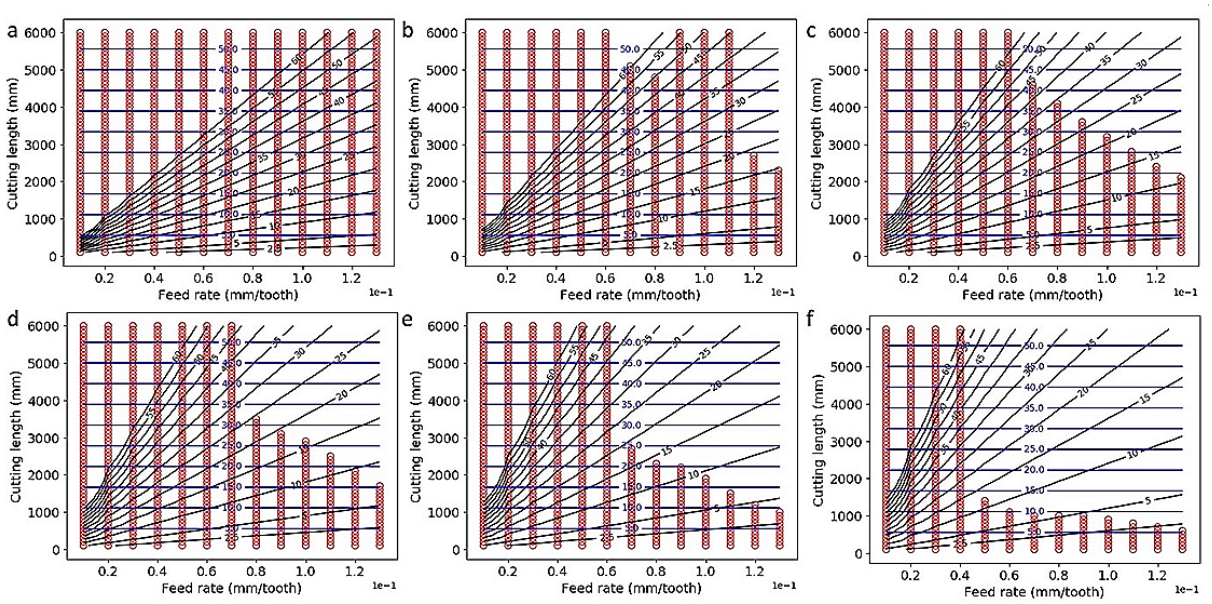

C.6 Graphical Summary of the GKRR ML model

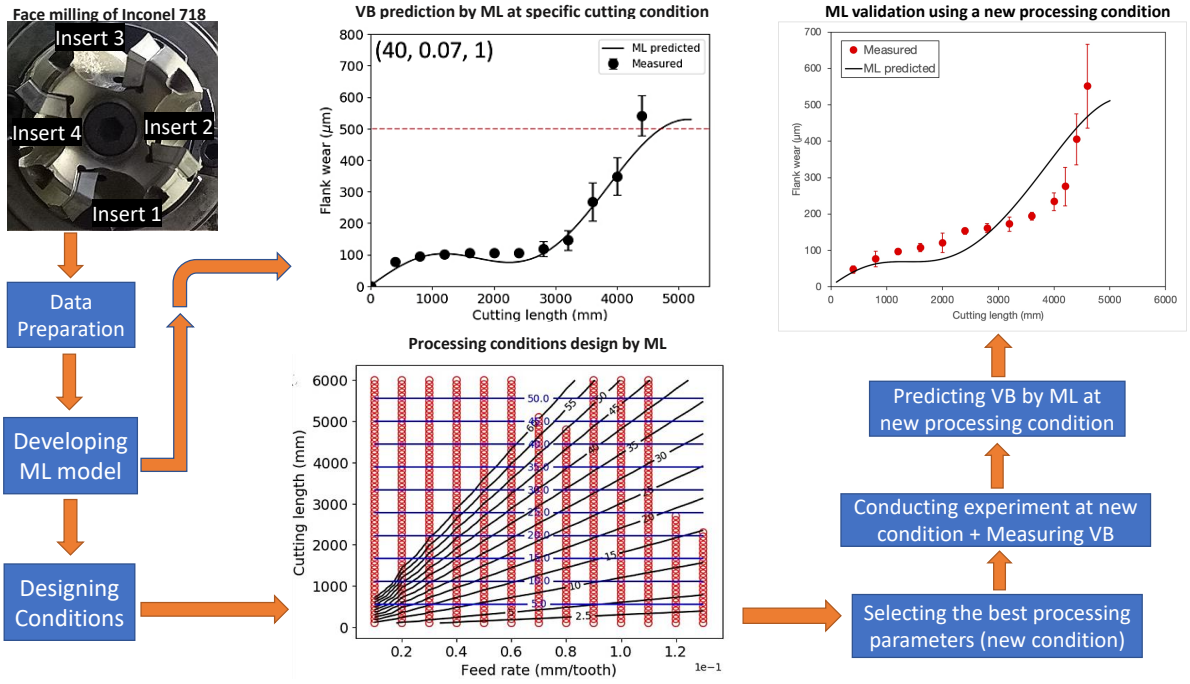

C.7 Failure modes and wear mechanisms analysis during GKRR

Optical micrograph of TiAlN/NbN-coated carbides inserts at $V_c = 40mm/min$, $f_t = 0.08mm/tooth$, $a_p = 0.9mm$, and $a_e = 12.5mm$ after cutting length of (a) 1200, (b) 4000, (c) 4400, and (d) 4600 mm. Secondary electron images of the dotted-line region in (c) and (d) showing the localized chipping caused by abrasion and cyclic adhesion after cutting length of (e) 4400, and (f) 4600 mm.

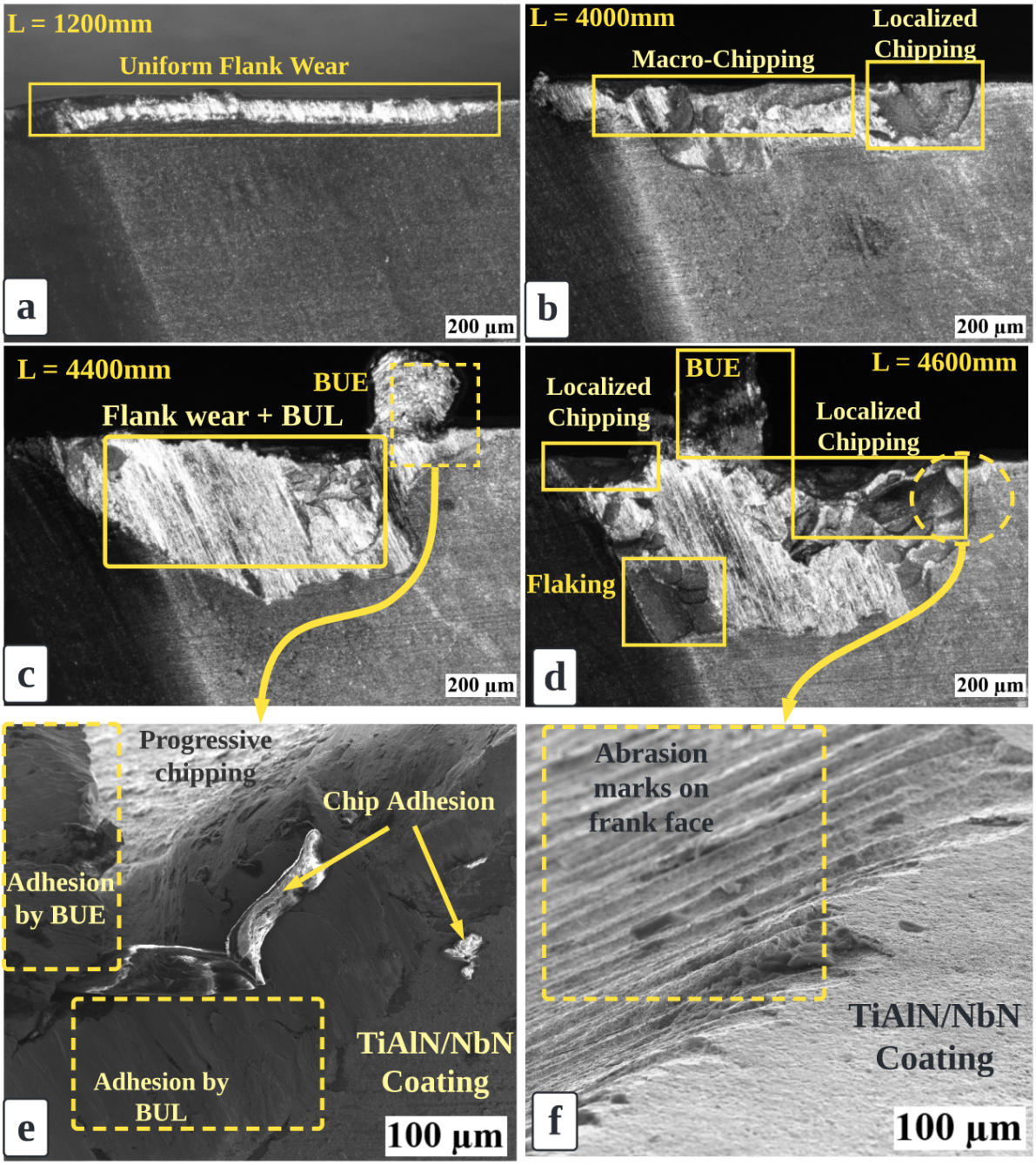

Appendix D

Machine Learning MATLAB Programs

D.1 Data Acquisition Codes

D.1.1 Setting Up the Arduino Uno Micro-controller and Camera

3/16/23 12:28 PM C:\Users\Tiyamike\Des...\arduinoSetup.m 1 of 1

```
%initialize the Arduino Uno using the arduino function in MATLAB
% with the appropriate COM port and board type parameters.
% Set up the sensor pins using the configurePin function.
% Specifying the pin number and pin mode (digital input or analog input).
% Finally, set up the camera controls by configuring the appropriate pins using ↙
configurePin.

function arduinoSetup()

% Initialize Arduino Uno
a = arduino('COM3', 'Uno');

% Set up sensor pins
configurePin(a, 'D2', 'DigitalInput');
configurePin(a, 'D3', 'DigitalInput');
configurePin(a, 'A0', 'AnalogInput');
configurePin(a, 'A1', 'AnalogInput');

% Set up camera controls
configurePin(a, 'D4', 'DigitalOutput');
configurePin(a, 'D5', 'DigitalOutput');
configurePin(a, 'D6', 'DigitalOutput');
configurePin(a, 'D7', 'DigitalOutput');

end
```

D.1.2 Auto-Capturing the Flank Wear Images

3/18/23 6:10 PM C:\Users\...\camera_IR_capture_24_2_23.m 1 of 1

```
% Connect to Arduino hardware
a = arduino;

% Configure pin 7 as an input
configurePin(a, 'D7', 'DigitalInput');

% Connect to the camera
camList = webcamlist;
cam = webcam(1);

% Specify the directory to save the images
dir = 'C:\Users\Tiyamike\Desktop\Documents\Pictures\Online Image Acquistion';

% Loop to continuously check the value of the IR sensor
while true
    % Read the value of the IR sensor
    irValue = readDigitalPin(a, 'D7');

    % If the value is 0 (ie something is blocking the sensor), take a picture
    if irValue == 0
       img = snapshot(cam);

        % Generate a unique file name for the image
        filename = [dir, num2str(floor(now * 10^5)), '.jpg'];

        % Save the image to disk
        imwrite(img, filename);

        % Display the image
        imshow(img);

        % Pause for 33.333 milliseconds to slow down the loop (30fps)
        pause(1/30);


    else
        disp('no object')
        pause(0.2)
    end
end
```

D.1.3 Data Save and Transfer Function

3/18/23 3:39 PM C:\Users\...\Data_save_transfer_script.m 1 of 1

```
%% Save and Transfer Image Data during MV-TCM
function []=Data_save_transfer_script()

%% Define the file location, day, date, time, number, and name
file_location = 'C:\Users\Tiyamike\Desktop\Documents\Pictures\Online Image↙
Acquistion';  % Change this...
% to the desired location
day = datetime("now", 'ddd');
date = datetime("now", 'yyyy-mm-dd');
time = datetime("now", 'HH-MM-SS');
number = '0001';  % Change this to the desired number
name = 'image';

%% Create the directory if it doesn't exist
if ~exist([file_location day '\' date], 'dir')
    mkdir([file_location day '\' date]);
end

%% Capture the image
% Call the image capturing fucntion to acquire img;
%% Save the image to the file
imwrite(img, file_name);

%% Transfer the file to a remote location
remote_location = 'C:\Users\Tiyamike\Desktop\Documents\Pictures\Online Image↙
Acquistion';  % Change this to the desired...
% remote location
command = ['pscp.exe ' file_name ' ' remote_location];  % Change this to the path of↙
pscp.exe on...
% your system
[status, output] = system(command);

%% Check if the transfer was successful
if status ~= 0
    error('Error transferring file: %s', output);
else
    disp('File transfer successful');
end
```

D.2 Binary classifier Main code

3/18/23 5:59 PM C:\Users\Tiyamike\...\binaryclassifier.m 1 of 1

```
%% changing all thermal images to gray image
load('trainedNet3.mat')
filenames = dir(fullfile(image_folder, '*.tif'));
total_images = numel(filenames);
tday = datetime(now,'Format','yyyy-MM-dd','convertFrom','datenum');
ttime = datetime(now,'Format','HH.mm.ss','convertFrom','datenum');
mainfolder = fullfile(outputdestination,'Wear Inserts');
    if ~exist(mainfolder,'dir')
        mkdir(mainfolder)
    end
wearfoldername = 'Wear Insert %s';
wearfolder = sprintf(wearfoldername,tday);
wearfolder2 = fullfile(mainfolder,wearfolder);
    if ~exist(wearfolder2, 'dir')
       mkdir(wearfolder2)
    end
wearfiles = sprintf(wearfoldername,ttime);
wearfiles2 = fullfile(wearfolder2,wearfiles);
mkdir(wearfiles2)
 for n = 1:total_images
     full_name= fullfile(image_folder, filenames(n).name);
     our_images = imread(full_name);
     ds = augmentedImageDatastore(imageSize, our_images, ...
    'ColorPreprocessing', 'gray2rgb');
     imageFeatures = activations(net1, ds, featureLayer, ...
    'MiniBatchSize', 32, 'Outputas','columns');
     label1 = predict(classifier, imageFeatures, 'ObservationsIn','columns');
     switch label1
           case 'WearInserts'
                A = our_images;
                [image_folder, baseFileNameNoExtenstion, ext] = fileparts(full_name);
                newFilename = [baseFileNameNoExtenstion, '.tif'];
                newfoldername = fullfile(wearfolder2,wearfiles);
                newFile = fullfile(newfoldername, newFilename);
                newfilepath = fullfile(pwd,newFile);
                imwrite(our_images, newFile,'tif');
           case 'Residues'
                A = our_images;
                [image_folder, baseFileNameNoExtenstion, ext] = fileparts(full_name);
                newFilename = [baseFileNameNoExtenstion, '.tif'];
                newfoldername = fullfile(wearfolder2,wearfiles);
                newFile = fullfile(newfoldername, newFilename);
                newfilepath = fullfile(pwd,newFile);
                imwrite(our_images, newFile,'tif');
     end
 end
```

D.3 The multi-sectional SVD Code

D.3.1 Enhanced SVD

3/19/23 1:40 AM C:\Users\Tiyamike\Desk...\SVD_Enhanced.m 1 of 2

```
function [U,S,V,rmse,Relative_Norm,compression_ratio, PSNR,SNR,SSIM_val]= ↙
SVD_Enhanced(Image)

%% Processing RGB image channels
[m,n,k]=size(Image);
q=60;
Wear_Image=double(Image); U=zeros(m,m);
S=zeros(m,n);V=zeros(n,n);
Relative_Norm=zeros(q,k);
compression_ratio=zeros(q,1);
rmse=zeros(q,k);
for i=1:k
[U(:,:,i),S(:,:,i),V(:,:,i)]=svd(Wear_Image(:,:,i));
end
for r=1:q
    ca=zeros(m,n,k);
    compression_ratio(r)=m*n/(r*(m+n+1));
    for i=1:k
        cai=zeros(m,n,k);
        [ca(:,:,i),cai(:,:,i)]=deal(U(:,1:r,i)*S(1:r,1:r,i)*V(:,1:r,i)');
        Relative_Norm(r,i)=S(r+1,r+1,i)/S(1,1,i);
        rmse(r,i)=sqrt(sum(sum(((Wear_Image(:,:,i)-ca(:,:,i)).^2)))/(m*n));
        [PSNR(r,i), SNR(r,i)] = psnr(ca(:,:,i), Wear_Image(:,:,i));
        [SSIM_val(r,i),SSIM_map(r,i)] = ssim(ca(:,:,i),Wear_Image(:,:,i));
        imwrite(uint8(cai), sprintf('%dr%d.jpg',r,i));
    end
    imwrite(uint8(ca), sprintf('%dr.jpg', r));
end

%% Plotting performance graphs
% % Plotting the room mean square errors of each image section
% figure
% plot(1:q,rmse_A1,'MarkerEdgeColor','r','MarkerEdgeColor','g'); hold on;
% plot(1:q,rmse_A2,'MarkerEdgeColor','r','MarkerEdgeColor','g'); hold on;
% plot(1:q,rmse_A3,'MarkerEdgeColor','r','MarkerEdgeColor','g'); hold on;
% plot(1:q,rmse_A4,'MarkerEdgeColor','r','MarkerEdgeColor','g'); hold on;
% xlabel('Approximation Rank r');
% ylabel('Root Mean Square Error');

% % Plotting the compression ratio of each image section
% figure
% plot(1:q,compression_ratio_A1); hold on;
% plot(1:q,compression_ratio_A2); hold on;
% plot(1:q,compression_ratio_A3); hold on;
% plot(1:q,compression_ratio_A4); hold on;
% plot(1:q,compression_ratio_A5); hold off;
% xlabel('Approximation Rank r');
% ylabel('Compression Ratio'); xlim([1 q])
```

D.3.2 Multi-sectional SVD Features Extraction

3/19/23 1:48 AM C:\Users\Tiyami...\multi_sectional_SVD.m 1 of 3

```
function F_i = multi_sectional_SVD(Image)
%This function has an input called Image. The function is used to divide the image ↙
into 160-sections
% This function is calls a function calls SVD_Enhanced to decompose the sections
% From each section, 55 singular values are extracted to compute the magnitudes by ↙
using l2-norm
% The maximum values of each row are combined to create an F_i feature
%% Loading an Image and segmenting
Image = im2gray(Image);
img1 = Image;
R = 180; C = 96;q=60;
NumberofBlocks = size(img1,1)*size(img1,2) / (R*C);
dividedImage = zeros([R C NumberofBlocks]);
ImageRows = 1;
ImageColumns = 1;
try
    for count=1:NumberofBlocks
        NewImage(:,:,count) = img1(ImageRows:ImageRows+R-1,ImageColumns: ↙
ImageColumns+C-1);
        ImageColumns = ImageColumns + C;
        if(ImageColumns >= size(img1,2))
            ImageColumns = 1;
            ImageRows = ImageRows + R;
            if(ImageRows >= size(img1,1))
                ImageRows = 1;
            end
        end
    end
end
%% separate the blocks of image
% first row
A3B3 = NewImage(:,:,43); A4B3 = NewImage(:,:,44); A5B3 = NewImage(:,:,45); A6B3 = ↙
NewImage(:,:,46);
A7B3 = NewImage(:,:,47); A8B3 = NewImage(:,:,48); A9B3 = NewImage(:,:,49); A10B3 = ↙
NewImage(:,:,50);
A11B3 = NewImage(:,:,51); A12B3 = NewImage(:,:,52);
% second row
A3B4 = NewImage(:,:,63); A4B4 = NewImage(:,:,64); A5B4 = NewImage(:,:,65); A6B4 = ↙
NewImage(:,:,66);
A7B4 = NewImage(:,:,67); A8B4 = NewImage(:,:,68); A9B4 = NewImage(:,:,69); A10B4 = ↙
NewImage(:,:,70);
A11B4 = NewImage(:,:,71); A12B4 = NewImage(:,:,72);
% third row
A3B5 = NewImage(:,:,83); A4B5 = NewImage(:,:,84); A5B5 = NewImage(:,:,85); A6B5 = ↙
NewImage(:,:,86);
A7B5 = NewImage(:,:,87); A8B5 = NewImage(:,:,88); A9B5 = NewImage(:,:,89); A10B5 = ↙
NewImage(:,:,90);
A11B5 = NewImage(:,:,91); A12B5 = NewImage(:,:,92);
% fourth row
```

```
A3B6 = NewImage(:,:,103); A4B6 = NewImage(:,:,104); A5B6 = NewImage(:,:,105); A6B6 = ↙
NewImage(:,:,106);
A7B6 = NewImage(:,:,107); A8B6 = NewImage(:,:,108); A9B6 = NewImage(:,:,109); A10B6 = ↙
NewImage(:,:,110);
A11B6 = NewImage(:,:,111); A12B6 = NewImage(:,:,112);

%% Apply SVD in each section of the sub-image
%first row
[~,S_A3B3,~,~,~,~,~,~]= SVD_Enhanced(A3B3); [~,S_A4B3,~,~,~,~,~,~]= SVD_Enhanced ↙
(A4B3);
[~,S_A5B3,~,~,~,~,~,~]= SVD_Enhanced(A5B3); [~,S_A6B3,~,~,~,~,~,~]= SVD_Enhanced ↙
(A6B3);
[~,S_A7B3,~,~,~,~,~,~]= SVD_Enhanced(A7B3); [~,S_A8B3,~,~,~,~,~,~]= SVD_Enhanced ↙
(A8B3);
[~,S_A9B3,~,~,~,~,~,~]= SVD_Enhanced(A9B3); [~,S_A10B3,~,~,~,~,~,~]= SVD_Enhanced ↙
(A10B3);
[~,S_A11B3,~,~,~,~,~,~]= SVD_Enhanced(A11B3); [~,S_A12B3,~,~,~,~,~,~]= SVD_Enhanced ↙
(A12B3);
%second row
[~,S_A3B4,~,~,~,~,~,~]= SVD_Enhanced(A3B4); [~,S_A4B4,~,~,~,~,~,~]= SVD_Enhanced ↙
(A4B4);
[~,S_A5B4,~,~,~,~,~,~]= SVD_Enhanced(A5B4); [~,S_A6B4,~,~,~,~,~,~]= SVD_Enhanced ↙
(A6B4);
[~,S_A7B4,~,~,~,~,~,~]= SVD_Enhanced(A7B4); [~,S_A8B4,~,~,~,~,~,~]= SVD_Enhanced ↙
(A8B4);
[~,S_A9B4,~,~,~,~,~,~]= SVD_Enhanced(A9B4); [~,S_A10B4,~,~,~,~,~,~]= SVD_Enhanced ↙
(A10B4);
[~,S_A11B4,~,~,~,~,~,~]= SVD_Enhanced(A11B4); [~,S_A12B4,~,~,~,~,~,~]= SVD_Enhanced ↙
(A12B4);
%third row
[~,S_A3B5,~,~,~,~,~,~]= SVD_Enhanced(A3B5); [~,S_A4B5,~,~,~,~,~,~]= SVD_Enhanced ↙
(A4B5);
[~,S_A5B5,~,~,~,~,~,~]= SVD_Enhanced(A5B5); [~,S_A6B5,~,~,~,~,~,~]= SVD_Enhanced ↙
(A6B5);
[~,S_A7B5,~,~,~,~,~,~]= SVD_Enhanced(A7B5); [~,S_A8B5,~,~,~,~,~,~]= SVD_Enhanced ↙
(A8B5);
[~,S_A9B5,~,~,~,~,~,~]= SVD_Enhanced(A9B5); [~,S_A10B5,~,~,~,~,~,~]= SVD_Enhanced ↙
(A10B5);
[~,S_A11B5,~,~,~,~,~,~]= SVD_Enhanced(A11B5); [~,S_A12B5,~,~,~,~,~,~]= SVD_Enhanced ↙
(A12B5);
%fourth row
[~,S_A3B6,~,~,~,~,~,~]= SVD_Enhanced(A3B6); [~,S_A4B6,~,~,~,~,~,~]= SVD_Enhanced ↙
(A4B6);
[~,S_A5B6,~,~,~,~,~,~]= SVD_Enhanced(A5B6); [~,S_A6B6,~,~,~,~,~,~]= SVD_Enhanced ↙
(A6B6);
[~,S_A7B6,~,~,~,~,~,~]= SVD_Enhanced(A7B6); [~,S_A8B6,~,~,~,~,~,~]= SVD_Enhanced ↙
(A8B6);
[~,S_A9B6,~,~,~,~,~,~]= SVD_Enhanced(A9B6); [~,S_A10B6,~,~,~,~,~,~]= SVD_Enhanced ↙
(A10B6);
```

3/19/23 1:49 AM C:\Users\Tiyami...\multi_sectional_SVD.m 3 of 3

```
[~,S_A11B6,~,~,~,~,~,~]= SVD_Enhanced(A11B6); [~,S_A12B6,~,~,~,~,~,~]= SVD_Enhanced ↙
(A12B6);

%% calculating magnitude of the eigen values with rank 60 for all image slices
% magnitudes for the first row
Magnitude_A3B3 = norm(S_A3B3(6:60,:).^2); Magnitude_A4B3 = norm(S_A4B3(6:60,:).^2);
Magnitude_A5B3 = norm(S_A5B3(6:60,:).^2); Magnitude_A6B3 = norm(S_A6B3(6:60,:).^2);
Magnitude_A7B3 = norm(S_A7B3(6:60,:).^2); Magnitude_A8B3 = norm(S_A8B3(6:60,:).^2);
Magnitude_A9B3 = norm(S_A9B3(6:60,:).^2); Magnitude_A10B3 = norm(S_A10B3(6:60,:).^2);
Magnitude_A11B3 =norm(S_A11B3(6:60,:).^2);Magnitude_A12B3 = norm(S_A12B3(6:60,:).^2);
Magnitude_B3 = max(Magnitude_A3B3,Magnitude_A4B3,Magnitude_A5B3,Magnitude_A6B3, ↙
Magnitude_A7B3,Magnitude_A8B3,...
    Magnitude_A8B3,Magnitude_A9B3,Magnitude_A10B3,Magnitude_A11B3,Magnitude_A12B3);
% magnitudes for the second row
Magnitude_A3B4 = norm(S_A3B4(6:60,:).^2); Magnitude_A4B4 = norm(S_A4B4(6:60,:).^2);
Magnitude_A5B4 = norm(S_A5B4(6:60,:).^2); Magnitude_A6B4 = norm(S_A6B4(6:60,:).^2);
Magnitude_A7B4 = norm(S_A7B4(6:60,:).^2); Magnitude_A8B4 = norm(S_A8B4(6:60,:).^2);
Magnitude_A9B4 = norm(S_A9B4(6:60,:).^2); Magnitude_A10B4 = norm(S_A10B4(6:60,:).^2);
Magnitude_A11B4 =norm(S_A11B4(6:60,:).^2);Magnitude_A12B4 = norm(S_A12B4(6:60,:).^2);
Magnitude_B4 = max(Magnitude_A3B4,Magnitude_A4B4,Magnitude_A5B4,Magnitude_A6B4, ↙
Magnitude_A7B4,Magnitude_A8B4,...
    Magnitude_A8B4,Magnitude_A9B4,Magnitude_A10B4,Magnitude_A11B4,Magnitude_A12B4);
% magnitudes for the third row
Magnitude_A3B5 = norm(S_A3B5(6:60,:).^2); Magnitude_A4B5 = norm(S_A4B5(6:60,:).^2);
Magnitude_A5B5 = norm(S_A5B5(6:60,:).^2); Magnitude_A6B5 = norm(S_A6B5(6:60,:).^2);
Magnitude_A7B5 = norm(S_A7B5(6:60,:).^2); Magnitude_A8B5 = norm(S_A8B5(6:60,:).^2);
Magnitude_A9B5 = norm(S_A9B5(6:60,:).^2); Magnitude_A10B5 = norm(S_A10B5(6:60,:).^2);
Magnitude_A11B5 =norm(S_A11B5(6:60,:).^2);Magnitude_A12B5 = norm(S_A12B5(6:60,:).^2);
Magnitude_B5 = max(Magnitude_A3B5,Magnitude_A4B5,Magnitude_A5B5,Magnitude_A6B5, ↙
Magnitude_A7B5,Magnitude_A8B5,...
    Magnitude_A8B5,Magnitude_A9B5,Magnitude_A10B5,Magnitude_A11B5,Magnitude_A12B5);
% magnitudes for the fourth row
Magnitude_A3B6 = norm(S_A3B6(6:60,:).^2); Magnitude_A4B6 = norm(S_A4B6(6:60,:).^2);
Magnitude_A5B6 = norm(S_A5B6(6:60,:).^2); Magnitude_A6B6 = norm(S_A6B6(6:60,:).^2);
Magnitude_A7B6 = norm(S_A7B6(6:60,:).^2); Magnitude_A8B6 = norm(S_A8B6(6:60,:).^2);
Magnitude_A9B6 = norm(S_A9B6(6:60,:).^2); Magnitude_A10B6 = norm(S_A10B6(6:60,:).^2);
Magnitude_A11B6 =norm(S_A11B6(6:60,:).^2);Magnitude_A12B6 = norm(S_A12B6(6:60,:).^2);
Magnitude_B6 = max(Magnitude_A3B6,Magnitude_A4B6,Magnitude_A5B6,Magnitude_A6B6, ↙
Magnitude_A7B6,Magnitude_A8B6,...
    Magnitude_A8B6,Magnitude_A9B6,Magnitude_A10B6,Magnitude_A11B6,Magnitude_A12B6);
%% Computing the F_i Feature
F_i = Magnitude_B3 + Magnitude_B4 + Magnitude_B5 + Magnitude_B6;
```

D.4 Failure Modes Detection Main Code

3/18/23 6:30 PM C:\Users\Tiyam...\tool_wear_prediction.m 1 of 2

```
%% model deployment for different images.

%obtain the newest folder from the imagefolder
cameradestination = ('C:\Users\user\Pictures\Baumer Image Records\VCXU-65M.R');
run('obtainnewestfolder.m');

%% Data daving and file transfer code

%specify the destination of output
outputdestination = pwd;

%Specify the folder of the images
image_folder = 'C:\Users\Tiyamike\Desktop\Documents\Pictures\Online Image ↙
Acquistion';
run('binaryclassifier.m');
addpath(mainfolder,wearfolder2,wearfiles2);
clearvars -except mainfolder wearfolder2 wearfiles2;
wearfolderdir = wearfiles2;

%loads the trained network
warning('off','all');
load('mainnetrev3.mat');
close(fig);
%% Loading folder from online data acquisition
% change to the folderpath that store the images
imageStorageFolder = wearfiles2;
% get the all the jpg images in the folder
imageFolder = dir(imageStorageFolder);
% identifying the number of files in the folder
nfiles = numel(imageFolder);
% the newest folder will be the last folder
currentFolderName = imageFolder(nfiles).name;
currentFolder = imageFolder(nfiles).folder;
currentFolderPath = fullfile(currentFolder,currentFolderName);
% access the lastest folder and read the total number of images inside
ImageList = dir(fullfile(currentFolder, '*.tif'));
total_images = numel(ImageList);
% resize the image to [227 227 3] for conv1;
inputSize = baseNetwork.Layers(1).InputSize;
imds_our_images = imageDatastore(imageStorageFolder);
featureLayer = 'conv1';
Image_Montage = cell(total_images,1);
bottomposition = [0 800];
%%
for i = 1:total_images
     current_imagename = ImageList(i).name;
     current_image = imread(current_imagename);

     if ndims(current_image) == 2  %#ok<ISMAT>
```

```
    % It's a 2D image.  Convert to 3-D.
        current_image = cat(3, current_image, current_image, current_image);
     end
     Image_Rot = imrotate(current_image,180);
     %CLAHE
     LAB = rgb2lab(Image_Rot+30);
     L = LAB(:,:,1)/100;
     L = adapthisteq(L,'NumTiles',[8 8],'ClipLimit',0.005);
     LAB(:,:,1) = L*100;
     Image_CLAHE = lab2rgb(LAB);
     %enlarging
     RegionInterest = [100 100 900 900];    % please fine tune the size of this rect↙
to get the best result [0 0 1100 900] [100 0 1200 1100]
     Image_Enlarge = imcrop(Image_CLAHE,RegionInterest);
     %Resizing
     imdsReSz=im2single(imresize(Image_Enlarge,networkInputSize(1:2)));
     %I = imdsReSz;
     %I = Image_CLAHE;
     I = Image_Enlarge;
     %% Yolov3 detector to display image and B-Box
     [bboxes,scores,labels] = detect(yolov3Detector,I);
     % filter based on confidence
     conffilter = 0.1;
     scoresbelow = find(abs(scores)<conffilter);
     scoresupper = find(abs(scores)>conffilter);
     scores(scoresbelow) = 0;
     scoresfiltered = scores(scores~=0);
     bboxesfiltered = bboxes(scoresupper,:);
     labelsfiltered = labels(scoresupper,:);
     % Display the detections on image.
     Final_Image = insertText(I,bottomposition,↙
current_imagename,'BoxColor','black','FontSize',50,'TextColor','white');
     if ~isempty(scoresfiltered)
           Final_Image = insertObjectAnnotation(Final_Image,'rectangle',↙
bboxesfiltered,labelsfiltered,'LineWidth',5,'TextBoxOpacity',0.5,'FontSize',40);
     end
     Image_Montage{i} = Final_Image;
end
run("showfigure.m");
save(append(wearfolderdir, '\Image Montage.mat'),"Image_Montage");
saveas(gca, fullfile(wearfolderdir, 'wearmontage'), 'jpeg');
```

D.5 Description of the Inductive-Reasoning

D.5.1 Determining Wear Mechanisms and Failure Modes

3/19/23 11:29 PM C:\Users\Ti...\predict_wear_mechanism.m 1 of 1

```
function [mechanisms] = predict_wear_mechanism(I)

%This function takes an image file name, a speed value, and...
% a feed value as input parameters. It loads the image file, extracts features...
% using image processing algorithms, and classifies the features into wear labels...
% using machine learning algorithms. Then, for each wear label, it predicts a wear...
% mechanism based on a switch statement that maps each wear label to a wear ↙
mechanism...
% Finally, it prints the wear label, wear mechanism, speed, and feed values for each ↙
wear...
% label using the fprintf function.   % Predict wear mechanisms for each label using ↙
a loop

  [~,~,labels] = detect(yolov3Detector,I); % Extracting failure modes from the ↙
YOLOv3-TWDM
  if isfield(predicted_labels, 'label')
      % Execute function for predicted label
      if predicted_labels.labels == 1
          for i = 1:length(labels)
                label = labels(i);
                switch label
                    case 'Uniforn flank wear'
                        mechanisms = 'abrasion,minor adhesion';
%                         bboxesfiltered = bboxes(scoresupper,:);
%                         Bh_FW = bboxesfiltered (4);
%                         Failure_magnitude = Bh_FW;
                    case 'notching'
                        mechanisms = 'abrasion,high impact force';
                    case 'flaking'
                        mechanisms = 'diffusion,abrasion,adhesion,oxidation';
                    case 'BUE'
                        mechanisms = 'Adhesion';
                    case 'chipping'
                        mechanisms = 'severe abrasion, cyclic adhesion';
%                         bboxesfiltered = bboxes(scoresupper,:);
%                         Bw_chipping = bboxesfiltered (3);
%                         Bh_chipping = bboxesfiltered (4);
%                         Failure_magnitude = [Bh_chipping,Bw_chipping];
                 end
                fprintf('Wear label: %s\n', label);
                fprintf('Wear mechanism: %s\n', mechanisms);
          end
      end
      else
    disp('No predicted label found');
  end
```

D.5.2 Determining the LTV and Process Parameters

3/19/23 11:26 PM C:\Users\Tiya...\determine_speed_feed.m 1 of 2

```
function [v, f] = determine_speed_feed(v_initial,f_initial)
%The code defines the initial cutting speed (v_initial), initial feed rate ↙
(f_initial),...
% and wear thresholds (LTV).
% The calculate_speed_feed function takes the limiting values of LTV...
% It checks if any LTV exceeds the limit for each flank wear level
% Calculates the adjusted cutting speed (v) and feed rate (f) based on the highest ↙
percentage of LTV...

Optimal_parameter_1 = v_initial;                % Initial cutting speed (m/min)
Optimal_parameter_2 = f_initial;                % Initial feed rate (mm/tooth)

LTV1_Fi = 2000000; LTV2_Fi = 4000000; LTV3_Fi = 5000000; LTV4_Fi = 7000000;
LTV1_BhFW = 90; LTV2_BhFW = 170; LTV3_BhFW = 250; LTV4_BhFW = 430;
LTV1_BhChip = 30; LTV2_BhChip = 70; LTV3_BhChip = 100; LTV4_BhChip = 170;
LTV1_BwChip = 80; LTV2_BwChip = 180; LTV3_BwChip = 270; LTV4_BwChip = 420;

% Fi_limits = [LTV1_Fi,LTV2_Fi,LTV3_Fi,LTV4_Fi];                    % initial ↙
feature 1 (pixels)
% BhFW_limits = [LTV1_BhFW,LTV2_BhFW,LTV3_BhFW,LTV4_BhFW];          % initial ↙
feature 2 (pixels)
% BhChip_limits = [LTV1_BhChip,LTV2_BhChip,LTV3_BhChip,LTV4_BhChip]; % initial ↙
feature 3 (pixels)
% BwChip_limits = [LTV1_BwChip,LTV2_BwChip,LTV3_BwChip,LTV4_BwChip]; % initial ↙
feature 4 (pixels)

F_i = multi_sectional_SVD(Image);

 [~,~,labels] = detect(yolov3Detector,I); % Extracting failure modes from the YOLOv3- ↙
TWDM
    for i = 1:length(labels)
          label = labels(i);
                switch label
                    case 'Uniforn flank wear'
                         bboxesfiltered = bboxes(scoresupper,:);
                         BhFW = bboxesfiltered (4);
                    case 'chipping'
                         bboxesfiltered = bboxes(scoresupper,:);
                         BwChip = bboxesfiltered (3);
                         BhChip = bboxesfiltered (4);
                end
    end

if Fi <= LTV1_Fi || BhFW <= LTV1_BhFW || BhChip <= LTV1_BhChip || BwChip <= ↙
LTV1_BwChip
    mechanisms = predict_wear_mechanism(I);
    wear_percentage = max([(Fi/LTV1_Fi);(BhFW/LTV1_BhFW);(BhChip/LTV1_BhChip); ↙
(BwChip/LTV1_BwChip)]);
    % Calculate the adjusted cutting speed and feed rate
```

```
    v = Optimal_parameter_1 * (1 + wear_percentage);
    f = Optimal_parameter_2 * (1 - wear_percentage);

elseif (LTV1_Fi < F_i) && (F_i <= LTV2_Fi) || (LTV1_BhFW < BhFW) && (BhFW <= ↙
LTV2_BhFW) ...
        || (LTV1_BhChip < BhChip) && (BhChip <= LTV2_BhChip) || (LTV1_BwChip < ↙
BwChip) && (BwChip <= LTV2_BwChip)
    disp('It is a uniform wear stage');
    mechanisms = predict_wear_mechanism(I);
    wear_percentage = max([(Fi/LTV2_Fi);(BhFW/LTV2_BhFW);(BhChip/LTV2_BhChip); ↙
(BwChip/LTV2_BwChip)]);
    % Calculate the adjusted cutting speed and feed rate
    v = Optimal_parameter_1 * (1 + wear_percentage);
    f = Optimal_parameter_2 * (1 - wear_percentage);

elseif (LTV2_Fi < F_i) && (F_i <= LTV3_Fi) || (LTV2_BhFW < BhFW) && (BhFW <= ↙
LTV3_BhFW) ...
        || (LTV2_BhChip < BhChip) && (BhChip <= LTV3_BhChip) || (LTV2_BwChip < ↙
BwChip) && (BwChip <= LTV3_BwChip)
    disp('It is the critical region, so tools can failure any time');
    mechanisms = predict_wear_mechanism(I);
    wear_percentage = max([(Fi/LTV3_Fi);(BhFW/LTV3_BhFW);(BhChip/LTV3_BhChip); ↙
(BwChip/LTV3_BwChip)]);
    % Calculate the adjusted cutting speed and feed rate
    v = Optimal_parameter_1 * (1 + wear_percentage);
    f = Optimal_parameter_2 * (1 - wear_percentage);

elseif Fi > LTV3_Fi || BhFW > LTV3_BhFW || BhChip > LTV3_BhChip || BwChip > ↙
LTV3_BwChip
    disp('The tools have reached the failure stage, no action is required');
    mechanisms = predict_wear_mechanism(I);

elseif Fi > LTV4_Fi || BhFW > LTV4_BhFW || BhChip > LTV4_BhChip || BwChip > ↙
LTV4_BwChip
    disp('Tools have failed, stop cutting and change them');
    mechanisms = predict_wear_mechanism(I);
else
    disp('Continue with the current process parameters');
end

fprintf('Wear label: %s\n', label);
fprintf('Wear mechanism: %s\n', mechanisms);
fprintf('Wear mechanism: %s\n', v);
fprintf('Wear mechanism: %s\n', f);
```

Appendix E

MV-TCM Assembly Drawing

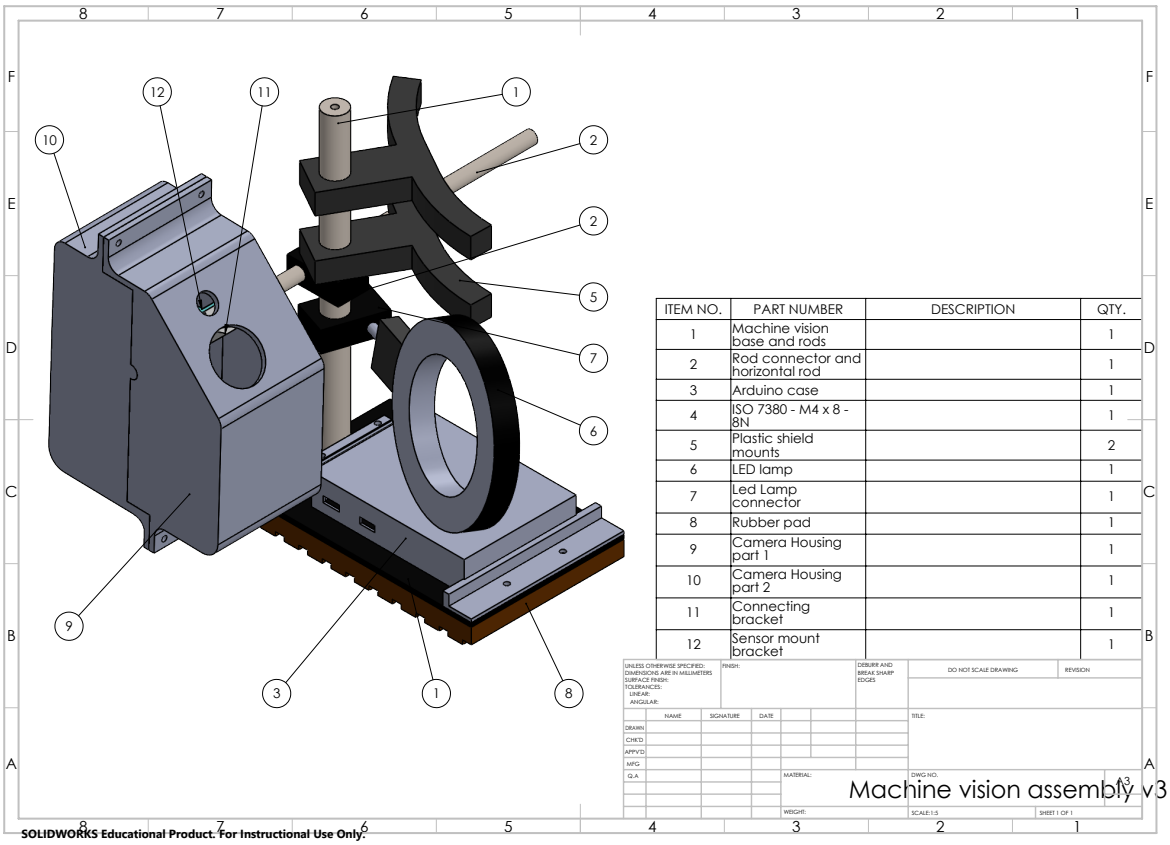

ITEM NO.	PART NUMBER	DESCRIPTION	QTY.
1	Machine vision base and rods		1
2	Rod connector and horizontal rod		1
3	Arduino case		1
4	ISO 7380 - M4 x 8 - 8N		1
5	Plastic shield mounts		2
6	LED lamp		1
7	Led Lamp connector		1
8	Rubber pad		1
9	Camera Housing part 1		1
10	Camera Housing part 2		1
11	Connecting bracket		1
12	Sensor mount bracket		1

UNLESS OTHERWISE SPECIFIED: DIMENSIONS ARE IN MILLIMETERS SURFACE FINISH: TOLERANCES: LINEAR: ANGULAR:
FINISH:
DEBURR AND BREAK SHARP EDGES
DO NOT SCALE DRAWING
REVISION

	NAME	SIGNATURE	DATE
DRAWN			
CHK'D			
APPV'D			
MFG			
Q.A			

TITLE:
MATERIAL:
DWG NO.
Machine vision assembly v3
WEIGHT:
SCALE:1:5
SHEET 1 OF 1

SOLIDWORKS Educational Product. For Instructional Use Only.

Appendix F

Validation Data

F.1 Condition 1: $V_c = 40m/min$, $f_t = 0.08mm/tooth$ and $a_p = 0.9mm$

F.1.1 Average values for Replicate 1

Table F.1: Comparison of the Actual and Predicted Values for Replicate 1

L(mm)	$F.mode_a$	$Bh_{chip(a)}$	$Bw_{chip(a)}$	VB_a	$F.Mode_p$	$Bh_{chip(p)}$	$Bw_{chip(p)}$	VB_p
400	UFW	-	-	84	UFW	-	-	80
800	UFW	-	-	88	UFW	-	-	86
1200	UFW	-	-	112	UFW	-	-	76
1600	UFW	-	-	116	UFW	-	-	80
2000	UFW	-	-	120	UFW	-	-	97
2400	UFW	-	-	120	UFW	-	-	125
2800	BUE	-	-	120	BUE	-	-	116
3200	BUE	-	-	121	BUE	-	-	118
3600	BUE	-	-	120	BUE	-	-	117
4000	BUE	-	-	124	BUE	-	-	126
4400	CW,BUE	96	292	144	CW,BUE	92	279	142
4800	CW,BUE	112	248	145	CW	118	240	141
5200	CW,BUE	84	144	164	CW	80	148	167
5600	CW,BUE	132	328	208	CW,BUE	135	320	203
6000	CW,BUE	236	456	284	CW	246	445	278
6400	CW,BUE	260	716	360	CW	268	700	352
6800	CW,FW	508	828	724	CW,FW	502	802	748

F.1.2 Average values for Replicate 2

Table F.2: Comparison of the Actual and Predicted Values for Replicate 2

L(mm)	$F.mode_a$	$Bh_{chip(a)}$	$Bw_{chip(a)}$	VB_a	$F.Mode_p$	$Bh_{chip(p)}$	$Bw_{chip(p)}$	VB_p
400	UFW	-	-	92	UFW	-	-	100
800	UFW	-	-	88	UFW	-	-	84
1200	UFW	-	-	92	UFW	-	-	96
1600	UFW	-	-	92	UFW	-	-	80
2000	UFW	-	-	100	UFW	-	-	102
2400	UFW	-	-	104	UFW	-	-	98
2800	CW	76	172	96	CW	90	143	121
3200	CW	196	200	100	UFW,CW	232	190	105
3600	UFW,CW	72	176	100	UFW	83	158	123
4000	UFW,CW	104	184	108	UFW	128	165	118
4400	UFW,CW	96	184	108	UFW,CW	118	160	125
4800	UFW,BUE	-	-	135	UFW,BUE	-	-	150
5200	CW,BUE	724	868	424	CW,BUE	256	866	326
5600	CW,BUE	424	562	482	CW,BUE	507	517	428
6000	CW,FW	176	936	816	CW,FW	200	832	604

F.2 Condition 2: $V_c = 60m/min$, $f_t = 0.08mm/tooth$ and $a_p = 0.9mm$

F.2.1 Average values for Replicate 1

Table F.3: Comparison of the Actual and Predicted Values for Replicate 1

L(mm)	$F.mode_a$	$Bh_{chip(a)}$	$Bw_{chip(a)}$	VB_a	$F.Mode_p$	$Bh_{chip(p)}$	$Bw_{chip(p)}$	VB_p
400	UFW	-	-	50.5	UFW	-	-	60.5
800	UFW	-	-	59.8	UFW	-	-	74
1200	UFW,CW	17.5	92.5	79	UFW	20	89	67
1600	UFW,CW	23	104	87	UFW	25.25	86	72
2000	UFW,CW	51.8	241	107	UFW,CW	51	207	95
2400	UFW,CW	56.5	255	111	UFW,CW	65.25	234	120
2800	BUE,CW	125	579	165	CW	143	552	166
3200	BUE,CW	187	893	261	BUE,CW	175	808	223
3600	BUE,CW,FW	402	904	474	CW	375	787	457

F.2.2 Average values for Replicate 2

Table F.4: Comparison of the Actual and Predicted Values for Replicate 2

L(mm)	$F.mode_a$	$Bh_{chip(a)}$	$Bw_{chip(a)}$	VB_a	$F.Mode_p$	$Bh_{chip(p)}$	$Bw_{chip(p)}$	VB_p
400	UFW	-	-	75	UFW	-	-	68
800	UFW	-	-	75	UFW	-	-	71
1200	UFW,CW	23	96	81	UFW	27	65	65
1600	UFW,CW	45	152	95	CW	48	134	70
2000	UFW,CW	64	207	94	UFW,CW	66	195	88
2400	UFW,CW	114	341	111	CW	125	339	100
2800	BUE,CW	84	461	121	CW	106	478	117
3200	CW	85	385	148	CW	115	371	138
3600	CW,BUE,FW	215	887	331	CW	251	831	305

F.3 Condition 3: $V_c = 1000m/min$, $f_t = 0.15mm/tooth$ and $a_p = 0.9mm$

F.3.1 Average values for Replicate 1

Table F.5: Comparison of the Actual and Predicted Values for Replicate 1

L(mm)	$F.mode_a$	$Bh_{chip(a)}$	$Bw_{chip(a)}$	VB_a	$F.Mode_p$	$Bh_{chip(p)}$	$Bw_{chip(p)}$	VB_p
200	UFW	-	-	76	UFW	-	-	79
400	UFW,CW	17.75	136	80	CW	67	155	85
600	UFW,CW	35.25	387	89	CW	41	418	87
800	CW,BUE	177	616	364	CW	170	557	290
1000	CW,BUE,FW	403	1135	508	CW	346	740	554

F.3.2 Average values for Replicate 2

Table F.6: Comparison of the Actual and Predicted Values for Replicate 2

L(mm)	$F.mode_a$	$Bh_{chip(a)}$	$Bw_{chip(a)}$	VB_a	$F.Mode_p$	$Bh_{chip(p)}$	$Bw_{chip(p)}$	VB_p
200	UFW	-	-	70	UFW	-	-	75
400	UFW	-	-	81	UFW	-	-	76
600	UFW,CW	49	414	114	CW	47	266	88
800	CW	250	662	307	CW	192	639	292
1000	CW,BUE,FW	591	1202	625	CW	496	938	442